THE UNIVERSITY OF CHICAGO

ODD DYNAMICS OF COLLOIDAL CHIRAL MATTER

A DISSERTATION SUBMITTED TO
THE FACULTY OF THE DIVISION OF THE PHYSICAL SCIENCES
IN CANDIDACY FOR THE DEGREE OF
DOCTOR OF PHILOSOPHY

DEPARTMENT OF PHYSICS

BY
EPHRAIM SOLOMON BILILIGN

CHICAGO, ILLINOIS
MARCH 2023

To my partner, L. K.

TABLE OF CONTENTS

LIST OF FIGURES

LIST OF TABLES

ACKNOWLEDGMENTS

Reflecting on my graduate experience, and the larger story of my life leading up to this point, my years of academic and personal growth seem in some ways inevitable. But, upon closer inspection, it is clear that the path I've taken was scaffolded by many others, without whom I would never have been able to reach this point.

As a child, I was obsessive, detail-oriented, and easily frustrated by things I couldn't fully explain. There to guide my curiosity and emotions were my father and mother. While my academic trajectory has been linear, their trajectories have been marred by life-altering challenges, and their resilience characterized by a sense of courage that escapes my own understanding. Both made their own paths in a new country, and built a life for me and my siblings that, despite my parents' own upbringing, was filled with freedom to be creative and explore seemingly endless opportunities. With Yishak, Aster, and Beka, who endured and contributed to the chaos of our home alongside me, I've learned to be lighthearted, vulnerable, and reflective.

An uncountable group of teachers, counselors, friends, and family showed me how to channel my energy into learning. But, it wasn't until taking Steve Shapiro's introductory physics courses in high school that I felt I had real direction. From there, I have many research mentors to thank for edifying experiences that instilled in me a sense of belonging in the science world. Most importantly, at a moment of doubt in my abilities and disillusionment in physics as a whole, I met Karen Daniels, who entrusted me with a research project that gave me a chance to once again be an obsessive, detail-oriented (grown-up) child. Here, I found a home, and I was indoctrinated into a community of soft matter physicists that inspired me, drawing me to talks, conferences, and research overseas.

This newfound feeling of belonging drew me to the University of Chicago, the home of granular physics legends Sid Nagel and Heinrich Jaeger, who were regrettably not a part of my research, but invaluable mentors nonetheless. In my search for something new, I took on

what I thought would be a short-term endeavor with William Irvine. Instead, I walked into a GCIS basement lab filled with a perfect balance of dysfunction and enthusiasm, and ended up being absorbed into it. Among the many faces that have been a part of my experience in this lab, there are a few I want to highlight and thank.

In the early days, my experience was largely shaped by Noah Mitchell, who exuded the aura of a professor and taught me, if nothing else, to take my work seriously. His influence was outmatched by the chaos constantly injected by other characters, including Jiayi Wu and Sattvic Ray. Lastly, I have to thank Sofia Magkiriadou for being a source of optimism and giving me the tools to be a successful experimentalist. Without her, many of William's more outlandish ideas, including those he proposed to me, would never have made it to reality.

In more recent times, I thank Severine Atis for joining the lab and immediately bringing with her a sense of perspective on the world of science beyond our walls, and channeling that in the way she invested in everyone's work. Bringing another form of perspective, that of a theoretical physicist, was Yehuda Ganan. Since Yehuda joined our group, my days of agonizing over physics questions alone were gone. Among his many qualities, Yehuda is great at latching onto a problem and exhaustively reaching a solution, and I've definitely benefited from both seeing that mentality and sharing the resulting stress it entails. Finally, as I depart the lab, it's a relief to know that it is now in the capable hands of Matteo Sabato, Desmond Li, and Panyu Chen.

To two constants in my graduate adventure, Robert Morton and Takumi Matsuzawa, I owe a great deal of thanks. Some days, Bob and I spent more hours in conversation, some of it one-sided ranting, than we spent working. His willingness to listen to my unformed thoughts, answer my ill-posed scientific questions, and critique my poorly constructed plots is a testament to Bob's character. While Takumi and I never shared an office, he tended to spontaneously appear most days on the couch (and in conversation) between Bob and I. I've never met someone as tirelessly committed to producing astonishing scientific work, yet

so humble about what he's been able to accomplish. I thank Takumi not only for setting the standard in our lab, but being so willing to share his time. Both Bob and Takumi have, more than anyone, inspired the microscopic details of how I do science.

While he left the lab years ago, nobody embodies the lab's spirit more than Vishal Soni. I learned a great deal from Vish through working with him for only a few years, but I'm most thankful for the areas in which he did not explicitly guide me. Vish showed me how to be haphazardly creative and to dare to break things in the process. But, he was also always attuned to my ideas, and there to offer a willing ear in good times and bad.

There are too many other people in the basement of GCIS and elsewhere to name them all, but my graduate experience was also enlivened by the soft matter cohort from my class: Mike van der Naald, Colin Scheibner, Savannah Gowen, and of course fellow teacher's pet Chloe Lindeman. A number of other colleagues shaped my time and work, including my committee members Suri Vaikuntanathan and Paul Wiegmann, and fellow odd scientists Anton Souslov and Vincenzo Vitelli, who (partly by accident) inspired us to explore time-modulated rotation.

On a scientific front, this work was only possible through the contributions of many collaborators. Sofia, Yehuda, Vishal, and I all shared countless hours in the lab working on this long and winding project. In addition, I am grateful to Florencio Balboa Usabiaga, Leroy Jia, and Alexis Poncet for contributing to the simulations and theory that made the work in this dissertation possible, and to Stefano Sacanna for his colloid expertise. All of my graduate research has been guided by a trio that included Denis Bartolo and Michael Shelley, who I cannot thank enough for their support and their role in shaping my scientific identity. And of course, William Irvine had the vision to assemble this supergroup of scientists and gave me a chance to be a part of something that I, after five years, still think is cool. For that, I will always be grateful.

Time, distance, and a global pandemic have shaped the relationships I have with so

many people, but only one has been a constant. While the supporters I've mentioned above scaffolded my path, I wouldn't have the strength to navigate it without my partner, to whom this dissertation is dedicated. Along this journey, we've shown exceptional resolve to fight through numerous challenges together, but I've never felt alone, and I've always felt the unending love of an unwavering advocate. Oddly enough, the fact that I've made it to this point is not so much a reflection of my singular effort, but rather the growth we've undergone together.

ABSTRACT

The symmetries that underly conventional equilibrium matter provide the grounding for continuum mechanical models. In this work, we engineer a chiral material comprised of millions of spinning colloidal magnets as a testing ground for breaking these symmetries and observing the resulting odd dynamics. By activating the fluid phase at the single unit level, we observe macroscopic flows with no counterpart in conventional fluids. Along a boundary of the fluid, we observe unidirectional free-surface waves that propagate due to an interplay between viscous and odd rotational stresses. These waves are dissipated by both surface tension and odd viscosity, an anomalous transport coefficient permitted through broken time-reversal and parity symmetries. Then, we ask a deceptively simple question: what is the effect of adding transverse interactions on the solid phase? At the system scale, non-reciprocity causes colloidal spinners to organize into crystalline whorls which sustain super-diffusive mass transport that can be controlled over orders of magnitude. By combining experimental measurements with fully-resolved hydrodynamic and minimal model simulations, we find that this phase spontaneously arises from the interplay of intrinsic odd stresses and odd elastic moduli unconstrained by energy conservation, which conspire to enable the self-propulsion of topological defects. Finally, we lift the constraint of isotropy that underlies our viscous and elastic models, enabling spatiotemporal control of the morphology of chiral matter through the time-modulation of the drive.

CHAPTER 1

INTRODUCTION

Newton's *Principia* is cited in some form at the beginning of most classical mechanics textbooks, and from it come three non-negotiable rules. Among them is what is often labelled Newton's third law [1]:

> To any action there is always an opposite and equal reaction; in other words, the actions of two bodies upon each other are always equal and always opposite in direction.

These rules are natural, and explain much of what we experience in the everyday world, but fall short in many living and active systems. In this introduction, we will take these rules for granted and arrive at a description of conventional materials that, upon the introduction of *non-reciprocal* forces - those that violate Newton's third law - break down.

1.1 Odd continuum mechanics

In condensed matter physics, seeking to understand a system's behavior on the basis of individual interactions between constituent building blocks is often intractable. The pioneering work of Cauchy, Poisson, and Navier in 19^{th} century introduced the use of continuum mechanical theories, which are models of materials that ignore their discrete atoms [2]. Continuum mechanical models of fluids have been used to model the flows of liquids and gases via equations that describe infinitely small volumes of fluid, themselves representing even smaller underlying molecules [3]. The counterpart to fluid mechanics for solid bodies describes the deformation of continuous medium in lieu of representing the displacement of each individual atom [4].

Often rules like Newton's, while written for individual particles and bodies, can help us make statements regarding the symmetries of continuous media. These symmetries often

allow for the removal of generality in a system's equations of motion. For example, Newton's third law tell us that reciprocal forces conserve momentum and energy, which forms the basis for the description of fluids and solids. Conventional materials that follow these mechanical rules also abide by familiar symmetries: *time-reversal symmetry* means that a system evolves according to the same rules when time runs backwards, and *parity symmetry* means that a system's behavior is not changed if viewed under a mirror reflection.

For any material, regardless of symmetries, the continuum mechanical description is built from coarse-graining the microscopic interaction rules - the inter-particle forces that Newton's laws govern. From these atom-level interactions come models for the stresses experienced by an infinitesimal element of a fluid or solid, $\sigma_\alpha = \eta_{\alpha\beta}\dot{u}_\beta$ and $\sigma_\alpha = K_{\alpha\beta}u_\beta$, respectively. Here, $\eta_{\alpha\beta}$ and $K_{\alpha\beta}$ are the viscosity and elasticity tensors, objects that represent the linear relationship between stress (σ_α) and a continuous medium's deformation (u_β) or the rate thereof ($\dot{u}_\beta$). With this choice of representation, each entry of σ_α and u_β have a clear physical meaning:

$$\sigma_\alpha = \left(\quad \right), \qquad u_\beta = \left(\quad \right), \tag{1.1}$$

which represent dilation ( ), torque ( ), and shear (,) and their counterpart strains. While we will thoroughly delve into the components of these complex objects in this thesis, the aforementioned symmetries have a simple mathematical consequence: $\eta_{\alpha\beta} = \eta_{\beta\alpha}$ and $K_{\alpha\beta} = K_{\beta\alpha}$. That is: the reciprocal linear response at the level of individual particles is reflected in the reciprocal response of the continuum. For example, if a solid that is compressed experiences a torque, then it must experience a pressure when it is rotated.

These symmetries are often relaxed in soft, non-equilibrium condensed matter. In fluids, time-reversal and parity symmetries can be broken by, for instance, the constant activation of the fluid molecules by external injection of momentum. As a consequence, contributions to the viscosity that are *odd* in nature are permitted, and have the structure $\eta^o_{\alpha\beta} = -\eta^o_{\beta\alpha}$, enabling non-reciprocal couplings between stresses and strains. Among these is the *odd*

viscosity, a long theorized transport coefficient that redirects flows rather than dissipating them [5, 6, 7, 8, 9]. Meanwhile, the underlying conservation rules of elasticity can be broken through non-reciprocal interactions between atoms, likewise enabling a zoology of *odd elastic* coefficients. Recent theoretical work points to potential elastic moduli that, for example, could non-reciprocally relate dilation and rotation [10, 11]. One might then ask: *what can odd stress do for you?* With these recent generalizations of conventional continuum mechanics comes hope for explaining a wide range of systems including robotic metamaterials [12, 13], biological matter [14], chiral fluids [15, 16], and odd topological defects [17], through the inclusion of odd effects.

1.2 Overview of this thesis

In this thesis, we will take the rules of continuum mechanics as a starting point, and unlock new potential phenomenology by breaking the symmetries that underly their utility. To realize a continuous medium from which we can extract the spatiotemporal properties of millions of constituent elements, we utilize a colloidal model system. Then, to introduce the non-reciprocal interactions that are hallmarks of odd materials, we drive these particles rotationally. In Chapter 1, we treat the dense phase these colloids form as a chiral fluid. We demonstrate that this rotational drive causes a fundamental change in the particle interactions at the microscopic level, as diagramed in Figure 1.1. Here, the introduction of self-spinning produces an antisymmetric stress, known as the *odd stress*, that constantly powers the system through a uniform active torque density. By contrast to conventional fluids, this material sustains dynamics driven by viscosity rather than suppressed by it. In addition, the microscopic interactions are altered, breaking parity symmetry to enable the generation of transverse momentum as in (a-b). The consequence is the introduction of an odd viscosity that non-reciprocally couples transverse modes of shear flow (c), and is measured in experiments through its effect on the dissipation of surface waves.

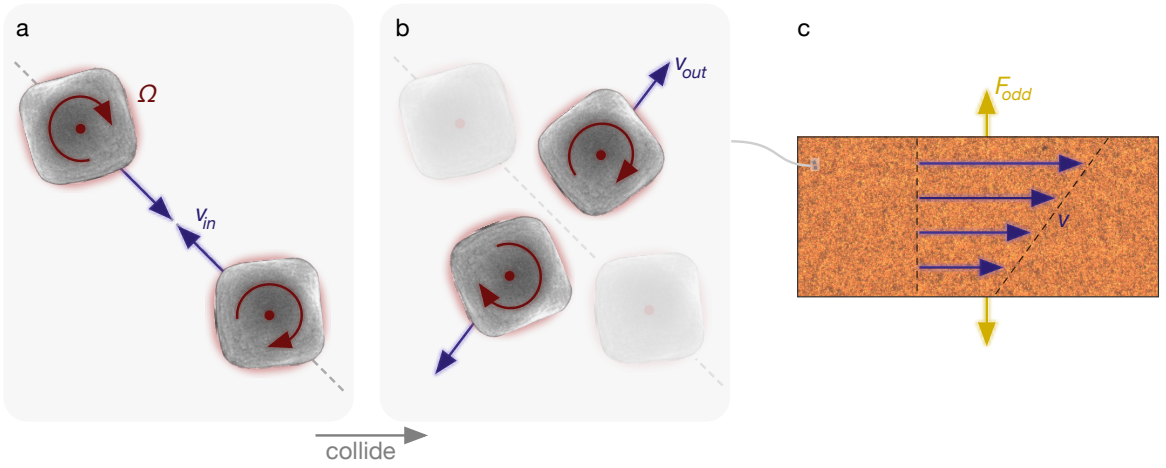

Figure 1.1: **Odd viscosity through rotational drive. a,** Two particles spin at a fixed rate Ω and collide at an incident velocity v_{in}. **b,** Due to rotational interactions, their resultant trajectories v_{out} need not conserve angular momentum. **c,** On a continuum level, consequently, gradients in flow can generate transverse stresses through odd viscosity.

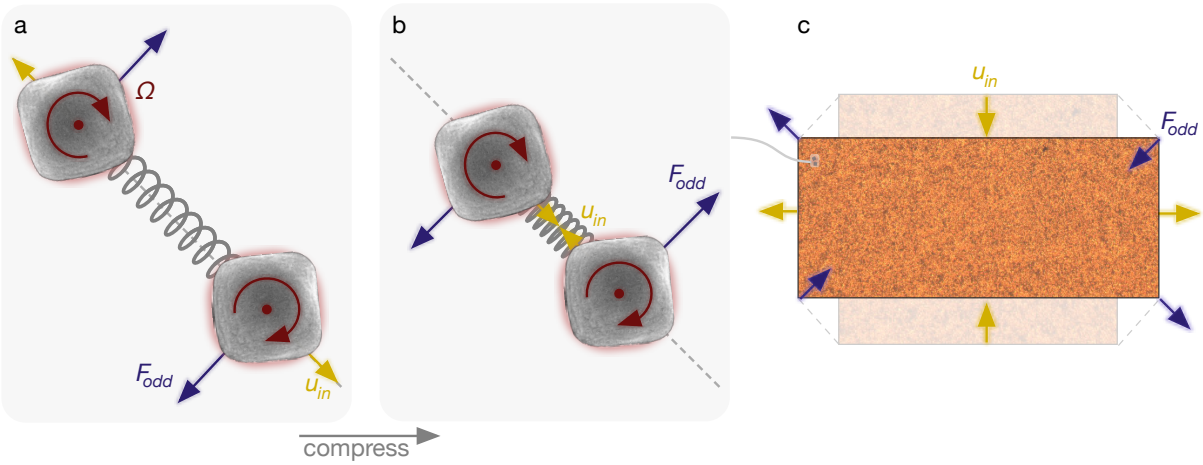

Figure 1.2: **Odd elasticity through transverse forces. a,** Two spinning particles exert non-reciprocal transverse forces that can be viewed as an odd spring. Under extension, there is a transverse force in one direction, **b,** and another direction under compression. **c,** A solid comprised of odd springs can sustain odd elasticity, wherein shear strain in one axis produces stresses in the transverse axis.

Upon closer inspection, we observe that the seemingly quiescent bulk of this fluid in fact sustains its own lively dynamics. Our observations of the system in a crystalline phase suggest not a hydrodynamic description, but rather a treatment of the material as a solid. In Chapter 2, we describe the crystalline 'whorl' phase that is formed when particle-level activation is

introduced to a conventional solid, and find that this odd crystal is spontaneously destabilized by the presence of self-propelled dislocations, or localized bits of crystalline fracture. While the mobility of dislocations is powered by odd stress, we notice structural responses to strain that are unexpected, but consistent with the presence of odd elastic moduli that arise from transverse spring-like interactions between particles as in Figure 1.2a-b. These non-reciprocal forces enable novel stress-strain couplings (c) that can melt an odd crystal from within.

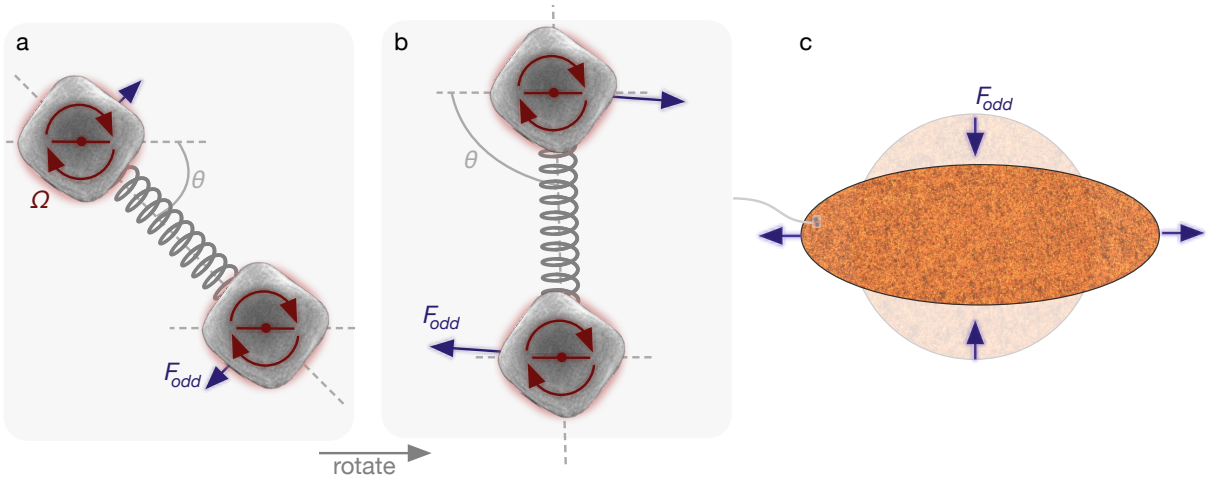

Figure 1.3: **Spatially anisotropic odd matter. a,** By modulating the rotation of particles to stall along a specified axis, the spring-like transverse forces can be **b,** tuned by the orientation of the inter-particle bond. **c,** A chiral medium subjected to time-modulation sustains an intrinsic stress imbalance that causes it to deform.

In the final part of this thesis, we revisit chiral matter and lift the constraint of isotropy by giving the dynamics of the particles a preferred axis. To do so, we apply a temporally-modulated rotational drive that arrests the rotation of the particles at specified temporal points that are correlated with one or multiple spatial axes. As depicted in Figure 1.3a-b, the odd spring that characterizes interactions between particles now has a notion of spatial orientation, leading to an orientation-dependence of the elastic parameters. The resulting phase is characteristically different in both the bulk and surface, giving rise to intrinsic structural fluctuations that generate surface stresses to produce novel, tunable morphologies (c). In addition, the successive breaking of conservation laws and symmetries of this odd

material unlocks new instability phenomenology reminiscent of conventional fluids with a chiral twist.

CHAPTER 2

SURFACE FLOWS OF A COLLOIDAL CHIRAL FLUID

This chapter is primarily comprised of material reproduced from the publication Ref. [18]: Soni, V.*, Bililign, E. S.*, Magkiriadou, S.*, Sacanna, S., Bartolo, D., Shelley, M. J., & Irvine, W. T. M. The odd free surface flows of a colloidal chiral fluid. *Nature Physics* **15**, 1188-1194 (2019). *Reproduced with permission from Springer Nature.*

In simple fluids, such as water, invariance under parity and time-reversal symmetry imposes that the rotation of constituent "atoms" is determined by the flow and that viscous stresses damp motion. Activation of the rotational degrees of freedom of a fluid by spinning its atomic building blocks breaks these constraints and has thus been the subject of fundamental theoretical interest across classical and quantum fluids. However, the creation of a model liquid which isolates chiral hydrodynamic phenomena has remained experimentally elusive. Here we report the creation of a cohesive two-dimensional chiral liquid consisting of millions of spinning colloidal magnets and study its flows. We find that dissipative viscous "edge-pumping" is a key and general mechanism of chiral hydrodynamics, driving uni-directional surface waves and instabilities, with no counterpart in conventional fluids. Spectral measurements of the chiral surface dynamics reveal the presence of Hall viscosity, an experimentally elusive property of chiral fluids. Precise measurements and comparison with theory demonstrate excellent agreement with a minimal but complete chiral hydrodynamic model, paving the way for the exploration of chiral hydrodynamics in experiment.

2.1 Introduction

Hydrodynamic theories describe the flow of systems as diverse as water, quantum electronic states [19], and galaxies [20] over decades in scale [21]. Since hydrodynamic equations are built on symmetry principles and conservation laws alone, systems with similar symmetries

have similar descriptions and flow in the same way.

For example, symmetry under parity and time reversal – conditions met by all conventional fluids at thermal equilibrium – constrains both the stress and viscosity tensors to be symmetric. These constraints are in principle alleviated in collections of interacting units that are driven to rotate [22, 23, 24, 25, 26, 27, 28]. This seemingly innocent twist on an otherwise structureless fluid represents, however, an elemental change with rich hydrodynamic consequences common to quantum Hall fluids, vortex fluids, and chiral condensed matter [29, 5, 15, 6, 7, 30, 31, 32]. Collections of spinning particles offer a natural opportunity to engineer and study the properties of such chiral fluids; experimental examples include rotating bacteria [33, 34], colloidal and millimeter-scale magnets [35, 36, 37, 38, 39, 40], ferrofluids in rotating magnetic fields [41, 42], and shaken chiral grains [43, 44]. Such systems have been shown to have non-trivial dynamics. For example, ferrofluids driven by AC fields can flow against external pressure [45] and small numbers of spinning particles self-assemble into dynamic crystalline clusters [35, 36, 37, 38, 46, 47, 48, 39, 40, 49].

2.2 A colloidal chiral fluid

We report the creation of a millimeter-scale cohesive chiral fluid (Fig. 2.1a) by spinning millions of colloidal magnets with a magnetic field (Figs. 2.1b, 2.1c), and we track its flows over hours. The macroscopic flow of our chiral fluid is reminiscent of free surface flows of Newtonian fluids: nearby droplets merge (Fig. 2.1d), fluid spreads on a surface under the influence of gravity (Fig. 2.1e), voids collapse (Fig. 2.1f), and thin streams go unstable, as revealed by flowing fluid past a solid object (Fig. 2.1g). We demonstrate that these seemingly familiar features are accompanied by unique free surface flows. We then exploit the odd interfacial dynamics of this prototypical chiral liquid to infer its material constants, which remain out of reach of conventional rheology.

In the following sections, we describe the experimental procedures by which this colloidal

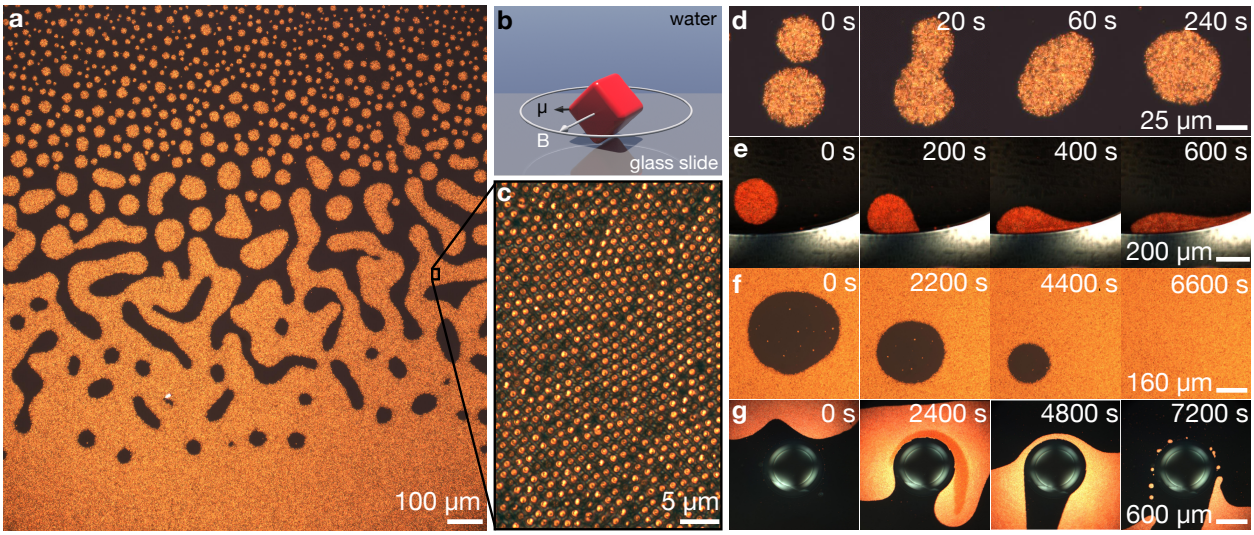

Figure 2.1: **A chiral fluid of spinning colloidal magnets. a,** Optical micrograph of the colloidal magnets in bulk, after a few minutes of spinning. **b,** Schematic of one colloidal particle. The $\sim$1.6 μm hematite colloidal cubes have a permanent magnetic moment (μ, black arrow). They are suspended in water, sedimented onto a glass slide, and spun by a rotating magnetic field (B, white arrow tracing the white circle). **c,** Optical micrograph of the colloidal magnets in bulk at increased magnification. **d-g,** The particles attract and form a cohesive material with an apparent surface tension that, over timescales from minutes to hours, behaves like a fluid: **d**, clusters coalesce and **e**, spread like liquid droplets when sedimented against a hard wall; **f**, void bubbles collapse; and **g**, when driven past an obstacle, the fluid flows around it, thinning and eventually revealing an instability to droplet formation. All images were taken through crossed polarizers.

chiral fluid is fabricated and driven (Section 2.2.1), the manner in which the flows of Figure 2.1 are generated (Section 2.2.2), and the tools we use to capture particle-level dynamical information using high-speed video microscopy (Section 2.2.3).

2.2.1 Experimental protocols & rotational drive

Colloidal synthesis We synthesize hematite cubes following the method described by Sugimoto et al in [50], and subsequently coat them in a thin silica shell using a Stöber method described in [51]. We suspend the cubes in water and, unless otherwise noted, we enclose the suspension in a glass chamber (see Figure 2.4a).

Magnetic field control We generate rotating magnetic fields by three pairs of coils. In all experiments we control the magnitude ($B = 1.3$ mT) and orientation of the magnetic field with a computer. We program the field parameters in a Python script and send them to a National Instruments DAQ card (PCIe-6363) via the PyDAQmx Python driver [52]. We then amplify the DAQ output voltage by a custom voltage-to-current amplifier that powers each coil pair. We record the currents through all coils continuously, so the orientation of the magnetic field at every moment in time is known.

Roll and drift compensation In order to observe dynamics at long timescales, care must be taken to minimize particle drift. Drift can occur either due to a tilt of the experimental setup with respect to gravity, which will cause sedimentation; or due to a misalignment of the spinning axis of the magnetic field, which will cause rolling (see Figure 2.2a-b). In the case of low-friction experiments, particles naturally collect in a locally flat region due to gravity, eliminating sedimentation. Meanwhile, for high-friction experiments, we minimize sedimentation by adjusting the tilt of the sample with the magnetic field off. As shown in Figure 2.2c, the rolling velocity is linearly proportional to the angle between the spinning axis and the normal to the substrate for a wide range of angles. We minimize rolling by

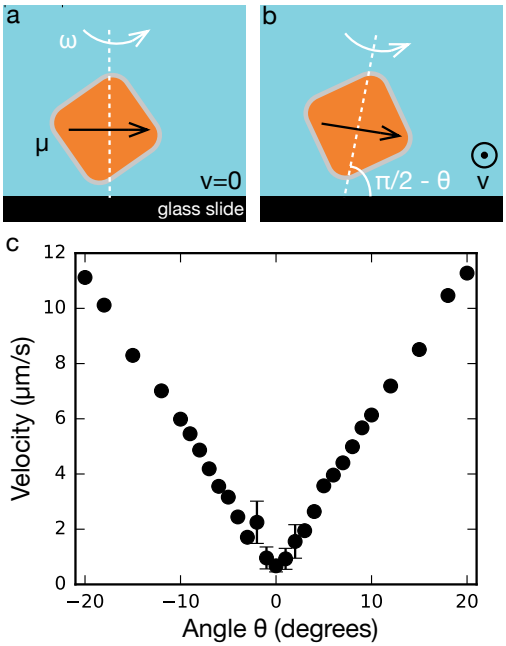

Figure 2.2: **Rolling motion. a,** If the rotation axis of the magnetic field is perpendicular to the substrate, the particle spins in place without rolling. Its translational velocity vanishes, $v = 0$. **b,** If the rotation axis of the magnetic field is not perpendicular to the substrate and deviates from the normal by an angle θ, the particle will roll as it spins and $v \neq 0$. **c,** The rolling speed depends linearly on the tilt angle θ for angles at least up to 20 degrees.

adjusting the relative amplitudes of the currents through all three coil pairs until particle clusters do not move by more than a couple of pixels within a couple of minutes. Our setup allows arbitrary control of the magnetic field axis, which enables rolling the particles in any desirable direction. This feature is very useful for the preparation of the initial state in many of our experiments.

2.2.2 Control of the initial conditions

Flat strip experiments In experiments that require flat strips of the spinner fluid, including the surface waves and hydrodynamic instability of Figures 2.6 and 2.26, we prepare strips by accumulating particles against a straight edge, either by rolling all particles to one side (see Figure 2.2), or by tilting the sample. We control the thickness of the strips by changing the concentration of the suspension.

Droplet coalescence To observe droplet coalescence, shown in Figure 2.1d, we spin particles for a few minutes until they form small clusters; these clusters then gradually coalesce into larger ones.

Droplet spreading For droplet spreading, shown in FFigure 2.1e, we cast a small amount of suspension ($\sim$2 μL) on a glass slide and seal it with a drop of UV-curable Norland Optical Adhesive (NOA 81), which creates a hard boundary around the suspension. We then spin the particles until they all assemble into a single drop. Finally, to guide the drop towards the wall, we tilt the microscope. This procedure is sketched in Figure 2.3a.

Bubble collapse For experiments on the collapse of bubbles, illustrated in Figure 2.1f, we enclose the suspension in a glass chamber that contains, on one wall, cured droplets of Norland Optical Adhesive (NOA 81). We guide the particles with a permanent magnet over a drop of the adhesive and then spin them until they all sediment downhill. We subsequently flip the sample upside-down, so that all particles and their void end up on the flat side of the chamber. This procedure is sketched in Figure 2.3b.

Flow past an obstacle For experiments involving flow past an obstacle, shown in Figure 2.1g, we use the same cured NOA 81 droplets as obstacles. We induce flow by tilting the microscope, thereby allowing the particles to sediment while spinning. This procedure is sketched in Figure 2.3c.

Interface experiments Low-friction experiments are performed by placing the particles at a fluid-fluid interface between water and either oil or air. In these experiments the particles are suspended in a water mixture with 15 wt% glycerol to mediate evaporation. In addition, we add a surfactant (4 mM Sodium dodecyl sulfate, Sigma-Aldrich), to prevent the particles from breaching the interface. We pipette a small amount of the particle suspension ($\sim$0.7 μL) on a glass slide and enclose it in a glass chamber. The remainder of the chamber is either

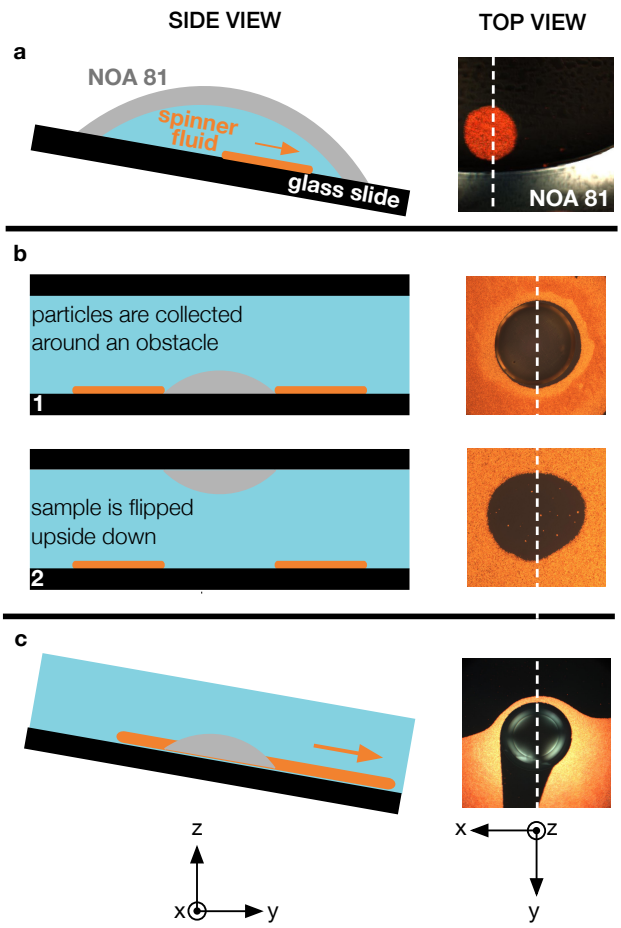

Figure 2.3: **Schematic of sample preparation.** Left column: side view; right column: top view, with the white dashed line marking the cross section represented in the side view. **a**, We enclose a droplet of aqueous suspension of hematite cubes between a glass slide and a drop of UV-curable Norland Optical Adhesive (NOA 81). After the particles have come together into a single droplet of spinner fluid, we tilt the sample to drive them towards the hard wall made by the cured NOA 81. **b**, To make a hole in the spinner fluid, we put the suspension of hematite cubes in a chamber that contains a cured droplet of NOA 81 on the bottom. We collect the particles around the NOA 81 and then flip the sample upside-down. **c**, To probe the flow of the spinner fluid past obstacles, we use the same cured droplets of NOA 81 as the obstacles, and we tilt the sample to create flow via sedimentation.

left empty (air interface experiments) or filled with pure silicone fluid (Clearco Products) of variable viscosity (oil interface experiments). The entire sample is then held such that the cubes sediment with gravity to the water/air (oil) interface. A typical sample geometry is illustrated in Figure 2.4b. The typical radius of curvature is $R{\sim}10^5\,\mu$m. For a typical

droplet of fluid $R{\sim}100\,\mu$m, this amount of curvature varies the particle rotation axis by an angle $\theta{\sim}0.2^\circ$ with respect to the substrate, resulting in negligible amounts of rolling motion (see Figure 2.2c).

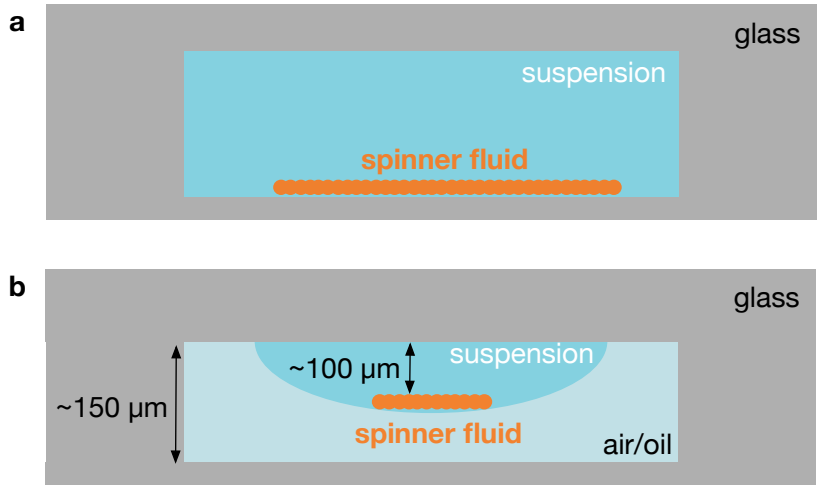

Figure 2.4: **Colloids at interfaces of variable friction. a**, In the conventional geometry cubes are sedimented onto a glass substrate. **b**, By contrast, to achieve lower substrate friction, a droplet of colloidal suspension is enclosed in glass chamber otherwise filled with either oil or air, allowing the colloids to sediment onto a fluid-fluid interface.

2.2.3 Imaging, particle tracking, and spinning-rate measurements

We observe the individual colloidal particles and the macroscopic flows of spinner fluids either with a Nikon Eclipse TE2000-U microscope and 10x-100x objectives, or with a Zeiss Axio Zoom.V16 microscope and a 2.3x objective that allows continuous magnification from 16.1x to 258x. We record slow dynamics ($\leq$5 fps) with a color camera (Grasshopper2 GS2-GE-20S4C-C, Grasshopper3 GS3-U3-123S6C-C) and fast dynamics ($\sim$1000 fps) with a black-and-white camera (Phantom v12, Phantom v2512, Phantom VEO 640S).

As mentioned previously, the colloidal particles are birefringent: when imaged through crossed polarizers, their intensity depends on their orientation. In particular, they blink

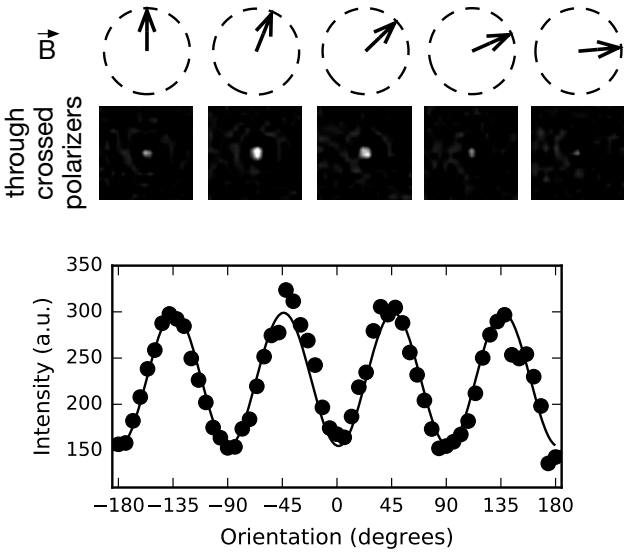

Figure 2.5: **Measuring the particles' spinning frequency.** **a**, When viewed through crossed polarizers, a hematite cube blinks four times during one full rotation. This allows us to confirm that, in our experiments, the particles spin at the frequency set by the rotating magnetic field. **b**, We hold several isolated particles (∼15) at fixed angles and we record their mean intensity. All particles blink four times in one full rotation of the magnetic field.

four times during one full rotation as illustrated in Figure 2.5 and Figure 2.7. Thus, by monitoring the intensity of the spinner fluid with a camera triggered in synchrony with the magnetic field, we confirm that the particles rotate at the rotating frequency of the driving magnetic field up to 15 Hz. After confirming that the particles rotate at the same rate Ω, we measure the instantaneous particle positions. We first average frames over one intensity oscillation, in order to avoid brightness fluctuations. We then identify particle positions and track their trajectories using the free python package trackpy [53].

2.3 Hydrodynamic theory of chiral fluid flow

In contrast to Newtonian fluids, the surface of our fluid supports a spontaneous unidirectional edge flow in its steady state, as well as unusual morphological dynamics such as the rotation of asymmetric droplets. These features, illustrated in Figure 2.1, follow from the breaking of parity through active rotation [43, 54, 44, 39].

To investigate these lively surface flows, we first look at surface excitations in a simple slab geometry, as shown in Fig. 2.6a. We measure the spectrum of surface fluctuations, $|h(k,\omega)|^2$, by tracing the height profile, $h(x,t)$, of the surface and Fourier-transforming it in space and time (see Section 2.5.3). We observe the spectrum to be peaked along a curve $\omega(k)$, revealing the existence of dispersive waves (see Fig. 2.6b). The curve has only one branch with odd parity, meaning that the waves are unidirectional. This behavior contrasts that of conventional surface waves that propagate in all directions.

These surface waves beg a hydrodynamic description. Chiral fluid hydrodynamics follows from conservation of momentum and angular momentum, and thus includes both the spinning rate of individual fluid particles as well as the momentum and angular momentum of their flow [24, 55, 43, 56, 57]. Because our colloids are birefringent, we are able to measure their individual spinning rate by imaging through crossed polarizers. We find that all particles rotate at the same rate, Ω, which is set by the rotating magnetic field (see Fig. 2.7a). From this it follows that the particles' rotational inertia is negligible; the torque exerted on each particle by the magnetic field instantly adjusts to balance the frictional torques exerted by the neighboring particles and the solid substrate. This fast response enables the decoupling of the angular momentum equation from the momentum equation. Nonetheless a strong signature of the microscopic angular momentum manifests as an 'odd' stress. A minimal hydrodynamic theory then balances the force generated by viscous and odd hydrodynamic stresses, $\partial_j \sigma_{ij}$, against friction with the substrate, $\Gamma_{ij} u_j = (\Gamma_u \delta_{ij} + \Gamma_\perp \epsilon_{ij}) u_j$ and surface tension γ at the fluid interface. In this theory, which has been used to capture the bulk flows of chiral granular fluids, the hydrodynamic stress tensor is given by:

$$\sigma_{ij} = -p\delta_{ij} + \eta\left(\partial_i v_j + \partial_j v_i\right) + \eta_R \epsilon_{ij}\left(2\Omega - \omega\right). \tag{2.1}$$

σ_{ij} includes the pressure p and ordinary viscous stress also present in Newtonian fluids with a shear viscosity η. The additional term containing the Levi-Civita symbol ϵ_{ij} and the

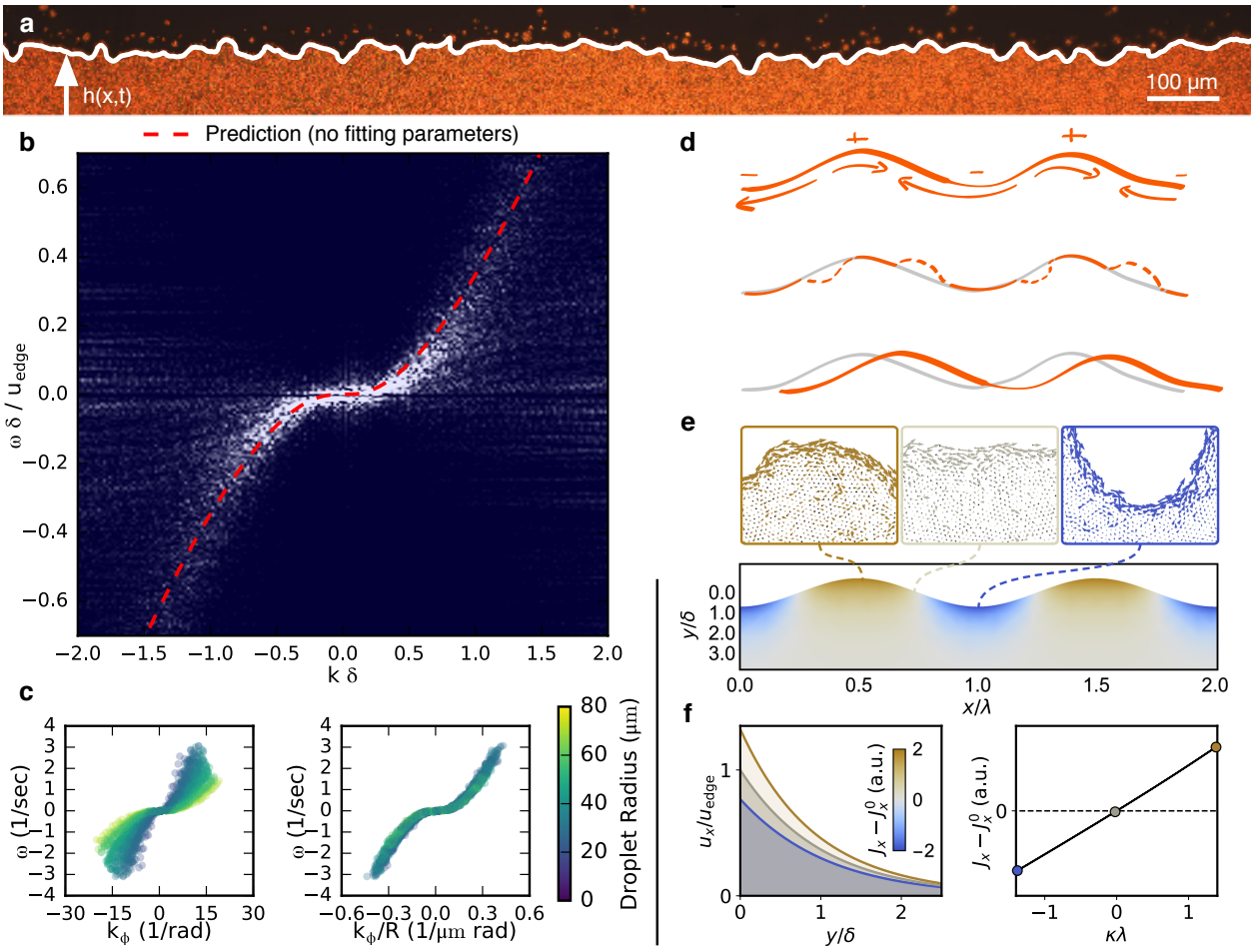

Figure 2.6: **Surface waves in a chiral spinner fluid. a,** Surface waves are excited by perturbing a strip of the spinner fluid. To characterize them, we track the height profile of the strip in time, $h(x,t)$. **b,** The resulting power spectrum from these waves $\langle|h(k,\omega)|\rangle$ is plotted versus the normalized wave vector $k\delta$ and frequency $\omega/(u_{\text{edge}}/\delta)$. The spectrum is peaked on a curve corresponding to the dispersion relation of the waves. Shown with the red dashed line is the theoretical prediction for the dispersion relation, obtained with the hydrodynamic parameters that we measure in Fig. 2.7; its long-wavelength asymptotic form is given in Eq. (2.22). **c,** The power spectrum $\omega(k)$ for surface waves on a perturbed circular droplet of spinner fluid (left panel) can be collapsed (right panel) by rescaling the angular wavenumber k by the droplet radius R. **d,** Sketch of the mechanism for wave propagation. The propagation of waves can be understood by considering the mass flux, plotted in **e**. The chiral fluid is displaced from the high curvature to the low curvature regions. This process explicitly breaks the left-right symmetry, thereby propagating surface waves along only one direction. **e,** Correction to the net mass flux along the interface due to a sinusoidal height perturbation, $J_x - J_x^0$, where J_x^0 is the mass flux in a flat strip and J_x is the mass flux in the presence of a perturbation of wavelength λ. The microscopic origin of this variation in mass flux can be inspected by measuring the flow over surfaces with positive, zero, and negative curvature κ. **f,** The integrated flow yields the mass flux, which scales with curvature.

dissipative coefficient η_R known interchangeably as "rotational viscosity," "spin viscosity," or "inter-rotor friction" captures the rotational friction between neighboring particles [9, 56, 55, 43, 24, 41, 15]. Such an odd stress builds up as the local spinning rate Ω deviates from half the local fluid vorticity $\omega = \hat{z}\cdot(\nabla \times v)$. In torque-free fluids, angular momentum conservation constrains these two quantities to be equal: odd stresses are unique to chiral fluids.

We finally simplify the model by assuming incompressibility and find this assumption to be supported by the agreement between theory and the experiments reported in this section. We also note that there is no direct appearance of the magnetic field or its stresses in this hydrodynamic description unlike in conventional ferrofluids. In this respect, our colloidal chiral fluid can be seen as a special type of driven ferrofluid in which weakly Brownian particles are densely packed and the only role of magnetic forces is to provide cohesion and induce chirality. In the following sections, we discuss at length the origins of the aforementioned equations of motion and explicitly perform a computation of the effect of magnetism on our system to justify the above assumptions.

2.3.1 Hydrodynamic equations of motion

Building on previous work [56, 58, 59, 43, 7, 6, 5, 15], we describe our system with a continuum hydrodynamic theory. The hydrodynamic variables are the mass density of spinners $\rho(\mathbf{x}, t)$, the momentum density $\rho(\mathbf{x}, t)u_i(\mathbf{x}, t)$ and the angular momentum density $I_0\Omega(\mathbf{x}, t)$, where I_0 is the spinner moment of inertia density. The conservation of momentum, angular momentum, and mass yields two-dimensional hydrodynamic equations. The first is conservation of mass:

$$(\partial_t + \mathbf{u}\cdot\nabla + \nabla\cdot\mathbf{u})\,\rho = 0$$

We will assume incompressibility in the following, reducing the above to

$$\nabla\cdot\mathbf{u} = 0 \tag{2.2}$$

The second is conservation of momentum. For a 2D homogeneous and isotropic fluid in contact with a solid substrate, it takes the generic form:

$$\rho\left(\partial_t + \mathbf{u}\cdot\nabla\right)u_i = -\partial_i p + \eta\nabla^2 u_i + \eta_D\partial_i(\nabla\cdot\mathbf{u}) + \eta_R\epsilon_{ij}\partial_j\left(2\Omega-\omega\right) - \Gamma_{ij}u_j + \eta_o\nabla^2\epsilon_{ij}u_j, \quad (2.3)$$

where ϵ_{ij} is the Levi-Civita symbol, p is the pressure, $\omega = \hat{\mathbf{z}}\cdot(\nabla\times\mathbf{u}) = \epsilon_{ij}\partial_i u_j$ is the vorticity (which in two dimensions is a scalar), η is the shear viscosity, η_D is the dilatational viscosity, η_R is the rotational viscosity, η_o is a pseudo-scalar material parameter known as the Hall viscosity (or odd viscosity) [7], and $\Gamma_{ij}u_j = \left(\Gamma_u\delta_{ij} + \Gamma_\perp\epsilon_{ij}\right)u_j$ the frictional force with the substrate, which in principle allows for two independent longitudinal and transverse friction coefficients. The dimensions of each quantity are: $[u] = L/T$, $[p] = M/T^2$, $[\rho] = M/L^2$, $[\omega] = 1/T = [\Omega]$, $[\Gamma_u] = [\Gamma_\perp] = M/(L^2T)$, $[\eta] = [\eta_D] = [\eta_R] = [\eta_o] = M/T$. The third is conservation of angular momentum:

$$I_0\left(\partial_t + \mathbf{u}\cdot\nabla + \nabla\cdot\mathbf{u}\right)\Omega = -\Gamma^\Omega\Omega - 2\eta_R\left(2\Omega-\omega\right) + D_\Omega\nabla^2\Omega + \tau, \quad (2.4)$$

where Γ^Ω is the rotational friction, D_Ω is the angular momentum diffusion constant, and τ the torque density field experienced by the spinners. In principle, friction with the medium surrounding the fluid could give rise to a torque that is proportional to ω. For simplicity, we do not treat this contribution independently of Γ^Ω and η_R. The dimensions of each quantity are: $[I_0] = M$, $[D_\Omega] = ML^2/T$, $[\Gamma^\Omega] = M/T$, $[\tau] = M/T^2$.

To estimate the relative contributions of each term, we interpret its role and estimate its magnitude by dimensional analysis. η and η_R both originate in the stresses nearby particles exert on each other, principally through the lubrication layer that separates them. Their value will therefore be comparable to η_{H_20}, up to a geometric factor and the ratio of the densities of the spinner fluid and water. Our measurements confirm this. η_o also originates from the stresses nearby particles exert on each other but also depends on the extent of

time-reversal symmetry breaking and is less straightforward to estimate. In theoretical studies of vortex fluids [5], electrons in magnetic fields [60, 61, 62], and fluids of chiral grains [15], $\rho\eta_o$ is proportional to the angular momentum per particle but we are not aware of a similar estimate in over-damped systems. We find from our measurement that η_o at typical frequencies of $\sim$10 Hz is comparable in magnitude to η. $(\Gamma_u/\rho)^{-1}$ corresponds to the time required to damp the linear motion of an individual colloid. From the sedimentation measurements, which are presented in Section 2.4.2, this is $< 10^{-6}$ s. The sedimentation experiments also put an upper bound to the ratio $\Gamma_\perp/\Gamma_u$ which is found to be negligible with a properly balanced field orientation (see Sections 2.2.1 and 2.4.2). In all that follows, we therefore approximate the friction tensor by its longitudinal component: $\Gamma_{ij} \equiv \Gamma_u\delta_{ij}$. γ is estimated by U_{int}/a, where U_{int} is the time-averaged interaction potential between the hematite magnetic dipoles, $U_{\text{int}}\sim\mu_0\mu^2/a^3$, a is the typical particle spacing, and μ is the dipole moment [63]. This approximation yields $\gamma\sim10^{-13}$ N, which is consistent with measurements presented in Section 2.5.

If we take as a characteristic velocity $\Omega\delta$ and characteristic gradient $1/\delta$, we find that the ratio of the material derivative term on the LHS to terms on the RHS is $< 10^{-2}$. We thus neglect the material derivative terms on the LHS of the momentum and angular momentum equations. Further assuming constant density $\rho \equiv \rho_0$ and spinning frequency $\Omega \equiv \Omega_0$ simplifies the problem considerably. The momentum equation Eq. (2.3), using $\nabla \cdot \mathbf{u} = 0$, becomes:

$$\eta\nabla^2 u_i - \partial_i\tilde{p} + \eta_R\epsilon_{ij}\partial_j\left(2\Omega - \omega\right) - \Gamma_u u_i = 0 \tag{2.5}$$

where $\tilde{p} = p + \eta_o\omega$ absorbs the bulk effects of Hall viscosity in an incompressible fluid. The bulk momentum equation is thus simply a Brinkman equation, as arises in modeling porous medium flow, with forcing by an anti-symmetric stress. The angular momentum equation

Eq. (2.4), using $\nabla \cdot \mathbf{u} = 0$, reduces to:

$$\frac{1}{2}\Gamma^{\Omega}\Omega + \eta_R\,(2\Omega - \omega) = \frac{\tau}{2} \tag{2.6}$$

In this system of equations the pressure instantly adjusts to maintain the divergence-free condition, while the torque τ adjusts to enforce constant rate of rotation. Hence, only the momentum equation, with the divergence-free condition, is required to compute the bulk flow. Given a constant Ω, and using that $-\epsilon_{ij}\partial_j\omega = \nabla^2 u_i$, yields

$$\delta^2\nabla^2\mathbf{u} - \nabla\bar{p} - \mathbf{u} = \mathbf{0} \tag{2.7}$$

or an (apparently) unforced Brinkman equation, where $\delta = ((\eta+\eta_R)/\Gamma_u)^{1/2}$ is the so-called hydrodynamic length, and $\bar{p} = \tilde{p}/(\Gamma_u)$. Note that the pressure satisfies $\nabla^2\tilde{p} = 0$. Taking the curl and using the divergence-free condition yields

$$\delta^2\nabla^2\omega - \omega = 0 \tag{2.8}$$

which is a screened Laplace (or Yukawa) equation for the vorticity. Both the Brinkman and Yukawa equations are solved as boundary value problems.

To consider free-surface flows, let D denote the chiral fluid domain in the plane, having boundary ∂D with outward facing normal $\hat{\mathbf{n}}$. If $\mathbf{v}$ is the velocity of ∂D, then we adopt the kinematic boundary condition

$$\mathbf{v} = \mathbf{u}|_{\partial D}, \tag{2.9}$$

giving that the boundary moves with the fluid velocity. We also assume the stress balance equation:

$$\boldsymbol{\sigma}\hat{\mathbf{n}}|_{\partial D} = \gamma\kappa\hat{\mathbf{n}} \tag{2.10}$$

where γ is the surface tension and κ is the curvature of ∂D. The stress tensor $\boldsymbol{\sigma}$ is given by:

$$\begin{aligned}\sigma_{ij} &= -p\delta_{ij} + (\eta_D - \eta)\,\delta_{ij}\partial_k u_k + \eta_R\epsilon_{ij}\,(2\Omega - \omega) + 2\eta\frac{1}{2}\left(\partial_i u_j + \partial_j u_i\right) \qquad (2.11)\\ &\quad + \eta_o\left(\partial_i\epsilon_{jk}u_k + \epsilon_{ik}\partial_k u_j\right)\\ &= -\left(p - \eta_o\omega\right)\delta_{ij} + \eta_R\epsilon_{ij}\,(2\Omega - \omega) + 2\eta\frac{1}{2}\left(\partial_i u_j + \partial_j u_i\right) - \eta_o O_{ij}, \qquad (2.12)\end{aligned}$$

where we have assumed $\partial_k u_k = 0$ and:

$$O_{ij} = \begin{pmatrix} -2\partial_y u_x & +2\partial_x u_x \\ -2\partial_y u_y & +2\partial_x u_y \end{pmatrix}. \qquad (2.13)$$

Eqs. (2.2, 2.7, 2.9, 2.10) are a closed set determining the dynamics of the chiral fluid domain. It is solved as a free-boundary problem, with boundary conditions Eq. (2.10) determining the instantaneous velocity field through solution of Eqs. (2.2, 2.7). The boundary is then evolved via the kinematic boundary condition Eq. (2.9).

Comments A few comments are in order:

- While the local stress in our colloidal chiral fluid differs from the local stress in a Newtonian fluid, the resulting flow Eq. (2.7) reduces to that of a Newtonian Brinkman fluid, implying that the bulk dynamics of Newtonian fluids and odd stress fluids are indistinguishable. The difference in the flows, and in particular the presence of surface edge-flows, arises from the difference in the stress at the boundary.

- The presence of an odd stress necessitates the application of a body torque by the following argument. Consider an infinitesimal region of characteristic size ℓ; the torque τ_k on this region is proportional to $\epsilon_{kij}\sigma_{ij}\ell^3$. The moment of inertia about the axis $\hat{x}_k$ is proportional to $\rho\ell^5$. Thus angular momentum conservation implies infinite acceleration as $\ell \to 0$. This implies that in the absence of a body torque there can be no

antisymmetric component to the stress.

- The presence of an odd stress in Eq. (2.7) breaks the invariance under parity transformations of the equations of motion. This can be seen by the following argument. Consider Eq. (2.7), keeping in mind that it models a 2D fluid embedded in three-dimensional space:

$$\eta\nabla^2 u_i - \partial_i p + \eta_R \hat{z}_k \epsilon_{kij} \partial_j \left(2\Omega - \hat{z}\cdot\nabla\times u_i\right) - \Gamma_u u_i = 0$$

  where u_i has no component in the $\hat{z}$ direction and is a function of (x, y) alone. Under the parity transformation $(x, y, z) \to (x, y, -z)$ the equation becomes:

$$\eta\nabla^2 u_i - \partial_i p + \eta_R \hat{z}_k \epsilon_{kij} \partial_j \left(-2\Omega - \hat{z}\cdot\nabla\times u_i\right) - \Gamma_u u_i = 0$$

  demonstrating that if one does not also reverse the direction of spin of the colloids, the equation is in general not invariant. Of course in the case of constant spinning motion in which the parity breaking term vanishes, the flow equation is parity invariant. Parity remains, however, broken by the corresponding stress boundary condition.

- The presence of a Hall viscosity η_o in Eq. (2.7) stems from the breaking of time-reversal symmetry in two dimensions [7, 6]. In theoretical studies of vortex fluids [5], electrons in magnetic fields [60, 61, 62] and fluids of chiral grains [15], $\rho\eta_o$ was shown to be proportional to the angular momentum per particle (or vortex circulation), but we are not aware of an estimate in active over-damped systems.

- In an incompressible fluid, Hall viscosity has no effect in the bulk, only on the boundary. As shown in Eqs. (2.11) and (2.12), the Hall stress tensor can be divided into a quantity with divergence that can be absorbed in the pressure and a component $-\eta_o O_{ij}$ which is divergence free: $\partial_j O_{ij} = 0$. The former has no effect in an incompressible fluid, however

the latter gives rise to stresses on the boundary. In particular, using $O_{ij}n_j = -2\partial_s u_j$:

$$\sigma_o \mathbf{n} = -2\eta_o \partial_s \mathbf{u} = -2\left(\partial_s u_s - \frac{u_n}{R}\right)\hat{\mathbf{s}} - 2\left(\partial_s u_n + \frac{u_s}{R}\right)\hat{\mathbf{n}}$$

where R denotes the surface radius of curvature with the convention that a circular droplet has a positive radius of curvature. From this it can be seen that Hall viscosity acts purely on the boundary, generating boundary stresses in proportion to variations of the surface flow *along* the boundary.

2.3.2 Magnetic interactions

Our colloidal system consists of magnetic particles suspended in water, and is thus reminiscent of conventional ferrofluids composed of magnetic nanoparticles suspended in water. In this section, we outline several key differences in the microscopic interactions that arise from the larger size of the magnetic particles. These differences conspire to reduce the importance of magnetic stresses in the hydrodynamic description, ultimately enabling us to accurately model our surface dynamics without explicit reference to magnetic stresses.

Crucially, Brownian dynamics do not play a significant role in our particle dynamics as evidenced by the following observations:

- Our magnetic particles sediment out of suspension. Their gravitational height is of the order of 20 nm. Thus, thermal fluctuations are not sufficient to keep the particles in suspension in the bulk.

- We observe that in the absence of magnetic field, the particles assemble into persistent magnetic chains that we have never observed to unbind.

- Within the range of magnetic fields used in our experiments the magnetic energy μB, where μ is the permanent dipole of the particles [63], is of the order of $\sim 10^3 k_{\mathrm{B}}T$ thereby

making orientational thermal fluctuations marginal to the particles' orientational dynamics.

The reduced role of Brownian dynamics reduces the role of magnetic forces to providing cohesion to the fluid and to constraining the spinning rate of the particles to be constant. Therefore, unlike conventional ferrofluids, the cohesion of our 2D chiral fluid does not rely on molecular surface tension but instead on the interactions between the magnetic particles. Furthermore the magnitude of the fluid's magnetization is constant, and its orientation is tied to that of the particles that compose the fluid itself. Consequently, magnetism appears implicitly in our equations of motion through the torque density $\tau = \mu_0 \vec{M} \times \vec{H}$ that is balanced by rotational friction and odd stress. While this torque density is ultimately responsible for driving flows, just as in the case of ferrofluids [64, 65, 66], magnetic forces do not play a direct role in surface dynamics. To highlight the essential effect of these differences on the interfacial dynamics, we explore below their impact on the celebrated Rosensweig surface instability [41].

2.3.2.1 Absence of Rosensweig instability

Physically, the difference between the classical un-saturated ferrofluid and our fluid has its origins in the fact that in the case of the induced field, the magnetization itself is augmented in the peaks of the perturbation, whereas in our case the magnetization is fixed. In a ferrofluid, the augmentation of the magnetization leads to a wavenumber-dependent magnetic stress that produces the famous spiking instability [41]. As noted above, unlike a conventional ferrofluid, our system sustains a uniform magnetization, which leads to important differences.

Let us first first reproduce the Rosensweig result for the stress in conventional ferrofluids, extended to rotating fields, then compute the magnetic stress in our fixed magnetization case and compare the two. In both calculations, we consider a semi-infinite geometry with magnetic fluid occupying the $(y < 0)$ half plane, with a sinusoidally perturbed interface

$h = \epsilon \cos(kx)$.

Rosensweig instability in conventional ferrofluids In the case of the conventional ferrofluid, we seek a solution for the magnetic potential ϕ from which the magnetic field $\boldsymbol{B} = \mu \boldsymbol{H}$, $\boldsymbol{H} = -\nabla\phi$ can be deduced. The magnetization $\boldsymbol{M} = (\mu/\mu_0 - 1)\boldsymbol{H}$ is taken to be $M\left(\cos\theta_R \hat{x} + \sin\theta_R \hat{y}\right)$ deep in the ferrofluid phase. We then find

$$\begin{aligned}
\boldsymbol{H}^+ &= \frac{M}{\mu - \mu_0}\left(\mu_0 \cos\theta_R \hat{x} + \mu_0 \sin\theta_R \hat{y}\right) + \delta\boldsymbol{H}^+, \\
\boldsymbol{H}^- &= \frac{M}{\mu - \mu_0}\left(\mu_0 \cos\theta_R \hat{x} + \mu \sin\theta_R \hat{y}\right) + \delta\boldsymbol{H}^-,
\end{aligned}$$

where $\boldsymbol{\delta H}^{\pm} = -\nabla\delta\phi^{\pm}$ represents the perturbation to the magnetic field due to the sinusoidal modification of the interface:

$$\begin{aligned}
\delta\phi^+ &= \epsilon \frac{M e^{ky}}{\mu + \mu_0} \mu_0 \sin\left(kx - \theta_R\right), \\
\delta\phi^- &= \epsilon \frac{M e^{-ky}}{\mu + \mu_0} \left[\mu \sin(\theta_R)\cos(kx) + \mu_0 \cos(\theta_R)\sin(kx)\right].
\end{aligned}$$

The $+$ expressions correspond to the solution in the lower half plane and the $-$ to the solution in the upper half plane. The field is perturbed as

$$\begin{aligned}
\delta\boldsymbol{H}^+ &= -\frac{\mu_0 M k e^{ky}}{\mu + \mu_0} k\epsilon \left[\cos\left(kx - \theta_R\right)\hat{x} + \sin\left(kx + \theta_R\right)\hat{y}\right], \\
\delta\boldsymbol{H}^- &= \frac{\mu_0 M k e^{-ky}}{\mu + \mu_0} \epsilon \cos\theta_R \left[-\cos\left(kx\right)\hat{x} + \sin\left(kx\right)\hat{y}\right] + \frac{\mu}{\mu + \mu_0} \sin\theta_R \left[\sin\left(kx\right)\hat{x} + \cos\left(kx\right)\hat{y}\right].
\end{aligned}$$

That the fields and potentials satisfy both Maxwell's equations and the boundary conditions, $\hat{n} \times (\boldsymbol{H}^+ - \boldsymbol{H}^-) = 0$ and $\hat{n} \cdot (\boldsymbol{H}^- - \boldsymbol{H}^+) = \hat{n} \cdot \boldsymbol{M}$, can be verified by explicit computation.

From the above, we obtain $\boldsymbol{B}^+ = \mu \boldsymbol{H}^+$ and $\boldsymbol{B}^- = \mu_0 \boldsymbol{H}^-$. The spatially-varying

magnetization is then given by

$$\boldsymbol{M} = M\left(\cos\theta_R\hat{x} + \sin\theta_R\hat{y}\right) - \frac{(\mu-\mu_0)Me^{ky}}{\mu+\mu_0}k\epsilon\left[\cos\left(kx-\theta_R\right) + \sin\left(kx-\theta_R\right)\right] \tag{2.14}$$

Finally, to obtain the surface stress, we evaluate the stress tensor,

$$T_{ij}^{\pm} = -\tfrac{1}{2}\delta_{ij}\boldsymbol{B}^{\pm}\cdot\boldsymbol{H}^{\pm} + \tfrac{1}{2}\left(H_i^{\pm}B_j^{\pm} + H_j^{\pm}B_i^{\pm}\right),$$

inside and outside the magnetized region. The surface stress follows from $\sigma_{nn} = T^{-}\cdot\hat{n} - T^{+}\cdot\hat{n}$. Evaluating yields a perturbation to the magnetic surface stress, $\delta\sigma_{nn} = \sigma_{nn} - \sigma_{nn}(\epsilon = 0)$, that is wavenumber-dependent and in-phase with the perturbation to the interface, pushing it to grow,

$$\delta\sigma_{nn} = -k\frac{\mu_0 M^2}{2}\epsilon\cos(kx)\left(\cos(2\theta_R) - \frac{\mu-\mu_0}{\mu+\mu_0}\right).$$

This expression agrees with the celebrated expression computed by Rosensweig for $\theta_R = \pi/2$ (magnetic field normal to the interface) [41]. Even when the stresses are averaged over a period of rotation, we find a destabilizing stress:

$$\langle\delta\sigma_{nn}\rangle_{\theta_R} = k\frac{M^2}{2}\epsilon\cos(kx)\frac{\mu-\mu_0}{\mu+\mu_0}. \tag{2.15}$$

Magnetic stresses in a saturated colloidal fluid Repeating the calculation for our fluid using a fixed magnetization $\boldsymbol{M} = M(\cos\theta_R\hat{x} + \sin\theta_R\hat{y})$ in contrast to the spatially-varying magnetization of Eq. (2.14), we find:

$$\delta\phi^{+} = \epsilon\frac{Me^{|k|y}}{2}\left[\frac{k}{|k|}\cos\theta_R\sin kx - \sin\theta_R\cos kx\right],$$
$$\delta\phi^{-} = \epsilon\frac{Me^{-|k|y}}{2}\left[\frac{k}{|k|}\cos\theta_R\sin kx + \sin\theta_R\cos kx\right],$$

The magnetic field is given by

$$\boldsymbol{H}^+ = -\frac{M}{2}\sin\theta_R\hat{y} + \delta\boldsymbol{H}^+,$$
$$\boldsymbol{H}^- = \frac{M}{2}\sin\theta_R\hat{y} + \delta\boldsymbol{H}^-,$$

where the perturbative pieces are

$$\delta\boldsymbol{H}^+ = -\epsilon\frac{Me^{|k|y}}{2}\left[\left(\frac{k^2}{|k|}\cos\theta_R\cos kx + k\sin\theta_R\sin kx\right)\hat{x} + \left(k\cos\theta_R\sin kx - |k|\sin\theta_R\cos kx\right)\hat{y}\right],$$
$$\delta\boldsymbol{H}^- = \epsilon\frac{Me^{-|k|y}}{2}\left[\left(k\sin\theta_R\sin kx - \frac{k^2}{|k|}\cos\theta_R\cos kx\right)\hat{x} + \left(k\cos\theta_R\sin kx + |k|\sin\theta_R\cos kx\right)\hat{y}\right].$$

Then, using $\boldsymbol{B}^- = \mu_0\boldsymbol{H}^-$ and $\boldsymbol{B}^+ = \mu_0(\boldsymbol{H}^+ + \boldsymbol{M})$, we can obtain the magnetic stress as above. In this case, the perturbation to the magnetic interfacial stress is:

$$\delta\sigma_{nn} = -k\frac{\mu_0 M^2}{4}\epsilon\left[\sin(2\theta_R)\sin kx + \mathrm{sgn}(k)\cos(2\theta_R)\cos kx\right].$$

When averaged over a period of rotation, $\langle\delta\sigma_{nn}\rangle_{\theta_R} = 0$, and:

$$\langle\sigma_{nn}\rangle_{\theta_R} = \frac{\mu_0 M^2}{8}. \tag{2.16}$$

we find that, by comparison to Eq. (2.15), the wavenumber-dependent part of the magnetic stress vanishes, leaving a constant magnetic pressure that would fail to drive the lively dynamics observed in our experiments.

2.4 Odd rheology & steady-state characterization

To make a quantitative comparison between our model and the flows we observe, we require a measurement of the hydrodynamic and friction coefficients η, η_R, Γ_u, and $\Gamma_\perp$. Fortunately, the prominent effect of odd stress at the free surface of our chiral fluid can be effectively

exploited to infer its bulk rheology. The homogeneous spinning motion of the colloidal particles gives rise to a net tangential edge flow even in the absence of pressure gradients. These tread-milling dynamics, characteristic of all chiral fluids [43, 27, 33, 39, 22], are illustrated in circular droplets in Figs. 2.7b-e. The tangential flow that is localized at the free surface is readily explained by expressing the hydrodynamic equation in terms of vorticity for an incompressible chiral fluid:

$$\left(\nabla^2 - \delta^{-2}\right)\omega = 0 \tag{2.17}$$

where $\delta = \sqrt{(\eta + \eta_R)/\Gamma_u}$. This Helmholtz equation indicates that the vorticity generated at the surface decays exponentially into the chiral fluid, with a characteristic penetration depth δ (see Figs. 2.7c, d, g). In this model, the loss of substrate friction causes the penetration depth to diverge, resulting in rigid-body rotation of the entire fluid, as observed in ferrofluid droplets [54]. The magnitude of the vorticity at the free surface, $\omega_{\text{edge}} = 2\Omega\,\eta_R/(\eta + \eta_R)$, is set by the stress-free boundary condition for a flat strip and expresses the competition between the odd and viscous stresses described in Section 2.3.1. We point out that ω_{edge} is directly proportional to η_R, which demonstrates the importance of odd stress for the dynamics.

We deduce all of the parameters found in the hydrodynamic equations of our spinner fluid experimentally as summarized below. We perform these measurements on circular droplets of spinner fluid, as shown in Figure 2.7. Comparison between experiment and prediction (Fig. 2.7d) yields the values of η and η_R in terms of Γ_u. The latter is then measured by tilting the substrate and measuring the sedimentation rate of droplets (see Fig. 2.7f). Ultimately, we find $\eta = 4.9 \pm 0.2 \times 10^{-8}$ Pa m s, $\eta_R = 9.1 \pm 0.1 \times 10^{-10}$ Pa m s, and $\Gamma_u = 2.49 \pm 0.03 \times 10^3$ Pa s/m. The sedimentation direction is aligned with gravity, which bounds $\Gamma_\perp \ll \Gamma_u$, so we take $\Gamma_\perp \to 0$ in the following. In the following section, we first explicitly write out the predictions for the steady-state edge flow in Section 2.4.1. Here, we describe two simplified geometries that provide us with insight applicable to a broader

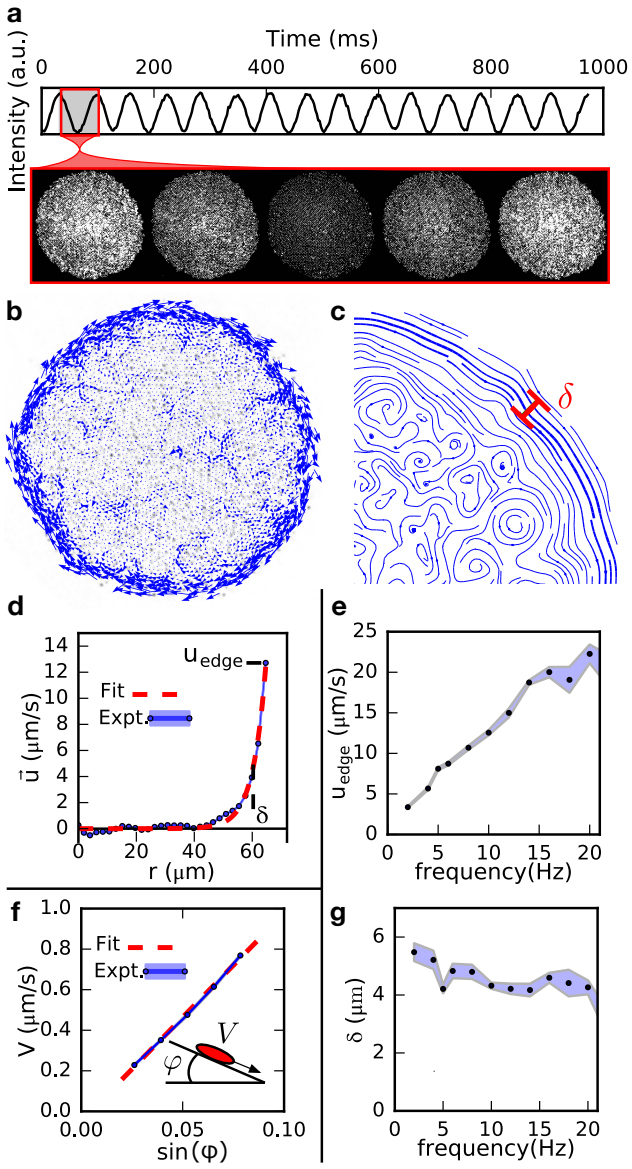

Figure 2.7: **Characterization of a droplet of chiral spinner fluid. a,** When viewed through crossed polarizers, the particles blink as they spin. This allows us to confirm that they all spin at the same frequency, set by the rotating magnetic field. **b,** By measuring the velocity of each particle within a cluster, we find a flow profile that is concentrated at the edge within a penetration layer δ shown in **c, d,** and **g**. **c,** A zoomed-in view of the flow streamlines, obtained by averaging several instantaneous velocity profiles such as the one shown in **b**. **d,** By measuring the flow profile, the edge current u_{edge} and penetration depth δ are extracted. **e, g,** By measuring the flow profile $u(r)$ at a range of frequencies, we extract the shear viscosity, η, and rotational viscosity, η_R, in terms of the substrate friction, Γ_u. **f,** Finally, by tilting a sample and measuring the sedimentation velocity of a droplet, we extract the substrate friction. All error bars represent standard deviations.

class of droplet morphologies. We then describe the tools we use to perform odd rheology to measure the substrate friction (Section 2.4.2) and the viscous coefficients (Section 2.4.3) summarized in Figure 2.7.

2.4.1 Steady-state solutions

We solve the hydrodynamic equations exactly for a circular droplet and in a slab geometry, as depicted in Figure 2.8, ultimately recovering Eq. (2.17).

2.4.1.1 The semi-infinite geometry

Consider a chiral fluid that occupies the region $y < 0$ of a plane. It is easy to verify that the following expression for ω satisfies the bulk equation (Eq. (2.8)):

$$\omega = \frac{\eta_R}{\eta + \eta_R} 2\Omega e^{y/\delta}. \tag{2.18}$$

for $|y| \leq 0$. The corresponding velocity has a non-zero component only in the $\hat{\mathbf{x}}$ direction and can be obtained by direct integration:

$$u_x = -\frac{\eta_R}{\eta + \eta_R} 2\Omega\delta e^{y/\delta}$$

The kinematic boundary condition is satisfied as there is no vertical component to the velocity. The normal stress boundary condition reduces to $\sigma_{yy} = p = p_0$ where p_0 is the pressure outside the slab which can be set to zero. The tangential stress boundary condition reduces to: $\sigma_{yx} = 2\eta_R\Omega - (\eta + \eta_R)\omega|_{y=0} = 0$, which is satisfied by Eq. (2.18).

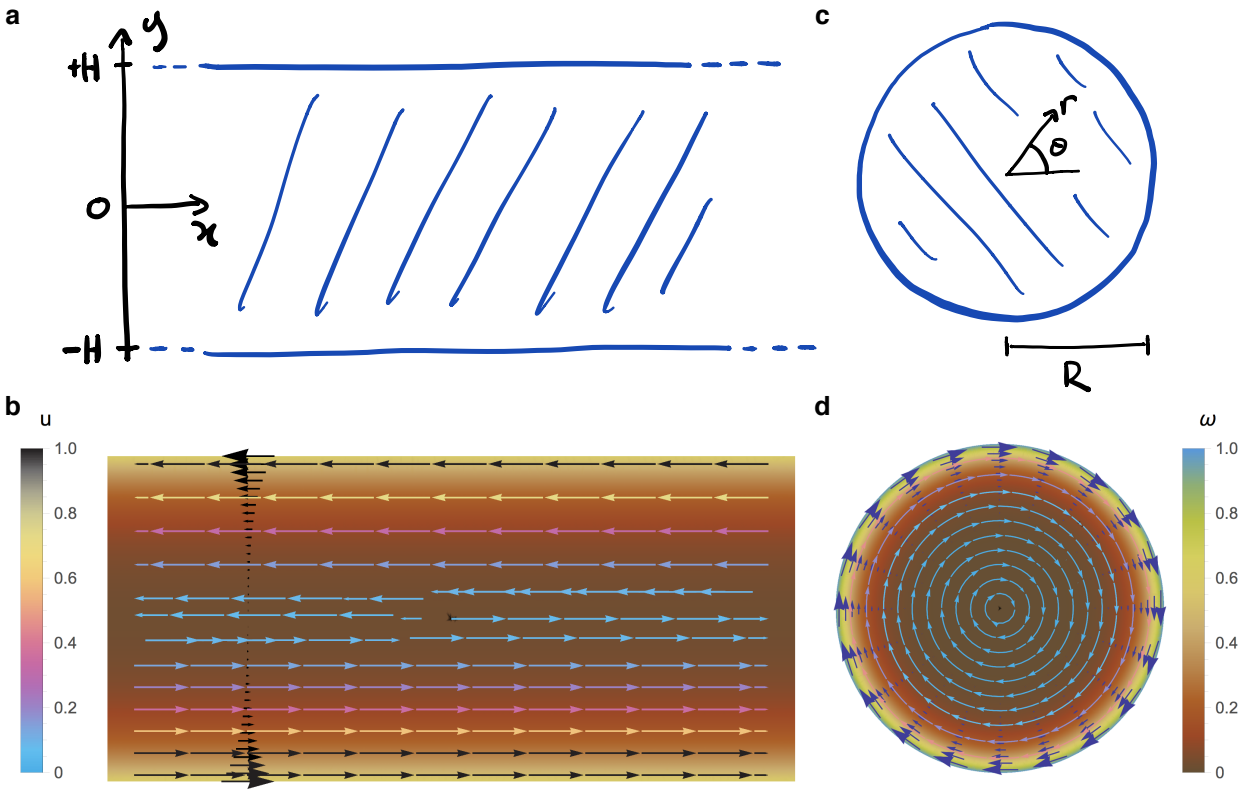

Figure 2.8: **The geometry of steady edge currents in a circular droplet and in a slab of chiral fluid. a**, Setting variables describing a chiral fluid slab of thickness $2H$. **b**, Chiral fluid flow field within the slab. **c**, Setting variables describing a circular chiral fluid droplet of radius R. **d**, Chiral fluid flow field in the droplet. In **b** and **d** the background color represents the magnitude of vorticity and the arrows represent the direction of flow, colored by the velocity magnitude. Note that in both cases, the flow speed drops exponentially to zero as we move away from the boundary.

2.4.1.2 The slab geometry

Consider a slab of chiral fluid with thickness H, as depicted in Figure 2.8a. It is easy to verify that the following expression for ω satisfies the bulk equation (Eq. (2.8)):

$$\omega = \frac{\eta_R}{\eta + \eta_R} 2\Omega \frac{\cosh\left(\frac{y}{\delta}\right)}{\cosh\left(\frac{H}{\delta}\right)}. \tag{2.19}$$

for $|y| \leq H$. The corresponding velocity has a non-zero component only in the $\hat{\mathbf{x}}$ direction and can be obtained by direct integration:

$$u_x = -\frac{\eta_R}{\eta + \eta_R} 2\Omega\delta \frac{\sinh\left(\frac{y}{\delta}\right)}{\sinh\left(\frac{H}{\delta}\right)}$$

As in the case of the semi-infinite slab, the kinematic boundary condition is satisfied as there is no vertical component to the velocity. The normal stress boundary condition reduces to $\sigma_{yy} = p = p_0$ where p_0 is the pressure outside the slab which can be set to zero. The tangential stress boundary condition reduces to: $\sigma_{yx} = 2\eta_R\Omega - (\eta + \eta_R)\omega|_{y=\pm H} = 0$, which is satisfied by Eq. (2.19).

Figure 2.8b depicts the flow field which consists of a left-moving, exponentially decaying current on the top surface and a right-moving, exponentially decaying current on the bottom surface.

2.4.1.3 The droplet geometry

Consider a circular droplet of chiral fluid with radius R, as depicted in Figure 2.8c. In cylindrical co-ordinates, assuming an azimuthal flow field $\mathbf{u} = u(r)\hat{\theta}$ and $\omega = \frac{1}{r}\partial_r(ru(r))$, we have for the radial component of the pressure: $\partial_r p(r) = 0$ and for the azimuthal component of the momentum equation:

$$r^2\partial_r^2 u + r\partial_r u - \left(1 + \frac{1}{\delta^2}r^2\right) u = 0$$

which is satisfied by $u(r) = AI_1(r/\delta)$ where I_1 is a modified Bessel function of the first kind. The boundary conditions $\sigma\hat{\mathbf{r}} = -\frac{\gamma}{R}\hat{\mathbf{r}}$ then fixes the constants p and A giving:

$$p = \frac{\gamma}{R} + \eta_o \frac{u(R)}{R} + p_0$$

and

$$u(r) = \frac{\eta_R I_1(r/\delta)}{\eta I_2\left(\frac{R}{\delta}\right) + \eta_R I_0\left(\frac{R}{\delta}\right)} 2\Omega\delta$$

for $0 \leq r \leq R$. The corresponding vorticity distribution is:

$$\omega(r) = \frac{\eta_R I_0(r/\delta)}{\eta I_2\left(\frac{R}{\delta}\right) + \eta_R I_0\left(\frac{R}{\delta}\right)} 2\Omega.$$

2.4.2 Substrate friction

While the colloidal particles comprising our fluid spin in the vicinity of a substrate, the hydrodynamic interaction between the particles and substrate can be modelled by an effective friction on each particle. As the individual particles spin, their linear motion is subdued by a drag force as they slide, rather than roll, along the substrate. Meanwhile, this linear motion induces a velocity-dependent hydrodynamic interaction with the substrate that can in principle cause the particles to tilt away from the field rotation axis. As illustrated in Figure 2.2, this can lead to a rolling transverse to the motion of a particle. For a particle travelling with velocity u, the magnitude and orientation of these frictional forces can be represented by $\Gamma_u u$ and $\Gamma_\perp u_\perp$, respectively. The frictional coefficients Γ_u and $\Gamma_\perp$ make up the friction tensor Γ_{ij} that is permitted to sustain odd terms in a parity-breaking fluid.

To measure these frictional coefficients, we observe droplets of spinner fluid as they sediment along a substrate tilted at an angle φ as in Figure 2.9a. To extract the frictional coefficients from the resulting dynamics, we consider a simple model in the plane of the substrate, in which a particle experiences a longitudinal and transverse force due to Γ_u and $\Gamma_\perp$, and a gravitational force proportional to $g' = g\sin\varphi$ that balances the frictional forces. In this model, $\theta = \arctan(\Gamma_\perp/\Gamma_u)$ represents the angle of the motion of the particle with respect to g.

First, we measure the longitudinal substrate friction, Γ_u, by measuring the speed of the

particles along the direction of gravity. The sedimentation speed v_{sed} (along $\theta = 0°$), the tilt angle of the substrate φ, and Γ_u are simply related by the force balance equation:

$$\Gamma_u v_{\text{sed}} = \rho g \sin\varphi \tag{2.20}$$

where g is the gravity acceleration and the density ρ is computed by dividing the mass of a particle by the average Voronoi cell area around a particle. We find, on a glass substrate,

$$\Gamma_{u,\text{glass}} = 2.49 \pm 0.03 \times 10^3 \text{ Pa s/m}.$$

A similar experiment is performed for particles sedimented to soft interfaces. For curved droplets, we only measure v_{sed} over sufficiently small displacements such that particle trajectories are linear. This yields a substantially reduced substrate friction at air interfaces,

$$\Gamma_{u,\text{air}} = 46 \pm 1 \text{ Pa s/m}.$$

At oil interfaces, we find Γ_u to increase with viscosity between $\Gamma_{u,\text{air}}$ and $\Gamma_{u,\text{glass}}$, as seen in Figure 2.13.

Then, to measure the transverse substrate friction, $\Gamma_\perp$, we measure θ for droplets ranging in size and moving at speeds on the order of u_{edge} (see Section 2.4.3). We observe $\theta = (0\pm3)°$ on a low-friction interface and $\theta = (1 \pm 3)°$ on a high-friction interface (see Figure 2.9b-c), allowing us to neglect $\Gamma_\perp$ in the remaining analysis: $\Gamma_\perp \ll \Gamma_u$. Meanwhile, the effect of a non-negligible transverse friction remains a fascinating problem that is addressed in Section 2.6.4.5.

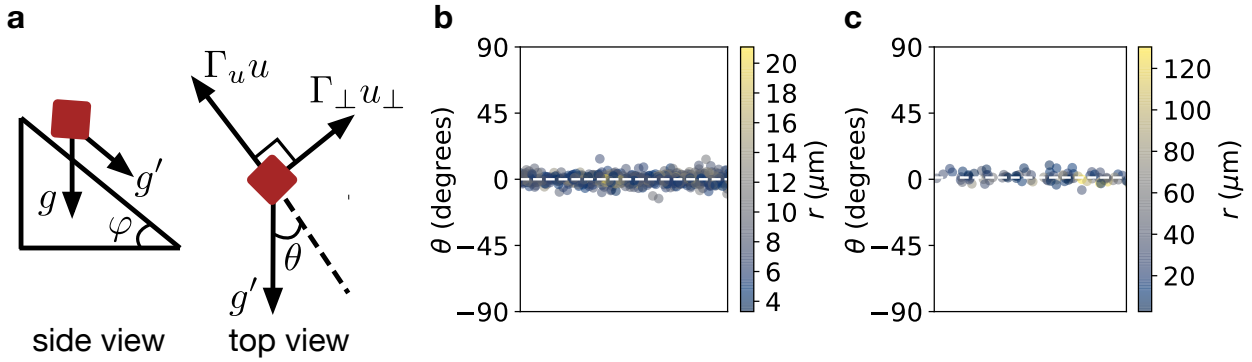

Figure 2.9: **Characterization of transverse friction. a,** From the side, a particle sediments on an inclined substrate. However, from the top, we see that the sedimentation occurs at an angle θ due to a competition between gravity and friction. **b,** On a low-friction interface, the size of this sedimentation angle is small and independent of feature size, ranging from single particles to droplets of fluid. **c,** Similarly, the sedimentation angle is small on a high-friction interface.

2.4.3 Velocity profile and rotational and shear viscosities

We also measure the rotational and shear viscosities of the spinner fluid. We infer them from the vorticity profile in axisymmetric droplets. Practically, these quantities can be extracted by measuring how the velocity component tangent to the edge of a droplet varies in the direction normal to the edge of the droplet. We construct the velocity field of the spinner fluid from the instantaneous velocities of the particles, using a bin size of 2–4 microns. We fit the radial velocity profile to a functional form obtained from the hydrodynamic equations in Section 2.4.1, assuming rotational symmetry:

$$u(r) = 2\Omega\delta \frac{\eta_R I_1(r/\delta)}{\eta I_2(R/\delta) + \eta_R I_0(R/\delta)}, \tag{2.21}$$

where

$$\delta = \sqrt{\frac{\eta + \eta_R}{\Gamma_u}}$$

is the penetration depth and I_k is a modified Bessel function of the first kind of order k (see Section 2.4.1).

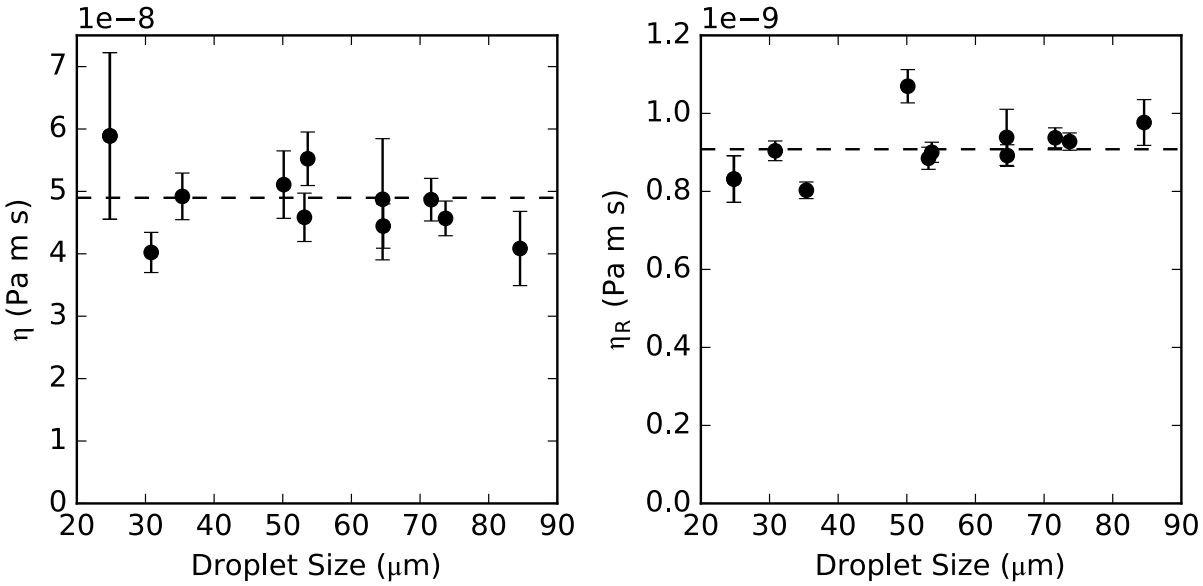

Figure 2.10: **Measurement of viscosities.** By fitting the tangential velocity profiles to Eq. (2.21), we measure the ordinary and rotational viscosities for a distribution of droplets larger than 4 penetration depths composed of particles spinning at 10 Hz. The dashed line shows the mean values.

A typical velocity profile, along with a best fit, is shown in Figure 2.7. From this fit we extract the shear viscosity η, and rotational viscosity η_R (see Figure 2.10). We find, from an ensemble of measurements for droplets of varying size:

$$\eta_{\text{glass}} = 4.9 \pm 0.2 \times 10^{-8} \text{ Pa m s}$$

$$\eta_{R,\text{glass}} = 9.1 \pm 0.1 \times 10^{-10} \text{ Pa m s.}$$

Using these values above, we infer a penetration depth of

$$\delta_{\text{glass}} = 4.5 \pm 0.1\,\mu\text{m},$$

which corresponds to $\sim$2 particle layers. Figure 2.11 shows $u_{edge}/2\Omega\delta$ measured for different

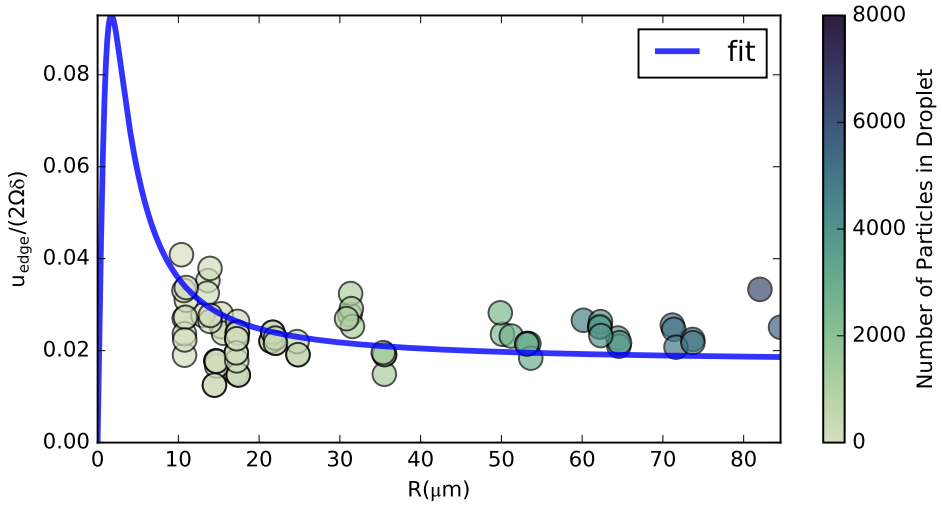

Figure 2.11: **Extracting viscosities from velocity profiles.** We collect velocity profiles from droplets of spinner fluid and we extract the edge current velocity u_{edge} and penetration depth δ. The figure shows $u_{edge}/2\Omega\delta$ plotted against the droplet radius, R, for each droplet.

droplet sizes. For a droplet of radius $R = 50$ μm with particles spinning at 10 revolutions per second, we obtain an edge velocity $u_{\text{edge}} = u(R) = 11.7 \pm 0.2\,\mu$m/s.

At low-friction interfaces, the delocalized edge flow in the chiral fluid induces a background rotation by dragging the interface with it. We therefore add a rigid body rotation term of the form $\Omega_R r$ to our theoretical prediction for the tangential velocity profile. A sample fit, analogous to the profile provided for a droplet on a glass substrate (Fig. 2.7d), demonstrates agreement to this form (see Figure 2.12a). We observe agreement between this procedure and a rigorous treatment of the flow profile incorporating the interaction of the chiral fluid with an interface, which we postpone to future work. Fitting to the form $u(r) + \Omega_R r$, we find a background rotation rate of $\Omega_R \sim 0.66\,1/$s and parameter estimates for a single droplet:

$$\eta_{\text{air}} = 2.5 \pm 0.4 \times 10^{-8} \text{ Pa m s}$$

$$\eta_{R,\text{air}} = 9.5 \pm 0.1 \times 10^{-10} \text{ Pa m s.}$$

These viscosity estimates are close to those on glass, but Γ_u is significantly decreased. Accordingly, we find a penetration depth of

$$\delta_{\text{air}} = 23.8 \pm 0.2\,\mu\text{m},$$

which demonstrates the delocalization of the edge current illustrated in Figure 2.16b.

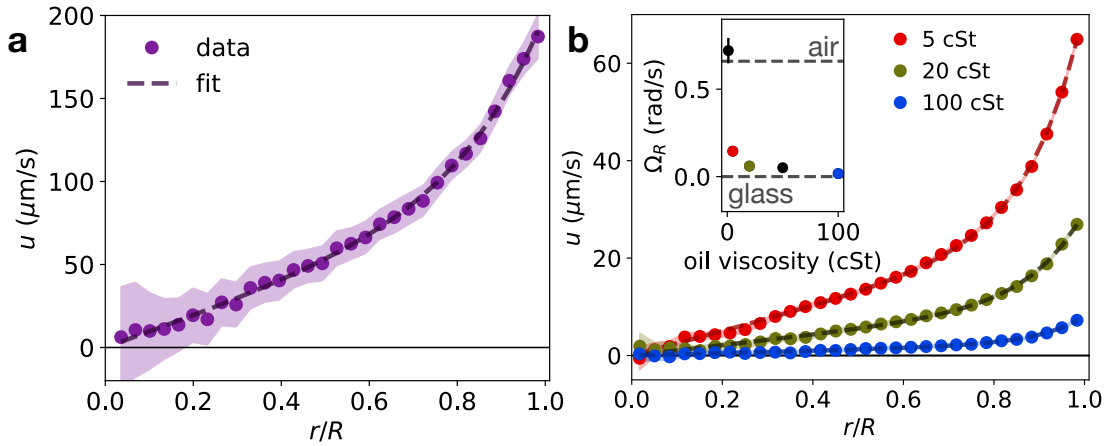

Figure 2.12: **Velocity profiles with background rotation. a,** On a low-friction substrate, like the air-water interface, the edge current is delocalized (c.f. Figure 4b). To extract hydrodynamic parameters from the associated tangential velocity profile, $u(r)$, we fit to the radial theory (Eq. (2.21)) with an additional rigid body rotation rate, yielding a good fit. **b,** A similar procedure accurately fits velocity profiles at oil interfaces, with both the velocity and the rigid body contribution decreasing with increasing viscosity.

We perform this fitting procedure for velocity profiles at oil interfaces of variable viscosity, again finding good agreement to the theory with an additional rigid body component. As the viscosity is increased, we expect a damping of the background fluid rotation. This expectation is supported by the decrease in the fit for Ω_R with increasing viscosity, as shown in Figure 2.12b. With this fitting approach, we find edge current localization to increase with the viscosity of the oil phase, as shown in Figure 2.13.

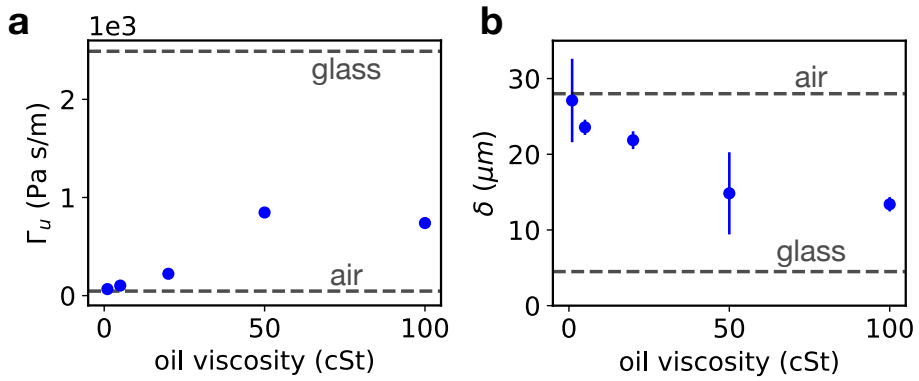

Figure 2.13: **Tuning the substrate friction. a**, The spinner fluid sits at an interface with oil of viscosity that we can control. By increasing the viscosity, we increase the substrate friction, and **b**, decrease the penetration depth, partially spanning the region between the air and glass extremes.

2.5 Chiral surface waves and 'edge pumping'

Equipped with the hydrodynamic coefficients we can now investigate the origin of the surface waves within our model. The mass flux in the tangential surface flow provides significant insight. This flow, sketched in Fig. 2.6d and plotted in Figs. 2.6e-f, is determined by the balance of the tangential odd stress at the boundary, the shear stress, and the substrate friction. In the presence of a perturbation to a free surface, the resistance to flow caused by the shear stress will be modulated in proportion to the curvature. For a sinusoidal perturbation, there is enhanced flow in positively curved regions (top of the wave) and decreased flow in negatively curved regions (bottom of the wave). This 'edge-pumping' mechanism (see Section 2.6.4.1) is reminiscent of the phenomenon of shifting sand dunes [67], in which an external wind moves material away from curved regions towards the flat wave front, giving rise to uni-directional wave motion. As the chiral liquid produces an intrinsic surface wind, these free surface waves are distinctly self-shifting.

A linear stability analysis of the hydrodynamic equations (Section 2.5.1 and Section 2.5.2) confirms this scenario and yields a prediction for the dispersion relation, dissipation rate, and flow fields of surface waves, which we plot in Fig. 2.6b (red dashed curves). With no fitting

parameters, our model shows excellent agreement with the experimentally measured dispersion relation. For surface waves $h \sim e^{i(kx+\omega t)}$ of long wavelength $k \ll 1/\delta$, the asymptotic dispersion relation is:

$$\omega(k) = 2\omega_{\text{edge}} \frac{\eta}{\eta + \eta_R} (k\delta)^3 = 2u_{\text{edge}} \frac{\eta}{\Gamma_u} k^3. \tag{2.22}$$

where $u_{\text{edge}} = 2\Omega\delta\,\eta_R/(\eta + \eta_R)$. This, and additional special cases are discussed in Section 2.5.1.4.

2.5.1 Perturbation of flow in a semi-infinite slab

In this section, we outline a calculation of the response of the otherwise flat interface of a chiral fluid that occupies the region $y \leq 0$.

2.5.1.1 Linearization scheme

Consider a flat interface at $y = 0$ which we perturb with a zero-mean perturbation $y = h(x,t) = \varepsilon g(x,t)$ with $\varepsilon << 1$. We represent the steady-state velocity, vorticity, and stress fields as $\bar{\mathbf{u}} = (\bar{u}, \bar{v})$, $\bar{\omega}$, and $\bar{\sigma}$, respectively, and introduce perturbations as

$$\begin{aligned}
u(x,y) &= \bar{u}(y) + \varepsilon\tilde{u}(x,y) \\
v(x,y) &= \varepsilon\tilde{v}(x,y) \\
\omega &= \bar{\omega}(y) + \varepsilon\tilde{\omega}(x,y) \\
\boldsymbol{\sigma} &= \bar{\boldsymbol{\sigma}}(y) + \varepsilon\tilde{\boldsymbol{\sigma}}(x,y) \\
p &= \varepsilon q(x,y)
\end{aligned}$$

2.5.1.2 Linear theory

Within this linearization scheme, the linearized equations and boundary conditions for the perturbed slab can be derived as follows.

Linearized bulk equations The linearized bulk equations are simply given by:

$$\left(\bar{\eta}\nabla^2 - \Gamma_u\right)\tilde{u}_i = \partial_i q \quad \text{and} \quad \nabla \cdot \tilde{\mathbf{u}} = 0 \tag{2.23}$$

where $\bar{\eta} = \eta + \eta_R$.

Linearized stress boundary conditions The stress boundary conditions relate the bulk fields to interfacial data. We take an upward normal $\hat{\mathbf{n}} \approx \hat{\mathbf{y}} - \varepsilon g_x \hat{\mathbf{x}}$ and the RHS of Eq. (2.10) is to linear order $\gamma\kappa\hat{\mathbf{n}} \approx \varepsilon\gamma g_{xx}\hat{\mathbf{y}}$. Expanding Eq. (2.10) to linear order, and using that $\bar{\sigma}(0)\hat{\mathbf{y}} = \mathbf{0}$ yields

$$\tilde{\boldsymbol{\sigma}}(x,0)\hat{\mathbf{y}} = \gamma g_{xx}(x)\hat{\mathbf{y}} + g_x(x)\bar{\boldsymbol{\sigma}}(0)\hat{\mathbf{x}} - g(x)\bar{\boldsymbol{\sigma}}_y(0)\hat{\mathbf{y}}$$

After some simplification we obtain:

$$\begin{aligned}
&\bar{\eta}\tilde{u}_y(x,0) + (\eta - \eta_R)\,\tilde{v}_x(x,0) + 2\eta_o\tilde{u}_x(x,0) = \bar{\eta}\bar{\omega}_y(0)\,g(x) + 2\eta_o\bar{\omega}(0)g_x(x) \\
&2\eta\tilde{v}_y(x,0) - q(x,0) + 2\eta_o\tilde{v}_x(x,0) = \gamma g_{xx}(x) - \left[(\eta - \eta_R)\,\bar{\omega}(0) + 2\eta_R\Omega\right] g_x(x)
\end{aligned} \tag{2.24}$$

Linearized kinematic boundary condition The linearized kinematic boundary condition is given by:

$$g_t + \bar{u}(0)\,g_x = \tilde{v}(x,0) \tag{2.25}$$

2.5.1.3 Solution

To solve Eqs. (2.23, 2.24, 2.25) we make use of Fourier transforms in the x direction to take advantage of translational invariance.

Solution of the linearized bulk equations Taking the Fourier transform in x:

$$\bar{\eta}\left(\partial_{yy}-k^2\right)\tilde{\mathbf{u}}-\Gamma_u\tilde{\mathbf{u}}-\left(ik,\partial_y\right)q=\mathbf{0}\ \text{ and }\ \left(ik,\partial_y\right)\cdot\tilde{\mathbf{u}}=0$$

Using that $\left(\partial_{yy}-k^2\right)q=0$ we obtain:

$$\begin{aligned}
q &= Ae^{|k|y}\\
\tilde{u} &= -\frac{ik}{\bar{\eta}}\delta^2 Ae^{|k|y}+Be^{|\star|y}\\
\tilde{v} &= -\frac{|k|}{\bar{\eta}}\delta^2 Ae^{|k|y}-\frac{ik}{|\star|}Be^{|\star|y}\\
\tilde{u}_y &= -\frac{ik\,|k|}{\bar{\eta}}\delta^2 Ae^{|k|y}+|\star|\,Be^{|\star|y}\\
\tilde{v}_y &= -\frac{|k|^2}{\bar{\eta}}\delta^2 Ae^{|k|y}-ikBe^{|\star|y}
\end{aligned}\tag{2.26}$$

Where $\star^2=k^2+\delta^{-2}$. The coefficients A and B are to be determined from the boundary conditions.

Application of the stress boundary conditions Inserting Eq. (2.26) into the linearized stress boundary conditions, Eq. (2.24), yields:

$$\begin{aligned}
\left[-2ik\,|k|\,\delta^2\frac{\eta}{\bar{\eta}}+2k^2\delta^2\frac{\eta_o}{\bar{\eta}}\right]A+\left[\frac{2\eta k^2+\bar{\eta}\delta^{-2}}{|\star|}+2ik\eta_o\right]B &= 2\left[\frac{\bar{\eta}}{\delta}+2ik\eta_o\right]\frac{\eta_R}{\bar{\eta}}\Omega g\\
\left[\left(1+2k^2\delta^2\frac{\eta}{\bar{\eta}}\right)+2ik|k|\delta^2\frac{\eta_o}{\eta}\right]A+\left[2ik\eta-2\eta_o\frac{k^2}{|\star|}\right]B &= \gamma k^2-4ik\eta_R\frac{\eta}{\bar{\eta}}\Omega g
\end{aligned}$$

which is a set of two linear equations for the unknowns A, B in terms of the surface perturbation amplitude g.

Application of the kinematic boundary condition Combining this with the kinematic boundary condition:

$$g_t + ik\bar{u}g = \tilde{v}$$

and substituting $\tilde{v}$ we can then compute the time evolution of a surface perturbation. In the section that follows, we discuss this evolution in the case of a sinusoidal perturbation of the height $g \sim \text{Re}\left[e^{ikx}\right]$.

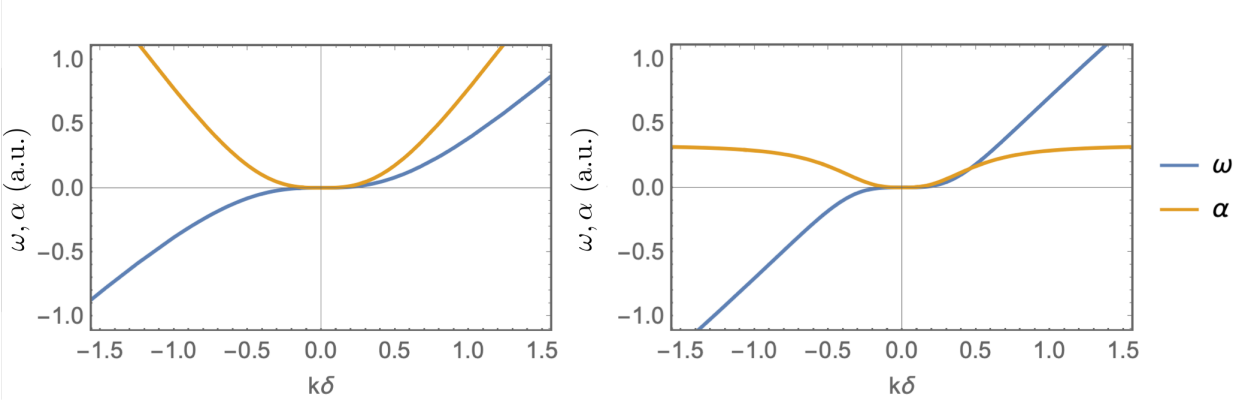

Figure 2.14: **Typical dependence of surface wave dispersion and dissipation on wavenumber** (a) The dispersion and dissipation in the absence of Hall viscosity and for finite surface tension (b) The dispersion and dissipation in the absence of surface tension in the presence of Hall viscosity. The wavenumber dependence of dispersion is generically $\propto k^n$ for odd $n \geq 3$ for small k and $\propto k$ for large k. Similarly, the wavenumber dependence of dissipation is generically $\propto |k|^n$ for odd $n \geq 3$ for small k and $\propto |k|$ for large k.

2.5.1.4 Visualization and asymptotics

The evolution of the surface corresponding to an infinitesimal sinusoidal perturbation of the height $g \sim \text{Re}\left[e^{ikx}\right]$ is given by $g \sim \text{Re}\left[e^{i(kx+\omega t)}e^{-\alpha t}\right]$ which corresponds to damped waves with dispersion $\omega(k\delta)$ and dissipation rate $\alpha(k\delta)$. Figure 2.14 shows typical wavenumber dependences $\omega(k\delta)$ and $\alpha(k\delta)$. From the anti-symmetry of the dispersion relation it can be seen that the surface waves are uni-directional. It is instructive to consider the long wavelength ($|k\delta| \ll 1$) and short wavelength ($|k\delta| \gg 1$) limits. The asymptotic expressions

are given by:

$$\omega(k) = \begin{cases} 2u_{\text{edge}}\dfrac{\eta}{\Gamma_u}k^3 & |k\delta| \ll 1 \\ -\dfrac{2\eta_R(\eta+2\eta_R)\Omega}{\eta^2+4\eta\eta_R+\eta_o^2+4\eta_R^2} + \left[\dfrac{1}{2}\dfrac{\gamma\eta_o}{\eta^2+\eta_o^2}\dfrac{\left(\eta^2+2\eta\eta_R+\eta_o^2+2\eta_R^2\right)}{\left(\eta^2+4\eta\eta_R+\eta_o^2+4\eta_R^2\right)} + u_{\text{edge}}\right]k & |k\delta| \gg 1 \end{cases}$$

$$\alpha(k) = \begin{cases} \left[\dfrac{\gamma}{\Gamma_u} + \dfrac{2\eta_o u_{\text{edge}}}{\Gamma_u}\right]|k|^3 & |k\delta| \ll 1 \\ \dfrac{2\eta_o\eta_R\Omega}{(\eta+2\eta_R)^2+\eta_o^2} + \left[\dfrac{\gamma(\eta+\eta_R)}{2\left(\eta^2+\eta_o^2\right)}\dfrac{\left(\eta^2+2\eta\eta_R+\eta_o^2\right)}{\left(\eta^2+4\eta\eta_R+\eta_o^2+4\eta_R^2\right)}\right]|k| & |k\delta| \gg 1 \end{cases}$$

The dispersion relation at high wavenumbers (short wavelengths compared to δ) is generally linear, corresponding to waves with a constant speed, while at short wavenumbers (long wavelengths compared to δ) it scales with k^3. Similarly, the dissipation rate displays a transition at small wavenumbers from $|k|^3$ to a linear scaling at larger wavenumbers. In order to gain insight on the physical origin of wave propagation and damping, it is instructive to consider the independent contributions of inter-rotor friction, odd viscosity and surface tension to dispersion and dissipation.

$\eta_o = \gamma = 0,\ \eta_R \neq 0$ In this limit surface waves are undamped, as $\alpha(k) = 0$, and the dispersion relation is given simply by:

$$\omega(k) = \begin{cases} 2u_{\text{edge}}\dfrac{\eta}{\Gamma_u}k^3 & |k\delta| \ll 1 \\ -\dfrac{2\eta_R\Omega}{\eta+2\eta_R} + u_{\text{edge}}k & |k\delta| \gg 1 \end{cases}$$

The physical origin of these freely propagating waves can be understood, in the long wavelength limit, in terms of a curvature-dependent resistance to the flow of the surface boundary layer, as discussed in Section 2.6.4. In the short wavelength limit, the linear dispersion corresponds to simple advection of perturbations by the edge current.

$\eta_o = 0,\ \gamma \neq 0,\ \eta_R \neq 0$ In this limit the dispersion relation is unchanged, but the surface fluctuations are now damped by surface tension:

$$\alpha(k) = \begin{cases} \dfrac{\gamma}{\Gamma_u}|k|^3 & |k\delta| \ll 1 \\ \dfrac{\gamma(\eta+\eta_R)}{2(\eta^2+2\eta\eta_R)}|k| & |k\delta| \gg 1 \end{cases}$$

Thus surface tension has a purely dissipative effect on surface waves. This is a consequence of the lack of inertia in our system: surface tension acts to flatten the interface which, once flattened, remains so.

$\eta_o \neq 0,\ \gamma = 0,\ \eta_R \neq 0$ As in the case for $\eta_o = 0$, the dispersion relation at large wavenumbers converges to a linear one with slope u_{edge} and only the intercept is modified to: $-\frac{2\eta_R(\eta+2\eta_R)\Omega}{\eta^2+4\eta\eta_R+\eta_o^2+4\eta_R^2}$ to reflect the dominant wave-propagating mechanism at play (edge-pumping or capillary-Hall driving). The dissipation, however, is strongly affected:

$$\alpha(k) = \begin{cases} \dfrac{2\eta_o u_{\text{edge}}}{\Gamma_u}|k|^3 & |k\delta| \ll 1 \\ \dfrac{2\eta_o\eta_R\Omega}{(\eta+2\eta_R)^2+\eta_o^2} & |k\delta| \gg 1 \end{cases}$$

In both limits, the Hall stress η_o in conjunction with the odd stress η_R damps the surface waves. At long wavenumbers the scaling is akin to that given by surface tension, but at large wavenumbers the scaling is wavenumber-independent. We discuss the origin of this damping in Section 2.6.4.

$\eta_o \neq 0,\ \gamma \neq 0,\ \eta_R = 0$ In this case, there is no edge current and the dynamics come from a balance of surface tension, Hall viscosity and substrate friction:

$$\omega(k) = \begin{cases} 4\dfrac{\gamma\eta_o}{\Gamma_u^2}\ k^5 & |k\delta| \ll 1 \\ \dfrac{1}{2}\dfrac{\gamma\eta_o}{\eta^2+\eta_o^2}\ k & |k\delta| \gg 1 \end{cases}$$

and:

$$\alpha(k) = \begin{cases} \dfrac{\gamma}{\Gamma_u}|k|^3 & |k\delta| \ll 1 \\ \dfrac{1}{2}\dfrac{\gamma\eta}{\eta^2+\eta_o^2}\ |k| & |k\delta| \gg 1 \end{cases}$$

which corresponds to damped unidirectional surface waves driven by a combination of surface tension and Hall viscosity. The driving mechanism for these waves can be understood in terms of a sequential mechanism in which surface tension drives a normal flow, and odd viscosity translates this into a propagation as discussed in Section 2.6.4. The full dispersion is a combination of all these effects. Our unidirectional surface waves can be driven by differential drag on the boundary current or Hall viscosity acting in conjunction with surface tension. They are damped by surface tension and Hall viscosity acting in concert with the boundary current.

2.5.2 Perturbation of flow in a nearly-circular droplet

To compute the surface modes of a circular droplet of chiral fluid, we followed a procedure similar to the one described above for the semi-infinite and finite slab flows. We defer details to a future publication but state the result here.

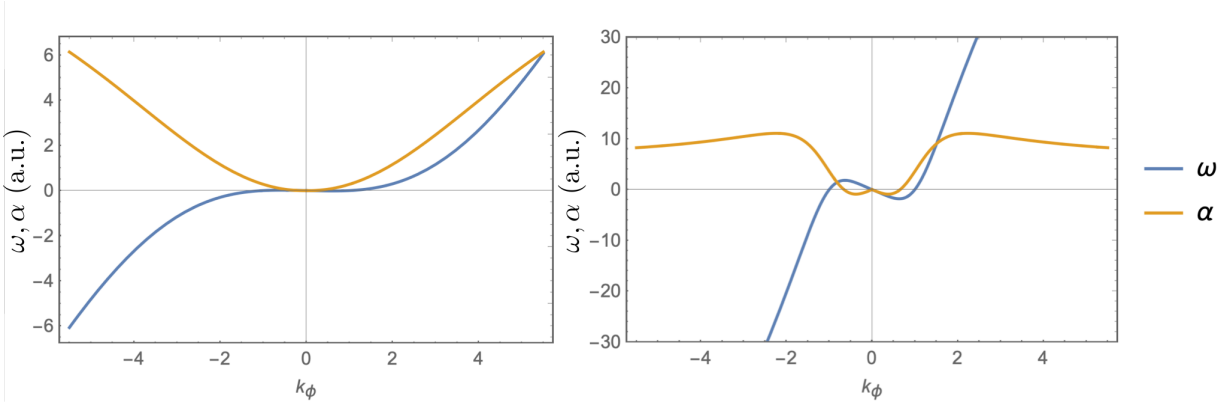

Figure 2.15: **Surface wave dispersion for perturbations of circular droplets.** (a) At $R/\delta \gg 1$ there is little change when compared to the semi-infinite slab problem. (b) For $R/\delta \sim 1$ the effects of finite radius become significant.

2.5.2.1 Solution and visualization

The spectrum $\omega(k_\phi)$ and dissipation rate $\alpha(k_\phi)$ of surface waves on circular droplets can be obtained as a function of the dimensionless azimuthal wavenumber k_ϕ by solving

$$\begin{aligned} i(\omega + i\alpha)\bar{R} &= -ik_\phi \delta\Omega \frac{\eta_R I_1\left(\frac{\bar{R}}{\delta}\right)}{\eta I_2\left(\frac{\bar{R}}{\delta}\right) + \eta_R I_0\left(\frac{\bar{R}}{\delta}\right)} \\ &\quad -|k_\phi\delta|\frac{\delta}{\bar{R}}\bar{R}^{|k_\phi|}\frac{1}{\eta+\eta_R}\frac{\beta_2\rho_1 - \beta_1\rho_2}{\alpha_1\beta_2 - \beta_1\alpha_2} \\ &\quad +\frac{1}{2ik_\phi}\left(I_{|k|+1}\left(\frac{\bar{R}}{\delta}\right) - I_{|k|-1}\left(\frac{\bar{R}}{\delta}\right)\right)\frac{\alpha_1\rho_2 - \alpha_2\rho_1}{\alpha_1\beta_2 - \beta_1\alpha_2}, \end{aligned}$$

where I_k are the modified Bessel functions of the first kind and:

$$\rho_1 = -\frac{\gamma}{\bar{R}}(k_\phi^2 - 1) - 2\Omega(\eta_o - ik_\phi\eta)\frac{\eta_R I_2\left(\frac{\bar{R}}{\delta}\right)}{\eta I_2\left(\frac{\bar{R}}{\delta}\right) + \eta_R I_0\left(\frac{\bar{R}}{\delta}\right)}$$

$$\rho_2 = -2ik\eta_o\Omega\frac{\delta}{\bar{R}}\frac{\eta_R I_1\left(\frac{\bar{R}}{\delta}\right)}{\eta I_2\left(\frac{\bar{R}}{\delta}\right)+\eta_R I_0\left(\frac{\bar{R}}{\delta}\right)} + 2\Omega\eta\frac{\eta_R I_2\left(\frac{\bar{R}}{\delta}\right)}{\eta I_2\left(\frac{\bar{R}}{\delta}\right)+\eta_R I_0\left(\frac{\bar{R}}{\delta}\right)}$$
$$- (\eta+\eta_R)\Omega\frac{\bar{R}}{\delta}\frac{\eta_R I_1\left(\frac{\bar{R}}{\delta}\right)}{\eta I_2\left(\frac{\bar{R}}{\delta}\right)+\eta_R I_0\left(\frac{\bar{R}}{\delta}\right)}$$

$$\alpha_1 = -\bar{R}^{|k_\phi|}\left[1+\frac{2}{(\eta+\eta_R)}\frac{\delta^2}{\bar{R}^2}(|k_\phi|-1)(\eta|k_\phi|-i\eta_o k_\phi)\right]$$

$$\alpha_2 = -\frac{\delta^2}{\bar{R}^2}\bar{R}^{|k_\phi|}\frac{2}{(\eta+\eta_R)}(|k_\phi|-1)(\eta_o|k_\phi|+i\eta k_\phi)$$

$$\begin{aligned}\beta_1 = {} & i\frac{\eta}{k_\phi\bar{R}}\left[(|k_\phi|-1)I_{|k|-1}\left(\frac{\bar{R}}{\delta}\right)+(|k_\phi|+1)I_{|k|+1}\left(\frac{\bar{R}}{\delta}\right)\right] \\ & +\frac{\eta_o}{|k_\phi|\bar{R}}\left[(|k_\phi|-1)I_{|k|-1}\left(\frac{\bar{R}}{\delta}\right)-(|k_\phi|+1)I_{|k|+1}\left(\frac{\bar{R}}{\delta}\right)\right]\end{aligned}$$

$$\begin{aligned}\beta_2 = {} & -\frac{\eta+\eta_R}{|k_\phi|\delta}I_{|k|}\left(\frac{\bar{R}}{\delta}\right) \\ & +\frac{\eta}{|k_\phi|\bar{R}}\left[(|k_\phi|+1)I_{|k|+1}\left(\frac{\bar{R}}{\delta}\right)-(|k_\phi|-1)I_{|k|-1}\left(\frac{\bar{R}}{\delta}\right)\right] \\ & +i\frac{\eta_o}{k_\phi\bar{R}}\left[(|k_\phi|+1)I_{|k|+1}\left(\frac{\bar{R}}{\delta}\right)+(|k_\phi|-1)I_{|k|-1}\left(\frac{\bar{R}}{\delta}\right)\right]\end{aligned}$$

and $\bar{R}$ is the unperturbed droplet radius. Representative plots of the resulting $\omega(k_\phi)$ and $\alpha(k_\phi)$ are shown in Figure 2.15.

2.5.3 Measurement of surface wave dispersion

To measure the dispersion relation, we excite surface waves on straight strips or nearly-circular droplets of chiral fluid, prepared as in Section 2.2.2, either by briefly rolling particles in the direction perpendicular to the fluid, or by letting nearby droplets merge with it. We then spin the particles for about 10 minutes and let the perturbations evolve in time (see Fig. 2.6a). As the strip or circular droplet equilibrates, small nearby clusters may coalesce with it, resulting in additional excitations.

We identify the edges of the strip or circular droplet by thresholding the images and using Canny edge detection. For the strip geometry, we take the height profile to be the distance from a straight line which spans the strip to the strip's perturbed edge. For the circular geometry, we take the radial profile to be the distance from the circumference of the droplet to its center of mass. For high-friction experiments, we record this height or radial profile over time at a sample rate between 1 fps and 4 fps. For low-friction experiments, the dynamics are substantially faster, so we record the same profile at a rate between 25 fps and 50 fps. We then perform a fast Fourier transform (FFT) on this data. We square the absolute value of this FFT to obtain a power spectrum in frequency ω, and wavenumber k. To obtain the final power spectrum we normalize each slice in k by the average power in that slice.

2.6 Chiral wave damping

The wave dynamics are thus crucially sensitive to boundary layer flows. A natural avenue for investigation, then, is to seek to increase the thickness of the boundary in order to increase its relative role. We now show how an increase of the penetration depth of the boundary layer amplifies chiral effects and reveals a long sought-after source of stress, commonly referred to as Hall viscosity.

We reduce the surface friction by allowing our chiral liquid to sediment upon an air-

water interface (Fig. 2.16b), as opposed to a glass surface (Fig. 2.16a). Due to the difficulty in maintaining a slab geometry in this regime, we examine surface fluctuations on circular droplets, using the results of Section 2.5.2.

As can be seen in Fig. 2.16a-b, the edge flow penetrates deeper into the chiral fluid as friction is reduced. The dispersion relations for high and low friction droplets display the same trend, although the range of accessible wave vectors normalized by the penetration length ($k\delta$) is larger in the low friction case. An extension of our theory to circular geometries (Section 2.5.2) again accurately captures the dispersion relations for high friction (Fig. 2.16a) and low friction (Fig. 2.16b).

The remarkable agreement between experiment and theory is however challenged when investigating the damping dynamics of the chiral waves. Experimentally, the damping rate α of chiral waves of wave vector k is given by fitting a Lorentzian to the width of the power spectrum (see Section 2.6.2); the resulting damping rates are shown in Fig. 2.16c-d. Our hydrodynamic theory predicts this damping rate to be proportional to surface tension. This is natural since surface tension flattens interfacial deformation: in the absence of inertia, the relaxation does not overshoot and capillary waves are overdamped. In the long wavelength limit ($k\delta \ll 1$), the damping rate $\alpha \sim (\gamma/\Gamma_u)|k|^3$ stems from the competition between surface tension and substrate friction. As seen in Fig. 2.16c, in the high friction case we again find excellent agreement between theory and experiment, which provides a direct measurement of surface tension. The value we find, $\gamma = 2.3 \pm 0.2 \times 10^{-13}$ N, is consistent with an estimate based on magnetic interactions between rotating dipoles, and further detailed in Section 2.6.2.

In the case of low surface friction, however, we observe a distinct new feature in the dissipation rate: a leveling off of the dissipation rate at short wavelengths which cannot be accounted for by the hydrodynamic theory discussed thus far, suggesting the presence of an additional mechanism for surface wave dissipation in our chiral fluid.

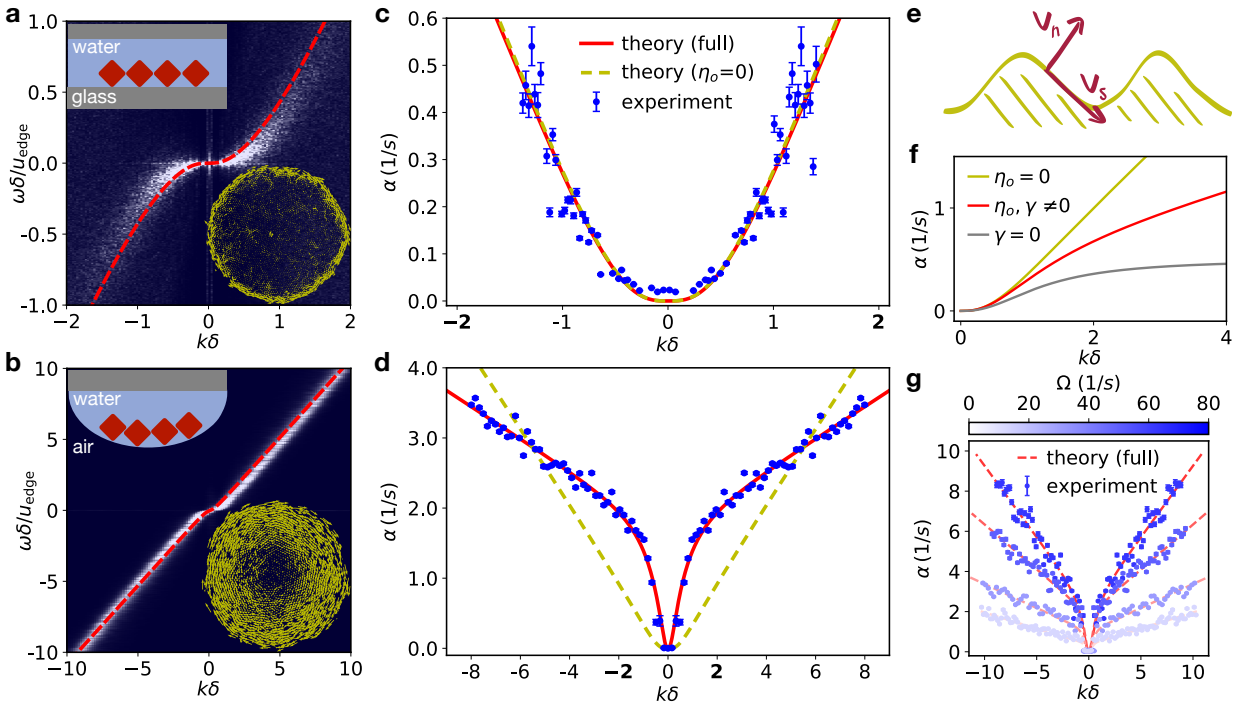

Figure 2.16: **Wave dissipation and measurement of Hall viscosity. a,** In the circular geometry, surface waves yield power spectra $\langle|R(k,\omega)|\rangle$, plotted here versus the normalized wave vector $k\delta$ and frequency $\omega\delta/u_{\text{edge}}$ (c.f. Fig. 2.6c for a collection of spectra). **b,** Power spectrum at a low friction air-water interface, for which the edge current is delocalized into the bulk when compared to a high friction interface as in **a** (see insets). **c,** The dissipation rate of waves on the surface of a circular droplet can be used to extract the surface tension, and the shape of $\alpha(k)$ can be captured by a theory with no odd viscosity ($\eta_o = 0$). **d,** Lowering substrate friction causes the dissipation to level off for large $k\delta$, which can only be captured by a theory including η_o. **e,** The tangential and normal components of velocity at the boundary give rise to a normal Hall stress (Eq. (2.27)). **f,** The dissipation for a chiral fluid with η_o in the absence of surface tension, γ, vs. the same for a fluid with γ in the absence of η_o. For small $k\delta$, the two curves are indistinguishable. For large $k\delta$, the η_o-dissipated fluid shows no k-dependence, while the γ-dissipated fluid shows linear k-dependence. Shown also for reference is the attenuation for a fluid with finite values of both γ and η_o **g,** With η_o-induced attenuation, $\alpha(k)$ varies with frequency with all other parameters held constant, a trend that is not observed for γ-dissipated fluids. All error bars represent fit uncertainty from the determination of $\alpha(k)$ from the power spectrum.

2.6.1 Hall viscosity

Seeking a hydrodynamic description, we recall that isotropic chiral fluids can in principle possess an additional stress in their constitutive relation, known interchangeably as "anoma-

lous viscosity." "odd viscosity," or "Hall viscosity" [5, 6, 7, 8]. This non-dissipative, transverse stress is linked by Onsager relations to the breaking of time-reversal symmetry.

Theoretically, odd viscosity has indeed been shown to arise in the hydrodynamics of plasmas [60, 61, 62], systems of spinning molecules [31, 15], as well as quantum Hall fluids and vortex fluids [8, 5, 68]. A signature of Hall viscosity was further revealed in the transport properties of magnetized 3D dilute gases [32]. We here conjecture our dense chiral fluid to support an additional Hall stress $\sigma^{\mathrm{o}}_{ij} = \eta_o \left(\partial_i \epsilon_{jk} v_k + \epsilon_{ik} \partial_k v_j\right)$. In incompressible fluids such as the one considered here, the effect of odd viscosity can solely be seen at the edge. This is because in the bulk flow Hall stress is merely absorbed into the fluid pressure. The signature of odd viscosity in our chiral fluid is thus an additional boundary stress. The component normal to the interface σ_{nn}, after absorbing a vortical component into the pressure, is given by

$$\sigma_{nn} = 2\eta_{\mathrm{o}} \left(\partial_s v_n + \frac{v_s}{R(s)}\right), \tag{2.27}$$

where v_n (resp. v_s) is the velocity normal (resp. tangential) to the surface (see Fig. 2.16e), and $R(s)$ is the local radius of curvature.

In our system, where odd stress powers a boundary-layer edge flow, we thus expect odd viscosity to flatten surface deformation in a manner akin to surface tension, $\sigma^{\mathrm{o}} \sim \eta_{\mathrm{o}} v_s / R$. The excellent agreement between our measurements and predictions from a full hydrodynamic theory confirms this simplified picture and establishes the presence of Hall viscosity in our colloidal chiral fluid (see Fig. 2.16d, f-g). From the fit we obtain $\eta_{\mathrm{o}} = 1.5 \pm 0.1 \times 10^{-8}$ Pa m s.

The clearly visible decrease in slope in the damping relation is the most visible signature of Hall viscosity in our data and can be understood on dimensional grounds. In the long wavelength limit, the wave relaxation time is controlled by the competition of either surface tension or Hall stress with substrate friction. Dimensionally this implies a scaling $\alpha \sim |k|^3$ since the ratios γ/Γ_u and $\eta_{\mathrm{o}} v_s / \Gamma_u$ have dimension of volume per unit time. In contrast, in the short wavelength limit, surface friction plays no role and damping stems from the competition

of surface tension or Hall stress and bulk viscosities alone. In this case dimensional analysis requires linear scaling with wavenumber in the case of surface tension, and wave-number independence in the case of Hall stress. This change in wavenumber dependence brings about a visible rollover to a decreased slope in the wave damping rate, and is interpreted at length in Section 2.6.4.

We note that for small ranges of $k\delta \sim [-1, 1]$, characteristic of spectral measurements in the presence of high surface friction, the leveling off cannot be seen and the relative roles of Hall viscosity and surface tension become hard to separate. This is the case for the damping shown in Fig. 2.16c which can be fit well by both a non-zero and zero value of Hall viscosity. The disambiguation of these parameters is a topic of discussion in Section 2.6.3.

2.6.2 Measurement of surface wave dissipation

The experimentally observed power spectrum shows dissipative waves with a clear dispersion relation in both geometries, as shown in the left panel of Figure 2.17 and in Figure 2.6b,c (strip) and Figure 2.16a,b (droplet). Taking the form of excitations to be proportional to $e^{i\omega t - \alpha t}$, where ω characterizes the propagation of waves and α the dissipation, the power $P_k(\omega)$ at each k is given by the relation

$$P_k(\omega) \propto \frac{1}{\alpha(k)^2 + [\omega - \omega(k)]^2}, \tag{2.28}$$

where the functions $\omega(k)$ and $\alpha(k)$ define the dispersion relation and dissipation rate, respectively, of the linear waves.

There are often small background drifts in the chiral fluid which may result in a secondary linear feature in the power spectrum. While this additional feature varies between samples, the main dispersion curve remains unchanged. We thus fit the spectrum at each k to a sum of two peaks of the form in Eq. (2.28) (see also right panel in Figure 2.17a). By selecting

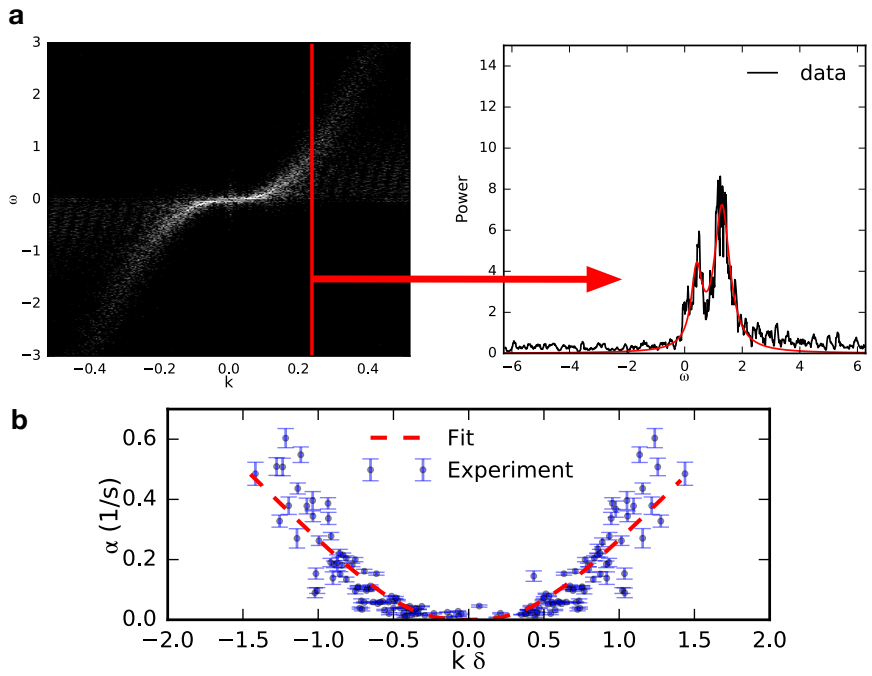

Figure 2.17: **Extracting wave dissipation rates from the power spectrum. a,** By fitting each slice using the relation in Eq. (2.28) we obtain values for the dissipation α at each wavenumber k. **b,** We fit these values to the analytical solution, to infer the fluid's surface tension. Shown with the red dashed line is a fit to the theoretical prediction for the damping rate of the chiral waves.

the peaks closest to the dispersion curve, we obtain the value of α at each k, as shown in Figure 2.17b).

For low-friction experiments, we observe a background rotation of the chiral fluid (see Section 2.4.3). As a result, we correct $\omega(k)$ by subtracting the background rate of the interface, Ω_R, in Figure 2.16b. This correction does not have any effect on the dissipation of waves $\alpha(k)$ as it preserves the width of the spectra at each k.

By fitting $\alpha(k)$ to the full analytical solution for the dissipation ignoring contributions from η_o (see Section 2.5.1.4 for an asymptotic approximation in the strip geometry) we infer the surface tension of the fluid γ. At the glass interface and in the strip geometry, we find

$$\gamma_{\text{glass}} = 2.3 \pm 0.2 \times 10^{-13} \text{ N}.$$

We obtain the same result for a circular droplet geometry within measurement error. The fitted dissipation data are presented in Figure 4c (droplet) and Figure 2.17 (strip). When fitting to the full analytical solution for the dissipation adding contributions from η_o we obtain the same result for γ, with $\eta_{\text{o,glass}} = 0 \pm 2 \times 10^{-9}$ Pa m s.

On air interfaces, we are no longer able to fit the dissipation without including contributions from η_o. In this case, for a droplet geometry, we obtain

$$\gamma_{\text{air}} = 3.7 \pm 0.2 \times 10^{-13} \text{ N},$$

$$\eta_{o,\text{air}} = 1.5 \pm 0.1 \times 10^{-8} \text{ Pa m s}.$$

2.6.3 Disambiguating Hall viscosity and surface tension

As noted in Section 2.6.1 disentangling the relative role of Hall viscosity η_o and surface tension γ relies on observing wave dissipation $\alpha(k)$ over a large range of rescaled wavelengths

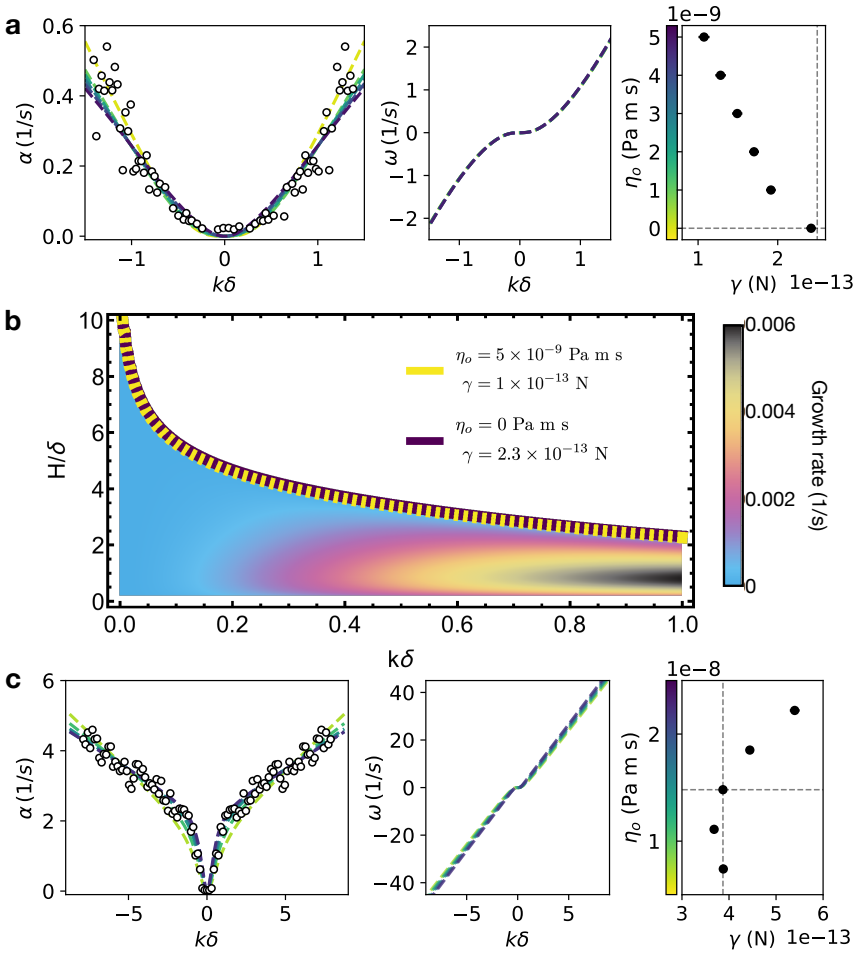

Figure 2.18: **Disambiguating Hall viscosity and surface tension. a,** For high-friction experiments, the acquired wave dissipation data are limited to $k\delta{\sim}1$, and can be fit to both zero and non-zero Hall viscosity (left), yielding no discrepancy in the dispersion (middle), by altering the apparent surface tension (right). **b,** The boundary between stable and unstable modes constructed using a non-zero value of Hall viscosity is indistinguishable from the boundary for $\eta_o = 0$. Here, each boundary curve is shown over the calculated diagram for $\eta_o = 0$. **c,** In the large $k\delta$ regime, similarly to **a**, we can fit the low-friction experimental data to a wide range of Hall viscosity values (left-middle), in this case finding an opposite correlation to **a** (right).

$k\delta$. On a glass substrate, the typical range of $k\delta$ is too small to observe these features. The dispersion $\omega(k)$ is not useful in lifting this ambiguity, because it is unchanged by the inclusion of non-zero η_o, as shown in Figure 2.18a. Moreover, the dissipation can be modeled by the hydrodynamic theory (see Section 2.5.2) incorporating non-zero η_o by compensating with γ, as can be seen from the asymptotic form of $\alpha(k)$ at small $k\delta$, $\alpha{\sim}k^3(\gamma + \eta_o)$ (see

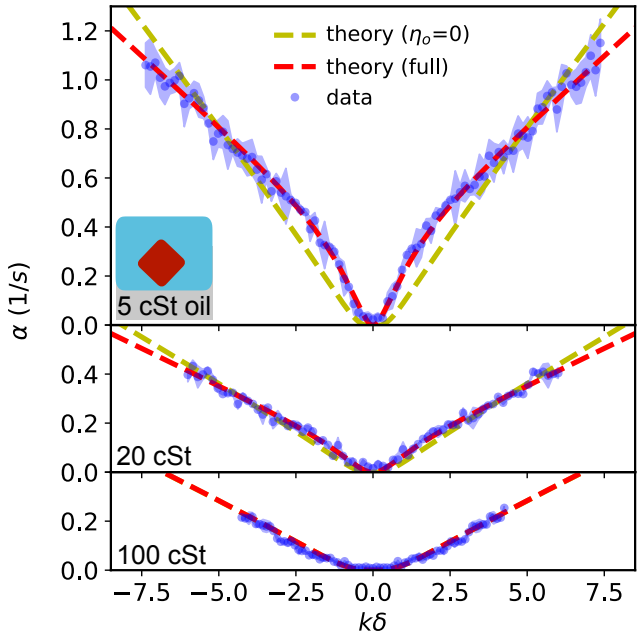

Figure 2.19: **Hall viscosity emerges for low substrate friction.** When the spinner fluid is over a water-oil interface, the wave dissipation can be measured at larger $k\delta$ for lower viscosities of oil, which lead to lower substrate friction and thus larger penetration depth δ. With this extended scope, we are better able to distinguish the effects of surface tension γ and Hall viscosity η_o, by fitting to the theory with and without η_o.

Section 2.5.1.4) and shown in Figure 2.18a.

However, we obtain a clear signature of Hall viscosity in the dissipation when we decrease the substrate friction Γ_u, by replacing the glass substrate with an oil or air interface, as demonstrated in Section 2.6.1. By changing the oil viscosity we can tune Γ_u between these two regimes (see Section 2.2.2) and explore the emergence of this qualitative signature of Hall viscosity. This procedure regulates δ, thus controlling the range of $k\delta$ over which surface waves are observed. We plot the wave dissipation $\alpha(k)$ for representative values of oil viscosity in Figure 2.19. As the viscosity is decreased (and hence also the substrate friction), the presence of η_o is more discernible through leveling-off at large $k\delta$, and the quality of fits with $\eta_o = 0$ becomes increasingly poor. By contrast, the dissipation on a high viscosity interface can be captured using both a non-zero or zero value of η_o, just as observed

for the glass substrate experiments (c.f. Figure 4c).

We note that there is also an ambiguity in distinguishing the effects of Hall viscosity and surface tension for data containing wave dissipation at $k\delta \gg 1$. To see this, we fit $\alpha(k)$ for waves measured at an air interface to the full hydrodynamic theory for γ, by imposing values of η_o $\pm 50\%$ of $\eta_{o,\mathrm{air}}$. We find that the data is fit well for a wide range of values of η_o by tuning γ to compensate, as in Figure 2.18c. To explain the correlation of η_o and γ in this regime, as presented in the right panel, we consider the large $k\delta$ asymptotic $\alpha \sim k\gamma/(1+\eta_o^2)$. The dispersion does not resolve this correlation, as $\omega(k)$ is not strongly-dependent on η_o.

2.6.4 Physical interpretation of dynamics

Having established the presence of Hall viscosity by examining wave damping, it follows to ask whether it has an effect on wave propagation. The first term in Eq. (2.27) suggests that Hall viscosity and surface tension could act together to support wave propagation. Surface tension acts on a sinusoidal surface deformation by pulling down peaks and pushing up troughs, generating an in-phase normal velocity component. The normal Hall stress $\partial_s v_n$ would then act out of phase on the inflection points of the sinusoidal perturbation to propagate it in a chiral fashion. Our full theory confirms that this additional wave-driving mechanism indeed exists and generates waves even in the absence of edge currents. However, for our hydrodynamic parameters, their effect on the dispersion is minimal. In this section, we examine the roles of surface tension, shear viscosity, Hall viscosity and rotational viscosity in determining the surface dynamics of the chiral fluid.

2.6.4.1 Surface waves driven by "edge pumping"

We begin by considering the propagation of waves in the limit $\eta_o = \gamma = 0,\ \eta_R \neq 0,\ \eta \to 0$. In this limit, the surface waves are undamped ($\alpha(k) = 0$). The asymptotic dispersion relation

computed in Section 2.5.1 for a semi-infinite slab:

$$\omega(k) = \begin{cases} 2u_{\text{edge}} \dfrac{\eta}{\Gamma_u} k^3 & |k\delta| \ll 1 \\ -\dfrac{2\eta_R \Omega}{\eta + 2\eta_R} + u_{\text{edge}} k & |k\delta| \gg 1 \end{cases}$$

provides a basis for discussion. The dispersion relation suggests that in the limit $\eta \to 0$, surface dynamics might be suppressed. This is indeed the case!

Consider the limit $\eta = \eta_o = 0$. The stress boundary condition, Eq. (2.10), reduces simply to $p|_{\partial D} = 0$ and $\omega|_{\partial D} = 2\Omega$. Since $\nabla^2 p = 0$ we have $p \equiv 0$ and, hence, $\nabla p \equiv 0$. This reduces the bulk flow equations to

$$\mathbf{u} = \frac{\eta_R}{\Gamma_u} \left(-\partial_y \omega, \partial_x \omega \right). \tag{2.29}$$

Evaluating this expression on the boundary ∂D, contracting it against the normal, and applying the kinematic boundary condition yields

$$\mathbf{v} \cdot \mathbf{n} = \frac{v_s}{\Gamma_u} \frac{\partial}{\partial s} \omega|_{\partial D} \equiv 0$$

where the last equality uses that ω is constant on the boundary. Hence, the normal velocity of the boundary is zero, and ∂D is static.

Lack of surface dynamics does not imply a lack of edge flow; Indeed, Eq. (2.29) establishes a direct connection between a gradient in vorticity and transverse flow. As already noted, the vorticity satisfies the screened Laplace equation:

$$\left(\nabla^2 - \frac{1}{\delta^2} \right) \omega = 0$$

with the boundary condition $\omega = 2\Omega_0$ (for $\eta = \eta_o = 0$). Vorticity at the surface is thus screened on the interior, with the value dropping to zero at distances of a few δ from the

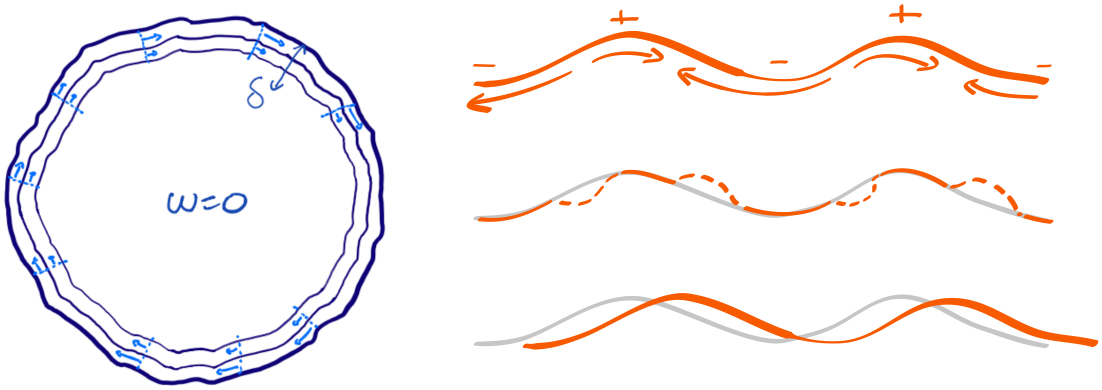

Figure 2.20: **The edge-pumping effect**. (Left:) in the absence of viscosity and surface tension, the boundaries of our chiral fluid droplets do not move; they simply have an exponentially screened edge current glued to them. (Right:) In the presence of viscosity, differential mass flux in the edge current shifts fluid from one region to another, which in the case of a sinusoidal perturbation results in wave propagation.

boundary. Eq. (2.29) implies that a gradient of vorticity corresponds to flow perpendicular to the gradient, thus the fluid flows along the equi-vorticity lines. Since the vorticity deep in the fluid is zero, the total mass flux of the edge current – obtained by integrating the gradient of the vorticity along a line from the interior of the chiral fluid to its surface – is proportional to the value of the vorticity at the surface. In the absence of viscosity η and Hall viscosity η_o, the latter is constant and the mass flux is constant at all points along the surface. *Thus in the absence of viscosity (and surface tension), the boundary of our chiral fluid droplets does not move, and simply has an exponentially screened edge current glued to it.*

In the presence of viscosity η, however, the value of vorticity at the surface will be increased (decreased) in positively (negatively) curved regions of the boundary, giving rise to enhanced (reduced) mass flux in response to reduced (increased) viscous drag. The differential mass flux then effectively pumps fluid from one region of the surface to another, giving rise to dynamics. A sketch of the resulting flow in the case of a sinusoidal perturbation is shown in Figure 2.20. In this case the result is wave propagation. *This "edge-pumping" effect*

is the fundamental mechanism that gives rise to free surface dynamics of our chiral fluids.

Sidenote 1: We note that an analogy can be made between vorticity in our system and the electric potential inside a conducting medium, with penetration depth δ. The velocity at the edge depends on the curvature of the surface, roughly as $|\mathbf{u}| = (1 + C\kappa)2\Omega\delta$ for small curvature κ; in the electrostatic analogy, the latter is proportional in magnitude to the surface charge on the conductor which in turn depends on the curvature of the surface. Crucially then, the mass flux in this tangential surface flow is determined by the vorticity ω on the surface: integrating $\frac{\eta_R}{\Gamma_u}\nabla\omega$ from the center (where $\omega = 0$) to the edge is at once equal to $(\eta_R/\Gamma_u)2\Omega$, and hence proportional to the value of the vorticity at the boundary, and equal to the total mass flux.

Sidenote 2: For nonzero surface tension (and zero Hall viscosity), it is straightforward to show that the surface dynamics when $\eta = 0$ is curve-shortening. Consider a droplet of chiral fluid whose boundary length is $L(t)$. A standard equality is then $\dot{L} = \int_{\partial D} ds\kappa\ \mathbf{v}\cdot\mathbf{n}$. Using the bulk flow equation and that $\omega_s = 0$ on the boundary yields

$$\dot{L} = -\frac{1}{\gamma\Gamma_u}\int_{\partial D} ds\ p\ \frac{\partial p}{\partial \mathbf{n}} = -\frac{1}{\gamma\Gamma_u}\int_D dA\ |\nabla p|^2 < 0 \tag{2.30}$$

where in the last identity we used the divergence theorem and that p is harmonic. Hence, the long-time behavior is simply relaxation to a circular drop.

2.6.4.2 Effects of Hall stress

For an incompressible fluid, the Hall viscosity has no effect on bulk flows. Its influence is instead felt on the boundary where it exerts a stress whose normal component is

$$\sigma^o_{nn} = \eta_o\left(\partial_s v_n + \frac{v_s}{R}\right)$$

Here, v_s and v_n are the tangential and normal components of velocity. Note that in the absence of odd stress η_R and drive, or surface tension γ, there is no flow at the surface and Hall viscosity has no effect.

2.6.4.3 Hall damping

The presence of Hall viscosity does not affect surface dynamics in the absence of both surface tension and odd stress, as the Hall surface stress is proportional to the surface flow. Thus the effect that Hall viscosity has on both the propagation and damping of waves originates from the combined effect of Hall viscosity and surface tension, or Hall viscosity and the localized edge current glued to the boundary of our fluid.

In the absence of surface tension, but in the presence of odd stress, the damping of surface waves on a semi-infinite slab $\alpha(k)$ is given by:

$$\alpha(k) = \begin{cases} \dfrac{2\eta_o u_{\text{edge}}}{\Gamma_u}|k|^3 & |k\delta| \ll 1 \\ \dfrac{2\eta_o \eta_R \Omega}{(\eta + 2\eta_R)^2 + \eta_o^2} & |k\delta| \gg 1 \end{cases}$$

This damping originates from the normal component to the boundary Hall stress $\frac{\eta_o u_{\text{edge}}}{R}$, where R is the radius of curvature of the surface. This stress has identical form to the stress arising from surface tension and thus acts to reduce the curvature of the interface (see Figure 2.21).

Dimensionally, for long waves (small wavenumbers compared to δ), a competition of Hall surface stress and substrate friction:

$$\left[\frac{\eta_o u_{\text{edge}}}{\Gamma_u}\right] \sim \frac{L^3}{T}$$

suggests a scaling with k^3 as found by the calculation above. For short waves however (large

Figure 2.21: **Hall tension.** The edge current induces a Hall stress that acts like surface tension to flatten the interface.

wavenumber compared to δ), the substrate friction is no longer relevant and the relevant quantities (in the absence of surface tension) are: $\eta_o, \eta_R, \eta, \Gamma, \Omega, k$. These have dimensions:

$$[\eta_o] = [\eta_R] = [\eta] = \frac{M}{T}, \qquad [\Omega] = \frac{1}{T}, \qquad [k] = \frac{1}{L}$$

Since the viscosities η_o, η_R, η must appear as ratios, the only quantity with the required units of T^{-1} is Ω and the wavenumber k drops out of the problem. This is in contrast to the case of surface tension where the units of length associated with the surface tension $[\gamma] = ML/T^2$ give rise to a linear wavenumber dependence.

These surface stresses lead to the exponential decay of surface perturbations. This role of Hall stress in the damping of surface waves may seem unusual as Hall viscosity is a transverse, conservative stress. This arises in our case from the over-damped nature of our dynamics.

2.6.4.4 Capillary Hall waves

For a sinusoidal perturbation to the surface height $h \sim \cos(kx)$, we expect surface tension to drive an in-phase flattening flow $v_n \propto \cos(kx)$. This results in an out-of-phase Hall stress $\eta_o \partial_s v_n \sim \eta_o \sin(kx)$ which acts on the inflection points of the sinusoidal perturbation. The result is uni-directional propagation of the sinusoidal perturbation (see Figure 2.22). These

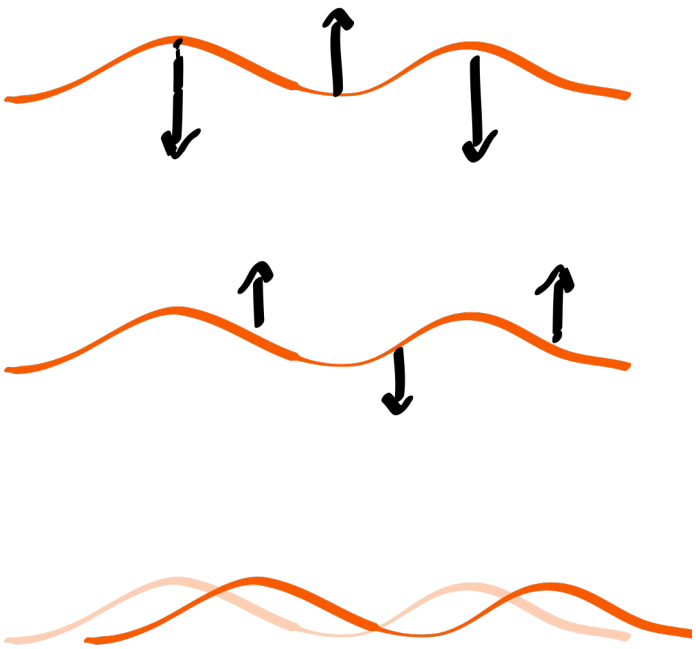

Figure 2.22: **Capillary-Hall mechanism.** Surface tension induces a flattening of the interface which the Hall stress $\eta_0 \partial_s v_n$ converts into wave propagation.

waves are in turn damped by surface tension:

$$\alpha(k) = \begin{cases} \dfrac{\gamma}{\Gamma_u}|k|^3 & |k\delta| \ll 1 \\ \dfrac{1}{2}\dfrac{\gamma\eta}{\eta^2+\eta_o^2}\ |k| & |k\delta| \gg 1 \end{cases}$$

In the absence of u_{edge}, and thus of the edge-pumping mechanism, waves can still propagate, as evidenced by the dispersion relation for waves on a semi-infinite slab (with $\gamma = \eta_R = 0$):

$$\omega(k) = \begin{cases} 4\dfrac{\gamma\eta_o}{\Gamma_u^2}\ k^5 & |k\delta| \ll 1 \\ \dfrac{1}{2}\dfrac{\gamma\eta_o}{\eta^2+\eta_o^2}\ k & |k\delta| \gg 1 \end{cases}$$

Both the drive and damping in this case come from a combination of surface tension γ and Hall viscosity η_o. The mechanism giving rise to these uni-directional waves can be understood in simple terms from the contribution to the normal component to the boundary Hall stress: $\eta_o \partial_s v_n$.

It would be interesting to consider this kind of capillary-Hall waves as a feature of underdamped interfaces as well.

2.6.4.5 Effects of finite odd substrate friction

In the calculation of Section 2.5.1, we neglected the transverse component $\Gamma_\perp$ of the substrate friction tensor Γ_{ij}, as a measurement of the substrate friction (Section 2.4.2) excluded the contribution of transverse friction to the observed dynamics. In this section, we investigate the effect that a finite $\Gamma_\perp$ would have on the surface dynamics of our chiral fluid. We find that transverse friction introduces corrections to the dispersion $\omega(k)$ and dissipation rate $\alpha(k)$ of surface waves. For long wavelengths, the contribution to $\alpha(k)$ from $\Gamma_\perp$ resembles that of surface tension γ and odd viscosity η_o; at short wavelengths, however, the contribution of $\Gamma_\perp$ drops off, unlike γ and η_o.

Repeating the calculation of Section 2.5.1 for finite $\Gamma_\perp$, we obtain the dispersion $\omega(k)$ and dissipation rate $\alpha(k)$ plotted in Figure 2.23a. From this result we can extract the corrections, to leading order in k, to the dispersion and dissipation rate due to transverse friction. In the long wavelength limit, $|k\delta| \ll 1$, the asymptotic dispersion and dissipation rates are:

$$\omega(k) = -\gamma \frac{\Gamma_u \Gamma_\perp}{\bar{\Gamma}^3} \sqrt{\frac{\Gamma_u}{\bar{\Gamma}}} k^3 + \left(\frac{\Gamma_u}{\bar{\Gamma}} \frac{\eta}{\Gamma_u} - \frac{\Gamma_\perp}{\bar{\Gamma}} \frac{\eta_o}{\Gamma_u} \right) \frac{\Gamma_u}{\bar{\Gamma}} u_{\text{edge}} k^3,$$
$$\alpha(k) = \gamma \frac{\Gamma_u^2}{\bar{\Gamma}^3} \sqrt{\frac{\Gamma_u}{\bar{\Gamma}}} |k|^3 + \left(\frac{\Gamma_\perp}{\bar{\Gamma}} \frac{\eta}{\Gamma_u} + \frac{\Gamma_u}{\bar{\Gamma}} \frac{\eta_o}{\Gamma_u} \right) \frac{\Gamma_u}{\bar{\Gamma}} u_{\text{edge}} |k|^3,$$

where $\bar{\Gamma} = \sqrt{\Gamma_u^2 + \Gamma_\perp^2}$. By comparison to Section 2.5.1.4 and 2.6.4, we see that $\Gamma_\perp$ causes a rescaling of dispersive terms that originate from edge-pumping. Then, by comparison to Sec-

tion 2.5.1.4 and 2.6.4.3, we see a similar rescaling of the dissipative terms that originate from surface tension and Hall stress. Further, $\Gamma_\perp$ introduces a correction to the long-wavelength dispersion due to both surface tension and Hall viscosity and an addition to the dissipation rate mediated by the shear viscosity η. The latter can be understood as illustrated in Figure 2.23b:

($\eta = 0$) Without shear viscosity the mass flux is constant, so the transverse friction generates a uniform pressure over the surface.

($\eta \neq 0$) Meanwhile, the presence of shear viscosity enables a differential mass flux (see Section 2.6.4) that couples the curvature to the dissipation rate, such that the transverse friction acts like a surface tension.

Apparently, the dissipation rate due to Hall viscosity η_o, transverse friction $\Gamma_\perp$, and surface tension γ scales as $|k|^3$ for $|k\delta| \ll 1$.

In the short wavelength limit, $|k\delta| \gg 1$, the $\mathcal{O}(1)$ and $\mathcal{O}(k)$ contributions to the dispersion and dissipation rate (see Section 2.5.1.4) are unchanged. We find however for $\gamma = \eta_o = 0$, the correction to the dissipation is

$$\alpha(k) = \frac{\Gamma_\perp}{2\Gamma_u} \frac{\eta_R(\eta + \eta_R)\Omega}{\eta(\eta + 2\eta_R)} \frac{1}{|k\delta|},$$

such that the damping associated with transverse friction rapidly falls off for large $|k\delta|$. By contrast, the damping due to Hall viscosity is wavelength-independent in this limit, as illustrated in Figure 2.23a. As the effect of Hall viscosity and transverse friction arise as a transverse boundary stress, the qualitative similarity in damping behavior between η_o and $\Gamma_\perp$ up to intermediate $|k\delta|$ begs the question: to what extent can $\Gamma_\perp$ mimic the effects of η_o? In the following sections, we inspect the wave dissipation rate over a finite range of $k\delta$ and see that transverse friction could indeed mimic Hall viscosity. We show, however, that this potential ambiguity is eliminated by our measurement of transverse friction.

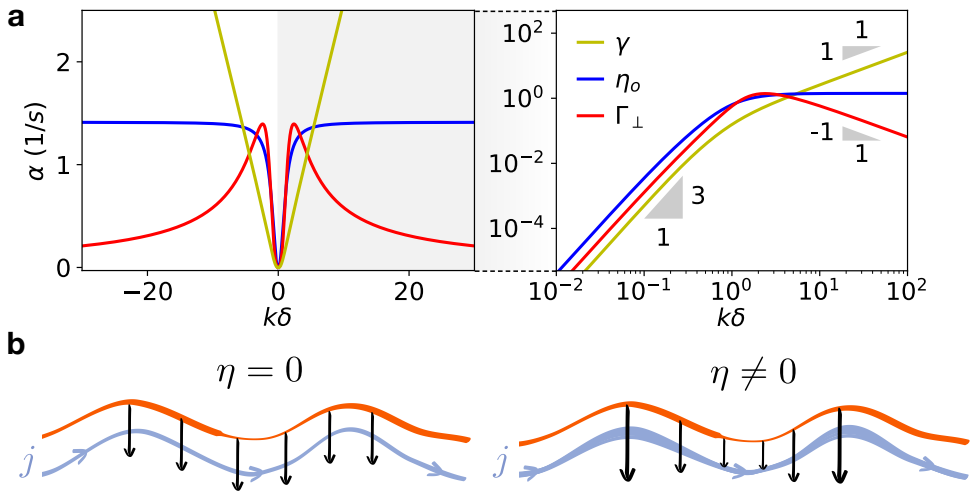

Figure 2.23: **Wave damping due to transverse friction. a,** The wave damping associated with Hall viscosity η_o, transverse friction $\Gamma_\perp$, and surface tension γ scales as $|k|^3$ for $|k\delta| \ll 1$. However, at $|k\delta| \gg 1$, the damping rates scales as $|k|^0$, $|k|^{-1}$, and $|k|^1$ respectively. **b,** In the limit $|k\delta| \ll 1$, when $\eta \neq 0$, the mass flux j varies with curvature, so that the transverse friction acts like a surface tension. In the absence of a shear viscosity η, the mass flux at a free surface is constant, such that the force of transverse friction is to induce a constant pressure.

Modelling wave dissipation with transverse friction. We first investigate the possibility that finite $\Gamma_\perp$ and γ, in the absence of η_o might account for the dissipation rate measured within a finite range of $|k\delta| < 10$. Here, we find that this is indeed possible, but only for large values of $\Gamma_\perp/\Gamma_u$, which are ruled out by direct measurement of the friction coefficients in Section 2.4.2.

We proceed as in Figure 4d in which we fit the low-friction dissipation rate for Hall viscosity η_o and surface tension γ with $\Gamma_\perp = 0$. Now, consider the case $\eta_o = 0$ for finite values of $\Gamma_\perp$ and γ. Figure 2.24a shows that we find excellent agreement between this modified theory and the fit curve of Figure 4d, for $\Gamma_\perp/\Gamma_u \sim 2.6$ and $\gamma \sim 4.7 \times 10^{-13}$ N. We stress that this estimate of $\Gamma_\perp$ is, however, inconsistent with our sedimentation measurements (see Section 2.4.2) from which we showed that $\Gamma/\Gamma_\perp \ll 1$

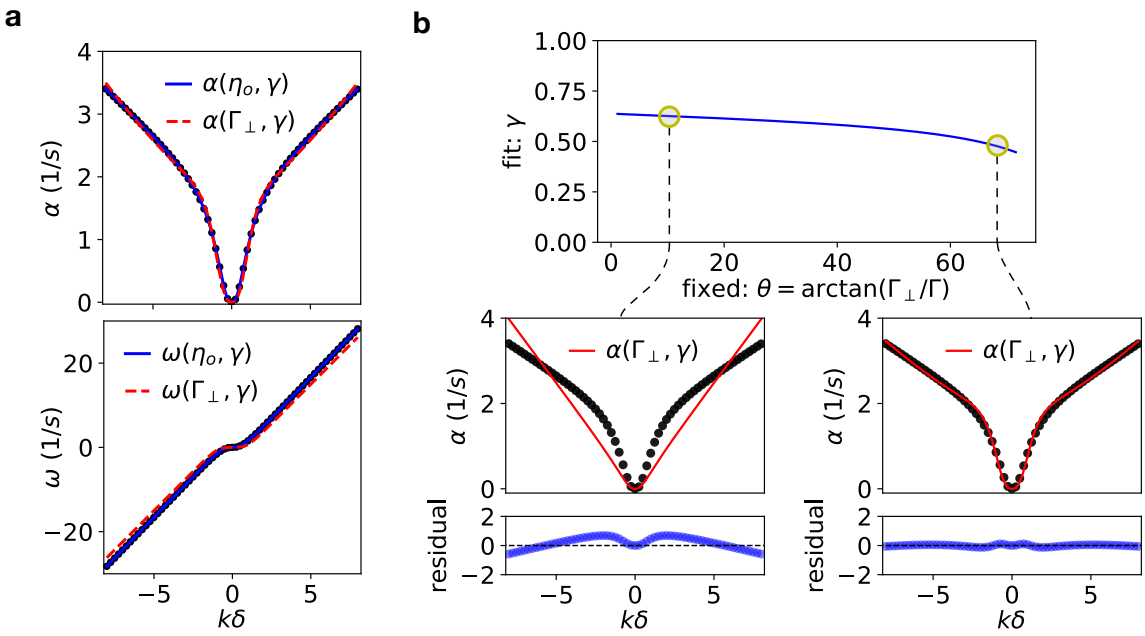

Figure 2.24: **Disambiguating Hall viscosity and transverse friction. a,** The dissipation and dispersion measured in the low-friction experiments can be captured by the hydrodynamic theory in the limit $\eta_o = 0$ or $\Gamma_\perp = 0$, but **b,** $\Gamma_\perp/\Gamma_u$ must be large to permit this agreement.

To investigate the correlation between $\Gamma_\perp$ and γ, we fix the value of $\Gamma_\perp$ and fit the dissipation rate for γ. We repeat this procedure for values of $\Gamma_\perp/\Gamma_u$ in the range $(0.2, 3)$ and present our results in Figure 2.24b. The value of γ is not strongly effected by the value of $\Gamma_\perp$, and a large value of $\Gamma_\perp$ is required to produce a good fit. This demonstrates that the transverse friction must be large compared to the longitudinal friction to produce the hallmark features of Hall viscosity.

Interplay of Hall viscosity and transverse friction. In this section, we fit the theory curve of Figure 4d to a theory including η_o, $\Gamma_\perp$, and γ to investigate the interplay of Hall viscosity and transverse friction. We find that the dissipation rate can be fit well by such a comprehensive theory for $\eta_o \sim 8 \times 10^{-9}\,\mathrm{Pa\,m\,s}$, $\Gamma_\perp/\Gamma_u = 1$, and $\gamma \sim 4 \times 10^{-13}\,\mathrm{N}$, as in Figure 2.25a.

In this procedure, however, there is a high level of parameter uncertainty due to the

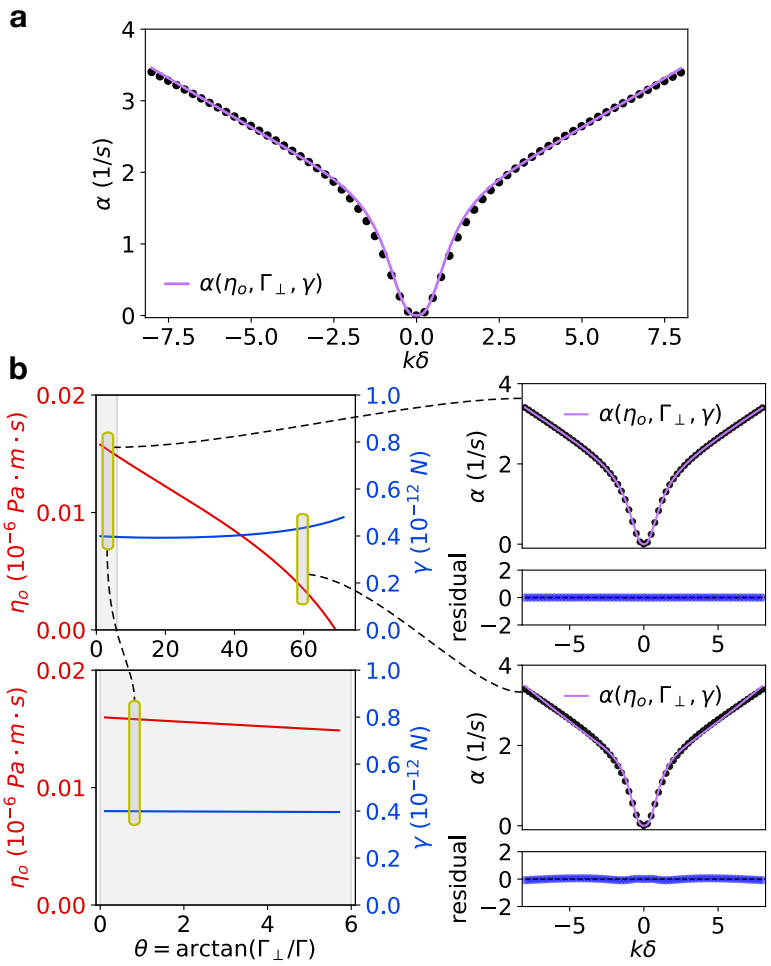

Figure 2.25: **Transverse friction does not contribute to the dissipation rate. a,** The low-friction dissipation rate can be modelled by a theory including η_o and $\Gamma_\perp$, but the relative size of these coefficients is not uniquely determined. **b,** Fixing $\Gamma_\perp$ and fitting for η_o and γ demonstrates that $\Gamma_\perp$ and η_o can be interchanged to predict the dissipation, but in the physical limit ($\Gamma_\perp/\Gamma_u \ll 1$), Hall damping is the dominant contribution to the model.

overlap in qualitative behavior between the damping due to each parameter for $|k\delta| \ll 1$. With this in mind, we consider the problem of fitting the dissipation rate with a range of constrained transverse friction values. While the damping can be adequately captured for both small and large $\Gamma_\perp/\Gamma_u$, the relative role of η_o decreases with increasing $\Gamma_\perp$ (Figure 2.25b top). Using the physical reasoning of Section 2.4.2, which constrains $\theta = \arctan(\Gamma_\perp/\Gamma_u) \ll 1$, we find that the measurements of η_o and γ are largely unresponsive to the inclusion of $\Gamma_\perp$ (Figure 2.25b bottom). This demonstrates that the dominant contributions to the observed

dissipation rate are surface tension γ and Hall viscosity η_o.

2.7 An odd hydrodynamic instability

In much of the phenomenology we have discussed, surface dynamics are essentially boundary layer dynamics. Another natural question, then, is what happens when two boundary layers meet? Draining fluid past a curved obstacle brings about the progressive thinning of a curved strip of chiral fluid, as shown in Fig. 2.1g. The flow is smooth until the strip thickness becomes comparable to the penetration depth δ; at that point the flow goes unstable, resulting in the formation of circular droplets. We study this novel pearling mechanism in experiment by creating a sequence of strips of decreasing thickness, as shown in Fig. 2.26a. We find that over a period of 10 minutes the strips of chiral fluid are stable for thicknesses above $\sim 32\,\mu$m and unstable below. A comprehensive description of this experimental protocol is provided in Section 2.7.1.

Although visually reminiscent of the Rayleigh-Plateau instability of a thin fluid cylinder jet [69], this instability is fundamentally different. In our two-dimensional system, surface tension is a purely stabilizing force, as seen in the wave analysis discussed previously. Instead, the instability originates from the chiral surface dynamics of our fluid. A visual signature of this origin is the consistent offset in the phase between top and bottom perturbations at the moment the instability occurs in all strips: Fig. 2.26b shows one such example.

A linear stability analysis (see Section 2.7.2 for details) of a thin strip of chiral fluid quantitatively predicts the existence of unstable modes which consist of wave-like perturbations on the top and bottom surfaces that have a relative phase offset, as sketched in Fig. 2.26d. These are accompanied by a stable mode with an opposite relative phase. The associated stability diagram is shown in Fig. 2.26e, together with our experimental observations. As the Hall stress has little effect on the stability of modes for small δ (see Section 2.6.2 and Section 2.6.4.3), here we set $\eta_o = 0$.

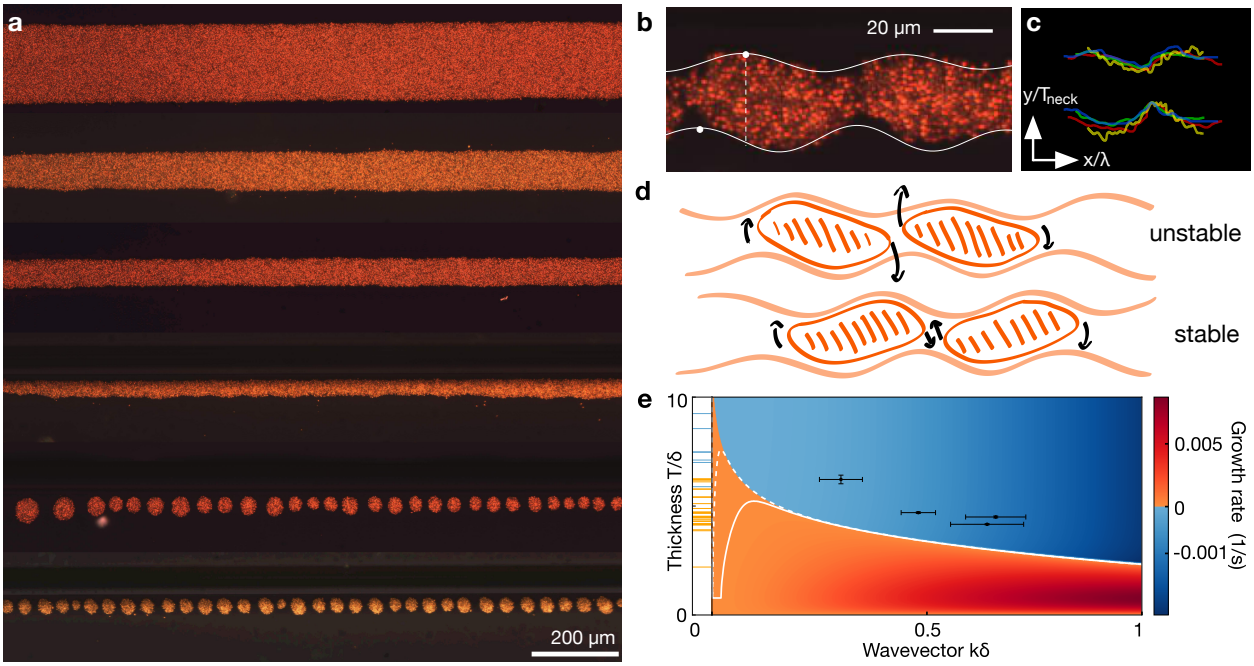

Figure 2.26: **A hydrodynamic instability. a,** Strips of chiral fluid with different thicknesses. Above 32 μm, the strips are stable, as observed over the course of $\geq$ 10 minutes. Below 32 μm the strips break into droplets within 1 minute. **b,** Chiral fluid strip approaching instability. Continuous white lines represent the sum of the most prominent Fourier modes of the strip outline. The relative phase difference between interfaces is emphasized by the two white dots and vertical dashed line. **c,** Overlay of strip outlines at four breakup points; each color corresponds to a different instability occurrence. The x-axis is rescaled by the most prominent wavelength, λ, and the y-axis is rescaled by the thickness at the narrowest point, T_{neck}. The relative phase between the top and bottom interface is consistent with theory. **d,** Schematic of the instability mechanism. Thin strips of chiral fluid are like a collection of elongated droplets rotating in the direction of the edge current. This leads to the breakup (top) or stabilization (bottom) of the strip. **e,** Stability diagram, calculated with linear stability analysis using our experimentally extracted values for the hydrodynamic coefficients, with $\eta_o = 0$ (see Section 2.7.1). The thinner the strip, the larger the range of unstable wavelengths. A surface fluctuation at an unstable wavelength will grow exponentially: orange denotes a positive growth rate and blue denotes a negative growth rate, namely damping. Contour lines mark growth rates corresponding to 10 minutes (continuous) and 1 day (dashed). Black points represent experimental data from unstable strips; wavelengths were measured by Fourier-transforming the strip outline. Error bars in thickness correspond to the standard deviation in the measurement at various points. Error bars in wavelength correspond to the half-width of the Fourier peaks. Horizontal lines on y-axis mark the recorded strip thicknesses: orange and blue lines correspond to unstable and stable strips, respectively.

An intuitive picture for the mechanism driving the instability is illustrated in Fig. 2.26d. The geometry of a thin slab with out-of-phase perturbations on the top and bottom surfaces can be approximated by a collection of elongated droplets of chiral fluid all canted in the same direction. Droplets of this kind rotate in the direction of the edge current, in this case clockwise (see Fig. 2.1d). Depending on the phase difference between the two interfaces, the rotation of these effective droplets will either increase the amplitude of the perturbation, resulting in the breakup of the strip (top); or decrease the amplitude of the perturbation and restore the flat interface (bottom). The consistent observation of this phase relation between the top and bottom perturbations across many experiments of strips going unstable (Fig. 2.26c) further corroborates our theoretical picture of the instability.

2.7.1 Characterization of the strip instability

We prepare strips of spinner fluid as described in Section 2.2.2. To get strips of different thicknesses, like the ones shown in Figure 2.26a, we vary the concentration of the original suspension. We characterize the thickness of a strip before it goes unstable (if it does) by measuring the thickness at various points and taking the mean. To measure the wavelength of the instability in unstable strips, we take the fast Fourier transform of the strip's outline, as described in Section 2.5.3, up to the breakup point. The unstable modes appear as fast-growing peaks in this Fourier transform.

As explained above, our intuitive understanding of the mechanism for the instability demands that the outline of the strips at the break-up point be asymmetric. We characterize this asymmetry by collecting the outlines at several of these break-up points, rescaling them by the strip thickness at the thinnest point and by the unstable wavelength in each case, and overlaying them, as shown in Figure 2.26c.

Just as the Hall viscosity fails to impact the propagation or dissipation of waves of our chiral fluid on a glass substrate, so too does it fail to alter the stability diagram. As in

Figure 2.18b, we see that the line separating stable from unstable modes is nearly unchanged by the addition of an η_o associated with the maximal value in Figure 2.18a.

2.7.2 Perturbation of flow in a finite slab

We now examine the response of the steady-state slab solution to small perturbations from the bounding surfaces being flat.

2.7.2.1 Linearization scheme

Consider a flat interface at $y = 0$ which we perturb with a zero-mean perturbation $y = h(x,t) = \varepsilon g(x,t)$ with $\varepsilon << 1$. We will shift this result to the upper and lower surfaces when needed. We represent the steady-state velocity, vorticity, and stress fields as $\bar{\mathbf{u}} = (\bar{u}, \bar{v})$, $\bar{\omega}$, and $\bar{\sigma}$, respectively, and introduce perturbations as

$$\begin{aligned} u(x,y) &= \bar{u}(y) + \varepsilon\tilde{u}(x,y) \\ v(x,y) &= \varepsilon\tilde{v}(x,y) \\ \omega &= \bar{\omega}(y) + \varepsilon\tilde{\omega}(x,y) \\ \boldsymbol{\sigma} &= \bar{\boldsymbol{\sigma}}(y) + \varepsilon\tilde{\boldsymbol{\sigma}}(x,y) \\ p &= \varepsilon q(x,y) \end{aligned}$$

2.7.2.2 Linear theory

In this section we derive the linearized equations for the perturbed slab.

Linearized bulk equations The linearized bulk equations are given by:

$$\left(\bar{\eta}\nabla^2 - \Gamma_u\right)\tilde{u}_i = \partial_i q \quad \text{and} \quad \nabla\cdot\tilde{\mathbf{u}} = 0 \tag{2.31}$$

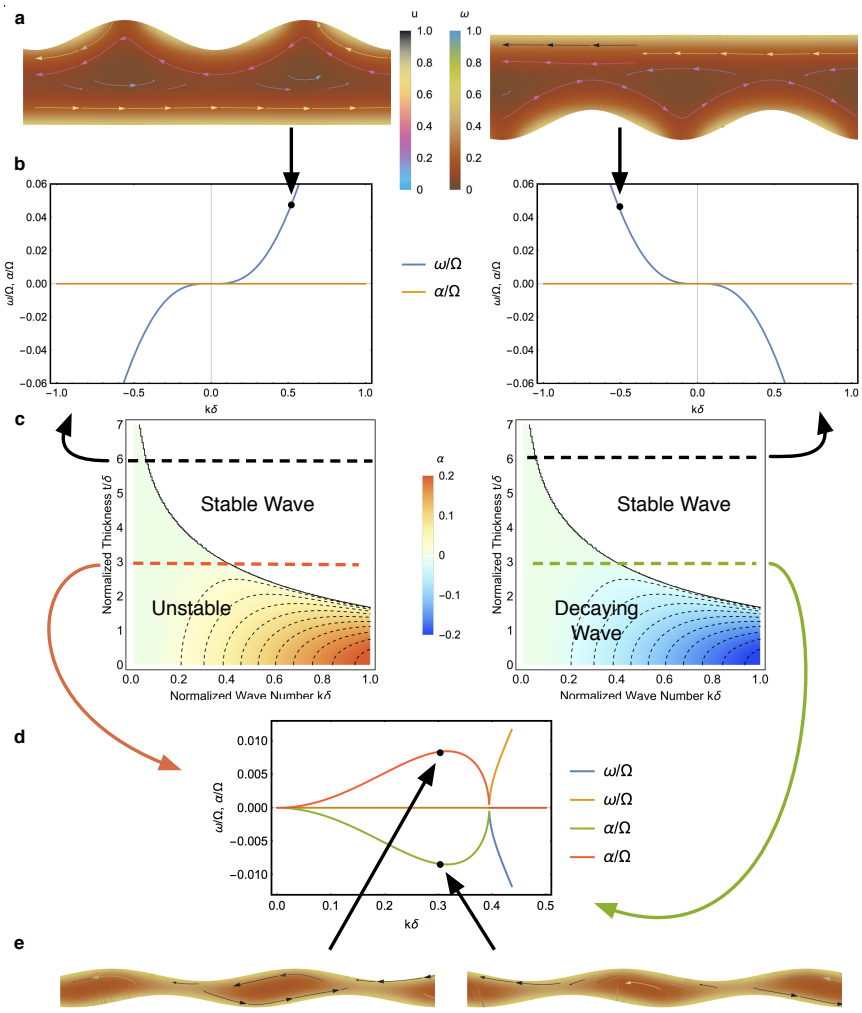

Figure 2.27: **The nature of solutions to the linearized slab dynamics, in the absence of surface tension and Hall viscosity.** (a) Flow fields for the two branches of dispersive surface waves on a large thickness slab. (b) The dispersion relation (blue) and growth/decay rate for these surface waves. While difficult to discern due to its small magnitude, the latter is nonzero (positive at left, negative at right) near $k = 0$. (c) Stability diagram, showing the growth (red) or decay (blue) rates, as a function of normalized wavenumber and slab thickness. Stable waves are purely dispersive, having zero linear growth rate. Contours are levels of constant growth/decay rate. (d) The growth (red) and decay (green) rates, as a function of normalized wavenumber, for the unstable/stable modes on a slab. (e) The associated flow fields, and surface deformations, for the unstable (left) and stable (right) modes.

where $\bar{\eta} = \eta + \eta_R$.

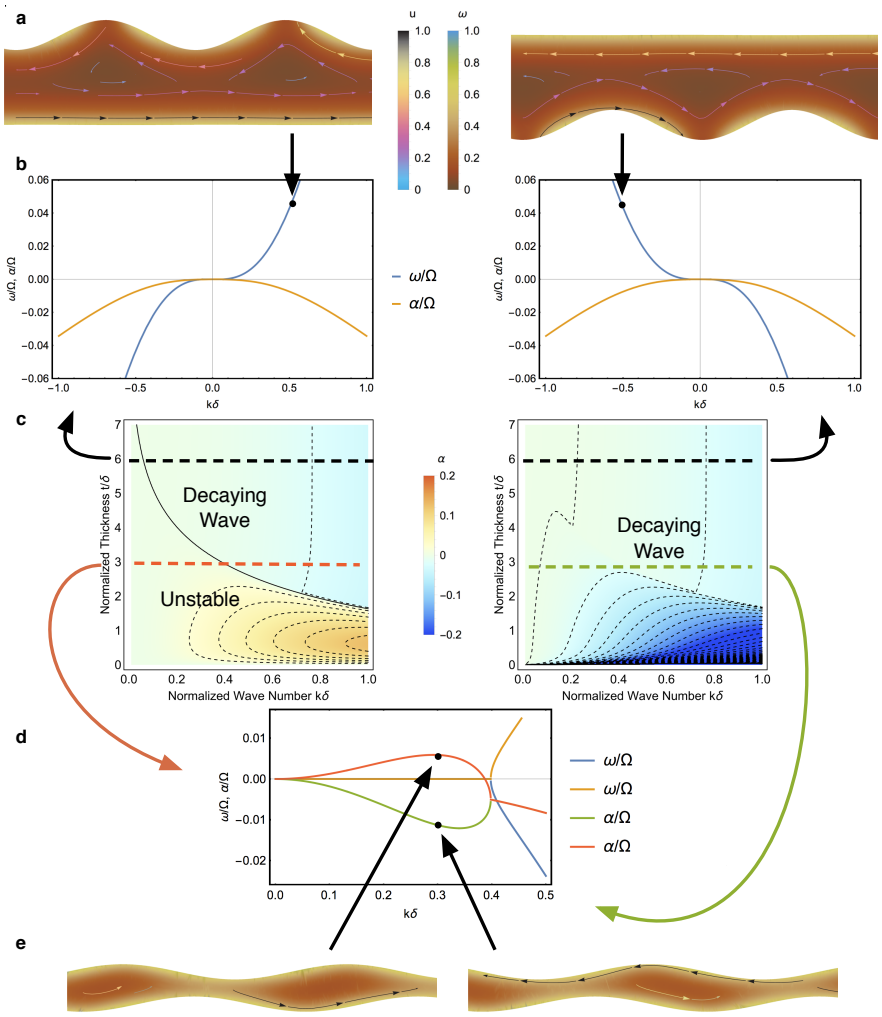

Figure 2.28: **The nature of solutions to the linearized slab dynamics, in the presence of surface tension (in the absence of Hall viscosity).** (a) Flow fields for the two branches of damped, dispersive surface waves on a large thickness slab. (b) The dispersion relation (blue) and decay rates (red) for such surface waves. (c) Stability diagram, showing the growth (shades of red) or decay (shades of blue) rates, as a function of normalized wavenumber and slab thickness. Contours are levels of constant growth/decay rate. (d) The growth (red) and decay (green) rates, as a function of normalized wavenumber, for the unstable/stable modes on an unstable slab. (e) The associated flow fields, and surface deformations, for the unstable (left) and stable (right) modes.

Linearized stress boundary conditions The stress boundary conditions relate the bulk fields to interfacial data. We take an upward normal $\hat{\mathbf{n}} \approx \hat{\mathbf{y}} - \varepsilon g_x \hat{\mathbf{x}}$ and the RHS of Eq. (2.10) is to linear order $\gamma\kappa\hat{\mathbf{n}} \approx \varepsilon\gamma g_{xx}\hat{\mathbf{y}}$. Expanding Eq. (2.10) to linear order, and using that

$\bar{\sigma}(0)\hat{\mathbf{y}} = \mathbf{0}$ yields

$$\tilde{\boldsymbol{\sigma}}(x,0)\hat{\mathbf{y}} = \gamma g_{xx}(x)\hat{\mathbf{y}} + g_x(x)\bar{\boldsymbol{\sigma}}(0)\hat{\mathbf{x}} - g(x)\bar{\boldsymbol{\sigma}}_y(0)\hat{\mathbf{y}}$$

After some simplification we obtain:

$$\begin{aligned}
&\bar{\eta}\tilde{u}_y(x,0) + (\eta - \eta_R)\,\tilde{v}_x(x,0) + 2\eta_o\tilde{u}_x(x,0) = \bar{\eta}\bar{\omega}_y(0)\,g(x) + 2\eta_o\bar{\omega}(0)g_x(x) \\
&2\eta\tilde{v}_y(x,0) - q(x,0) + 2\eta_o\tilde{v}_x(x,0) = \gamma g_{xx}(x) - \left[(\eta - \eta_R)\,\bar{\omega}(0) + 2\eta_R\Omega\right] g_x(x)
\end{aligned} \tag{2.32}$$

Note: for the lower surface, where the normal points downwards, the sign of the surface tension term is reversed to maintain the right relation of curvature to normal direction.

Linearized kinematic boundary condition The linearized kinematic boundary condition is given by:

$$g_t + \bar{u}(0)\,g_x = \tilde{v}(x,0) \tag{2.33}$$

2.7.2.3 Solution

To solve Eqs. (2.32, 2.33, 2.31) we make use of Fourier transforms in the x direction to take advantage of translational invariance.

Solution of the linearized bulk equations Taking the Fourier transform in x:

$$\bar{\eta}\left(\partial_{yy} - k^2\right)\tilde{\mathbf{u}} - \Gamma_u\tilde{\mathbf{u}} - \left(ik, \partial_y\right) q = \mathbf{0} \;\text{ and }\; \left(ik, \partial_y\right)\cdot\tilde{\mathbf{u}} = 0$$

Using that $\left(\partial_{yy} - k^2\right) q = 0$ we obtain:

$$\begin{aligned}
q &= A^+ e^{|k|y} + A^- e^{-|k|y} \\
\tilde{u} &= -\frac{ik}{\bar{\eta}}\delta^2 \left(\mu_k^\pm A\right) + \left(\mu_\star^\pm B\right) \\
\tilde{v} &= -\frac{|k|}{\bar{\eta}}\delta^2 \left(\Delta_k^\pm A\right) - \frac{ik}{|\star|}\left(\Delta_\star^\pm B\right) \\
\tilde{u}_y &= -\frac{ik\,|k|}{\bar{\eta}}\delta^2 \left(\Delta_k^\pm A\right) + |\star|\left(\Delta_\star^\pm B\right) \\
\tilde{v}_y &= -\frac{|k|^2}{\bar{\eta}}\delta^2 \left(\mu_k^\pm A\right) - ik\left(\mu_\star^\pm B\right)
\end{aligned} \tag{2.34}$$

Where $\star^2 = k^2 + \delta^{-2}$ and $\mu_k^\pm f = e^{\pm|k|H} f^+ + e^{\mp|k|H} f^-$ and $\Delta_k^\pm f = e^{\pm|k|H} f^+ - e^{\mp|k|H} f^-$. The coefficients $A^\pm$ and $B^\pm$ are to be determined from the boundary conditions.

Application of the stress boundary conditions Inserting Eq. (2.34) into the linearized stress boundary conditions Eq. (2.32) yields:

$$\begin{aligned}
-2ik\,|k|\,\delta^2\frac{\eta}{\bar{\eta}}\left(\Delta^\pm A\right) + \frac{1}{|\star|}\left[2\eta k^2 + \bar{\eta}\delta^{-2}\right]\left(\Delta_\star^\pm B\right) + 2\frac{\eta_o}{\bar{\eta}}k^2\delta^2\left(\mu^\pm A\right) + 2ik\eta_o\left(\mu_\star^\pm B\right) \\
= \left[\pm\eta_R\frac{2\Omega}{\delta}\tanh\left(\frac{H}{\delta}\right) + i2k\eta_o\frac{\eta_R}{\bar{\eta}}\Omega\right] g^\pm
\end{aligned}$$

and

$$\begin{aligned}
\left[1 + 2\frac{\eta}{\bar{\eta}}\,|k|^2\,\delta^2\right]\left(\mu^\pm A\right) + 2ik\eta\left(\mu_\star^\pm B\right) - 2i\frac{\eta_o}{\bar{\eta}}k|k|\delta^2\left(\Delta^\pm A\right) + 2\eta_o\frac{k^2}{|\star|}\eta\left(\Delta_\star^\pm B\right) \\
= \left(\pm\gamma k^2 + i2k\frac{\eta\eta_R}{\bar{\eta}}2\Omega\right) g^\pm
\end{aligned}$$

which is a set of four linear equations for the four unknowns $A^\pm, B^\pm$ in terms of the top and bottom surface perturbations $g^\pm$. A very tedious calculation which we suppress here to maintain excitement yields an inversion of these relations.

Application of the kinematic boundary condition Combining this with the kinematic boundary condition:

$$g_t^{\pm} + ik\bar{u}^{\pm} g^{\pm} = \tilde{v}^{\pm}$$

and substituting $\tilde{v}^{\pm}$ we have:

$$g_t^{+} - ikUg^{+} = -\frac{|k|}{\bar{\eta}}\delta^2 \Delta_k^{+} A - \frac{ik|}{|\star|}\Delta_\star^{+} B$$
$$g_t^{-} + ikUg^{-} = -\frac{|k|}{\bar{\eta}}\delta^2 \Delta_k^{-} A - \frac{ik|}{|\star|}\Delta_\star^{-} B$$

These equations can be solved to yield the evolution of the surface of a perturbed slab of finite width. Explicit analytical computation of these modes becomes tedious at this point.

2.7.2.4 Visualization and asymptotics

The evolution of the surface corresponding to a sinusoidal perturbation of the height $g \sim \mathrm{Re}\left[e^{ikx}\right]$ is given by $g \sim \mathrm{Re}\left[e^{i(kx+\omega t)}e^{-\alpha t}\right]$ where $i\omega - \alpha = \sigma$, the eigenvalue of the linearized coupled evolution equations. There are, generally, two eigenvalues and associated eigenvectors. The real part of the eigenvalues $\alpha(k)$ indicates whether the wave amplitude decreases, remains the same, or grows exponentially in time.

In general, we find that for thick slabs ($|kH| \gg 1$, $H \gg \delta$), the eigenvalues and eigenvectors correspond to two copies of the semi-infinite slab problem, with damped surface waves on the bottom surface propagating in a direction opposite to those on the top surface. For thin slabs ($H \leq \delta$) we find unstable modes, whose growth rate is reduced by both surface tension and Hall viscosity.

Since the algebra can get quite tedious, we present our results by first considering the problem in the absence of Hall viscosity and subsequently considering the changes brought about by the presence of Hall viscosity. In the absence of Hall viscosity, substituting the

solutions for $A^{\pm}, B^{\pm}$ in terms of Δg and μg give evolution equations of the form:

$$\begin{bmatrix} \Delta g_t \\ \mu g_t \end{bmatrix} = \mathbf{M}_k \begin{bmatrix} \Delta g \\ \mu g \end{bmatrix} = \begin{bmatrix} \gamma a_\Delta & i2\Omega b_\mu \\ i2\Omega b_\Delta & \gamma a_\mu \end{bmatrix} \begin{bmatrix} \Delta g \\ \mu g \end{bmatrix} \tag{2.35}$$

The dispersion relation and stability diagrams follow from the eigenvalues of $\mathbf{M}_k$. The coefficients $a_{\Delta,\mu}$ and $b_{\Delta,\mu}$ are complicated, but real, functions of the system parameters and wavenumber k, except for the surface tension γ and the (forcing) spinning frequency 2Ω which appears only multiplicatively in $\mathbf{M}_k$ as shown. Hence, in the absence of surface tension the eigenvalues of $\mathbf{M}_k$ are either a purely imaginary, complex conjugate pair, or a real-valued positive/negative pair.

Regions of stability and instability are depicted in Figure 2.27c in the limit of vanishing surface tension and in Figure 2.28c for finite surface tension.

Intermediate surface waves For finite wavenumber $k\delta$, above a certain thickness $2H$, the eigenvalues correspond to propagating waves that are damped in the presence of surface tension. A representative dispersion $\omega(k)$ relation and damping rate α for the waves are depicted in Figures 2.27b and 2.28b. The corresponding flow fields are depicted in Figures 2.27a and 2.28a. The two eigenvalues correspond in this case to surface waves that propagate to the left in on the top surface and to the right on the bottom surface.

Taking the limit of large thickness $|kH| \gg 1$, and long wavelength $|k\delta| \ll 1$, and restricting our attention to the upper surface, we find the following asymptotic expression:

$$i\omega + \alpha = 2iu_{\text{edge}}\frac{\eta}{\Gamma_u}k^3 + \frac{\gamma}{\Gamma_u}|k|^3$$

which corresponds to waves moving in the same direction as u_{edge}, damped by surface tension.

This reflects the intuitive expectation that for $H \gg \delta$ the problem should reduce to two

copies of the semi-infinite slab problem. Adding Hall viscosity, computing the finite slab spectrum numerically and comparing it to the semi-infinite slab problem with Hall viscosity further confirms this intuition.

Short waves For finite thickness, and sufficiently large wavenumber $k\delta \gg 1$, $kH \gg 1$, Eq. (2.35) simplify to

$$\begin{bmatrix} \Delta g_t \\ \mu g_t \end{bmatrix} = \begin{bmatrix} -\tilde{\gamma}|k| & i2\frac{\eta_R}{\bar{\eta}}\delta\Omega \tanh\left(\frac{\bar{h}}{\delta}\right)|k| \\ i2\frac{\eta_R}{\bar{\eta}}\delta\Omega \tanh\left(\frac{\bar{h}}{\delta}\right)|k| & -\tilde{\gamma}|k| \end{bmatrix} \begin{bmatrix} \Delta g \\ \mu g \end{bmatrix} \tag{2.36}$$

with $\tilde{\gamma} = \frac{\gamma}{2\eta_R\left(2-\frac{\eta}{\bar{\eta}}\right)} > 0$. Seeking exponential solutions $(\Delta g, \mu g) = e^{\sigma t}(\Delta g_0, \mu g_0)$ yields

$$\sigma = -\tilde{\gamma}|k| \pm i\frac{\eta_R}{\bar{\eta}}\delta 2\Omega \tanh\left(\frac{\bar{h}}{\delta}\right)|k|$$

Hence, small length-scales are stabilized by surface tension in a manner consistent with classical results for the two-dimensional Stokes equations [70] while the gyroscopic drive produces waves.

Unstable long-wavelength modes For finite thickness slabs, $\eta_o = 0$, and long waves, $|k|H << 1$, one of the eigenvalues is always unstable, as can be seen in Figures 2.27c and 2.28c. Representative dependences on wavenumber of the growth/decay rates of the eigenvalues in this regime are shown in Figures 2.27d and 2.28d, together with the corresponding flow fields (Figures 2.27e and 2.28e). In this limit, Eq. (2.35) simplify to

$$\begin{bmatrix} \Delta g_t \\ \mu g_t \end{bmatrix} = \begin{bmatrix} -\gamma\beta_1 k^4 & i2\Omega\alpha_1 k^3 \\ -i2\Omega\alpha_2 k & -\gamma\beta_2 k^2 \end{bmatrix} \begin{bmatrix} \Delta g \\ \mu g \end{bmatrix}$$

where $\beta_1 = H\delta^2/\bar{\eta}$, $\beta_2 = \delta^2/\bar{\eta}H$, $\alpha_1 = 2\delta^3\left(\eta\eta_R/\bar{\eta}^2\right)\tanh\left(\frac{H}{\delta}\right)$, and $\alpha_2 = \left(2\delta^2/H\right)\left(\eta\eta_R/\bar{\eta}^2\right)\mathrm{sech}^2\left(\frac{\mathrm{H}}{\delta}\right)$ are all positive constants. Seeking exponential solutions $(\Delta g, \mu g) = e^{\sigma t}(\Delta g_0, \mu g_0)$ yields

$$\sigma = \frac{1}{2}\left[-\gamma\beta_2 \pm \left((\gamma\beta_2)^2 + 2\Omega^2\alpha_1\alpha_2\right)^{1/2}\right]k^2 \tag{2.37}$$

Hence, at long wavelengths, there is always both a stable and an unstable mode. In each case, both surface tension and driving scale quadratically in k in the eigenvalue, and surface tension damps both stable and unstable modes generated by activity (i.e. $2\Omega^2 > 0$).

Performing the same calculation numerically in the presence of Hall viscosity presents a similar picture. Hall viscosity, like surface tension, generally acts as a stabilizing stress, albeit with a different wavenumber dependence, as illustrated in Figure 2.29.

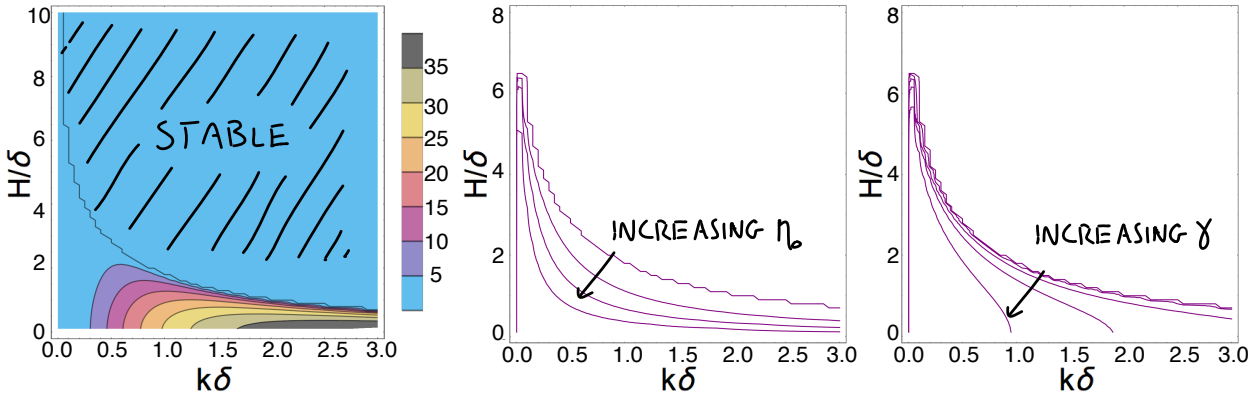

Figure 2.29: **Effect of surface tension and Hall viscosity on the stability of finite thickness slabs.** (a) The stability diagram in the absence of surface tension and Hall viscosity (c.f. Figure 2.27). (b) Increasing the Hall viscosity, η_o, moves the line separating stable from unstable modes as depicted. (c) Increasing the surface tension, γ, moves the line separating stable from unstable modes as depicted. In both cases the effect is to stabilize the interface by increasing the extent of the stable region. The large wavenumber dependence of the damping effects of surface tension and Hall viscosity accounts for the different effects they have on the stability diagram.

2.7.2.5 The role of odd stress

Here we give a simple geometric model that explains the nature of the stable and unstable modes of the slab, the latter of which leads to the formation of droplets in experiment. Consider the coupled surface modes for the slab computed above (see Eqs. (2.35, 2.37)). These consist of sinusoidal perturbations on the top and bottom surfaces, respectively, that have relative phases of either $\pi/2$ or $-\pi/2$, with their respective flow fields plotted in Figures 2.27e and 2.28e. In the unstable case the upper surface is shifted leftwards relative to the lower, and oppositely for the stable case. As depicted in Figure 2.26 the geometry of such a perturbed slab can be approximated by a collection of elongated droplets of chiral fluid, all canted in the same direction. In isolation, droplets of this kind would rotate clockwise. Because of their canted angle, the configuration shown in Figure 2.30 (top) would evolve into separate droplets, whereas that shown in Figure 2.30 (bottom) would evolve towards a flat slab-like configuration (stable). The former case is consistent with the reconstructed, unstable slab boundaries shown in Figure 2.26b.

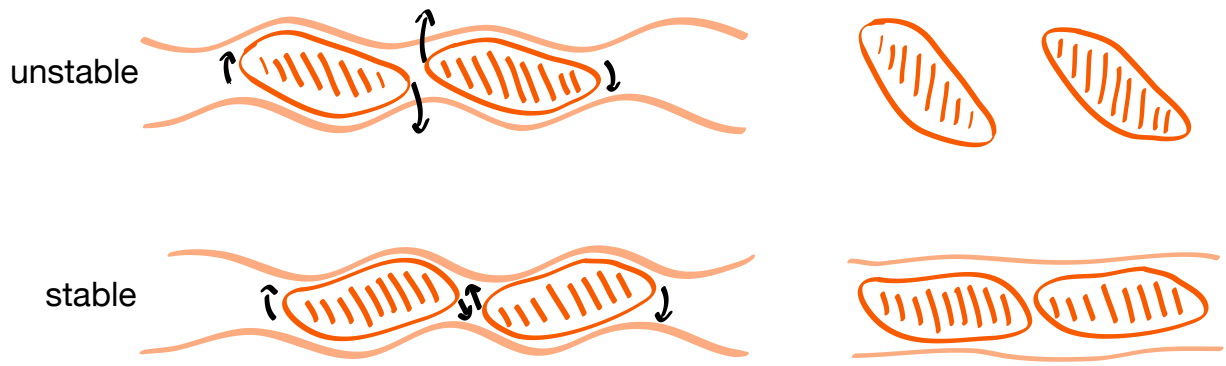

Figure 2.30: **Stability of chiral fluid slabs.** Cartoon of the phase relations of the bounding interfaces of a chiral fluid slab that give rise to growth (upper) and decay (lower) of perturbations.

2.8 Conclusion

We have broken parity symmetry at the microscopic level in a colloidal chiral fluid, resulting in the emergence of an odd stress that in turn generates lively surface flows. Likewise, we have broken time reversal symmetry, giving rise to Hall viscosity, a dissipationless transport property which has thus far remained experimentally elusive. The combination of these features drives rich interfacial dynamics with no analogues in conventional fluids. These dynamics include the uni-directional propagation and anomalous attenuation of surface waves and an asymmetric pearling instability. In principle, these chiral phenomena can be tuned, for instance by altering the colloidal particles' shape and their effective interactions. Colloidal chiral fluids enable the study of universal aspects of a new class of hydrodynamics, and provide a platform for engineering active materials with so far untapped, 'odd' behaviors.

CHAPTER 3

ODD ELASTICITY OF A COLLOIDAL CHIRAL CRYSTAL

This chapter is primarily comprised of material reproduced from the publication Ref. [71]: Bililign, E. S., Balboa Usabiaga, F., Ganan, Y. A., Poncet, A., Soni, V., Magkiriadou, S., Shelley, M. J., Bartolo, D., & Irvine, W. T. M. Motile dislocations knead odd crystals into whorls. *Nature Physics* **18**, 212-218 (2022). *Reproduced with permission from Springer Nature.*

3.1 Introduction

The competition between thermal fluctuations and potential forces governs the stability of matter in equilibrium, in particular the proliferation and annihilation of topological defects. However, driving matter out of equilibrium allows for a new class of forces which are neither attractive nor repulsive, but rather transverse. The possibility of activating transverse forces raises the question of how they affect basic principles of material self-organization and control. Here, we show that transverse forces organize colloidal spinners into odd elastic crystals crisscrossed by motile dislocations. These motile topological defects organize into a poly-crystal made of grains with tunable length scale and rotation rate. The self-kneading dynamics drive super-diffusive mass transport, which can be controlled over orders of magnitude by varying the spinning rate. Simulations of both a minimal model and fully resolved hydrodynamics establish the generic nature of this crystal-whorl state. Using a continuum theory, we show that both odd and Hall stresses can destabilize odd-elastic crystals, giving rise to a generic state of crystalline active matter. Adding rotations to a material's constituents has far-reaching consequences for continuous control of structures and transport at all scales.

3.2 An odd colloidal crystal

The celebrated interplay between configurational entropy and the energetics of topological defects in two-dimensional melting have provided a lens through which to understand the phases of condensed matter [72], such as superfluid films, colloids and liquid crystals [73, 74, 75, 76, 77, 78]. While these systems span a wide range of particle interactions, scales, and intermediate phases, they are all unified in that the forces between constituents are primarily longitudinal, their dynamics are equilibrium, and their interactions are symmetric under both time-reversal and parity. What happens if the inter-particle interactions include transverse forces as well [79, 35, 39, 27, 48, 80, 18, 81, 82]? This deceivingly minimal generalization can break these assumptions at a fundamental level.

In equilibrium, transverse forces cannot alter the phase behavior of condensed matter. However, there is no such guarantee out of equilibrium and such transverse interactions generically occur in collections of naturally and artificially spinning objects. Examples include planetary disks [83], spinning cell aggregates and membrane inclusions [84, 85], active colloids and grains [27, 22, 86, 49, 44, 25, 81, 82, 87], atmospheric scale dynamics [88, 89], parity-breaking fluids [90, 91, 5, 92, 15, 16] and simple models of turbulence [93]. How does this more general and ubiquitous form of matter generically self-organize, what are its stable phases, and how does it transition between them?

Figure 3.1a shows a $\sim 200 \times 200\,\mu$m region within a centimetre-scale monolayer of magnetic colloids. Each particle is uniformly spun by an externally applied magnetic field, resulting in their self-organization into a dynamic and dense phase, as described in Section 3.2.1 below. The active rotation of the magnets gives rise to both longitudinal magnetic attraction and sustained chiral transverse hydrodynamic interactions, as illustrated in the inset of Figure 3.1a. Crucially, the forces are separation-dependent and can be tuned by varying the rotation frequency, providing an ideal platform for exploring how transverse interactions shape the dense phases of chiral matter.

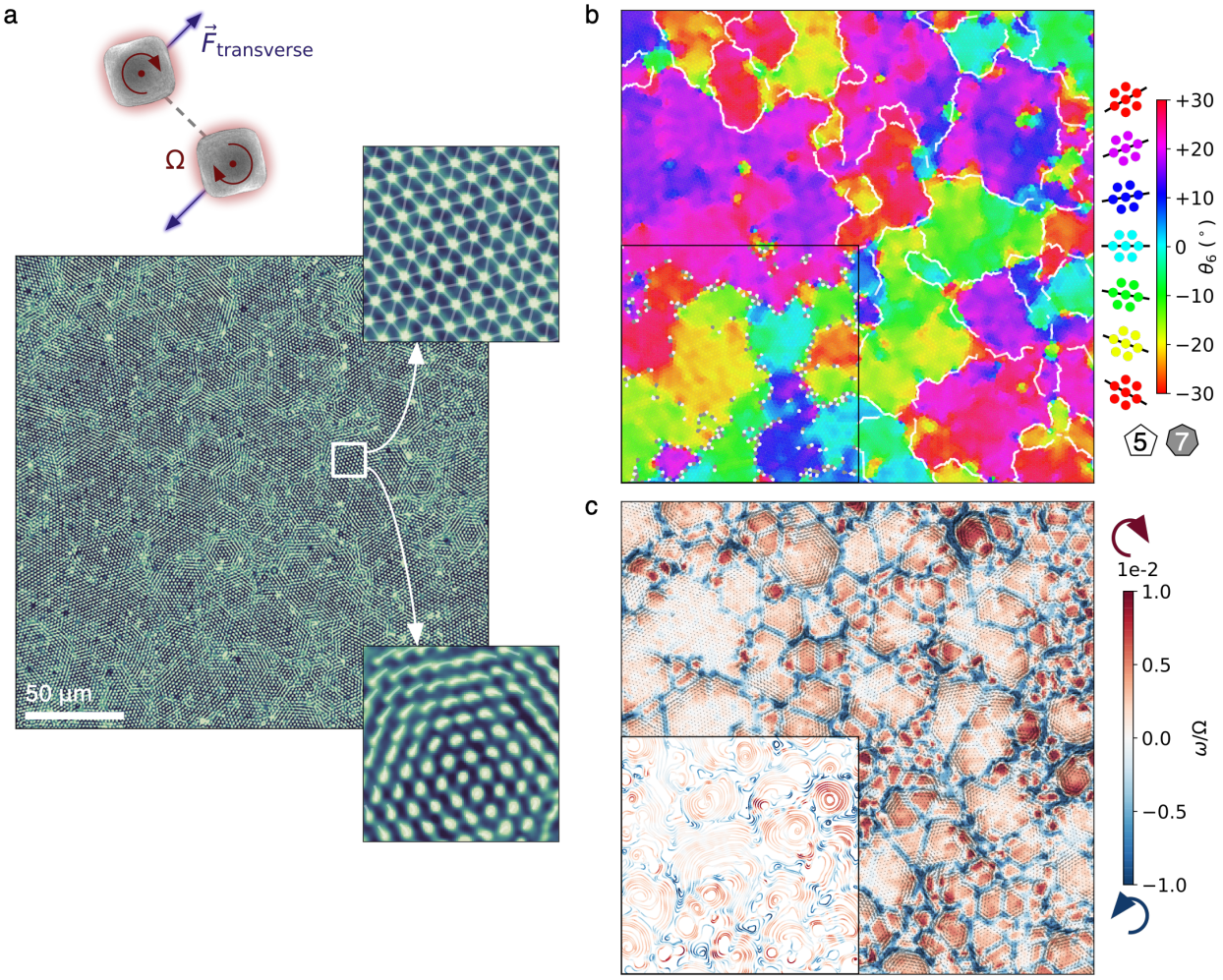

Figure 3.1: **A crystal whorl state. a,** A dense and dynamic phase of colloids spinning at a frequency Ω and interacting through both longitudinal and transverse pairwise interactions is directly imaged with a microscope through crossed polarizers. The rotation-averaged position of each particle appears as a bright spot and reveals intermittent crystalline order. Magnifying a region reveals a highly-ordered crystalline structure (top), and time-averaging further reveals a rotating flow (bottom). **b,** To further illuminate the polycrystalline structure of this phase, we color particles by the angle of the local bond-orientational order parameter θ_6. The polycrystal can be segmented into domains, and boundaries are drawn between them. The inset highlights the individual defects between grains, underlying grain boundaries. **c,** The polycrystal is dynamical and displays intermittent vortical flows as revealed when each region is colored by its vorticity ω. The inset presents the same vortical information through the streamlines of the particle flow.

Upon spinning our particles, we find that the system generically self-organizes into crystal 'whorls'. A snapshot, colored by the phase of the crystalline bond-orientational order parameter, $\psi_6(\boldsymbol{x})$ (see Figure 3.1b), reveals a polycrystalline arrangement of grains of triangular crystal order separated by topological defects organized into grain boundaries [94]. This picture is reminiscent of metallurgical crystalline phases with quenched disorder; however, unlike their crystalline static counterpart, the structure is continually evolving, grain boundaries move, collapse, and spontaneously emerge as crystalline domains rotate like vortical whorls (see Figure 3.1c). Segmenting the phase into crystalline domains enables us to study its statistical properties, revealing that after a short transient, the domains within this polycrystal settle to a constant characteristic size (Section 3.2.3). This scale can be tuned by altering the particle rotation rate alone, yielding either significantly larger or smaller crystalline whorls, as in Figure 3.21. In the following sections, we describe the procedure by which the polycrystal is separated into grains (Section 3.2.2) and characterize the steady-state (Section 3.2.3).

3.2.1 Colloidal magnets & their activation

Our colloidal particles are made of hematite, have a single magnetic domain and have the shape of a 'superball'. The particles were synthesized following the synthesis described by Sugimoto et al in [50], and coated in a thin silica shell following the methodology of [95]. In our experiments, the particles are suspended in water and allowed to sediment on a glass coverslip and imaged through crossed polarizers in an inverted microscope.

To create and drive the chiral phase, we apply a rotating magnetic field of magnitude $\sim$1 mT using a set of mutually perpendicular Helmholtz coils. We take care to balance the field rotation so that the rotation axis is perpendicular to the glass substrate. Once the drive is applied, the magnetic colloids attract and form a dense phase, as a result of the dipolar interactions which become attractive when averaged over a rotation.

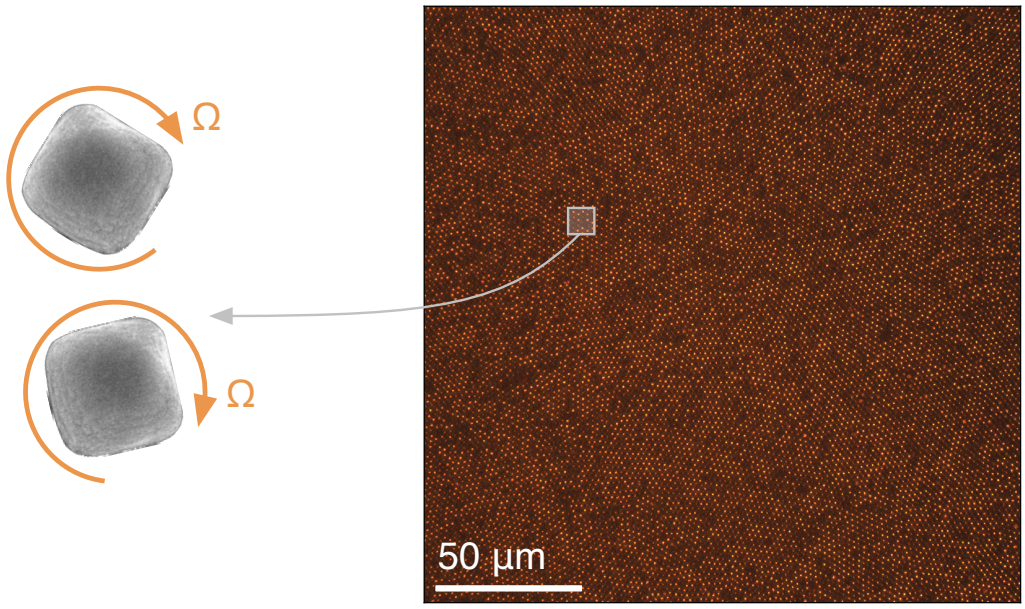

Figure 3.2: **A crystal of rotating colloidal magnets.** (A) A sketch of the experimental system, which consists of self-aggregating colloidal magnets on a flat surface. Each magnet spins at a constant rate. (B) A macroscopic view of this packing as seen through a microscope.

To prepare large crystalline domains, we alternate the drive between clockwise and counter-clockwise rotation at a high frequency ($10 - 15\,\mathrm{Hz}$). We characterize the polycrystalline order of our crystal whorl state by identifying grains and computing the grain size distribution and total grain boundary length, as in Section 3.2.2.

3.2.2 Crystalline grain detection

We define the local bond-orientational order of polycrystalline packings at the position $\boldsymbol{x}_j$ of the jth particle as

$$\psi_6(\boldsymbol{x}_j, t) = \frac{1}{N_j} \sum_{i=1}^{N_j} \exp\left(i6\theta_{ij}\right), \tag{3.1}$$

where the jth particle has N_j neighbors and θ_{ij} is the angle formed between the bond $\boldsymbol{x}_{ij} = \boldsymbol{x}_i - \boldsymbol{x}_j$ connecting the ith and jth particles and the x-axis. The local phase

$$\theta_6(\boldsymbol{x}_j, t) = \tfrac{1}{6}\arg\left[\psi_6(\boldsymbol{x}_j, t)\right], \tag{3.2}$$

represents the local crystalline angle of the spinner crystal, as illustrated in Figure 3.3A. In addition, the strength of crystalline order is defined by the magnitude $|\psi_6(\boldsymbol{x}_j, t)|$, as shown in Figure 3.3B. To enable the detection of grain boundaries, the field ψ_6 is coarse-grained by averaging over a particle's nearest neighbors prior to computing θ_6 and $|\psi_6|$ as used in the subsequent analysis.

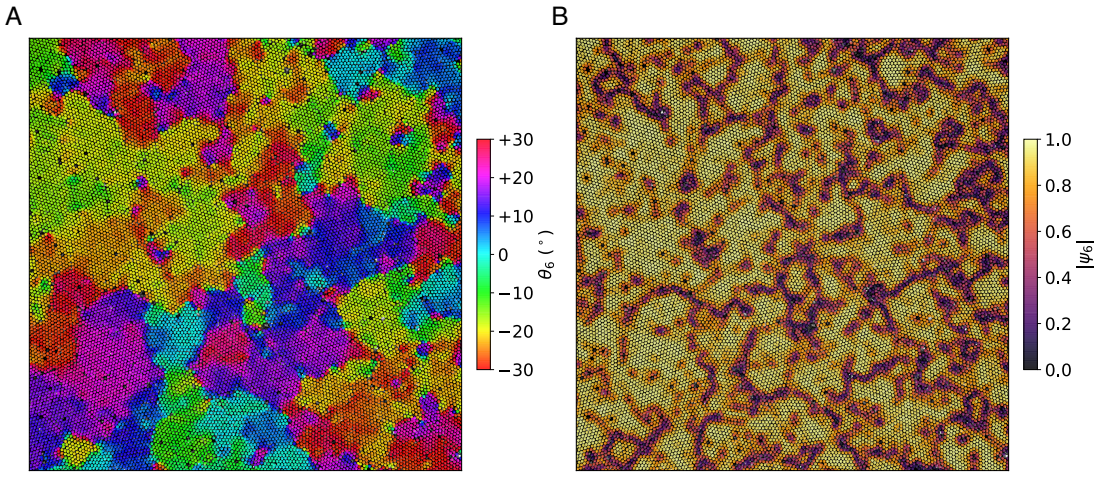

Figure 3.3: **The particle-based bond-orientational order parameter ψ_6.** Using the construction of Eq. (3.1), two measures of crystalline structure can be extracted: (A) the local crystalline orientation field θ_6, and (B) the local crystalline order field $|\psi_6|$.

To identify grain boundaries, we use an approach like that of Refs. [96, 97] and first segment the pointset into crystalline and non-crystalline particles according to a threshold in $|\psi_6(\boldsymbol{x}_j, t)|$. A crystalline particle is considered to be a part of a grain if it has at least three crystal-like neighbors with $\Delta\theta_6$ below a threshold. This algorithmic association of neighbors into grains is performed to fill space, and then pruned to omit small grains, as in [96]. In Figure 3.4A-B, we present a small patch of spinner crystal and color particles by

their bond-orientational order parameters. After omitting non-crystalline particles, we color the Voronoi cells of particles in a grain by the average θ_6 value of the grain as in Figure 3.4C.

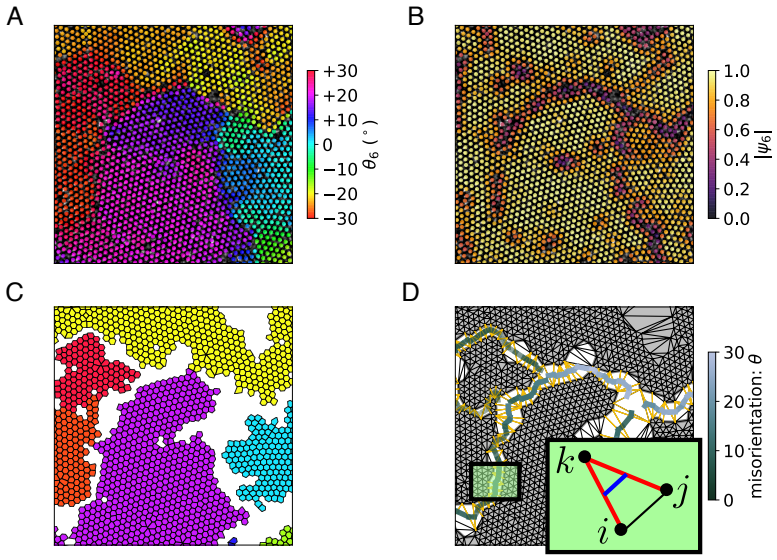

Figure 3.4: **Extracting grains and grain boundaries from the bond-orientational order.** The bond-orientational order parameter ψ_6 can be decomposed into an (A) angular component θ_6 and (B) a magnitude $|\psi_6|$, which are plotted spatially for a small subset of a spinner crystal. Same colormap as in Figure 3.3. (C) The crystalline space can be decomposed into domains with small variation in θ_6 and sufficiently strong hexatic order characterized by $|\psi_6|$. We can then color each particle's Voronoi cell according to its domain assignment. (D) By analyzing the bond network between adjacent domains, we can identify the boundary between grains and the angular misorientation between them.

Now, considering only crystalline particles, we construct a Delaunay triangulation, denoted by the thin black edges in Figure 3.4D. The particles corresponding to a domain boundary are identified, yielding a chain of bounding segments $i-j$ as in the inset. Repeating this for each domain, we can extract quantities such as domain area. Then, we consider only edges of the type $i-k$ or $j-k$ that connect particles associated with two distinct domains. As in the inset, we can link the centers of two consecutive connecting edges to obtain a grain boundary segment. Linking these segments end-to-end produces a full picture of the grain boundary, as shown in Figure 3.4D. Here, grain boundary segments are colored by the difference in orientation between the associated grains, using the definitions of [96],

reproduced below:

$$\text{misorientation} = \min\left(\left|\frac{\theta_{ki}+\theta_{kj}}{2}\right|, 60^\circ - \left|\frac{\theta_{ki}+\theta_{kj}}{2}\right|\right), \tag{3.3}$$

where θ_{ik} is the misorientation of a single edge in the triangulation,

$$\theta_{ik} = \min\left(|\theta_i - \theta_k|, 60^\circ - |\theta_i - \theta_k|\right), \tag{3.4}$$

for θ_j the coarse-grained value of θ_6 at the location of the jth particle.

3.2.3 Polycrystal characterization

Having identified the grains and grain boundaries, their distributions and relationships to rotational drive can be readily computed. Figure 3.5 shows a typical sequence of snapshots from experiments of various frequencies, their grain size and spacing statistics, and the time-evolution of the typical grain size and integrated grain boundary length. As readily illustrated in (A), grains tend to become more fragmented at higher frequencies, leading to an increase in the domain separation (B) and decrease in the average size (C-E). Meanwhile, as in (F-G), once the experimental system has reached the steady-state, quantities like the grain boundary length and average domain size tend to remain constant over many thousands of particle rotations.

3.3 Dislocation dynamics

Having observed that an odd crystal reaches a steady polycrystalline phase, we ask: what powers this lively steady state? Careful inspection reveals that the motion of topological defects in the crystalline structure is unlike the familiar motion of dislocations found in conventional passive materials. Conventional dislocations are either stationary or diffuse bi-

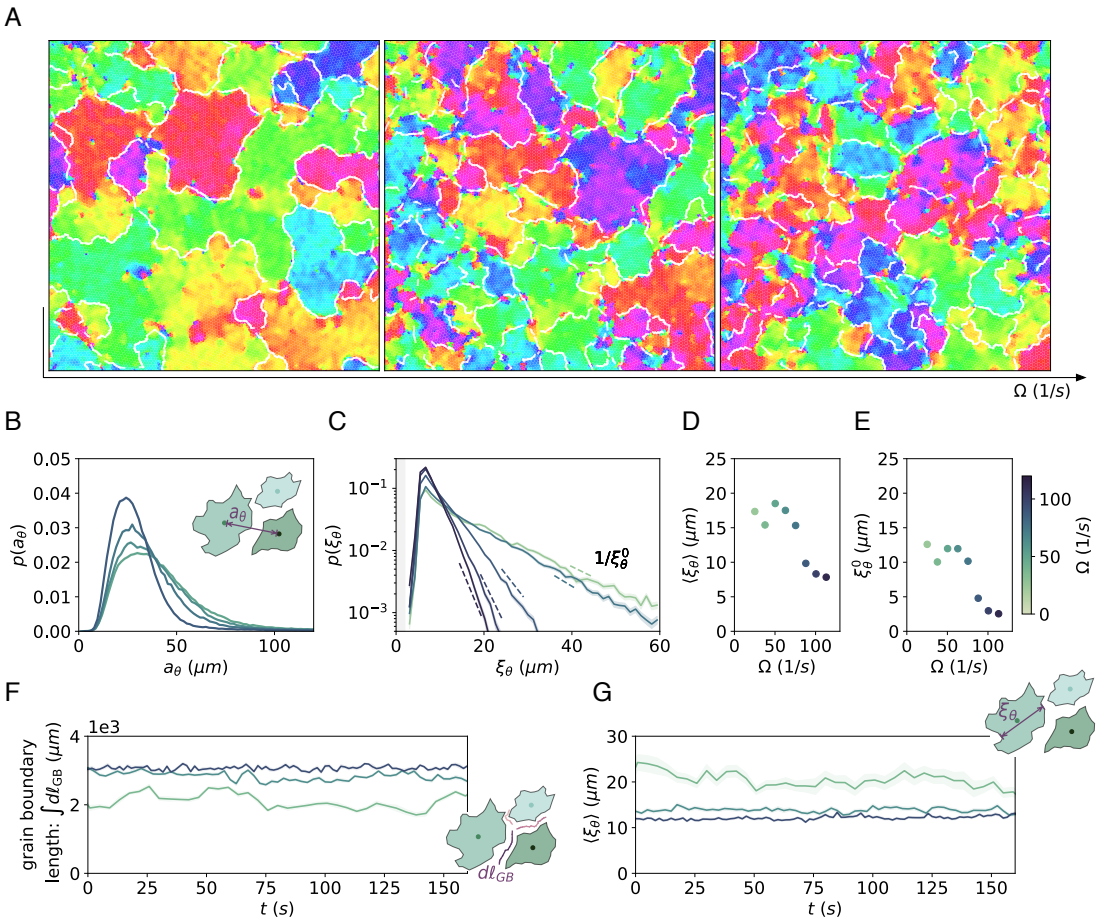

Figure 3.5: **The chiral whorl steady-state: crystalline structure.** (A) For spinner crystals in steady-state at increasing rotation frequencies, the crystalline structure tends to become increasingly fragmented, as illustrated by single temporal snapshots of the local crystalline orientation θ_6 and boundaries between segmented crystalline grains. (B) The distribution of inter-domain spacing a_θ is peaked strongly at small values for high frequencies and has an increasingly large tail at large values for low frequencies, demonstrating both a characteristic domain separation and the increase of characteristic domain size with decreasing rotation frequency. (C) The chiral whorl state is characterized by a nearly exponential distribution of domain sizes ξ_θ, obtained from taking the square root of domain areas, that tend towards smaller sizes as the rotation frequency is increased. (D) A characteristic domain size is then defined as the average $\langle \xi_\theta \rangle$. (E) By fitting the distribution to an exponential, we also extract a similar length scale ξ_θ^0. (F) Similarly, the total amount of grain boundary, $\int d\ell_{GB}$ increases with frequency, but is free of large-scale temporal fluctuations in the steady-state. (G) Likewise, the characteristic domain size remains constant in the steady-state.

directionally driven by thermal fluctuations; we observe instead that in our chiral medium they move ballistically as seen in Figure 3.6a.

We can gain an intuitive understanding of what powers dislocation motility by inspecting the plastic deformations of the crystal brought about by dislocation glide. As shown in Figure 3.6b, dislocation glide reflects the displacement of one crystal plane over the other. As this deformation is equal parts rotation and shear, it is naturally actuated by the rotational drive.

To isolate this phenomenon, we introduce a minimal model of the overdamped dynamics of spinners interacting via transverse, frequency-dependent forces and potential longitudinal forces (Section 3.3.1). This minimal approach is informed by full hydrodynamic simulations of particles that closely approximate our experimental system (Section 3.3.2). The transverse forces arise primarily from near-field hydrodynamic interactions, while the longitudinal interactions arise primarily from both steric repulsion and magnetic attraction (Section 3.3.3).

3.3.1 Minimal molecular dynamics simulations

We performed discrete particle dynamics simulations of a minimal model of $\sim 10^5$ particles having both longitudinal and transverse distance-dependent interactions. We find that their collective dynamics mirror closely those we observe in experiment. Perfect crystals are unstable and break up into a steady crystal whorl state. Isolated dislocations self propel and this self-propulsion can compete with elastic interactions between defects leading to defect unbinding and the modification of grain sizes. Density fluctuations can relax by dislocation pair production.

In this section we describe our minimal model in detail, describe its implementation in discrete particle dynamics simulations and highlight the dynamics we observe.

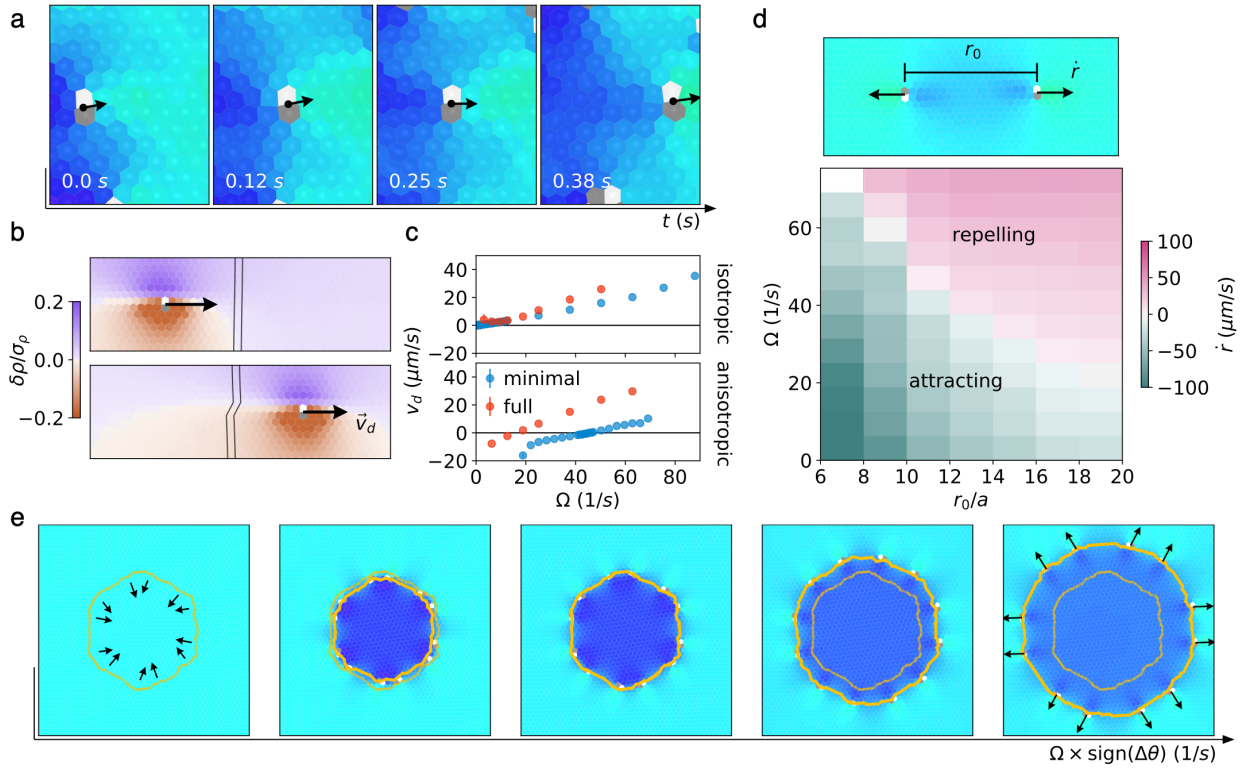

Figure 3.6: **Motile dislocations.** Dislocations in the chiral crystalline phase behave like active particles. **a,** In the experiment, dislocations are observed to move ballistically in the direction of their Burgers vector. Same colormap as in Figure 3.1b. **b,** This behavior is reproduced in simulations of both the full hydrodynamic and minimal models by initializing a configuration corresponding to a single dislocation in an otherwise undefected crystal. In a crystal of particles interacting via transverse forces, we can intuit the dislocation's direction of motion from the relative displacement of the crystal, which is colored by the relative density $\delta\rho = \rho - \bar{\rho}$ normalized by the standard deviation σ_ρ. **c,** The precise dislocation speed depends weakly on the details of the interactions. In both the minimal and full hydrodynamic models, the speed increases with frequency for isotropic dipole interactions (top). By contrast, dislocation motility is reversed at a frequency threshold for anisotropic dipole interactions (bottom). Error bars represent fit covariance (minimal) and standard error (full). **d,** By tuning the frequency and initial separation, two defects that would otherwise attract and annihilate can be made to repel, overwhelming even elastic forces with transverse ones. Same colormap as in Figure 3.1b. **e,** The collective dynamics of many defects arranged to form a grain boundary inherits this sensitivity to transverse forces. Such a grain boundary collapses when elastic forces dominate, and expands without bound when transverse forces dominate. Same colormap as in Figure 3.1b, orange line indicates position of grain boundary in both initial and present state for comparison.

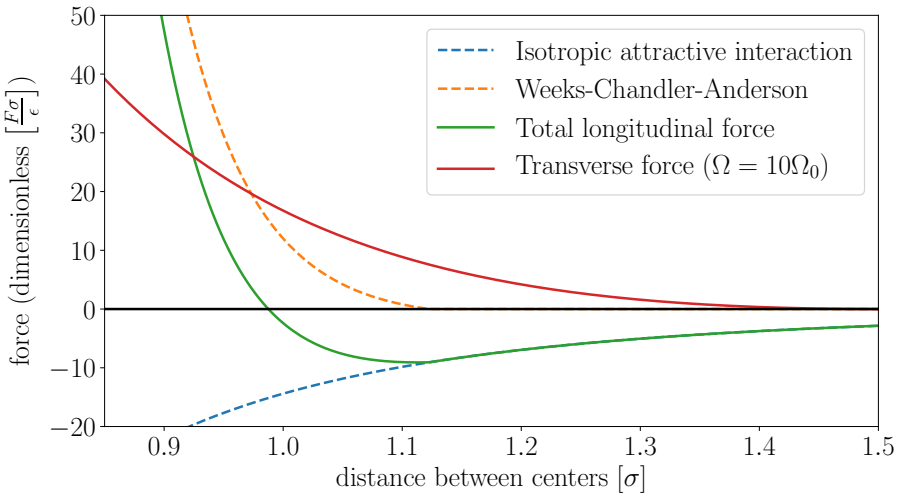

Figure 3.7: **Forces between colloids.** The interactions between colloids in the minimal model as a function of the distance between the center of the colloids.

3.3.1.1 Minimal model

Our minimal model consists of particles with overdamped dynamics that interact via longitudinal and transverse forces:

$$\gamma\dot{\mathbf{x}} = \mathbf{F}_{\text{longitudinal}} + \mathbf{F}_{\text{transverse}} \tag{3.5}$$

As described below and shown in Figure 3.7, the contributions to $\mathbf{F}_{\text{longitudinal}}$ include a Weeks-Chandler-Andersen potential and a power-law isotropic attraction term, whereas $\mathbf{F}_{\text{transverse}}$ is a smooth spatially decaying force.

Weeks-Chandler-Andersen potential To capture the steric interactions between particles in our experiment, we use a truncated shifted Lennard-Jones potential known as the

Weeks-Chandler-Andersen potential:

$$U_{\mathrm{LJ}}(r) = 4\epsilon\left[\left(\frac{\sigma}{r}\right)^{12} - \left(\frac{\sigma}{r}\right)^{6}\right]$$
$$U_{\mathrm{WCA}}(r) = \begin{cases} U_{\mathrm{LJ}}(r) - U_{\mathrm{LJ}}(r_{\mathrm{cutoff}}) & r < r_{\mathrm{cutoff}} \\ 0 & r \geq r_{\mathrm{cutoff}} \end{cases} \tag{3.6}$$

In the absence of additional longitudinal forces, this potential gives rise to a purely repulsive force at separations closer than $r_{\mathrm{cutoff}} = 2^{1/6}\sigma{\sim}1.12\sigma$. The repulsive force at a distance $r_{\mathrm{cutoff}} - \delta r$ scales as $\sim 57.14\epsilon/\sigma^2\delta r$.

Isotropic attraction To the Weeks-Chandler-Andersen potential, we add an isotropic attraction that mimics the time-averaged dipole-dipole attraction between our colloidal particles:

$$\mathbf{F}_{\mathrm{iso-dd}}(\mathbf{r}_{ij}) = -\frac{3}{2}\frac{A_{\mathrm{d}}}{r^4}\hat{\mathbf{r}}_{ij}. \tag{3.7}$$

We set the magnitude of the attraction to that of the time averaged magnetic interactions between the colloidal magnets via $A_{\mathrm{d}} = \frac{\mu_0}{4\pi}m^2$ where m is the dipole moment of a hematite cube. For measuring the velocity of isolated dislocation we also considered true anisotropic dipole interaction.

In our simulations we set $A_d = 9.6\epsilon\sigma^3$. The combined force that results from the Weeks-Chandler-Andersen repulsive potential and the isotropic attraction for this choice of A_d is shown in Figure 3.7 and corresponds to an equilibrium separation of $r{\sim}0.988\sigma$.

Transverse force Crucially, we introduce a force to describe transverse interactions between particles which in the experiment are mediated by hydrodynamic interactions between

rotating colloids. We use:

$$\mathbf{F}_{\text{transverse}}(\mathbf{r}_{ij}) = \begin{cases} \left(\frac{1}{r} - \frac{1}{r_{\text{cutoff}}}\right)^2 A_{\text{t}}\ \hat{\mathbf{z}} \times \hat{\mathbf{r}} & r < r_{\text{cutoff}} \\ 0 & r \geq r_{\text{cutoff}} \end{cases} \tag{3.8}$$

Where A_{t} is a constant. With a choice of $r_{\text{cutoff}} = 1.5\sigma$, $\mathbf{F}_{\text{rot}-\text{vis}}$ represents a generic spatially decaying transverse force that acts only on nearest neighbours in the lattice.

Choice of the parameters Overall, our minimal model includes the following dimensional parameters:

$$[\sigma] = L; [\epsilon] = \frac{ML^2}{T^2}; [\gamma] = \frac{M}{T}; [A_d] = \frac{ML^5}{T^2}; [A_{\text{t}}] = \frac{ML^3}{T^2} \tag{3.9}$$

This set gives rise to the following two dimensionless combinations:

$$\Pi_0 = \frac{A_t \sigma^2}{A_d} \qquad \Pi_1 = \frac{\epsilon \sigma^3}{A_d} \tag{3.10}$$

and a time-scale $\frac{\gamma\sigma^2}{\epsilon}$, we define the time unit to be $t_0 = 0.64\frac{\gamma\sigma^2}{\epsilon}$ and accordingly a frequency unit $\Omega_0 = \frac{2\pi}{t_0}$.

To mimic tuning the rotational frequency in the experiment, which has the primary effect of increasing transverse forces between our colloids, we tune the transverse force coefficient A_{t}. For convenience of comparison with experiment and full hydrodynamic simulations, we measure A_{t} with respect to a rotation rate Ω measured in units of Ω_0 by making the choice: $A_{\text{t}} = 2.4\epsilon\sigma\Omega/\Omega_0$.

Unless stated otherwise, these can be assumed to be the parameters of the simulations we present. As discussed in Section 3.6.4.2, this choice of parameters corresponds to a linearly stable regime for crystals in periodic domains.

3.3.1.2 Discrete particle dynamics implementation

We use HOOMD-Blue [98], developed by the Glotzer Group at the University of Michigan, to simulate the dynamics of this minimal model. The code simulates a Langevin equation

$$m\ddot{\mathbf{x}} = -\gamma\dot{\mathbf{x}} + \mathbf{F}_{\mathrm{WCA}} + \mathbf{F}_{\mathrm{iso-dd}} + \mathbf{F}_{\mathrm{rot-vis}} + \mathbf{F}_{\mathrm{B}}, \tag{3.11}$$

where thermal fluctuations are accounted by $\mathbf{F}_{\mathrm{B}}$, a Gaussian white noise defined by

$$\langle \mathbf{F}_{\mathrm{B}} \rangle = 0 \tag{3.12}$$

$$\langle |\mathbf{F}_{\mathrm{B}}|^2 \rangle = 4kT\gamma/\delta t \tag{3.13}$$

In terms of HOOMD internal units, we chose the following parameters in the majority of simulations:

$$\epsilon = 2 \qquad \sigma = 0.25 \qquad kT = 1 \cdot 10^{-4} \qquad \gamma = 50 \qquad \delta t = 10^{-4} \qquad m = 5 \cdot 10^{-2} \tag{3.14}$$

these choices ensure the dynamics are over-damped, and that the thermal fluctuations do not effect the dynamics. We implement a rotational drive by embedding in each particle a dipole that couples only to an externally applied B field. The uniform external field rotates, causing each particle to spin at the same frequency Ω.

3.3.2 Full hydrodynamic simulations

To test the robustness of our results to variations in particle shape and details of the interactions, we performed discrete particle dynamics simulations of a collection of colloidal particles, $\mathcal{B}_p$, immersed in a Stokes flow filling a half-space above an infinite wall [99, 100]. As described in this section, we find that the dynamics we observe in our simulations closely resemble those we see in experiment, and that variations in particle shape and interaction

do not have a strong effect on the collective dynamics we observe.

3.3.2.1 Simulation procedures

In the fluid domain, we take the fluid velocity $\boldsymbol{v}$ and pressure p to satisfy the incompressible Stokes equation:

$$-\boldsymbol{\nabla} p + \eta \boldsymbol{\nabla}^2 \boldsymbol{v} = 0, \tag{3.15}$$

$$\boldsymbol{\nabla} \cdot \boldsymbol{v} = 0. \tag{3.16}$$

The no-slip boundary condition is imposed both at the bottom wall, $\boldsymbol{v}(x, y, z = 0) = \boldsymbol{0}$, and at each colloids' surface where

$$\boldsymbol{v}(\boldsymbol{r}) = \boldsymbol{v}_p + \boldsymbol{\omega}_p \times (\boldsymbol{r} - \boldsymbol{q}_p) \;\text{ for } \boldsymbol{r} \in \partial\mathcal{B}_p, \tag{3.17}$$

with $\boldsymbol{v}_p$ and $\boldsymbol{\omega}_p$ the linear and angular velocities of colloid p and $\boldsymbol{q}_p$ its center. To close the equations we include the balance of forces and torques. Since inertia is neglected in our model, the hydrodynamic traction, $-\boldsymbol{\lambda}$, exerted to the surface of a colloid balances the external forces and torques ($\boldsymbol{f}$ and $\boldsymbol{\tau}$), or

$$\int_{\partial\mathcal{B}_p} \boldsymbol{\lambda}_p \, \mathrm{d}^2 r = \boldsymbol{f}_p, \tag{3.18}$$

$$\int_{\partial\mathcal{B}_p} (\boldsymbol{r} - \boldsymbol{q}_p) \times \boldsymbol{\lambda}_p \, \mathrm{d}^2 r = \boldsymbol{\tau}_p. \tag{3.19}$$

External forces are induced by gravity, magnetic and steric interactions, i.e. $\boldsymbol{f}_p = \boldsymbol{f}_p^g + \boldsymbol{f}_p^m + \boldsymbol{f}_p^s$ and similarly for the torque. The gravity simply pulls the colloids down with force $\boldsymbol{f}_p^g = -mg\boldsymbol{e}_z$. For the symmetric colloids that we consider gravity does not generate a torque. Each colloid has a permanent magnetic dipole moment, $\boldsymbol{m}_p$, which generates a

magnetic field away from its center [101]

$$\boldsymbol{B}_p(\boldsymbol{r}) = \frac{\mu_0}{4\pi r^3}\left(3\hat{\boldsymbol{r}}(\hat{\boldsymbol{r}}\cdot\boldsymbol{m}_p) - \boldsymbol{m}_p\right), \tag{3.20}$$

where μ_0 is the vacuum permeability. Additionally, we include a time dependent external magnetic field

$$\boldsymbol{B}_{\text{ext}}(t) = B_0(\cos(2\pi f t), \sin(2\pi f t), 0). \tag{3.21}$$

The total magnetic field acting on a colloid p is the sum of the external magnetic field and the one created by all the other colloids in the suspension

$$\boldsymbol{B}(\boldsymbol{q}_p, t) = \boldsymbol{B}_{\text{ext}}(t) + \sum_{q\neq p} \boldsymbol{B}_q(\boldsymbol{q}_p - \boldsymbol{q}_q), \tag{3.22}$$

it generates the force and torque [101]

$$\boldsymbol{f}_p^m(t) = \boldsymbol{\nabla}(\boldsymbol{m}_p \cdot \boldsymbol{B}(\boldsymbol{r}, t))|_{\boldsymbol{r}=\boldsymbol{q}_p}, \tag{3.23}$$

$$\boldsymbol{\tau}_p^m(t) = \boldsymbol{m}_p \times \boldsymbol{B}(\boldsymbol{q}_p, t). \tag{3.24}$$

To solve the hydrodynamic problem we use the Rigid Multiblob approach, equivalent to a regularized first boundary integral method [102]. The surface of each colloid is discretized by a small number of blobs, of hydrodynamic radius a and positions $\boldsymbol{r}_i$, that are constrained to move like a rigid body, i.e. without deformations. The discretization of the no-slip and the balance equations leads to a large linear system for the unknown colloidal velocities, $\boldsymbol{v}_p$

and $\boldsymbol{\omega}_p$, and the constraint forces on the blobs $\boldsymbol{\lambda}_i$,

$$\sum_j \boldsymbol{M}_{ij}\boldsymbol{\lambda}_j = \boldsymbol{v}_p + \boldsymbol{\omega}_p \times (\boldsymbol{r}_i - \boldsymbol{q}_p) \text{ for all } i \in \mathcal{B}_p, \tag{3.25}$$

$$\sum_{i\in\mathcal{B}_p} \boldsymbol{\lambda}_i = \boldsymbol{f}_p \quad \forall p, \tag{3.26}$$

$$\sum_{i\in\mathcal{B}_p} (\boldsymbol{r}_i - \boldsymbol{q}_p) \times \boldsymbol{\lambda}_i = \boldsymbol{\tau}_p \quad \forall p, \tag{3.27}$$

where the sum in (3.25) runs over all the blobs in the system. The mobility matrix $\boldsymbol{M}_{ij}$ is responsible for the hydrodynamic interactions, it couples the force acting on the blob j to the flow velocity generated at the blob i. We use the regularized mobility [103, 104]

$$\boldsymbol{M}_{ij} = \boldsymbol{M}(\boldsymbol{r}_i, \boldsymbol{r}_j) = \frac{1}{(4\pi a^2)^2} \int \delta(|\boldsymbol{r}' - \boldsymbol{r}_i| - a)\boldsymbol{G}(\boldsymbol{r}', \boldsymbol{r}'')\delta(|\boldsymbol{r}'' - \boldsymbol{r}_j| - a)\mathrm{d}^3r''\mathrm{d}^3r', \tag{3.28}$$

where $\delta(\boldsymbol{r})$ is the Dirac's delta function and $\boldsymbol{G}(\boldsymbol{r})$ is the Green's function of the Stokes equations in half-space [99, 100]. Analytical expressions for (3.28) can be found in Ref. [105]. The Rigid Multiblob method solves the full hydrodynamic problem, however, as we use a low resolution discretization, lubrication forces are not captured. To avoid overlapping between colloids, or colloids and the bottom wall, we include the repulsive potential between blobs and between blobs and the wall

$$U(r) = \begin{cases} U_0 + U_0 \frac{d-r}{b} & \text{if } r < d, \\ U_0 \exp\left(-\frac{r-d}{b}\right) & \text{if } r \geq d, \end{cases} \tag{3.29}$$

where we use $d = 2a$ for blob-blob interactions and $d = a$ for blob-wall interactions, therefore the potential decays exponentially fast when there is no overlap. The steric forces on the blobs generated from this pairwise potential, $\boldsymbol{f}_i^{\text{blob}}$, result in the steric forces and torques acting on the colloids, $\boldsymbol{f}_p^s = \sum_{i\in\mathcal{B}_p} \boldsymbol{f}_i^{\text{blob}}$ and $\boldsymbol{\tau}_p^s = \sum_{i\in\mathcal{B}_p} (\boldsymbol{r}_i - \boldsymbol{q}_p) \times \boldsymbol{f}_i^{\text{blob}}$, respectively.

Parameter	Value	Comment
Fluid viscosity	$\eta = 10^{-3}\text{mg}\,\mu\text{m}^{-1}\text{s}^{-1}$	that of water
Colloidal radius	$R = 1.39\,\mu\text{m}$	
Colloidal mass	$m = 1.64 \cdot 10^{-8}\,\text{mg}$	density $\sim$5000 kg/m^3
Gravity	$g = 9.81 \cdot 10^{6}\,\mu\text{m/s}^2$	
Magnetic dipole	$\lvert\boldsymbol{m}_p\rvert = 10^{-2}\,\text{A}\,\mu\text{m}^2$	
Vacuum permeability	$\mu_0 = 4\pi\,10^5\,\text{pN/A}^2$	
External magnetic field	$B_0 = 10^3\,\text{pN}/(\mu\text{mA})$	10^{-3} Teslas
Magnetic frequency	$f = 1 - 12\text{Hz}$	
Steric decay length	$b = a/10$	
Steric potential	$U_0 = 0.2\text{pN}\,\text{m}$	like the collodial gravitational energy at about 1.5 μm height
Steric blob-blob shift	$d = 2a$	
Steric blob-wall shift	$d = a$	
Blob radius	a	depends on the colloidal discretization

Table 3.1: **Full hydrodynamic simulation parameters.** Parameters used in the full hydrodynamic simulations in units of milligrams, micrometers, seconds and Amperes.

To solve the linear system (3.25)-(3.27) we use GMRES with a block diagonal preconditioner [102]. We employ a Fast Multipole Method to compute the magnetic (Eqs. (3.23)-(3.24)) and hydrodynamic interations ($\boldsymbol{M}_{ij}\boldsymbol{\lambda}_j$) with a linear cost in the number of particles [106, 107]. With this approach we are able to simulate suspensions with thousands of colloids. We give the parameters used in the simulations in Table 3.1.

3.3.3 Origin of transverse forces

Transverse forces between colloids drive the system out of equilibrium and generate the rich dynamics described in the previous sections, and we justify their presence in the full hydrodynamic and minimal model simulations here. Hydrodynamic interactions are the main source of these transverse forces, with transverse magnetic interactions between colloids being comparatively weak. In this section we use numerical simulations to estimate the strength of both magnetic and hydrodynamic contributions to the transverse interactions between colloidal particles.

3.3.3.1 Hydrodynamic forces

Because the Stokes equations (Eq. (3.15)) that describe the hydrodynamic problem are linear, the dynamic equation for N colloids can be written as the mobility problem [108]

$$\begin{pmatrix} \boldsymbol{M}_{tt} & \boldsymbol{M}_{tr} \\ \boldsymbol{M}_{tr}^T & \boldsymbol{M}_{rr} \end{pmatrix} \begin{pmatrix} \boldsymbol{f} \\ \boldsymbol{\tau} \end{pmatrix} = \begin{pmatrix} \boldsymbol{u} \\ \boldsymbol{\omega} \end{pmatrix}, \tag{3.30}$$

where the mobility components, $\boldsymbol{M}_{tt}, \ldots$, can be understood as operators that couple the translational and rotational (t, r) degrees of freedom. Here $\boldsymbol{f}$ and $\boldsymbol{\tau}$ are the non-hydrodynamic forces and torques on the colloids due to, for example, magnetic or steric interactions, while $\boldsymbol{u}$ and $\boldsymbol{\omega}$ are their linear and angular velocities, respectively. The dynamic problem can also be written as a resistance problem by inverting the linear system (3.30),

$$\begin{pmatrix} \boldsymbol{R}_{tt} & \boldsymbol{R}_{tr} \\ \boldsymbol{R}_{tr}^T & \boldsymbol{R}_{rr} \end{pmatrix} \begin{pmatrix} \boldsymbol{u} \\ \boldsymbol{\omega} \end{pmatrix} = \begin{pmatrix} \boldsymbol{f} \\ \boldsymbol{\tau} \end{pmatrix}. \tag{3.31}$$

From the resistance problem, we can write the balance of forces as [109]:

$$\boldsymbol{f}^{\text{total}} = \boldsymbol{f} - \underbrace{\boldsymbol{R}_{tt}\boldsymbol{u} - \boldsymbol{R}_{tr}\boldsymbol{\omega}}_{\text{hydrodynamic forces}} = 0. \tag{3.32}$$

This reflects that at zero Reynolds number, where inertia is neglected, Newton's equation, $\boldsymbol{f}^{\text{total}} = m\boldsymbol{a}$, simplifies to the balance of force $\boldsymbol{f}^{\text{total}} = 0$. In this limit, forces and torques externally applied to particles are instantaneously balanced by hydrodynamic forces. We can highlight the role of active torques in the system by solving for the angular velocity in (3.30) and substituting the result in (3.32):

$$\underbrace{\boldsymbol{f}}_{\text{external force}} - \underbrace{\boldsymbol{R}_{tr}\boldsymbol{M}_{tr}^T\boldsymbol{f}}_{\text{coupling force}} - \underbrace{\boldsymbol{R}_{tt}\boldsymbol{u}}_{\text{drag force}} - \underbrace{\boldsymbol{R}_{tr}\boldsymbol{M}_{rr}\boldsymbol{\tau}}_{\text{active force}} = 0. \tag{3.33}$$

The last three terms in (3.33) can all introduce transverse forces mediated by the fluid, but it is the last term that drives the system and breaks parity and time-reversal symmetry. Therefore, we focus on the active force

$$\boldsymbol{f}^{\text{active}} = -\boldsymbol{R}_{tr}\boldsymbol{M}_{rr}\boldsymbol{\tau}, \tag{3.34}$$

which can be decomposed into its longitudinal ($\parallel$) and transverse ($\perp$) components. It is important to note that the resistance and mobility operators ($\boldsymbol{R}_{tr}$, $\boldsymbol{M}_{rr}$, ...) depend on the entire particle configuration. However, to get an intuitive understanding on the form of the active forces we can use a mobility-resistance pair-wise approximation [110]. In the limit of large distances and ignoring the screening of the wall, we have:

$$f_{\parallel}^{\text{active}} = 0, \tag{3.35}$$

$$f_{\perp}^{\text{active}} = -R_{tr}M_{rr}\tau = -R_{tr}\omega = -6\pi\eta a^2\omega\left(\frac{a}{r}\right)^2, \tag{3.36}$$

where a is the colloidal radius. In this approximation the active forces only have transverse components proportional to their angular velocity ω.

For a more accurate characterization of the transverse forces in our experiments, we extract the active hydrodynamic forces from particle simulations using our full hydrodynamic model. In particular, we sought to determine the order of magnitude and form of these forces, their scaling with increasing system size and whether they can be approximated as time-independent forces. First we perform simulations of a system with only two colloids and measure the active force on each. We consider two cases: one where the particles are taken from a synthetic trajectory where the colloids remain at a constant distance and rotate with a constant angular velocity; the other where the particles trajectories were extracted from a many particle dynamic simulation; see Fig. 3.8. We name these two cases *synthetic* and *dynamic*, respectively. Figure 3.9 shows the time-averaged force versus distance for the

synthetic case. The transverse forces can be seen to decay faster than $\sim 1/r^2$, owing to the wall screening of the hydrodynamic interactions . For large distance between the two colloids and the wall Blake predicted the decay $\sim 1/r^3$ [99]. In our system the colloids remain close to the wall which increases the screening effect. The fast decay supports the use of a pairwise approximation for the transverse forces. We investigate this further below.

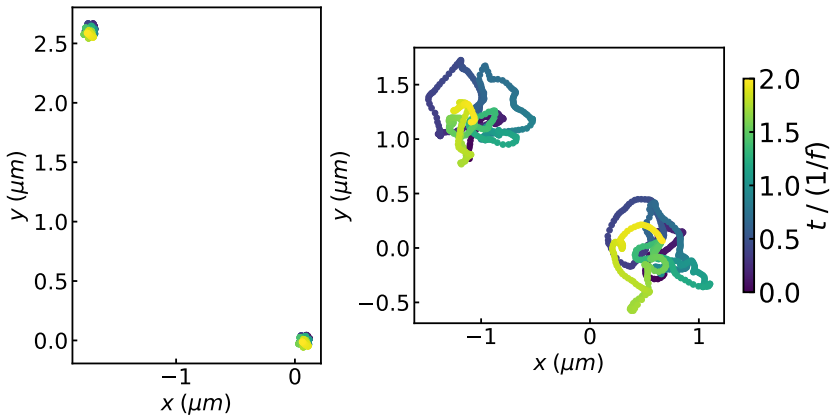

Figure 3.8: **Colloid trajectories during rotation.** For the dynamic many-particle case, trajectories during two periods of the rotating external magnetic field (period $1/f$) for two spheres (left) or superellipsoids (right) extracted from simulations.

Figure 3.10 shows the active hydrodynamic forces during two periods of the external magnetic field (period $1/f$). Again, we compare the forces computed in the synthetic and dynamic cases. For spherical colloids (left columns), the longitudinal force values, which average to zero, are near-identical. For superellipsoidal colloids (right columns) the traces fluctuate more significantly in time and with respect to each other, because these colloids move significantly in a single period; see Fig. 3.8. The extracted transverse forces differ more significantly for both spheres and superellipsoids, in both instantaneous value and average. The reason is that the lag between a colloid's dipole and the external magnetic field is larger in the dynamic case and therefore, the external torque, $\boldsymbol{\tau} = \boldsymbol{m} \times \boldsymbol{B}(t)$, is also larger. Furthermore, in the dynamic case we extracted the particle's trajectory from a many particle simulation. The neighbor particles exerted an additional drag on the colloids which

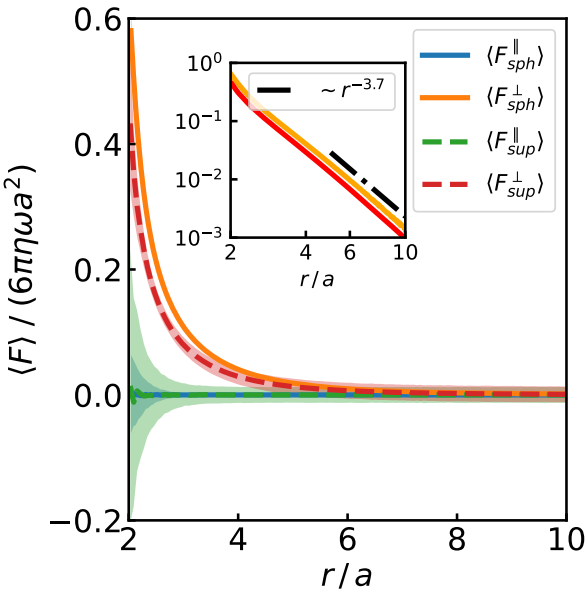

Figure 3.9: **Hydrodynamic force versus distance.** For the synthetic case, average longitudinal ($\parallel$) and transverse ($\perp$) components of the hydrodynamic force versus distance for spheres ("sph") and superellipsoids ("sup"). The shadowed regions represent the standard deviation of the forces. The transverse force decay, $\sim(1/r)^{3.7}$ is shown in the inset. To normalize the hydrodynamic force we define the superellipsoid radius through its volume, i.e. $a = (3V/(4\pi))^{1/3}$.

in turn required a larger torque to follow the magnetic field. To confirm this interpretation we computed the active forces for the dynamic case but assuming that the torque was $\boldsymbol{\tau} = \boldsymbol{M}_{rr}^{-1}\boldsymbol{\omega}$ with the same constant angular velocity $\boldsymbol{\omega}$ as in the synthetic case. The bottom panel of Fig. 3.10 shows the remarkable agreement for the transverse forces in this case. Although neither the longitudinal nor the transverse force is time-independent, we can see in that the force is approximately periodic. Since the dynamics of the chiral suspension is slow compared with the frequency of the magnetic field we assume that a time-independent approximation is valid to model transverse forces. Furthermore, the good agreement between the synthetic and dynamic cases suggest that these results are robust against particle movements during one magnetic period.

Finally, we explore whether the force scales with the system size. The resistance and

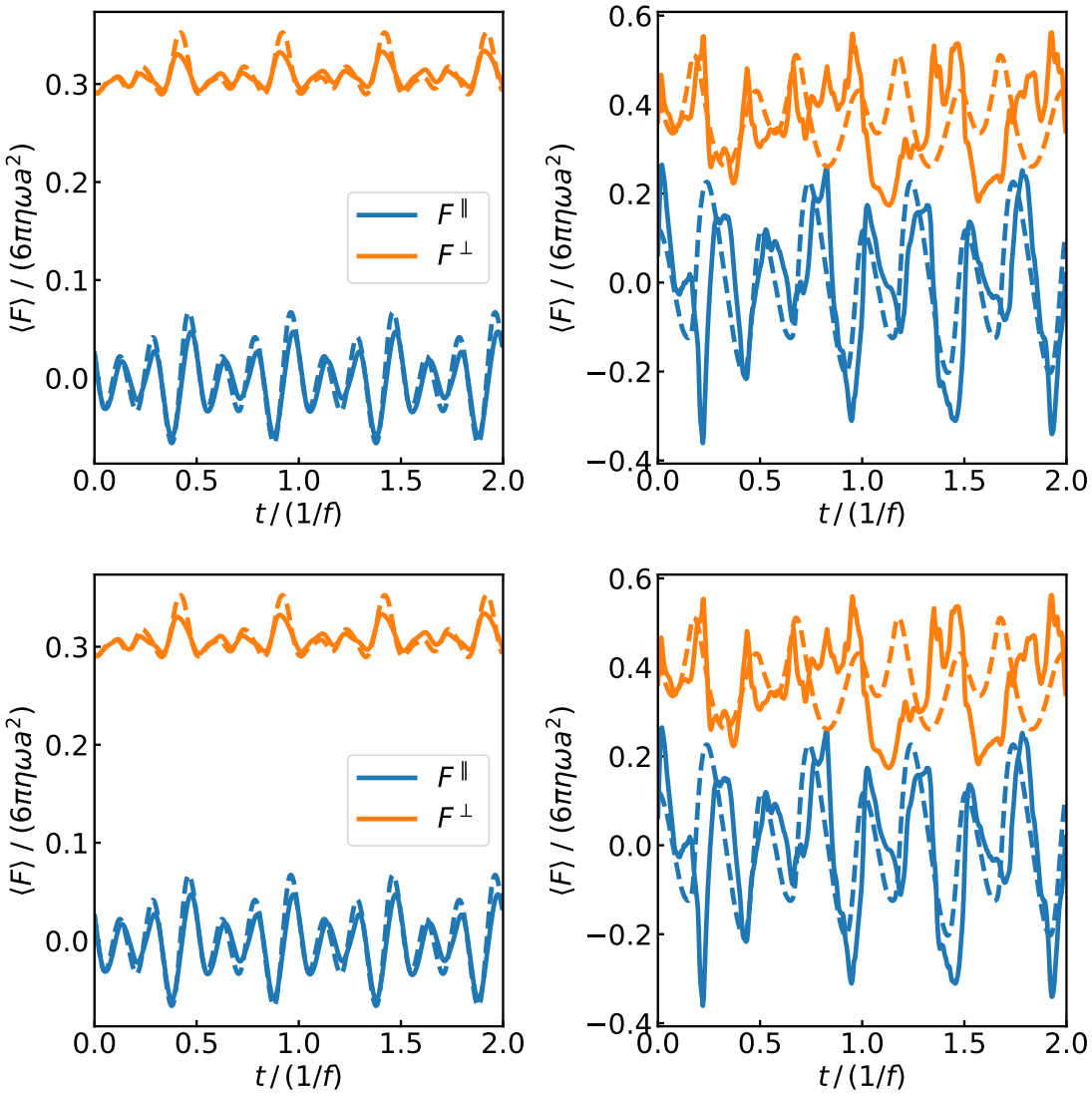

Figure 3.10: **Active hydrodynamic forces.** Longitudinal and transverse components of the active hydrodynamic forces for spheres (left) and superellipsoids (right) using Eq. (3.34). The dashed curves are computed from a synthetic simulation where two colloids rotate with a constant angular velocity at constant positions, with the force defined as $\boldsymbol{f}^{\text{active}} = -\boldsymbol{R}_{tr}\boldsymbol{\omega}$. The solid curves are computed from the dynamic trajectory of two colloids extracted from a many-particle simulation. To compute the torque in this case we used two methods. In the top panel we assume that the torque is $\boldsymbol{\tau} = \boldsymbol{m} \times \boldsymbol{B}^{\text{ext}}(t)$. Therefore in the many-particle simulation the external magnetic field, $\boldsymbol{B}^{\text{ext}}(t)$, exerts a higher torque due to the additional drag created by the other colloids. In the bottom panel we assume that the colloids rotate with constant angular velocity and that the torque is $\boldsymbol{\tau} = \boldsymbol{M}_{rr}^{-1}\boldsymbol{\omega}$.

mobility matrices, $\boldsymbol{R}_{rt}$, ..., depend in principle on the configuration of all the other particles. We extract the trajectory of a small cluster of particles from a many particle simulation and we measure the active forces between two colloids centered in the cluster; see Fig. 3.11 top panels. To measure the relative force between two particles we apply a constant torque $\boldsymbol{\tau} = \boldsymbol{M}_{rr}^{-1}\boldsymbol{\omega}$ to only two of the particles. However, as the other colloids reflect the hydrodynamic interactions they affect the result [111]. Figure 3.11 shows that the active forces converge quickly with the number of particles in the cluster, and reach the steady state for clusters with about 16 colloids. This result could have been expected from the fast decay of the force with distance presented in Fig. 3.9. We can also see that, as in the two particle simulation, the longitudinal component averages to zero while the transverse component reaches a finite value. These results demonstrate that the transverse forces can be taken to be independent of the system size as we did in the minimal model.

3.3.3.2 Magnetic dipole-dipole interactions

The magnetic force, $\boldsymbol{F}_{ij} = \boldsymbol{\nabla}(\boldsymbol{m}_i \cdot \boldsymbol{B}_j)$, on the colloid i exerted by the colloid j can be decomposed in transverse ($\perp$) and longitudinal ($\parallel$) components. Since the particle dipoles align with the external magnetic field it can be assumed that both dipoles are parallel, i.e. $\boldsymbol{m}_i = \boldsymbol{m}_j$, in that case [101]

$$F^{\parallel}(t) = \frac{3\mu_0 m_0^2}{4\pi r^4}\left[1 - 3\cos^2(2\pi f t)\right], \tag{3.37}$$

$$F^{\perp}(t) = \frac{6\mu_0 m_0^2}{4\pi r^4}\sin(\omega t)\cos(2\pi f t), \tag{3.38}$$

and averaging over one period (see Fig. 3.12)

$$\langle F^{\parallel}(t)\rangle = -\frac{3\mu_0 m_0^2}{8\pi r^4}, \tag{3.39}$$

$$\langle F^{\perp}(t)\rangle = 0. \tag{3.40}$$

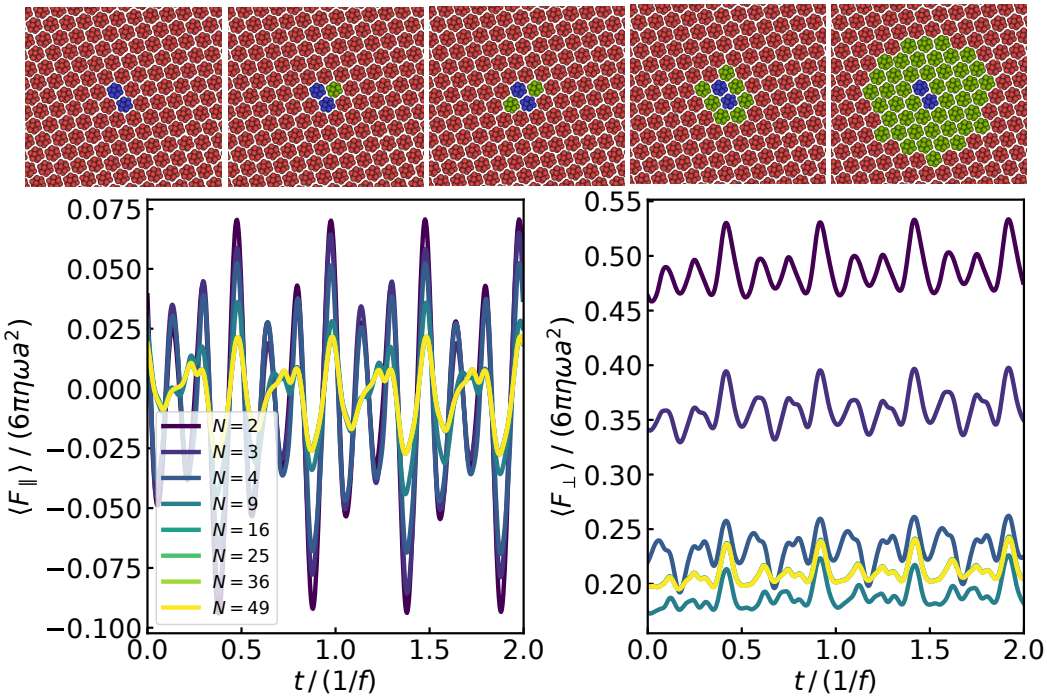

Figure 3.11: **Active force for several system sizes.** The top panels show a snapshot of the two colloids(in blue) subject to an external torque within a small cluster (in yellow). The trajectories of those particles are extracted from a 2000 particle simulation (in red) surrounding the cluster. The bottom panels show that the longitudinal and transverse components of the force converge quickly with cluster size.

To a first order approximation the dipole-dipole interactions do not generate transverse forces. In the chiral fluid small deviations from a perfect alignment exist. For example, it is possible that the lags between the dipoles and the external magnetic field depend on the local density (via friction). In that situation the dipole-dipole interactions could introduce weak transverse force proportional to the density gradient. Figures 3.12 and 3.13 show the component of the magnetic forces. The transverse components average to zero.

3.3.3.3 From full hydrodynamics to the minimal model

The full hydrodynamic model allows realistic simulations of the chiral fluid, however, the high computational cost of solving the Stokes equations prevents us to simulate systems

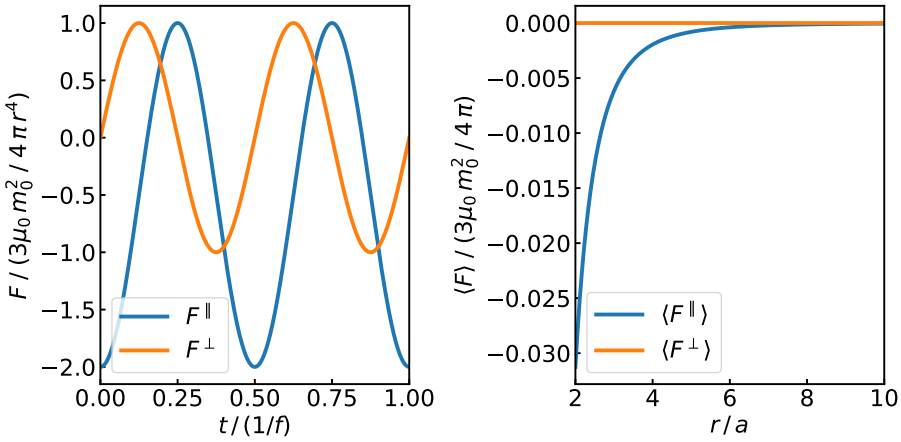

Figure 3.12: **Dipole-dipole magnetic forces.** (Left) Longitudinal and transverse components of the magnetic force versus time. (Right) Average magnetic force versus distance.

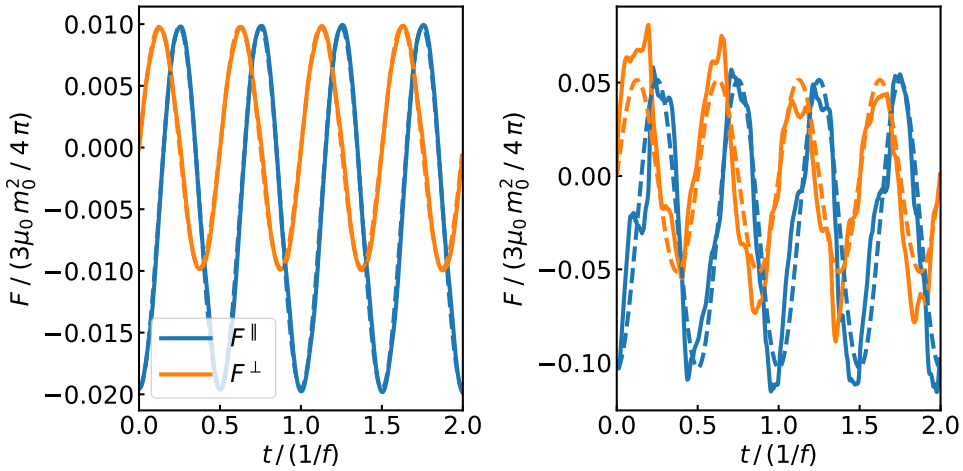

Figure 3.13: **Magnetic forces between colloids.** Longitudinal and transverse components of the magnetic force for spheres (left) and superellipsoids (right). The dashed curves are computed from synthetic trajectories (dipoles are parallel) while the solid curves are computed from dynamic trajectories extracted from a many-particle simulation.

with more than ∼2500 colloids. The minimal model of Sec. 3.3.1 has the advantage of a lower computational cost, which opens a window to simulate massive systems (∼10^5 colloids) during large periods of time. Both models can be connected through the mobility equation

(3.30), from which we can write the colloidal velocity as

$$\gamma \boldsymbol{u} = \gamma \boldsymbol{M}_{tt} \boldsymbol{f} + \gamma \boldsymbol{M}_{tr} \boldsymbol{\tau}, \tag{3.41}$$

where γ is a friction coefficient. Both terms in the right hand side of (3.41) can generate longitudinal and transverse forces. However, as discussed above, the active torque generates mostly transverse forces while the first term generates mostly longitudinal forces. We therefore simplify, Eq. (3.41) to Eq. (3.5) of the minimal model,

$$\gamma \dot{\mathbf{x}} = \mathbf{F}_{\text{longitudinal}} + \mathbf{F}_{\text{transverse}}. \tag{3.42}$$

By neglecting the many body hydrodynamic interactions, the minimal model reduces the computational cost while still capturing the nature of the main physical interactions between the colloids.

3.3.4 Dislocation self-motility & collective behavior

By initializing simulations with a single dislocation in an otherwise perfectly ordered triangular crystal, we are able to observe the motion of dislocations isolated from interactions with other defects in both minimal and full hydrodynamic simulations. As shown in Figure 3.6c, we observe that the glide speed is frequency dependent. When the longitudinal interactions between particles are isotropic, corresponding to time-averaged magnetic interactions (Section 3.3.5 and Section 3.3.6), the glide velocity is a monotonically increasing function, with a threshold (Figure 3.6c). This is consistent with the notion of a unidirectional propulsion resisted by local Peierls barrier [112, 113]. In the case of anisotropic dipolar interactions, at low frequencies we observe a correction to defect propulsion brought about by a competition between magnetic and rotational interactions (Figure 3.6c).

The motility of individual dislocations provides a significant twist on the collective dy-

namics of defects normally driven by elastic interactions [114, 115, 116, 117, 118, 17]. For example two defects that would normally attract and annihilate in response to elastic forces, can instead unbind when propelled by transverse forces as shown in Figure 3.6d.

The collective dynamics of several defects is similarly affected. Figure 3.6e shows snapshots from simulations in which we initialized a finite size grain in an otherwise perfect crystal and varied the rotation frequency. Altering the frequency affects transverse interactions most strongly and thus enables us to tune the balance between stabilizing elastic interactions and defect motility. As shown in Figure 3.6e, the grain size is set by the competition between motility and defect interactions. At low rotation frequencies the grains are stable, and their size becomes larger when the defect's propulsion direction is outwards. Similarly, they shrink and collapse for inwards defect motility. When the system is driven sufficiently strongly, the defect motility overpowers the elastic interactions resulting in unstable grain boundaries. In the following sections, we investigate these individual and collective dynamics at length in both the minimal model (Section 3.3.5) and full hydrodynamic (Section 3.3.6) simulations.

3.3.5 Dislocation dynamics in minimal model simulations

To isolate the novel dynamics of self-propelled dislocations in chiral crystals we create initial configurations corresponding to isolated dislocation, a pair of opposite dislocations, and closed circular grain-boundary. As illustrated in Figure 3.14, to generate the initial configuration we begin with a defect-less triangular lattice, and displace a triangular wedge (triangular wedges) whose tip coincides with the desired location(s) of the dislocation(s). We then insert two additional semi-infinite rows of particles in each resulting gap and perform a Delaunay triangulation to create a network of springs whose rest-length is the desired lattice spacing. We then relax the system of springs to a minimum energy configuration. This process results in an initial configuration that has the desired number and orientation of defects, and minimal residual even stresses.

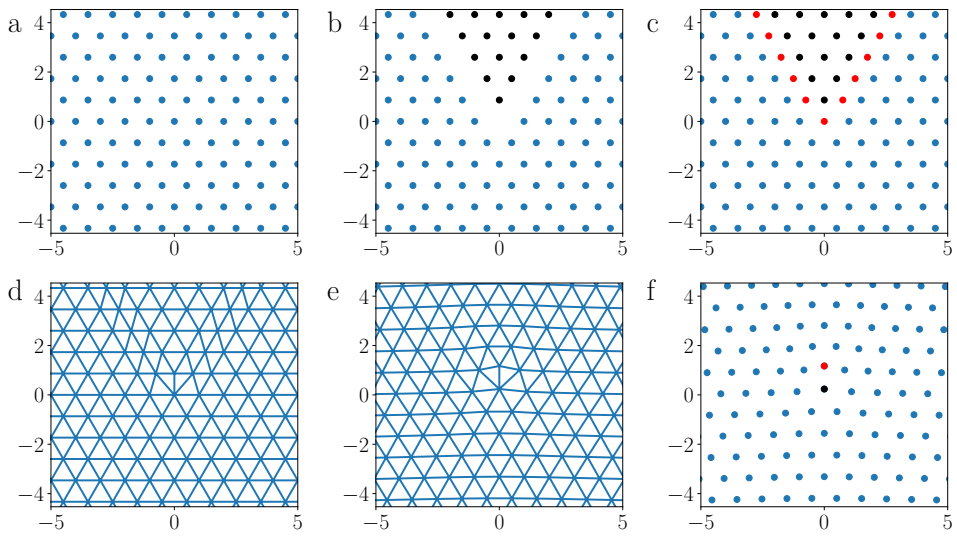

Figure 3.14: **Steps to create one dislocation**. **a.** A perfect hexagonal grid is used. **b.** Slicing a wedge of $\pi/3$ from the lattice and moving it one plane upward. **c.** The missing two lines are filled with new colloids, thus creating the topology of a defect. **d.** Each colloid is connected with springs to his neighbor. **e.** The spring system is simulated until it is fully relaxed. **f.** The resulted grid, with the dislocation in the middle in red and black

3.3.5.1 Dislocation self-propulsion by odd stress

We investigate the self-propulsion of dislocations by creating an initial configuration consisting of a single dislocation in an otherwise defect-free crystal. As shown in Figure 3.15, we find that the dislocation generically moves in the direction of the Burgers vector. By tracking the movement of the dislocation, we are able to extract the velocity-dependent motility displayed in Figure 3.15c. At frequencies $\Omega \geq 4\Omega_0$ the measurement is carried out before the lattice destabilizes to the crystal whorl state.

As discussed in Section 3.3.4, we interpret this behavior by looking on the density of the lattice surrounding the dislocation. Because the transverse interactions decrease with distance, a density gradient results in a net transverse body force on the lattice. The density above the dislocation is higher than the density below it resulting in an elastic shear that is precisely aligned to propel the dislocation to glide in the direction of the Burgers vector. The propulsion mechanism is thus analogous to a self-generated Peach-Koehler force. At

low enough frequencies, the dislocation does not move at all due to the Peierls potential. We note that in our system this occurs at frequencies that are ∼40 times lower than the transition frequency $4\Omega_0$.

We also considered full magnetic interaction between the colloids, where for low frequencies the magnetic stresses can revert the direction of the dipole movement. The colloids in this case were rotated at a constant angular frequency Ω and acted on each other with anisotropic dipole and with the transverse interaction defined in Eq. (3.8).

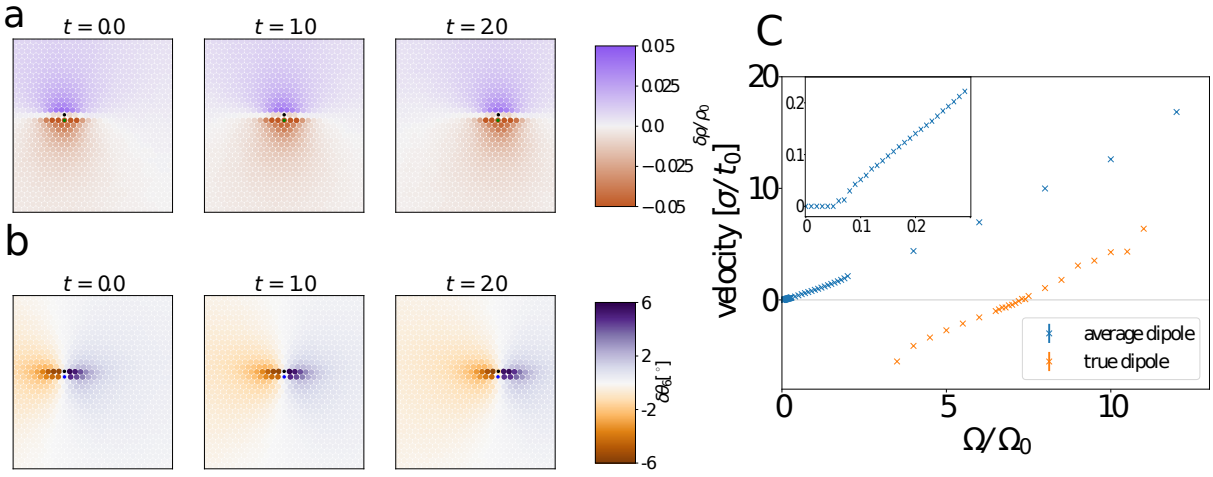

Figure 3.15: **Dislocation movement due to odd forces**. **a-b** show the movement of the dislocation in a representative simulation at $4\Omega_0$. **a.** The colloids are colored by the inverse area of the Voronoi cell around the particle, to show the local density of the crystal. The density above the lattice is 5% higher than the regular density of the crystal. **b.** Each colloid is colored by its orientation angle θ_6, we see a misalignment near the dislocation. The 5-7 pair is marked by black and blue. **c.** The average velocity of a dislocation vs. the frequency of the external field for average dipole (blue) and true dipole (orange) interaction. Inset - low frequencies for average dipole the dislocation does not move, presumably due to the Peierls potential.

3.3.5.2 Pair of opposed dislocations

Next, we examine the behavior of two dislocations having opposite Burgers vectors and thus opposite directions of motility. As illustrated in Figure 3.16, we find that, at any given

frequency, there is a threshold distance below which the dislocations travel towards each other and annihilate. Above this threshold, they travel apart indefinitely. The boundary between motility-driven dislocation unbinding and canonical annihilation is shown in Figure 3.16c.

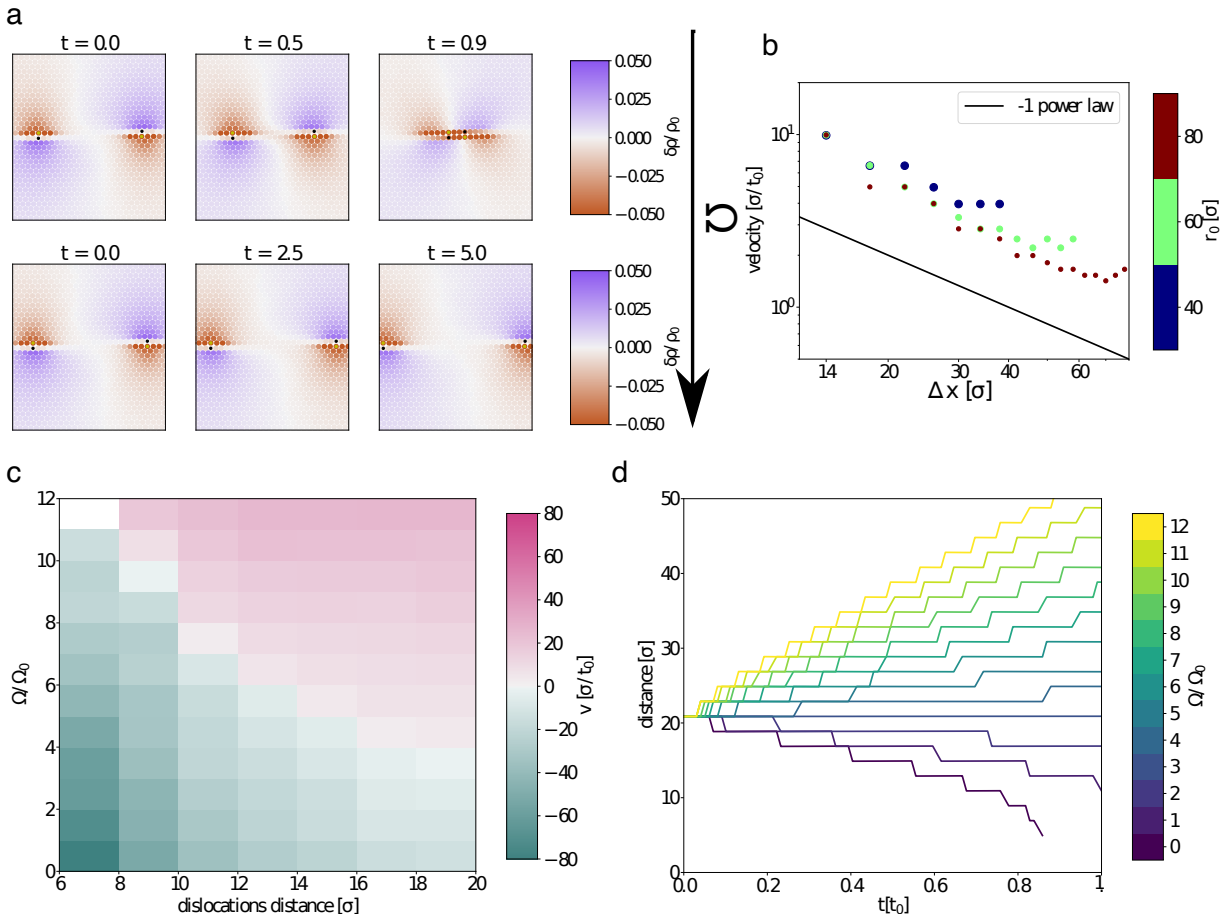

Figure 3.16: **The interaction between two dislocations. a.** Density field around two dislocations starting 20 lattice sites from each other. Without odd stresses the dislocations attract each other, the self propulsion created by the odd forces tear them apart. **b.** Velocity of the dislocations without odd stresses when starting far from each other. **c.** The velocity of the dislocations vs the initial distance and the frequency of the external field. White areas show zero velocity, where the dislocations are stable. **d.** Time series of the distance between the dislocations for $r_0 = 20\sigma$.

3.3.5.3 Circular grain boundary

Finally, we discuss the case of a circular grain. To create the initial configuration, we simply select particles within a radius of 20 lattice spacings from the center of a perfect crystal. We then rotate the region by 6 degrees about its center, and proceed as above by triangulating to create a lattice of springs and relaxing it to a minimal energy configuration. Finally we run the full MD simulation with transverse forces turned off. The process is illustrated in Figure 3.17. The result is a grain that is stable in the absence of transverse forces and is surrounded by a grain boundary consisting of dislocations whose Burgers vectors are perpendicular to the grain boundary.

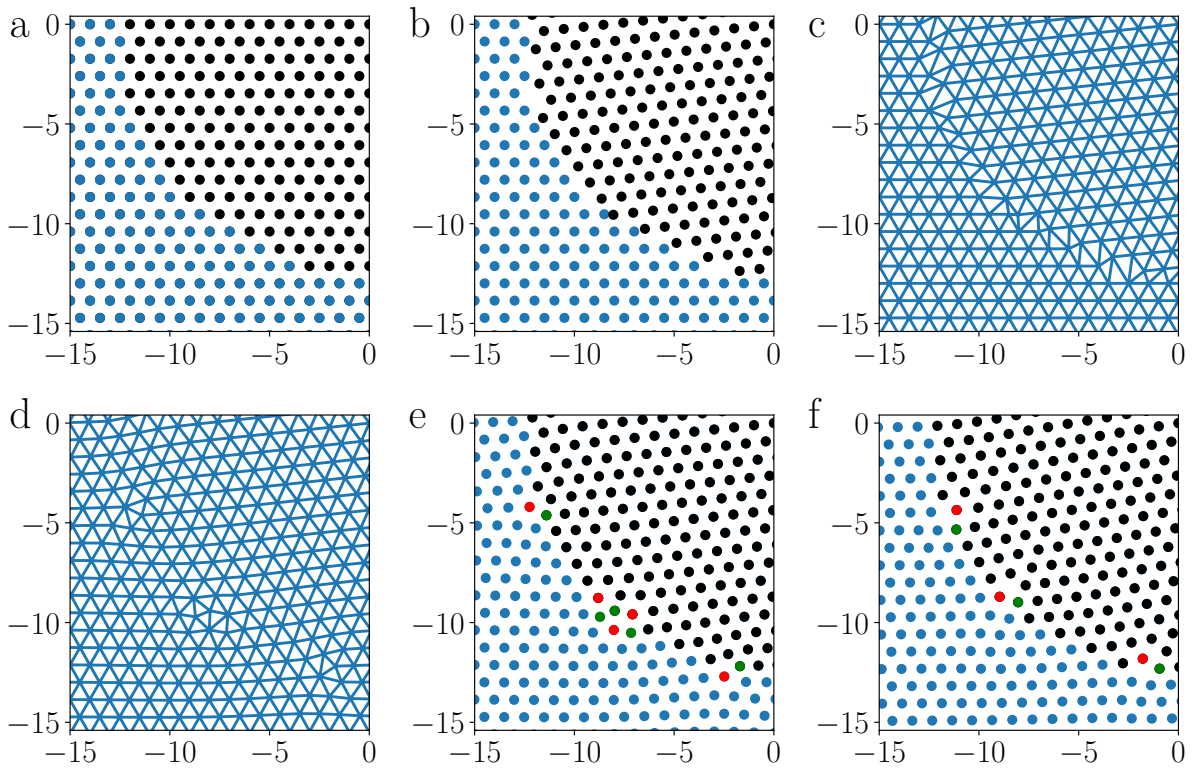

Figure 3.17: **Creating initial circular grain. a.** The original lattice with the grain in black. **b.** The grain is rotate by 6 degrees. **c.** The colloids are connected to the neighbors with springs. **d.** The spring system is relaxed . **e.** The resulted lattice after the spring system is relaxed. dislocations are shown in green and red. **f.** The fully relaxed system after running the simulation for a few second without odd stresses

When transverse forces are turned on, we observe a change in the radius of the grain as shown in Figure 3.18. As in (A), if the motility of the defects is outwards, the grain expands (right). For low motilities, the expansion stops at some point and a new bigger stable grain is constructed, while for higher motilities the grain keep expanding (see Figure 3.6). For sufficiently low motilities in either direction (middle), the grain is static. Finally, if the motility is inwards, the grain shrinks and fully disappears for sufficiently high motilities (left). The area of the central grain for various motilities in both directions is plotted in (B), showing each of these behaviors.

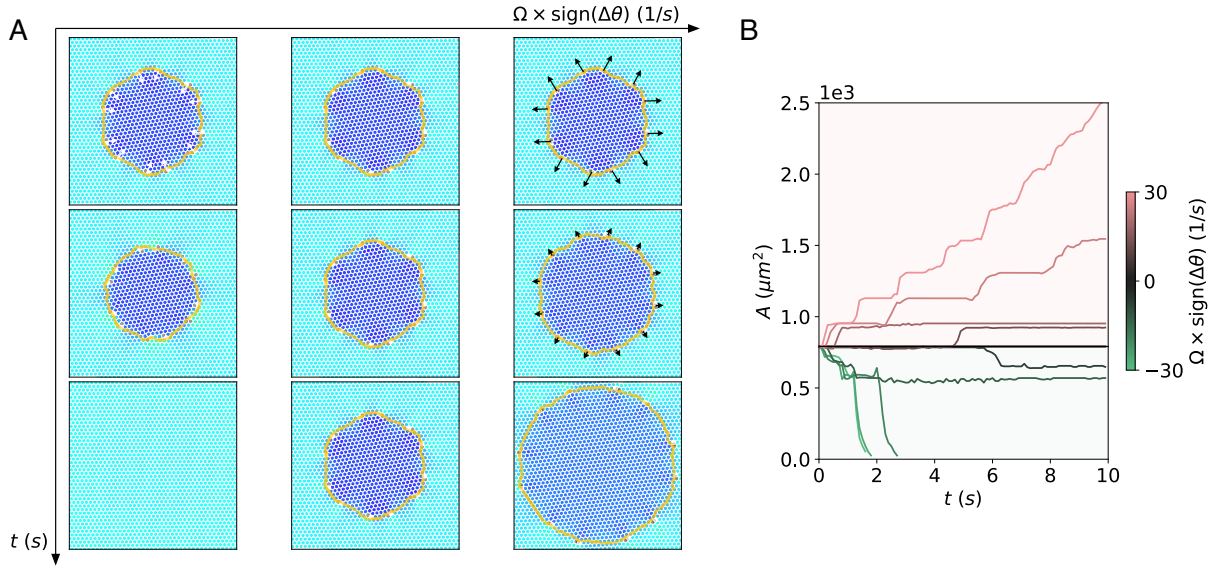

Figure 3.18: **Grain boundary motility.** (A) A circular grain can shrink (left) for inward dislocation motilities, and will annihilate for sufficiently high motilities. At low motilities, the grain is static (middle). For outward motilities, the same grain expands, with the growth unbounded for sufficiently high motilities. (B) The area of the grain is plotted versus time for systems driven to have inward motility ($\Omega \times \text{sign}(\Delta\theta) < 0$) and outward motility ($\Omega \times \text{sign}(\Delta\theta) > 0$), showing the aforementioned classes of behavior, where $\Delta\theta$ is the angle mismatch between the grain and outside.

3.3.5.4 Defect creation in a non-uniform density field

After exploring the dynamics of pre-existing dislocations in the lattice, we now demonstrate a mechanism for the creation of defect pairs in the lattice. We create a density gradient in a perfect lattice, by displacing particles in an otherwise uniform lattice by an amount:

$$\delta\mathbf{x} = a\mathbf{x} \cdot \exp\left(-\frac{x^2}{2\sigma_x^2} - \frac{y^2}{2\sigma_y^2}\right) \tag{3.43}$$

This transformation moves particles away from each other near the origin, the resulting less dense area is encircled by an annular region higher than normal density. By having different σ_x and σ_y, the state created has a stronger gradient in one direction, while the change in the other direction is more moderate.

In the result showed in Figure 3.19, the parameters used to apply the strain were $\sigma_x = 4\sigma, \sigma_y = 14\sigma$ and $a = 4\sigma$. As explained in Section 3.3.4 and discussed above, a sufficiently high density gradient produces a shear stress. If the stress is above the yield stress of the crystal, dislocation pairs unbind, producing defects with opposite Burgers vectors, which can then unbind powered by their motility. The production rate of the defects depends on the strength of the odd forces; the stronger the odd forces, the more dislocations will unbind from the initial density gradient, and the more dislocations will subsequently be produced.

3.3.6 Dislocation dynamics in full hydrodynamic simulations

Following the methods outlined in Section 3.3.5, we investigated the motility of isolated dislocations in the full hydrodynamic simulations and find a rotational frequency-dependent motility as shown in Figure 3.20. At moderate to high rotational drive frequency, the motility is a monotonically increasing function of frequency. At low frequencies, however, we find that the direction of motion depends on the details of the model for the magnetic interactions between colloids. For anisotropic dipolar interactions, the dislocation reverses direction at

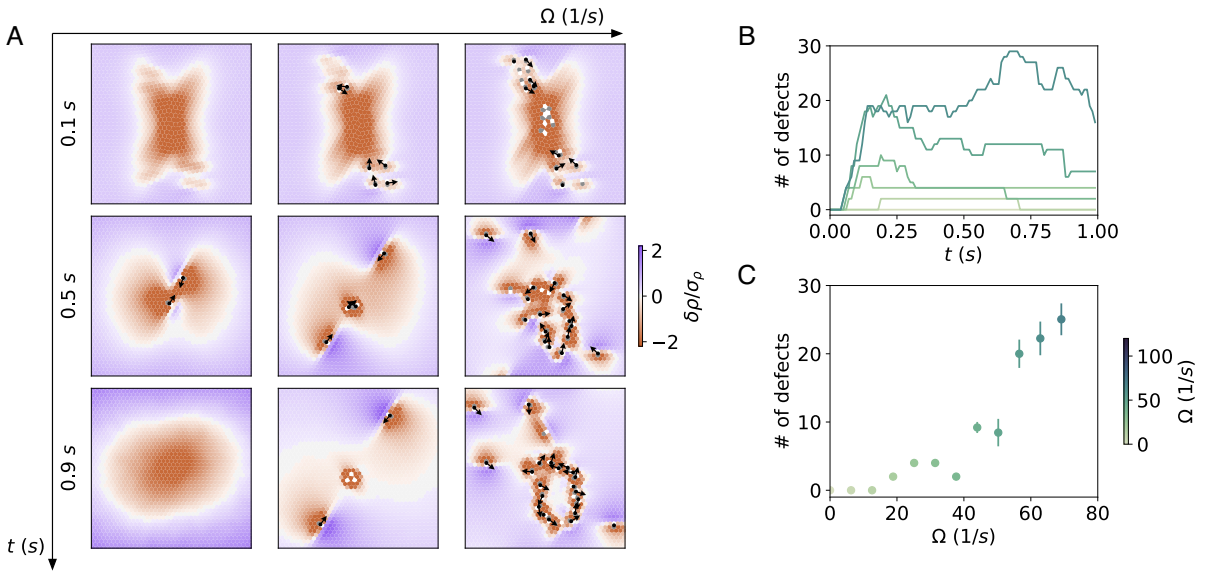

Figure 3.19: **Dislocations created from density field.** (A) As the frequency is increased, the relative density and dislocations are plotted at snapshots in time, revealing increased dislocation unbinding for stronger odd forces. (B) For a few frequencies, plotting the number of dislocations versus time reveals an initial period of unbinding followed by a slower merging and unbinding period. (C) The final number of dislocations grows with frequency above a threshold.

low frequencies, however for an isotropic dipolar interaction that corresponds to the average of the anisotropic dipolar interaction over a cycle, the motility is a monotonically increasing function with a frequency threshold. A similar behavior is observed in the minimal model simulations.

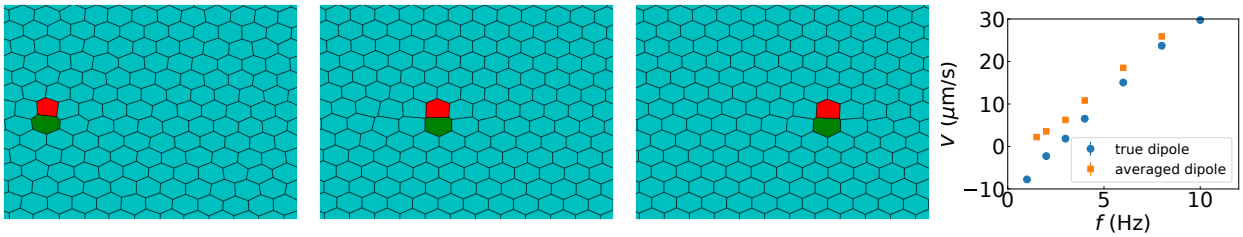

Figure 3.20: **Dislocation self-propulsion by odd stress.** A single dislocation propagates along a straight line with a frequency dependent speed. Results for true-dipole interactions (blue circles) and averaged dipole interactions (orange squares) between spherical colloids.

3.4 Transport & bulk flow of crystalline 'whorls'

In the polycrystalline state we observe in our experiments, the instability of grain boundaries results in the exchange of dislocations between adjacent grains, as well as defect proliferation. These nonlinear dynamics drive the system to the dynamical crystal whorl state erasing any memory of the initial configuration.

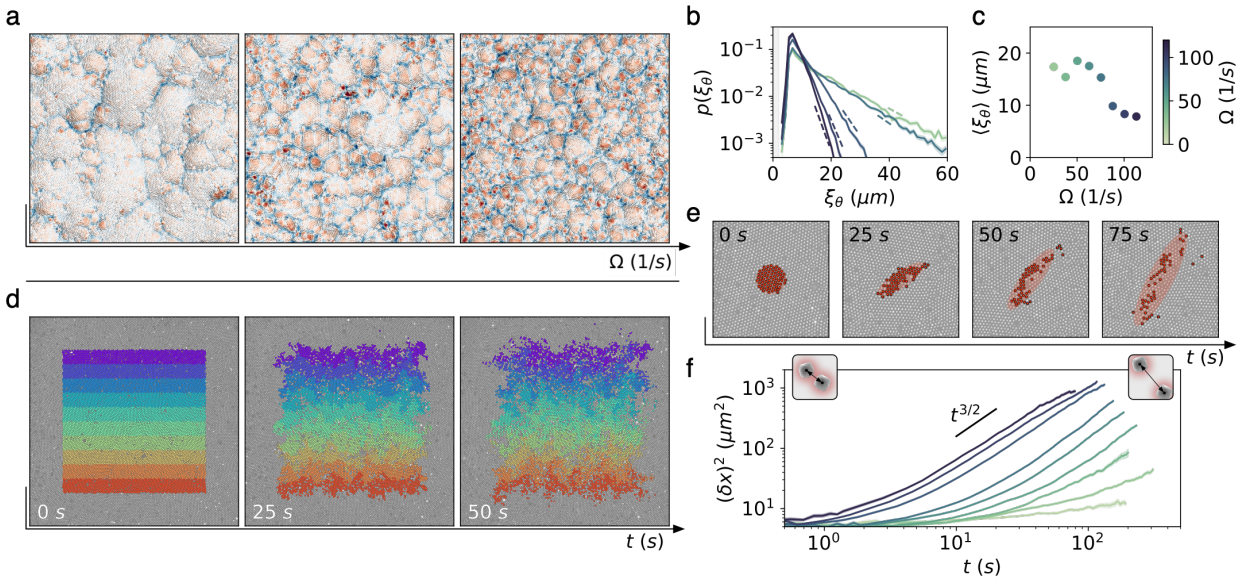

Figure 3.21: **Transport in the crystalline whorl state. a,** The self-kneading of crystalline patches of material is tunable through the rotation frequency to yield a range of scales. Same colormap as in Figure 3.1c. **b,** These states are characterized by an exponential distribution of grain sizes, dashed straight lines represent the slope of the associated exponential fit. **c,** Accordingly, the average size of grains in the steady-state tends to decrease with frequency. Error bars, which are smaller than markers, represent standard error. **d,** The constant structural kneading of the chiral whorl state by topological defects introduces novel mixing properties which can be imaged by artificially dying stratified layers in a crystal that subsequently bleed into each other. **e,** By contrast to conventional diffusive processes, the smearing of the fluid over time is a strongly anisotropic process, wherein an example blob of fluid is pulled apart by the flow between two chiral whorls. **f,** The pairwise separation $(\delta x)^2$ plotted versus time t for particles initially in close proximity suggests that this abnormal spreading gives rise to superdiffusive behavior, which itself is a function of rotational frequency. Error bars represent standard error.

The flow field $\boldsymbol{v}(\boldsymbol{x}_i)$ that emerges from the combination of motility and proliferation can be readily measured from individual particle trajectories and its corresponding vortic-

ity $\omega(\boldsymbol{x}_i)$ is shown in Figure 3.1c. When time-averaged, this flow field corresponds to a quiet bulk (Section 3.4.1) and a lively edge [18]. However our time-resolved measurements reveal instantaneous dynamics shaped by unsteady vortical flows illustrated in Figure 3.1c. The dynamical and structural pictures of this chiral whorl state are aligned. As seen in Figure 3.1b-c, the grain boundaries support strongly localized flows having a vorticity opposite to the particle rotation. By contrast, the grains correspond to low positive vorticity, intermittently interrupted by isolated dislocations zipping through.

In this chaotic stationary state, the balance between even and odd forces remains the controlling parameter that determines the characteristic size of the chiral whorls, which can be viewed through the vorticity in Figure 3.21a and the distribution of crystalline grains in Figure 3.21b-c. We present this characterization for experiments (Section 3.2.3 and Section 3.4.1), minimal model simulations (Section 3.4.2), and full hydrodynamic simulations (Section 3.4.3). The sustained proliferation and annihilation of motile dislocations is reminiscent of active nematics where motile disclinations power spatiotemporal chaos [119]. Here dislocations give rise to self kneading crystal whorls.

This self-kneading of the crystal phase results in enhanced mixing which can be qualitatively captured by artificially tagging the colloids and watching them spread; see Figure 3.21d. As shown in Figure 3.21e, an artificially dyed blob spreads anisotropically before disintegrating into separate blobs, hinting at a mechanism reminiscent of Richardson diffusion in turbulence. We investigate this quantitatively by tracking the mean squared separation between pairs of particles in the chiral phase. Figure 3.21f shows that pair separation is super-diffusive above a separation that corresponds to the characteristic grain size due to a punctuated mix of conventional diffusion within crystalline whorls and Richardson-like diffusion between them. Note that tuning the frequency of rotation alters both the basic unit of time as well as the domain size (Figure 3.21d and e) enabling effective diffusion rates to be tuned over orders of magnitude.

Is the crystal whorl state generic? We repeated the experiments shown in Figure 3.1 while varying the applied magnetic field strength, adding a static vertical component of magnetic field, and varying the shape of the magnetic particles (Section 3.4.4) Additionally, we varied the microscopic interactions in our minimal model simulations (Section 3.6.4.3). Finally, in full hydrodynamic simulations, we simulated spheres and cubes that interact both magnetically and via isotropic attraction potentials (Section 3.4.3). In all cases we find that when transverse interactions dominate, the systems self-organizes into a crystal whorl state, supporting the notion that this state is generic. In the sections that follow, we characterize the whorl states and show that they are generic.

3.4.1 Vorticity characterization

We extract the velocity field $\boldsymbol{v}_i$ from the trajectories $\boldsymbol{x}_i(t)$ of the tracked particles. The local vorticity at the site of the ith particle, ω_i can then be readily measured at the single particle level by computing the associated circulation $\oint \boldsymbol{v} \cdot d\boldsymbol{l}$ around each Voronoi cell and dividing by the area of the cell. We can then perform coarse-graining of the vorticity field as in Section 3.2.2. Alternatively, the vorticity can be directly computed from the rate-of-strain tensor of the interpolated velocity field for simulation data.

Upon interpolating the particle level vorticity to field $\omega(\boldsymbol{x})$, we present in Figure 3.22 a typical vorticity map and arrows representing the particle level flow for various rotation frequencies (A). The distribution of vorticities (B) reveals a skewed distribution that broadens rapidly with rotation frequency. By thresholding, binarizing, and segmenting the interpolated vorticity field, we can segment the experimental volume into individual vortices, and then compute the average particle level vorticity therein. As in (C), the vorticity is roughly independent of the size of these vortices, ξ_ω, but does scale with the rotation rate at the particle level. Finally, we demonstrate in (D) the correlation between vortical and crystalline structure by plotting the average vorticity for particles with varying local crystalline order

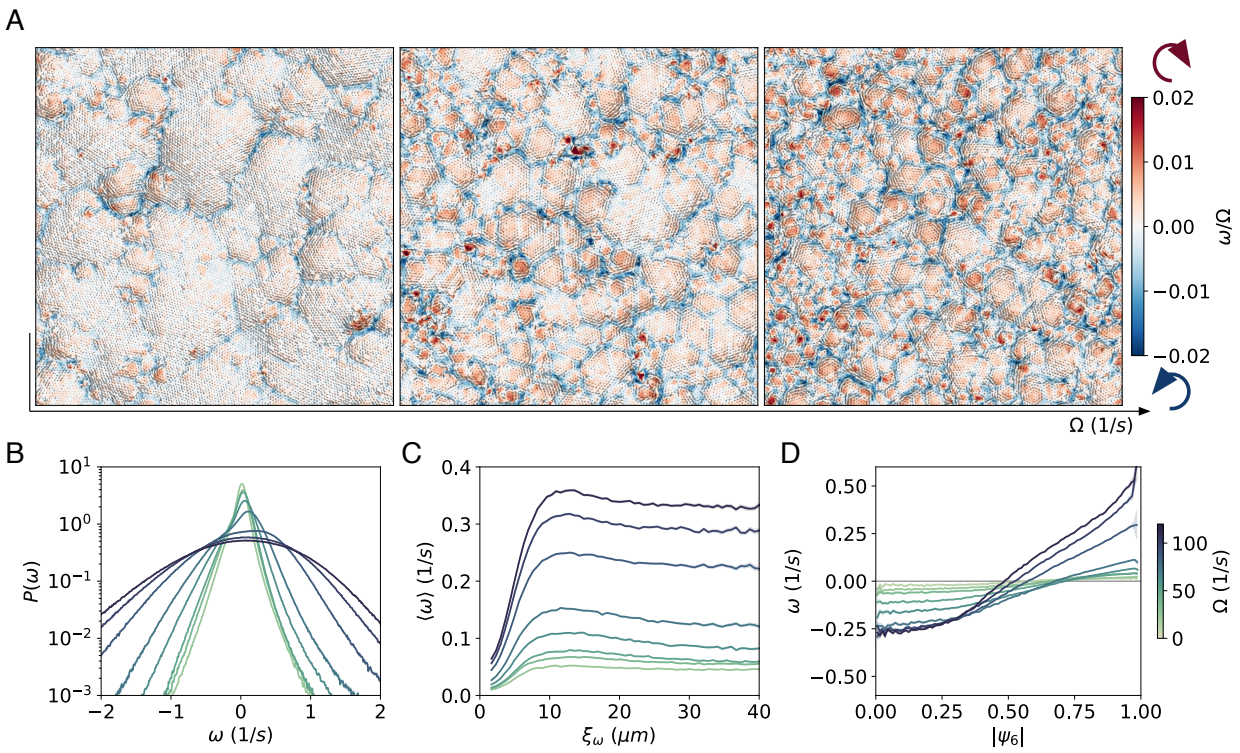

Figure 3.22: **The chiral whorl steady-state: vortical structure.** (A) Given a set of particle velocities, we estimate the vorticity on each particle. These measurements can be interpolated to extract a local vorticity field. Snapshots of the vorticity field are presented for increasing particle rotation frequencies. (B) For crystals driven over a range of frequencies, the distribution of vorticity is slightly asymmetric and tends to broaden with frequency. (C) Meanwhile, within the ordered regions, there is no strong correlation between the size of a vortex patch, ξ_ω, and the average vorticity within the patch $\bar{\omega}$ for sufficiently large vortices. (D) At the location of each particle, the vorticity field can be compared with the bond-orientational order to observe that vorticity tends to be positive in ordered regions (grains) and negative in disordered regions (grain boundaries).

$|\psi_6|$, showing rotation with the external field within crystals and counter-rotation in the less ordered regions between.

The bulk flows of the chiral whorl state are intermittent, and the structure therein only survives over small timescales. To illuminate this distinction between these short-lived flows and the long-lived currents on the free surface of a chiral medium, we compute the time-averaged velocity and vorticity, as plotted in Figure 3.23A-B. From these snapshots, we extract the mean squared velocity $\bar{v}^2$, variance in the velocity $\langle (v - \bar{v})^2 \rangle$, and variance in the

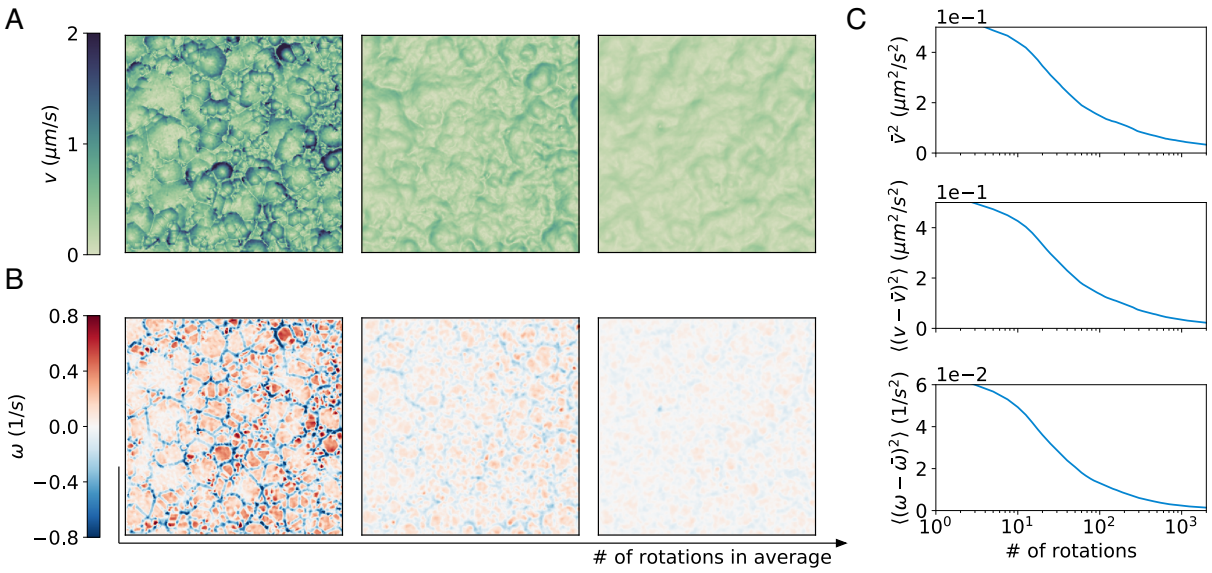

Figure 3.23: **Time-averaged flows over various scales.** Snapshots of the (A) flow $\boldsymbol{v}(\boldsymbol{x})$ ($v \equiv |\boldsymbol{v}|$) and (B) vorticity $\omega(\boldsymbol{x})$ time-averaged over a specified number of particle rotations. (C) The mean squared velocity $\bar{v}^2$, variance in the velocity $\langle (v - \bar{v})^2 \rangle$, and variance in the vorticity $\langle (\omega - \bar{\omega})^2 \rangle$ as a function of time-averaging window.

vorticity $\langle (\omega - \bar{\omega})^2 \rangle$, as plotted in (C), demonstrating that beyond a very small number of rotations, the flows average out and become unstructured.

3.4.2 Crystalline whorls in minimal model simulations

Simulations of a large droplet with 250,000 particles reveal that for spinning frequencies $\Omega \leq 4\Omega_0$, the bulk crystal structure is stable. For frequencies $\Omega > 4\Omega_0$, the transverse forces are strong enough to break the lattice structure. The behavior is shown in Figure 3.24, where we show snapshots of the (A) crystalline order θ_6 and (B) vorticity ω extracted as in Section 3.2.2 and Section 3.4.1 for late times from four different frequencies: $2\Omega_0$ where the crystal is stable, $5\Omega_0$ where low angle grain boundaries appear but the crystal does not fully break, $8\Omega_0$ where the crystal breaks, and $11\Omega_0$ where the crystal breaks into smaller crystallites.

In addition, we segment the crystal into domains and identify grain boundaries as in

Section 3.2.2, yielding an exponential distribution of domain sizes (C), and showing that the typical domain size rapidly drops at the critical frequency separating stable and unstable crystals (D). The same trend is observed in both the unweighted (E) and weighted (F) grain boundary length, which increases with frequency. This behavior closely resembles the steady state phase behavior we observe in our experiments.

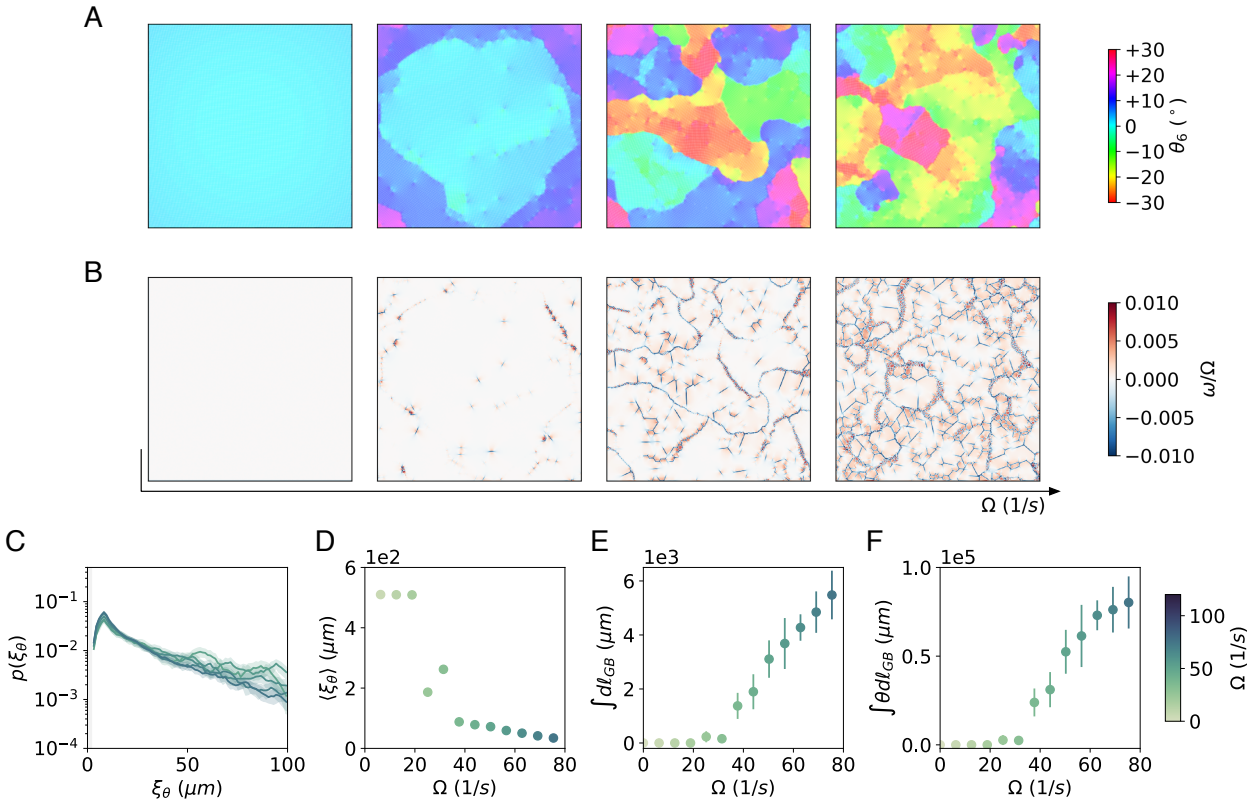

Figure 3.24: **Steady-state characterization.** Snapshots from the steady-state of large droplet simulations are plotted to show (A) the bond-orientational angle parameter θ_6, and (B) the vorticity field ω. (C) The exponential distribution of domain sizes ξ_θ suggests a (D) typical size $\langle\xi_\theta\rangle$ that decreases with frequency. The (E) grain boundary length and (F) weighted grain boundary length increase with frequency.

3.4.3 Crystalline whorls in full hydrodynamic simulations

As shown in Figure 3.25, we find that our simulations produce steady states that closely resemble those observed in our experiments. At low frequencies the system remains crystalline,

with the order punctuated by occasional motile dislocations originating at the boundary and traversing the system. As the rotational drive is increased, we find the droplets destabilize to the crystal whorl state, which is characterized by both polycrystalline structure (Figure 3.25A), and vortical domains (Figure 3.25B). We characterize the polycrystalline steady state to extract the domain size distribution, mean grain size, and total length of grain boundary as in Figure 3.25C-F, revealing that the tuning of structure through rotational drive remains a generic feature across both experiments and simulations.

The crystal whorl state is robust to variations in the shape and potential interactions between the particles. Figure 3.26 shows snapshots of the steady state for all combinations of superellipsoidal and spherical particles with true dipolar and isotropic dipolar interactions. While the steady states of these systems are defined by variable levels of structure in the vorticity field, all fragment into a polycrystalline phase.

3.4.4 Variations of a chiral crystal

The crystal whorl phase discussed above is not unique to either the particle shape or the details of the particle rotations. To demonstrate the generic nature of the crystal whorl phase in our experiments, we prepare a crystal in the same way as described in Section 3.2.1, using hematite ellipsoidal particles with a dipole moment perpendicular to their long axis instead of hematite cubes. When spun, these colloids typically stand upright and rotate as illustrated in Figure 3.27, forming a colloidal polycrystal with a grain size distribution akin to that which is reported in Figure 3.21, as shown in Figure 3.27.

For the hematite cubes discussed elsewhere in this paper, we can also modify the properties of the rotating magnetic field, and in turn the details of the polycrystalline whorl phase. In Figure 3.28, we demonstrate that the magnetic field strength B_0/B_0^0, which is rescaled by the default magnetic field magnitude B_0^0, can be tuned sufficiently low to prevent the formation of a crystal whorl phase. Below a threshold magnetic field strength, the interaction

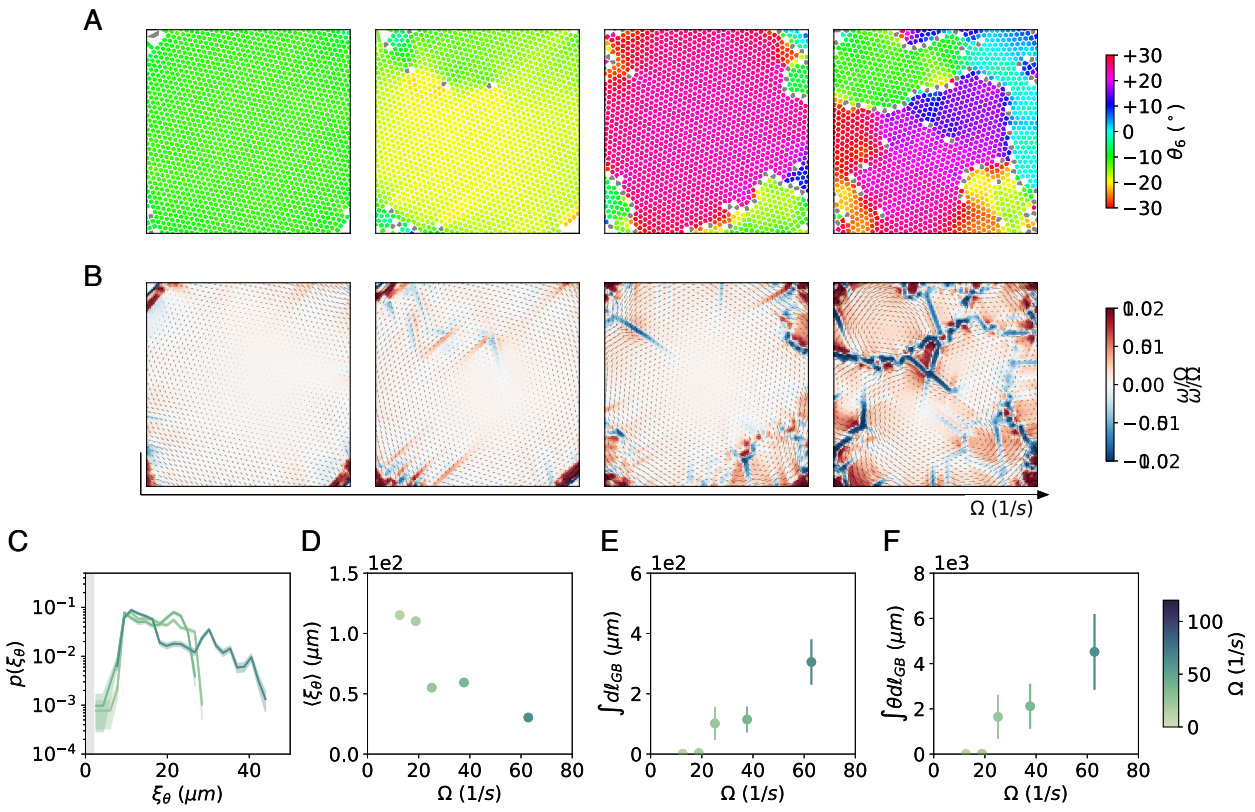

Figure 3.25: **Steady-state characterization.** A chiral polycrystalline steady-state is formed by spherical colloids spun with increasing frequency from left to right (f = 2, 3, 6, 10 Hz). (A) The Voronoi cells of each particle can be colored according to the angle θ_6 of the bond-orientational order parameter ψ_6, revealing that crystalline fragmentation increases with frequency. (B) The vortical structure of the flow formed by these particles reveals patches of vorticity corresponding to crystalline domains and interstitial flows corresponding to motile dislocations. (C) The polycrystalline structure can be analyzed by investigating the distribution $p(\xi_\theta)$ of domain sizes ξ_θ, (D) the average domain size $\langle\xi_\theta\rangle$ as a function of frequency, and the (E) unweighted and (F) weighted cumulative amount of grain boundary.

between the particles' magnetic dipoles is too weak to consistently rotate the particles at a constant rate. However, above a threshold, the distribution of domain sizes is no longer effected by this control parameter.

We can also tune the angle θ between the plane of particle rotation and the magnetic field, as illustrated in Figure 3.29. The effect on the magnetic dipoles can be viewed as a superposition of the usual pairwise interactions between rotating dipoles, which are on

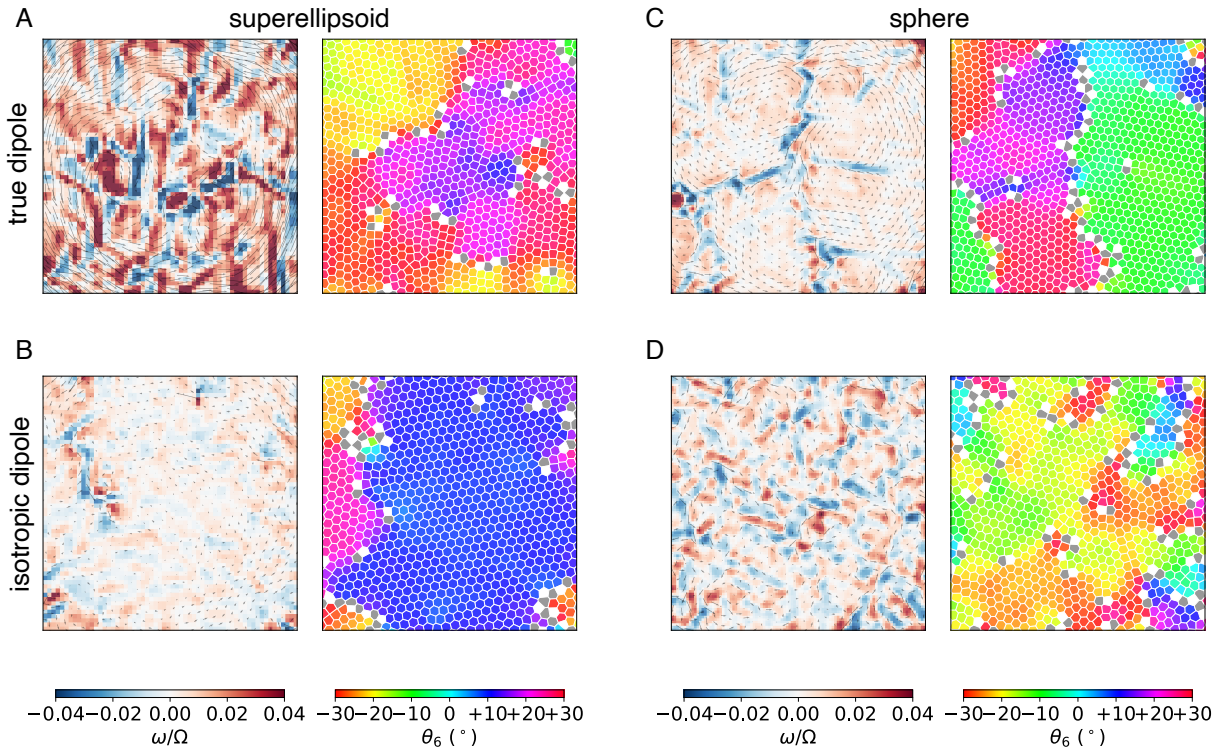

Figure 3.26: **A universal steady-state, independent of particle shape and interactions.** Local crystalline order and vorticity field for steady-state chiral whorl states composed of different particle shapes and interactions: superellipsoidal particles interacting through (A) true magnetic dipoles and (B) isotropically approximated dipoles; spherical particles interacting through (C) true magnetic dipoles and (D) isotropically approximated dipoles. In all cases the crystal breaks in domains at frequency $f = 10\,\mathrm{Hz}$.

average attractive, and repulsive interactions between vertically aligned dipoles. Thus, θ tunes the repulsion between particles, and in turn can be tuned to break up the crystalline phase.

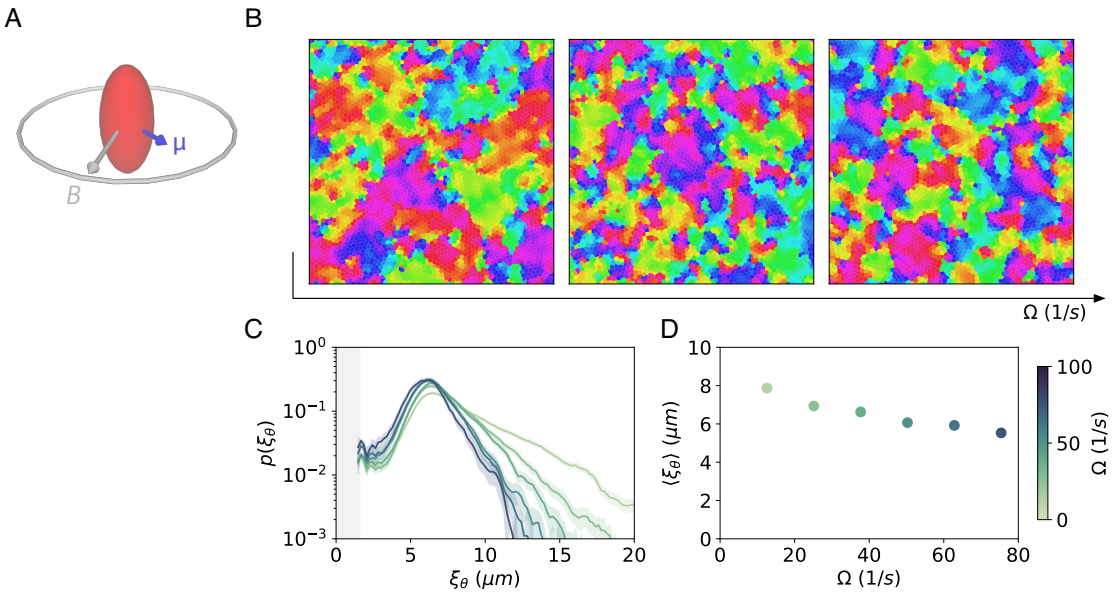

Figure 3.27: **Constructing a spinner crystal from ellipsoidal colloids.** (A) A crystal is constructed from ellipsoidal particles that spin about their long axis. (B) These ellipsoids form a crystalline phase reminiscent of the polycrystalline whorl phase shown in Figure 3.1. (C) By tuning the rotation frequency, the distribution of grains can be altered to yield (D) decreasing average grain sizes.

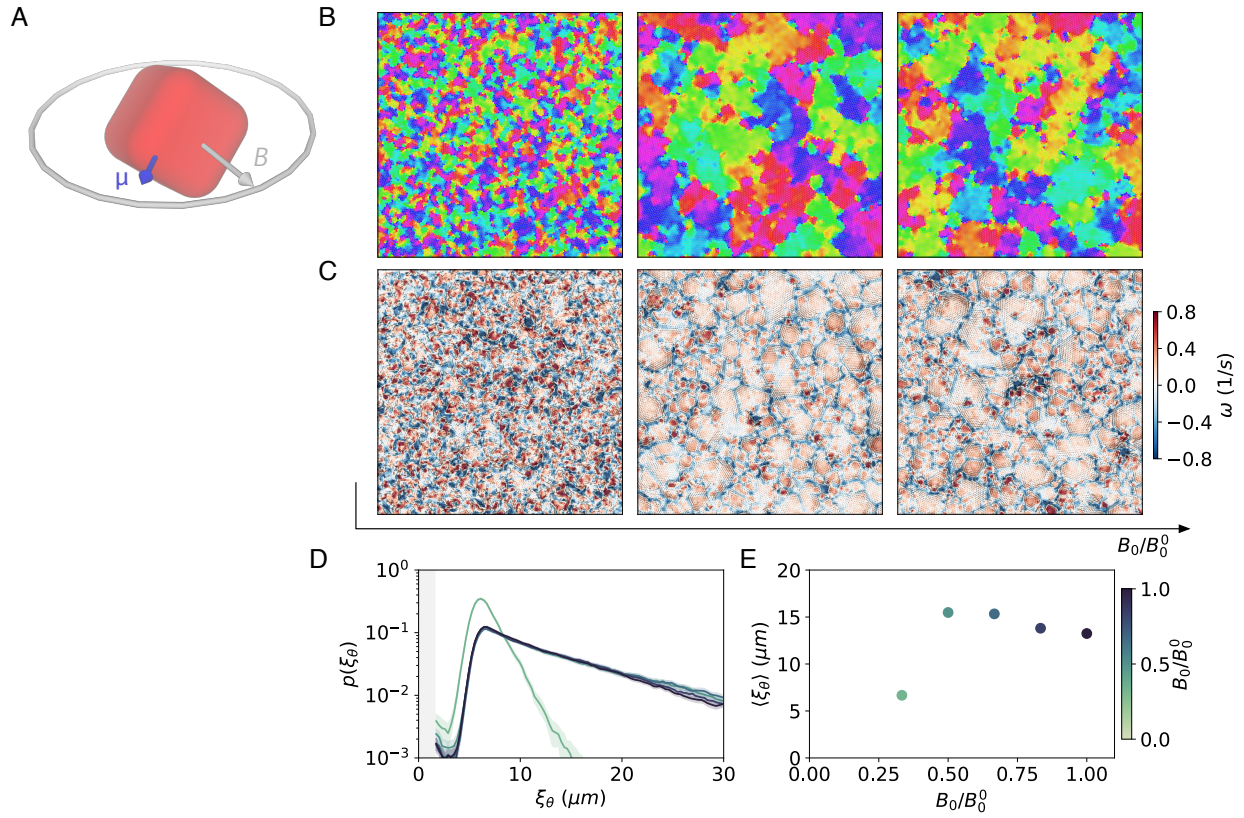

Figure 3.28: **A spinner crystal with inconsistent particle rotation.** (A) Magnetic hematite cubes are rotated with a magnetic field with magnitude B_0, which tuned to a fraction of the value reported elsewhere in this paper, B_0^0. (B) Above a threshold field strength, the polycrystalline whorl phase shown in Figure 3.1 is reproduced. Below this threshold, particle rotation is inconsistent and the whorl phase breaks apart. (C) The same structure is visible in the vorticity field. (D) By tuning B_0/B_0^0, the distribution of grains is not altered above this threshold, which is reflected in (E) constant average grain sizes.

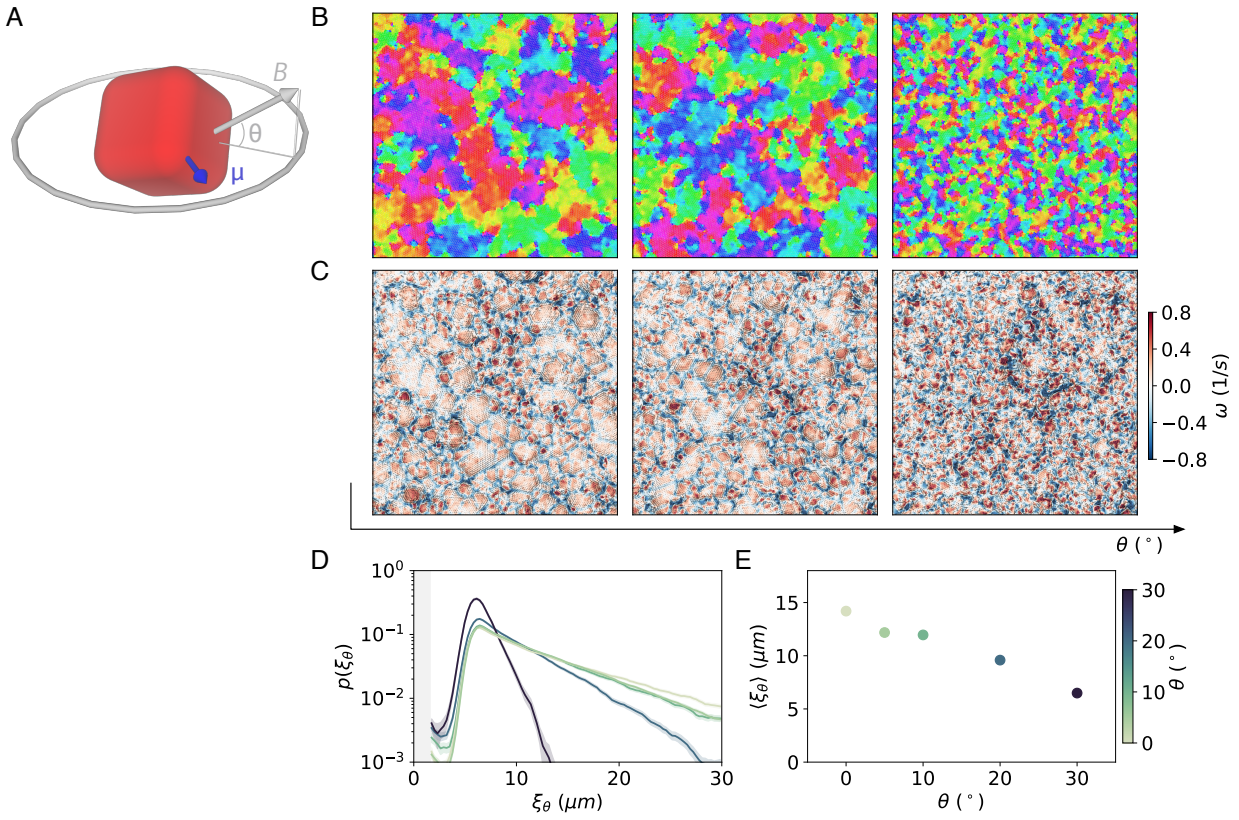

Figure 3.29: **A spinner crystal with repulsive magnetic interactions.** (A) The angle θ is tuned to reduce particle-particle attraction. (B) The polycyrstalline whorl phase is observed until the system becomes sufficiently repulsive. (C) The same structure is visible in the vorticity field. The polycrystal fragments steadily with θ, as seen in (D) the domain size distribution and (E) the average domain size.

3.5 Continuum elastic theory

To gain further insight into the origins of this new state of matter, we adopt a continuum perspective and investigate destabilization mechanisms within this approach. As illustrated in Figure 3.30, the microscopic rotational drive induces transverse interactions between the constituent particles which in turn give rise to active stresses in the crystal phase. To gain an essential insight, we first consider the simplified case of a material in which neighboring particles interact via constant pairwise transverse forces. Figure 3.6, shows how such interactions naturally give rise to a uniform anti-symmetric odd stress [56, 43, 18], as well as all elastic moduli that can arise in an isotropic solid when energy conservation cannot be assumed [10]. As shown in Figure 3.30b-c, the moduli originate geometrically through the changes in perimeter of an infinitesimal material patch. A dilation (b) does not alter the total force on the edge, but increases the perimeter, thereby coupling dilation and rotational stress. Similarly, a shear deformation (c) alternately increases and decreases the length of the edges giving rise to a rotated shear stress (Section 3.5.1.2).

The addition of spatial dependence to the interaction forces (Section 3.5.1.3) makes estimating the moduli more challenging, however it does not alter the basic conclusion that a crystal of spinning particles is a quintessential odd elastic solid. Measuring the deformation field in a collection of nearly-circular, mono-crystalline droplets (Figure 3.30e-f) provides corroborating evidence from experiments and simulations. The droplets rotate at a constant angular velocity that decreases with their radius R. Regardless of the droplet size, they consistently display a radial strain profile that varies from compressive in the center to dilational on the edge. Within an elastic description, this qualitative feature must originate from odd-elastic moduli. A continuum prediction of the strain field (Section 3.5.2.2) confirms this intuition and predicts the shape of the density profile, as illustrated in Figure 3.30d.

In the following sections, we discuss the origins of the elastic response that arises due to transverse forces in Section 3.5.1. Then, to compare with the results shown above, we com-

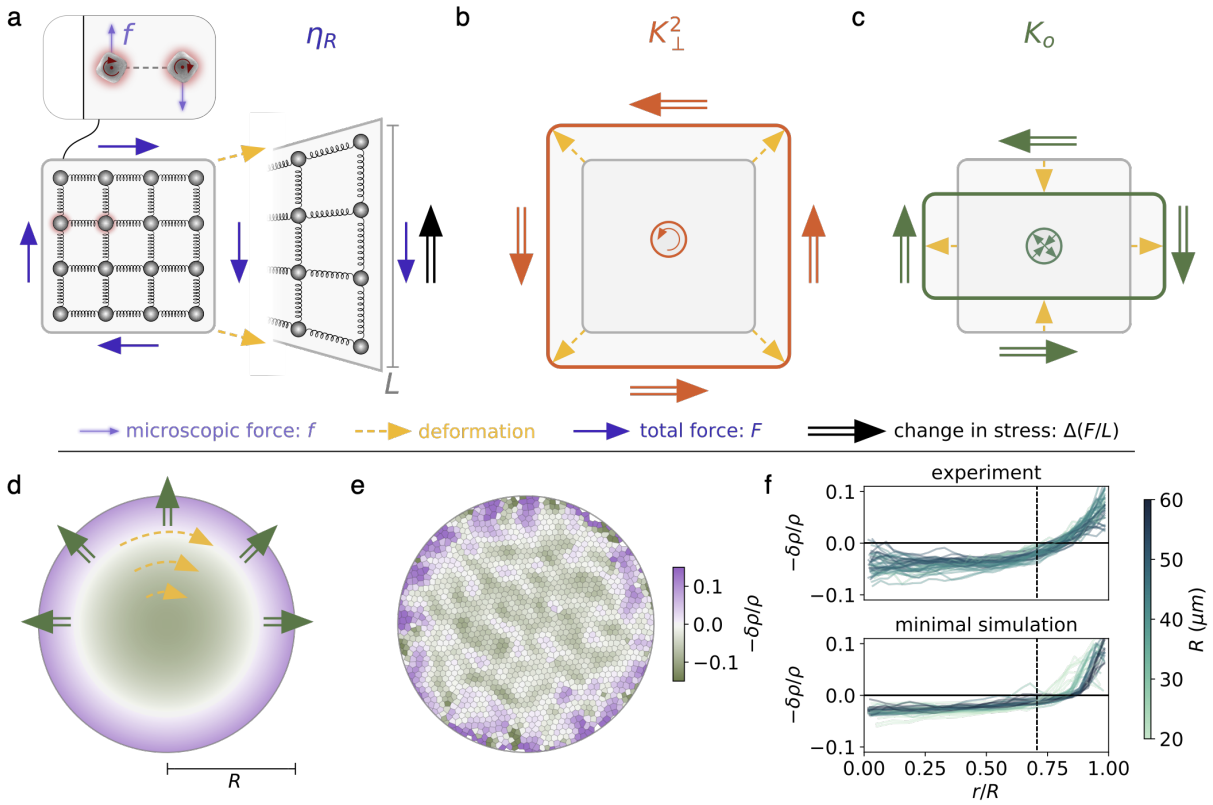

Figure 3.30: **Odd response in the steady-state. a,** A patch of material built of particles that interact with their neighbors via constant, separation-independent transverse forces f parallel to the material's edge sustains a net odd stress $2\eta_R\Omega = nf/L$ on its edge, where n is the number of particles on an edge of length L (see Section 3.5.1.2 for a more general discussion). On each edge, the macroscopic total force $F = nf$ is unchanged upon dilating the edge, but as the length L of the boundary is increased, there is a net change in stress $\Delta(F/L)$ in a direction opposite to the odd stress. **b,** For a uniform dilation, the deformation leads to a net counter-rotational stress. This coupling between dilation and rotation is denoted by $K_\perp^2$ in the elasticity tensor. **c,** Likewise, for a shear deformation, the system acquires a net rotated shear stress, representative of the odd elasticity K_o. **d,** In a droplet of crystalline material, the odd stress induces a net rotation, balanced by friction with the substrate. The naturally occurring azimuthal distortion generates, via the odd elastic moduli, a characteristic radial density dependence (Section 3.5.2.2). **e,** We observe this signature of odd elastic response in experiments on droplets by measuring the dilational component of the strain through the relative density $\delta\rho/\rho$. **f,** In both the experiments and simulations, $\delta\rho/\rho$ transitions radially within a droplet from contracting to dilating in a manner independent of droplet radius R. In both cases, we obtain excellent qualitative agreement with the theoretical prediction for the transition radius, denoted by the dashed line (Section 3.5.2.2).

pute the elastic steady-state for a sheared or rotated odd crystal in Section 3.5.2. We finally measure the elastic strain just as we did in Figure 3.30 for a spring model (Section 3.5.3.1), the experiment (Section 3.5.3.2), and the minimal model simulations (Section 3.5.3.3).

3.5.1 Continuum theory: elasticity in the presence of transverse forces

In this section we discuss the continuum elastic description of crystallites in our system. Works on parity breaking elasticity [10] and viscosity [18, 43, 6, 56] provide a natural framework. In Section 3.5.1.1 we recall the odd elastic description of a linear elastic medium in the absence of energy conservation (we leave the analogous discussion of viscosity for Section 3.6.1.1). In Sections 3.5.1.2-3.5.1.5 we examine approaches to the computation of elastic moduli from microscopic interactions, including constant transverse forces (Section 3.5.1.2), linearized forces restricted to nearest neighbors (Section 3.5.1.3), as well as more general interactions that extend beyond nearest neighbors (Sections 3.5.1.4 and 3.5.1.5). We also show that these coefficients can be numerically estimated by applying a finite strain to a triangular lattice of particles in Section 3.5.1.5.

3.5.1.1 Odd elasticity

As detailed in Ref. [10], the elastic stress-strain relation for isotropic media admits additional 'odd' elastic moduli in the absence of energy conservation. Restricting this analysis to two-dimensional isotropic solids, we recall the fully general elastic stress-strain relation $\sigma_{ij}^{\mathrm{E}} = K_{ijkl}u_{kl}$ for strain tensor $u_{ij} = \partial_i u_j$, of the form:

$$\sigma_{ij}^{\mathrm{E}} = \sigma_{ij}^{\mathrm{b,E}} + \sigma_{ij}^{\mathrm{v,E}} + \sigma_{ij}^{\mathrm{os,E}} + \sigma_{ij}^{\mathrm{o,E}} + \sigma_{ij}^{\perp,\mathrm{E}}, \tag{3.44}$$

which is comprised of the stresses:

$$\sigma_{ij}^{\mathrm{b,E}} = \lambda_0 \delta_{ij} \partial_k u_k, \tag{3.45}$$

$$\sigma_{ij}^{\mathrm{v,E}} = \mu(\partial_i u_j + \partial_j u_i - \delta_{ij} \partial_k u_k), \tag{3.46}$$

$$\sigma_{ij}^{\mathrm{os,E}} = -\mu_R \epsilon_{ij} \epsilon_{kl} \partial_k u_l, \tag{3.47}$$

$$\sigma_{ij}^{\mathrm{o,E}} = K_o \left(\partial_k \epsilon_{ik} u_j + \partial_i \epsilon_{jk} u_k \right), \tag{3.48}$$

$$\sigma^{\perp,\mathrm{E}} = \delta_{ij} K_\perp^1 \epsilon_{kl} \partial_k u_l + K_\perp^2 \epsilon_{ij} \partial_k u_k. \tag{3.49}$$

Using the compact representation of Ref. [10],

$$\begin{pmatrix} \text{⊕} \\ \text{↻} \\ \text{⊕} \\ \text{⊗} \end{pmatrix} = \begin{pmatrix} \lambda_0 & K_\perp^1 & 0 & 0 \\ K_\perp^2 & -\mu_R & 0 & 0 \\ 0 & 0 & \mu & K_o \\ 0 & 0 & -K_o & \mu \end{pmatrix} \begin{pmatrix} \square \\ \diamond \\ \square \\ \parallel \end{pmatrix}. \tag{3.50}$$

λ_0 and μ, are the canonical bulk and shear moduli, and in addition we have a rotational modulus μ_R analogous to the rotational viscosity, the odd elasticity K_o, and the elastic analog to the Magnus viscosities (Section 3.6.1.1), the moduli $K_\perp^{1,2}$ [10].

In addition to the elastic stress there are two constant stresses, namely the pressure $p\delta_{ij}$ and the odd stress $\sigma_{ij}^{\mathrm{spin}}$, discussed in Section 3.6.1.1. These stresses do not contribute to the dynamics inside the bulk, as this dynamic is related to the gradient of the stress, however they do contribute on the edge and near singularities such as dislocations and disclinations. The total stress in light of this correction is

$$\sigma_{ij} = \sigma_{ij}^{\mathrm{E}} - p\delta_{ij} + \sigma_{ij}^{\mathrm{spin}} \tag{3.51}$$

3.5.1.2 Odd moduli as a result of constant transverse force

In Ref [10], the odd elastic moduli arise as a result of spatial variation of the transverse force, and the equilibrium point for the transverse and the longitudinal forces are the same. In a more general case, which is also the case in all the systems under consideration in this work, the transverse force is nonzero at the equilibrium point of the longitudinal force. One feature of such a force, which was not discussed in previous works, is that it alone is enough to produce nonzero odd elasticity K_o and second analogous Magnus elastic modulus $K_\perp^2$.

The emergence of these odd stresses can be explained by a simple geometric argument, pictured in Figure 3.31. The forces on the edge of each Lagrangian element do not change by isotropic deformation. The stresses, however, are defined by the force divided by the length of the edge, therefore, the stresses σ_{ij} have a linear correction for an isotropic infinitesimal deformation of the lattice. When the deformation is not isotropic, this effect still exists, however there may be additional contributions arising as a result of a change in the direction of the force by the deformation. Nevertheless, by examining the direction of the changes that arise only from the change of the length, it is easy to see that both $K_\perp^2$ and K_o arise, as can be seen in the Figure 3.31. The contributions to the odd moduli can be realized by looking at the work done by the odd force when quasistatically moving a single bond along a closed strain cycle. The odd force does work on both angular sides of the cycle, but the work on the outer side is larger because the length of it is longer. See Figure 3.31(D). In the macroscopical description, work done by a strain cycle can only come from the odd moduli ($\delta W = \oint C_{ijmn} u_{ij} du_{mn}$).

Spatially varying microscopic transverse interactions also generally give rise to odd elastic coefficients. Connecting the elastic coefficients to the detailed microscopic interactions can be technically more challenging, as discussed in the following sections.

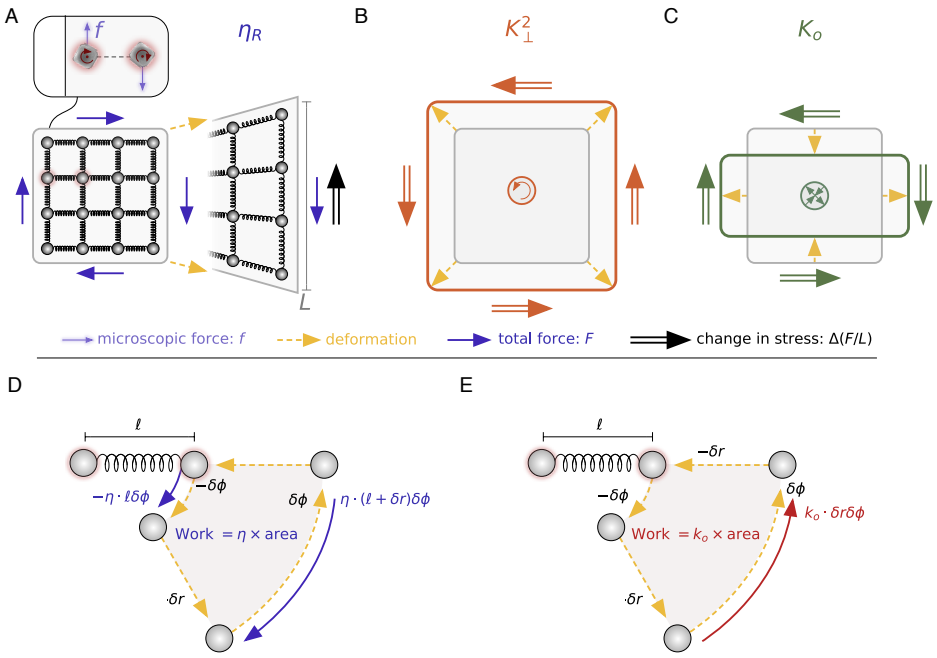

Figure 3.31: **Odd elastic moduli and cycles.** (A) A patch of material built of particles that interact with their neighbors via constant, separation-independent transverse forces f sustains a net odd stress $\sigma^{\text{odd}} = \alpha n f/L$ on its edge, where α is a geometrical factor and n is the number of particles on an edge of length L. On each edge, the macroscopic total force $F = \alpha n f$ is unchanged upon isotropic dilation of the edge, but as the length L of the boundary is increased, there is a net change in stress $\Delta(F/L)$ in a direction opposite to the odd stress. This argument also holds in case of anisotropic deformation, and additional contributions to the change in the stress may rise from changes in the geometrical factor α. (B) For a uniform dilation, the deformation leads to a net counter-rotational stress. This coupling between dilation and rotation is denoted by $K_\perp^2$ in the elasticity tensor. (C) Likewise, for a shear deformation, the system acquires a net orthogonal shear stress, representative of the odd elasticity K_o. (D) We take a bond between two particles that interact purely by odd force on a quasistatic strain cycle. The work done on the inner azimuthal segment is cancelled by the work done on the outer segment, yielding net positive work. (E) One can also obtain work from an odd spring, wherein the work done on the radial segments cancels, but there is again uncompensated work done on the outer azimuthal leg.

3.5.1.3 Odd spring model (nearest-neighbor interactions)

We consider an hexagonal lattice with particles at positions

$$\ell\left(n\sqrt{3}\hat{\mathbf{x}} + m\hat{\mathbf{y}}\right) \text{ and } \ell\left[\left(n+\frac{1}{2}\right)\sqrt{3}\hat{\mathbf{x}} + \left(m+\frac{1}{2}\right)\hat{\mathbf{y}}\right] \tag{3.52}$$

where ℓ is the lattice step and n and m are integers. Following [10] we define an odd spring model, where each vertex is connected to its nearest neighbors by a regular spring (with stiffness k) and an odd spring (of strength k_o) which induces a force in the transverse direction. We also add a constant odd force $\eta\ell$ to this model. Overall, each vertex exerts the following force on a neighbor at distance r and angle θ:

$$\mathbf{F}(r,\theta) = -k\,(r-\ell)\,\hat{\mathbf{r}} + (\eta\ell - k_o\,(r-\ell))\,\hat{\boldsymbol{\theta}}. \tag{3.53}$$

Our goal is to compute the stress tensor of the system $\sigma = (\mathbf{T}^x, \mathbf{T}^y)^T$ where $\mathbf{T}^x$ is the force by unit of length across a cut normal to $\hat{\mathbf{x}}$ (exterted by the right part onto the left one) and $\mathbf{T}^y$ is the force by unit of length across a cut normal to $\hat{\mathbf{y}}$ (exterted by the top part onto the bottom one). As the interactions are only between nearest neighbors, and using the periodicity of the lattice, one finds that

$$\mathbf{T}^x = -\frac{1}{\ell}\left\{\mathbf{F}\left(\ell, \frac{\pi}{6}\right) + \mathbf{F}\left(\ell, -\frac{\pi}{6}\right)\right\} = -\sqrt{3}\eta\hat{\mathbf{y}}, \tag{3.54}$$

$$\mathbf{T}^y = -\frac{1}{\sqrt{3}\ell}\left\{2\mathbf{F}\left(\ell, \frac{\pi}{2}\right) + \mathbf{F}\left(\ell, \frac{\pi}{6}\right) + \mathbf{F}\left(\ell, \frac{5\pi}{6}\right)\right\} = \sqrt{3}\eta\hat{\mathbf{x}}. \tag{3.55}$$

This corresponds to a constant odd stress $\sigma_{ij} = (-\epsilon_{ij})\sigma^{\text{odd}}$ with $\sigma^{\text{odd}} = \sqrt{3}\eta$ in the absence of deformation. We now investigate the four deformation modes: rotation, dilation, pure shear 1 and pure shear 2.

Response to a rotation The unperturbed stress tensor (which is a twice-contravariant tensor) is invariant with respect to rotations. Therefore, there is no response to rotations: $K_1^{\perp} = \mu_r = 0$.

Response to a dilation We consider a dilation of factor $\varepsilon \ll 1$. This corresponds to multiplying all distances by $\alpha = 1 + \varepsilon$ include the unit distances in the x and y directions.

The forces by unit distance become

$$\mathbf{T}^x = -\frac{1}{\alpha\ell}\left\{\mathbf{F}\left(\alpha\ell, \frac{\pi}{6}\right) + \mathbf{F}\left(\alpha\ell, -\frac{\pi}{6}\right)\right\}, \tag{3.56}$$

$$\mathbf{T}^y = -\frac{1}{\sqrt{3}\alpha\ell}\left\{2\mathbf{F}\left(\alpha\ell, \frac{\pi}{2}\right) + \mathbf{F}\left(\alpha\ell, \frac{\pi}{6}\right) + \mathbf{F}\left(\alpha\ell, \frac{5\pi}{6}\right)\right\}. \tag{3.57}$$

Performing the computation at order ε, we find a dilation component ($\mathbf{T}^x \propto \hat{\mathbf{x}}$, $\mathbf{T}^y \propto \hat{\mathbf{y}}$) and an antisymmetric component ($\mathbf{T}^x \propto -\hat{\mathbf{y}}$, $\mathbf{T}^y \propto \hat{\mathbf{x}}$). The dilation is associated with a bulk modulus λ_0 while the antisymmetric components yields a Magnus coefficient $K_\perp^2$:

$$\lambda_0 = \frac{\sqrt{3}}{2}k, \qquad\qquad K_\perp^2 = -\frac{\sqrt{3}}{2}\left[k_o + \eta\right]. \tag{3.58}$$

Response to a shear deformation The first shear mode of deformation with amplitude ε corresponds to a dilation of amplitude ε along the x direction and a compression the same amplitude along the y direction. The polar coordinates are transformed according to

$$(r, \theta) \mapsto (r', \theta') = (r[1 + \varepsilon\cos(2\theta)], \theta - \epsilon\sin(2\theta)).$$

Assuming that $r = \ell$, the force (3.53) transforms as

$$\mathbf{F}(r', \theta') = \eta\ell\hat{\boldsymbol{\theta}} + \varepsilon\left[-k\ell\cos(2\theta) + \eta\ell\sin(2\theta)\right]\hat{\mathbf{r}} - \varepsilon k_o\ell\cos(2\theta)\hat{\boldsymbol{\theta}}. \tag{3.59}$$

We use Eq. (3.54) with a unit length $(1-\varepsilon)\ell$ and Eq. (3.55) with a unit length $(1+\varepsilon)\ell$ and obtain

$$\mathbf{T}^x = -\sqrt{3}\eta(1+\varepsilon)\hat{\mathbf{y}} + \varepsilon\frac{\sqrt{3}}{2}k\hat{\mathbf{x}} + \varepsilon\frac{\sqrt{3}}{2}\left[k_o - \eta\right]\hat{\mathbf{y}}, \tag{3.60}$$

$$\mathbf{T}^y = \sqrt{3}\eta(1-\varepsilon)\hat{\mathbf{x}} - \varepsilon\frac{\sqrt{3}}{2}k\hat{\mathbf{y}} + \varepsilon\frac{\sqrt{3}}{2}\left[k_o - \eta\right]\hat{\mathbf{x}}. \tag{3.61}$$

The stress tensor has a shear 1 components ($\mathbf{T}^x \propto \hat{\mathbf{x}}$, $\mathbf{T}^y \propto -\hat{\mathbf{y}}$) associated with a shear modulus μ, and a shear 2 component ($\mathbf{T}^x \propto \hat{\mathbf{y}}$, $\mathbf{T}^y \propto \hat{\mathbf{x}}$) associated with an odd elastic coefficient K_o. These two coefficients read

$$\mu = \frac{\sqrt{3}}{4}k, \qquad\qquad K_o = \frac{\sqrt{3}}{4}\left[3\eta - k_o\right]. \tag{3.62}$$

One now needs to check that the response to a deformation along the second pure shear mode is consistent with the values of μ and K_o found for the first pure shear mode. This can be done explicitly by realizing that the cuts along / across the crystal axes are no longer normal to $\hat{\mathbf{x}}$ and $\hat{\mathbf{y}}$. The new normal vectors are $\hat{\mathbf{x}}' = \begin{pmatrix} \cos\varepsilon \\ -\sin\varepsilon \end{pmatrix}$ and $\hat{\mathbf{y}}' = \begin{pmatrix} -\sin\varepsilon \\ \cos\varepsilon \end{pmatrix}$ where ε is the amplitude of the shear mode. The unit lengths normal to these vectors are not modified (ℓ and $\sqrt{3}\ell$). At linear order $\mathbf{T}^x = \mathbf{T}^{x'} + \varepsilon\mathbf{T}^{y'}$ and $\mathbf{T}^y = \mathbf{T}^{y'} + \varepsilon\mathbf{T}^{x'}$. One indeed finds a pure shear stress 2 and a pure shear stress 1 consistent with the values of μ and K_o written above. Last, one checks that the stress tensor resulting for shear deformations is independent of the orientation of the lattice.

In conclusion, we have recovered the structure of Eq. (3.50) from the microscopic details of the odd-elastic springs on an hexagonal lattice. The explicit values of the coefficients are given above. We note that there is an additional constant odd stress due to the non-vanishing transverse force applied at a distance of a lattice spacing.

3.5.1.4 Beyond nearest-neighbors interactions

In the previous subsection, we investigated the elastic response of an hexagonal lattice with nearest-neighbors interactions only. A natural question is what happens if we allow for the particles to interact at an arbitrary distance. We now consider generic interaction forces

with isotropic radial and transverse components

$$\mathbf{F}(r,\theta) = f_{\rm rad}(r)\hat{\mathbf{r}} + f_{\rm trans}(r)\hat{\theta}. \tag{3.63}$$

We consider successive shells of nearest neighbors and next-nearest neighbors in the lattice defined by Eq. (3.52). We index these shells by $p = 1, 2, \ldots$. The corresponding distances are

$$\ell_1 = \ell, \qquad \ell_2 = \sqrt{3}\ell, \qquad \ell_3 = 2\ell, \qquad \ell_4 = \sqrt{7}\ell, \qquad \ell_5 = 3\ell. \tag{3.64}$$

The computation of $\mathbf{T}^x$ can be done similarly to Eq. (3.54). The successive shells involve a summation over n_p interactions between the right and the left parts of the system: $n_1 = 2, n_2 = 4, n_3 = 4, n_4 = 12, n_5 = 6$. The crucial parameter is the sum of the projections of the vectors on the x axis,

$$\alpha_p = \sum_{k \in S_p} \cos\theta_k \tag{3.65}$$

where S_p is shell p and θ_k is the angle of the vector with the x axis. The lowest orders are

$$\alpha_1 = \sqrt{3}, \qquad \alpha_2 = 3, \qquad \alpha_3 = 2\sqrt{3}, \qquad \alpha_4 = 14\sqrt{\frac{3}{7}}, \qquad \alpha_5 = 3\sqrt{3}. \tag{3.66}$$

The computation with a force given by Eq. (3.63) leads to the following even elastic coefficients

$$\sigma_{\rm pressure} = -\frac{1}{\ell}\sum_{p\geq 1} \alpha_p f_{\rm rad}(\ell_p), \tag{3.67}$$

$$\lambda_0 = -\frac{1}{2\ell}\sum_{p\geq 1} \alpha_p \left[\ell_p f'_{\rm rad}(\ell_p) - f_{\rm rad}(\ell_p)\right], \tag{3.68}$$

$$\mu = -\frac{1}{4\ell}\sum_{p\geq 1} \alpha_p \left[\ell_p f'_{\rm rad}(\ell_p) + 3 f_{\rm rad}(\ell_p)\right] \tag{3.69}$$

where σ_{pressure} is a constant pressure term. The odd-elastic coefficients are

$$\sigma^{\text{odd}} = \frac{1}{\ell} \sum_{p \geq 1} \alpha_p f_{\text{trans}}(\ell_p), \tag{3.70}$$

$$K_{\perp}^2 = \frac{1}{2\ell} \sum_{p \geq 1} \alpha_p \left[\ell_p f'_{\text{trans}}(\ell_p) - f_{\text{trans}}(\ell_p) \right], \tag{3.71}$$

$$K^o = \frac{1}{4\ell} \sum_{p \geq 1} \alpha_p \left[\ell_p f'_{\text{trans}}(\ell_p) + 3 f_{\text{trans}}(\ell_p) \right]. \tag{3.72}$$

The nearest-neighbors computation of the previous section corresponds to $p = 1$ only.

The key point is that while the full summation over interactions in the crystal is not tractable analytically, the structure of Eq. (3.50) extends to higher orders of next nearest neighbors. The radial interaction forces give rise to even elastic coefficients (only) while the transverse forces induce odd elasticity.

3.5.1.5 Numerical estimates of elastic moduli

In this section we examine the computation of elastic moduli numerically. We first compare our results using this method to the prediction of moduli in spring networks and subsequently apply this approach to the computation of the elastic moduli in the minimal model simulations.

Estimating elastic coefficients by finite strain The elastic coefficients in the stress-strain relation can, alternatively, be estimated numerically by constructing a finite size lattice and applying a specific strain (i.e. ). Measuring the forces on the boundary of the patch and dividing by the length of the boundary, we can then extract the stresses (i.e. ). By gradually increasing the magnitude of the applied strain from zero, we verify the linear relationship between stresses and strains and deduce each of the entries in Eq. 3.50 from the slope. This procedure is illustrated in Figure 3.32 for the specific case of measuring K_o from applying a shear deformation.

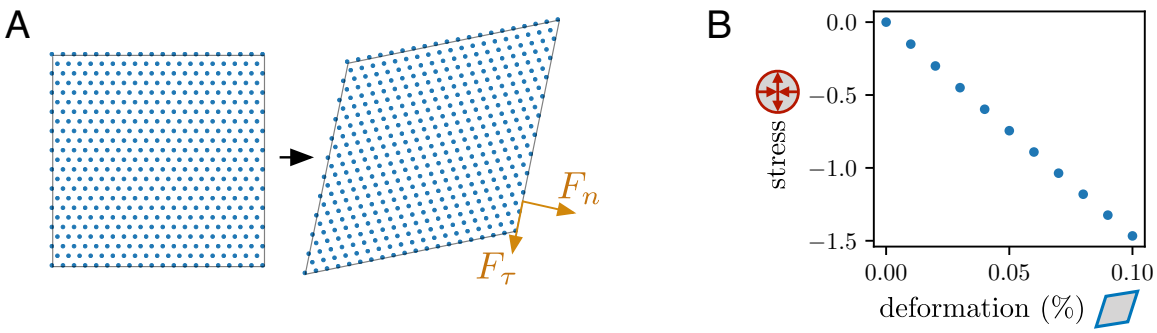

Figure 3.32: **Measuring elastic coefficients.** (A) A cartoon representation of a strain ( ) being applied to a lattice, from which the normal and tangential forces on its boundary are measured. (B) The resulting relationship between the strain ( ) and stress ( ), as computed from these forces, can be fit to a line with a slope that estimates the odd elasticity K_o.

Spring simulations To test this numerical approach, we apply it to a network of springs (see Section 3.5.3.1) and compare the result to that obtained from the analytical coarse-graining procedure presented above. The results are shown in Table 3.2. We find that the

modulus	Analytical Value	16 particles on edge	20 particle on edge
σ^{odd}	0.1732	0.1764 (1.0185)	0.1758 (1.015)
λ_0	0.4330	0.4410 (1.0185)	0.4395 (1.015)
μ	0.2165	0.2205 (1.018)	0.2198 (1.015)
K_o	-0.0866	-0.0882 (1.0183)	-0.0879 (1.015)
$K_\perp^2$	-0.5196	-0.5292 (1.0185)	-0.5275 (1.015)

Table 3.2: **Elastic moduli in an odd spring network.** Result of the numerical evaluation of the elastic moduli and the analytical value from coarse-graining. In brackets - the ratio between the numerical result and the analytical value. $k = k_o = 0.5, \eta = 0.1$.

numerical approach is in excellent agreement, with all moduli within 2% of the analytical value.

Minimal molecular dynamics simulations In this section we compute the elastic coefficients of our minimal simulational model.

Because the longitudinal forces in this model are both long ranged (magnetic attraction) and nonlinear (WCA), the estimation of elastic coefficients is challenging. In particular the

estimated coefficients depend critically on the assumed lattice density.

We therefore apply our numerical method on the initial state of our lattices, as well as in a state obtained by relaxing the lattice via the longitudinal forces alone. In the initial state the particles repel each other, and the lattice will have a nonzero pressure. The results for the elastic moduli in the initial condition where the lattice spacing is 1σ are (All values are in natural HOOMD units):

$$\begin{aligned} \lambda &= 11000 \\ \mu &= 5200 \\ K_\perp^2 &= -330\frac{\Omega}{\Omega_0} \\ K_o &= -70\frac{\Omega}{\Omega_0} \\ \sigma^{\text{odd}} &= 95\frac{\Omega}{\Omega_0} \\ p &= 285 \end{aligned} \tag{3.73}$$

The constant pressure in the lattice allows the lattice to expand if the boundary conditions do not limit this expansion. If this expansion is allowed it will be carried until the lattice spacing is 1.015σ, at this point the pressure of the lattice is zero. Because of the nonlinearity of the microscopical forces, the elastic moduli in this point are different:

$$\begin{aligned} \lambda &= 8000 \\ \mu &= 4000 \\ K_\perp^2 &= -310\frac{\Omega}{\Omega_0} \\ K_o &= -70\frac{\Omega}{\Omega_0} \\ \sigma^{\text{odd}} &= 85\frac{\Omega}{\Omega_0} \\ p &= 0 \end{aligned} \tag{3.74}$$

Note that the the bulk moduli changed by $\sim$20% as a result of 1% change in the lattice

spacing.

3.5.2 Continuum theory: elastic steady-state

When the strain rates are low, the spinner crystal phase can be treated as an elastic solid with negligible viscous stresses. In this section, we discuss special cases in which this assumption holds, namely: a stable semi-infinite slab in which no defects are created (Section 3.5.2.1), a small stable droplet driven at low particle rotation frequencies (Section 3.5.2.2), and a perfect crystal with a single dislocation that is self-propelled by odd stress (Section 3.5.2.3).

3.5.2.1 Semi-infinite slab symmetry

Assume that we are looking on an infinite or periodic slab in the x direction, with an edge in $y = c$, for some constant c. In the steady-state, the total force on each solid element is zero, this gives inside the bulk:

$$F_x = \partial_x \sigma_{xx} + \partial_y \sigma_{xy} = 0 \tag{3.75}$$

$$F_y = \partial_x \sigma_{yx} + \partial_y \sigma_{yy} = 0 \tag{3.76}$$

Additionally, the symmetry in the x direction dictates:

$$\forall i : \partial_x \sigma_{ix} = 0 \tag{3.77}$$

This set of equations shows that σ_{yy} and σ_{xy} are uniform across the system. This symmetry also forces $\epsilon_{xy} = \partial_x u_y = 0$. In general, slab symmetry does not force $\epsilon_{xx} = \sigma_x u_x = 0$, as a uniform stretch in the x direction is possible, this kind of stretch will show itself as a $\epsilon_{xx} = \alpha$

across the system. The boundary conditions on the edge give:

$$-(\sigma \cdot \hat{y}) \cdot \hat{y}\Big|_{y=c} = \sigma_{yy}\Big|_{y=c} = -p_0, \tag{3.78}$$

$$-(\sigma \cdot \hat{y}) \cdot \hat{x}\Big|_{y=c} = -\sigma_{xy}\Big|_{y=c} = 0. \tag{3.79}$$

Where p_0 is the external pressure, which can be taken to be 0. These variables are uniform across the bulk. Now we can use Eq. (3.49) to get:

$$\sigma_{yy} = \lambda(\epsilon_{yy} + \alpha) + \mu(\epsilon_{yy} - \alpha) - K_o\epsilon_{yx} - p = 0 \tag{3.80}$$

$$\sigma_{xy} = K_\perp^2(\epsilon_{yy} + \alpha) + \mu\epsilon_{yx} + K_o(\epsilon_{yy} - \alpha) + \sigma^{\text{odd}} = 0$$

These equations force $\epsilon_{yx} = \beta$ and $\epsilon_{yy} = \gamma$ to be uniform.

If we now consider a case where the boundary conditions in the x direction are periodic, and not fully infinite, a uniform stretch in the x direction is no longer possible so $\alpha = 0$. We get:

$$\boldsymbol{u}(\boldsymbol{r}) = \beta y\hat{x} + \gamma y\hat{y} \tag{3.81}$$

This is the sum of uniaxial stretch and simple shear, as these are the only two strains allowed by the symmetry. Equation (3.80) gets the form:

$$\begin{pmatrix} -K_o & \lambda + \mu \\ \mu & K_o + K_\perp^2 \end{pmatrix} \begin{pmatrix} \beta \\ \gamma \end{pmatrix} = \begin{pmatrix} p \\ -\sigma^{\text{odd}} \end{pmatrix}, \tag{3.82}$$

The solution is:

$$\beta = -\frac{\sigma^{\text{odd}}(\lambda + \mu) + p(K_\perp^2 + K_o)}{\mu(\lambda + \mu) + K_o(K_\perp^2 + K_o)} \tag{3.83}$$

$$\gamma = \frac{-\sigma^{\text{odd}}K_o + \mu p}{\mu(\lambda + \mu) + K_o(K_\perp^2 + K_o)}$$

And for a linear system with triangular lattice and nearest neighbor interactions (discussed in Section 3.5.3.1) we get:

$$\beta = -\frac{4k \cdot \eta}{k^2 + k_o^2 - 10/3 k_o \eta + \eta^2} \tag{3.84}$$
$$\gamma = \frac{4\eta \left[k_o - 3\eta\right]}{3\left(k^2 + k_o^2 - 10/3 k_o \eta + \eta^2\right)}$$

Note that γ can change sign by changing the ratio between the odd spring constant and the constant odd force.

3.5.2.2 Droplet symmetry

Next, we analyze the case for a circular droplet. We assume that the deformation $\boldsymbol{u} = u_r(r)\hat{r} + u_\theta(r)\hat{\theta}$ is not a function of θ. We start by writing the stress strain relations in polar coordinates.

$$\sigma_{rr} = -K_o r \partial_r(u_\theta/r) + \lambda \frac{1}{r}\partial_r(r u_r) + \mu \partial_r u_r - \mu \frac{u_r}{r} - p, \tag{3.85}$$
$$\sigma_{r\theta} = K_o r \partial_r(u_r/r) + K_\perp^2 \frac{1}{r}\partial_r(r u_r) + \mu r \partial_r(u_\theta/r) - \sigma^{\text{odd}}, \tag{3.86}$$
$$\sigma_{\theta r} = K_o r \partial_r(u_r/r) - K_\perp^2 \frac{1}{r}\partial_r(r u_r) + \mu r \partial_r(u_\theta/r) + \sigma^{\text{odd}}, \tag{3.87}$$
$$\sigma_{\theta\theta} = K_o r \partial_r(u_\theta/r) + \lambda \frac{1}{r}\partial_r(r u_r) - \mu \partial_r u_r + \mu \frac{u_r}{r} - p. \tag{3.88}$$

We now look for a solution where the droplet rotates as a rigid body in angular frequency Ω_{rb}. The substrate friction applies force in the theta direction, this force is $\boldsymbol{F} = -\Omega_{rb} r \Gamma \hat{\theta}$. Including this force we get for the force balance equation:

$$\partial_r \sigma_{rr} + \frac{1}{r}\sigma_{rr} - \frac{1}{r}\sigma_{\theta\theta} = 0, \tag{3.89}$$
$$\partial_r \sigma_{\theta r} + \frac{1}{r}(\sigma_{r\theta} + \sigma_{\theta r}) - \Gamma \Omega_{rb} r = 0 \tag{3.90}$$

In addition, the stress boundary conditions can be expanded into the pair of boundary equations

$$-K_o r\partial_r(u_\theta/r)\Big|_{\bar{R}} + \lambda\frac{1}{r}\partial_r(ru_r)\Big|_{\bar{R}} + \mu\partial_r u_r\Big|_{\bar{R}} - \mu\frac{u_r(\bar{R})}{\bar{R}} - p(\bar{R}) = \frac{\gamma}{\bar{R}}, \tag{3.91}$$

$$K_o r\partial_r(u_r/r)\Big|_{\bar{R}} - K_\perp^2\frac{1}{r}\partial_r(ru_r)\Big|_{\bar{R}} + \mu r\partial_r(u_\theta/r)\Big|_{\bar{R}} + \sigma^{\text{odd}} = 0. \tag{3.92}$$

Where $\bar{R}$ is the radius of the droplet. The solution is

$$\begin{aligned}
\Omega_{rb} &= \frac{4}{\Gamma\bar{R}^2}\left[\sigma^{\text{odd}} - \frac{K_\perp^2(p+\gamma/\bar{R})}{\lambda}\right], \\
A &= \frac{\Gamma\Omega_{rb}}{\mu(\lambda+\mu) + K_o(K_o+K_\perp^2)}, \\
u_r &= -\frac{AK_o}{8}\left(r^3 - r\bar{R}^2\right) + \frac{p+\gamma/\bar{R}}{2\lambda}\, r, \\
u_\theta &= \frac{A(\mu+\lambda)r^3}{8}.
\end{aligned} \tag{3.93}$$

The main signature of this solution is the non-trivial dependence between the radial deformation and the radius, which only appears when there is odd elasticity.

3.5.2.3 Self-propelled dislocation

One other consequence of the odd elastic response of our system is the motility of dislocations, discussed previously in Section 3.3. Here, we present an argument based on odd stress that predicts these dynamics.

Peach-Koehler forces We consider a dislocation with Burgers vector $\boldsymbol{b}$ located at the origin and show that under the action of odd stress, a dislocation glide results in an elastic energy gain. This change in the elastic energy is what defines the so-called Peach-Koehler force powering dislocation dynamics.

For any counterclockwise contour γ around the dislocation

$$\oint_\gamma du_j = \oint_\gamma u_{ij} dx_i = b_j, \tag{3.94}$$

where $u_{ij} = \partial_i u_j$. We therefore define the displacement $\mathbf{u}(\mathbf{r})$ as a single-valued field everywhere in space but along a semi-infinite branch cut $\mathcal{L}$ starting from the origin. The singularity in the deformation tensor then reads

$$u_{ij}^{\text{sing}}(\mathbf{r}) = -\hat{n}_i b_j \mathbb{1}(\mathbf{r} \in \mathcal{L}) \tag{3.95}$$

where $\hat{\mathbf{n}}$ is the unit vector normal to $\mathcal{L}$, and $\mathbb{1}$ denotes a Dirac delta function localized on $\mathcal{L}$.

We can now compute the work δW associated to the translation of the dislocation along a vector $\delta\mathbf{r}$. By definition, δW is the work done by the bulk forces $-\partial_i \sigma_{ij}$ and the surface forces $\hat{n}_i \sigma_{ij}$,

$$\delta W = \int_S \left(-\partial_i \sigma_{ij}\right) \delta u_j dS + \int_{\delta S} \hat{n}_i \sigma_{ij} \delta u_j d\ell = \int_S \sigma_{ij} \delta u_{ij} = \int_S \sigma_{ij}^{\text{ext}} \delta u_{ij}, \tag{3.96}$$

where σ^{ext} is the external contribution to the stress tensor, viz the stress which is not generated by elastic deformations induced by the dislocation itself.

The problem then reduces to the determination of the variation of the deformations δu_{ij} induced by the constraint (3.95). We are free to choose the orientation of the discontinuity line $\mathcal{L}$. We then conveniently choose it to be aligned with displacement vector: $\mathcal{L} = \{y \frac{\delta\mathbf{r}}{\|\delta\mathbf{r}\|}, y \in [0, \infty)\}$. The coordinates of the normal vector are

$$\hat{n}_i = \epsilon_{ki} \frac{\delta r_k}{\|\delta\mathbf{r}\|} \tag{3.97}$$

where ϵ is the Levi-Civita symbol. We also define the line $\mathcal{L}' = \{y \frac{\delta\mathbf{r}}{\|\delta\mathbf{r}\|}, y \in [\|\delta\mathbf{r}\|, \infty)\}$ which corresponds to the discontinuity of the translated dislocation. From Eq. (3.95), the variation

of deformation due to the topological singularity is given by

$$\delta u_{ij}^{\text{sing}}(\mathbf{r}) = -\hat{n}_i b_j \left[\mathbb{1}(\mathbf{r} \in \mathcal{L}') - \mathbb{1}(\mathbf{r} \in \mathcal{L})\right] = \hat{n}_i b_j \|\delta\mathbf{r}\| \delta(\mathbf{r}) = b_j \epsilon_{ki} \delta r_k \delta(\mathbf{r}), \tag{3.98}$$

where $\delta(\mathbf{r})$ is the 2D Dirac delta function. We can then compute the work done by the external stress due to existence of a topological singularity using Eqs. (3.96) and (3.98). We find

$$\delta W = \epsilon_{ki} \sigma_{ij}^{\text{ext}}(0) b_j \delta r_k \tag{3.99}$$

where we emphasized that the stress tensor is evaluated at the position of the dislocation. This mechanical work defines the so-called Peach-Koehler force $\mathbf{F}^{\text{PK}}$ as $\delta W = \mathbf{F}^{\text{PK}} \cdot \delta\mathbf{r}$. It takes the compact form

$$F_k^{\text{PK}} = \epsilon_{ki} \sigma_{ij}^{\text{ext}}(0) b_j. \tag{3.100}$$

Impact of odd elasticity and odd stress on Peach-Koehler forces We now consider a dislocation of Burgers vector $\boldsymbol{b} = b\hat{\mathbf{e}_x}$ in a generic chiral elastic crystal with finite even elasticity (λ_0 and μ), odd elasticity ($K_\perp^2$ and K_o) and driven by a constant odd stress $\sigma_{ij}^{\text{spin}} = 2\eta_R \Omega \epsilon_{ij}$. The full stress tensor then reads

$$\sigma_{ij} = \sigma_{ij}^{\text{disloc,even}} + \sigma_{ij}^{\text{disloc,odd}} - 2\eta_R \Omega \epsilon_{ij}. \tag{3.101}$$

The expression of the stresses are in Ref. [17]. In polar coordinates, they are given by

$$\sigma^{\text{disloc,even}}(r,\theta) = \frac{(1-\nu) b \lambda_0}{2\pi r} \begin{pmatrix} -\sin\theta - \cos\theta \sin(2\theta) & \cos\theta\cos(2\theta) \\ \cos\theta\cos(2\theta) & -\sin\theta + \cos\theta\sin(2\theta) \end{pmatrix} \tag{3.102}$$

$$\sigma^{\text{disloc,odd}}(r,\theta) = \frac{(1-\nu) b K_\perp^2}{2\pi r} \begin{pmatrix} \cos\theta\cos(2\theta) & \sin\theta + \cos\theta\sin(2\theta) \\ -\sin\theta + \cos\theta\sin(2\theta) & -\cos\theta\cos(2\theta) \end{pmatrix}. \tag{3.103}$$

The Poisson ratio is

$$\nu = \frac{\mu(\lambda_0 - \mu) + K_o(K_\perp^2 - K_o)}{\mu(\lambda_0 + \mu) + K_o(K_\perp^2 + K_o)}. \tag{3.104}$$

Let us first discuss the status of odd elastic effects with respect to the Peach-Koehler formula (3.100). Firstly, we note that an odd elastic solid enjoys a mechanical equilibrium state when an isolated dislocation perturbs the rest configuration of the crystal. Secondly, considering a dislocation in an even elastic solid and adding odd elasticity perturbatively, one can readily check that the odd elastic stress integrated around the dislocation core vanishes. This implies that there is no far-field energy gain, or loss, associated with dislocation motion. Generically, odd elasticity does not contribute to the Peach-Koehler forces and to dislocation motion in chiral crystals.

In contrast, the odd stress plays a prominent role in dislocation dynamics. This can be seen using the Peach-Koehler formula (3.100). A constant odd stress results in an effective force

$$\mathbf{F}^{\mathrm{PK}} = 2\eta_R \Omega \boldsymbol{b} \tag{3.105}$$

which effectively drives the gliding motion of dislocations. Simply put, odd elasticity changes the elastic deformation pattern around a dislocation leaving its position unchanged while odd stress powers the dislocation dynamics.

3.5.3 Elastic strain field in a crystal

Now, equipped with an elastic theory describing the strains experienced by odd crystalline lattices in the slab (Section 2.4.1.2) and circular droplet (Section 2.4.1.3) geometries, we can make comparisons with our simulations and experiments.

3.5.3.1 Elastic strain in spring-and-ball network simulations

First, a network of particles that interact with their neighbors via linear forces, both along and transverse to the bond that joins them, provides an ideal setting to compare predictions of linear elasticity with force-balanced configurations. As discussed in Section 3.5.1.3, the linearity and locality of the spring interactions ensures that the macroscopic elastic coefficients can be accurately obtained by coarse-graining the microscopic interactions. The predictions of linear elasticity can then be easily compared to the observed steady-state simulation results.

Simulation protocol We initialize our simulations by creating a triangular lattice, with either periodic boundary conditions or open, stress-free boundary conditions. The connectivity of the lattice is fixed throughout the simulation. In some simulations, we add small amount of noise to the location of each particle. The magnitude of the displacement for each particle is a random number taken from Gaussian distribution, and the angle is a uniformly random number between 0 and π. We consider three geometries: a circular domain, a rectangular lattice with periodic boundary conditions in one direction only, and a square domain with periodic boundary conditions in both directions. A typical lattice contains up to $\sim 10,000$ particles.

The interaction between each pair of connected particle is taken to be:

$$\mathrm{F}_{ij} = -k\left(r_{ij} - \ell\right)\hat{r}_{ij} + \left(\eta\ell - k_o\left(r_{ij} - \ell\right)\right)\hat{\theta}_{ij} \tag{3.106}$$

Where ℓ is the lattice spacing, $\eta\ell$ is a constant odd force, k is the regular spring stiffness, k_o is the odd spring stiffness, r_{ij} is the distance between the particles, $\hat{r}_{ij}$ is the unit vector between them, and θ_{ij} is the unit vector perpendicular to it.

We simulate this system in the overdamped limit, such that for each particle: $\boldsymbol{F}_{\text{total}}^{\text{interaction}} = \Gamma\boldsymbol{v}$. The system is then integrated using a GPU implementation of fourth order Dormand-

Prince integrator, where the step size is chosen such that the sum of the absolute value of the truncation errors is lower than 10^{-6}.

Force-balanced configurations, comparison with linear elastic predictions In this section we consider a circular disk geometry and a rectangular slab with periodic boundary conditions in the x-direction. We run each simulation until force-balance is achieved and the elastic strains cease to evolve. The system then either rotates as a rigid body at a constant angular velocity (droplet geometry) or is static (rectangular semi-periodic geometry).

Semi-infinite slab symmetry The force-balanced configuration of a rectangular slab with periodic boundary condition in the x-axis is shown in Figure 3.33. In red we show half of the lattice in its original triangular configuration, in blue we show the other half of the lattice in its static strained configuration. The straight lines in the figure show that the strain field is uniform. The steady configuration can be expanded (a) or compressed (b) by changing the parameters of the transverse force.

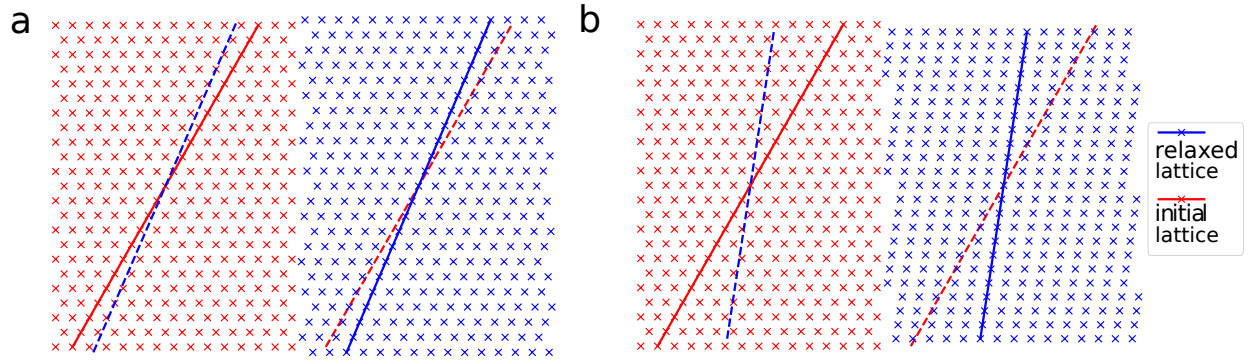

Figure 3.33: **Slab symmetry deformation.** The structure of the slab symmetry lattice in the initial state (red) and after being strained as a result of the odd stress (blue) for parameters (a) $k = k_o = 0.5, \eta = 0.03$. and (b) $k = 0.5, k_o = 0.1, \eta = 0.05$

Figure 3.34 shows a comparison of the observed strain with the continuum elastic prediction made in Section 3.5.1 using the coarse grained elastic coefficients discussed in Section 3.5.1.3. We obtain excellent agreement between the analytical predictions and the

simulation results when the strains rates are less than ∼7%. As expected, for high strains the linear elastic prediction begins to deviate from the observed strains. This excellent

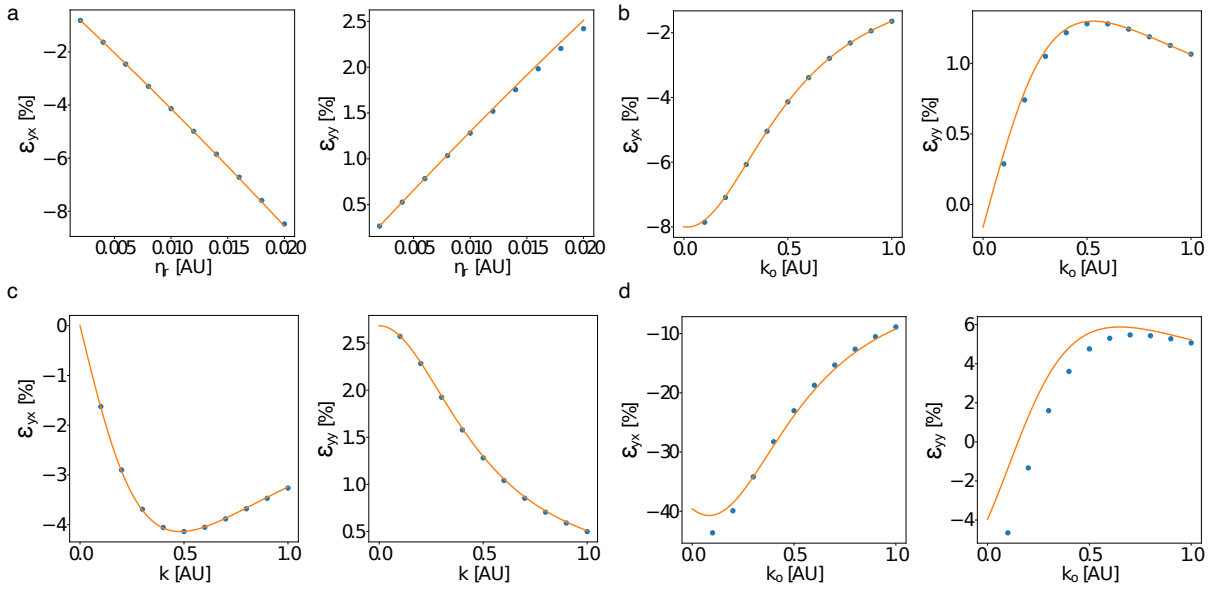

Figure 3.34: **Verification of the elastic solution for slab symmetry.** (a) Strains vs. η for $k = k_o = 0.5$. (b) Strains vs. k_o for $k = 0.5; \eta = 0.01$. (c) Strains vs k for $k_o = 0.5; \eta = 0.01$. (d) Strains vs. k_o for $k = 0.5; \eta = 0.05$. In all plots, simulation results are denoted by blue points and theoretical predictions by orange lines.

agreement confirms the validity of the use of linear elasticity in predicting force-balanced configurations of networks interacting via linear transverse forces, extending the predictions of Ref [10] to include constant transverse forces.

Droplet symmetry The force-balanced configuration of a circular disk is shown in Figure 3.35. The configuration rotates with a constant angular velocity.

Figure 3.36 shows a comparison of the observed strain with the continuum elastic prediction made in Section 3.5.1 using the coarse grained elastic coefficients discussed in Section 3.5.1.3. As before, excellent agreement between the analytical predictions and the simulation can be seen. This agreement confirms the validity of the use of linear elasticity in predicting force-balanced configurations of networks interacting via linear transverse forces,

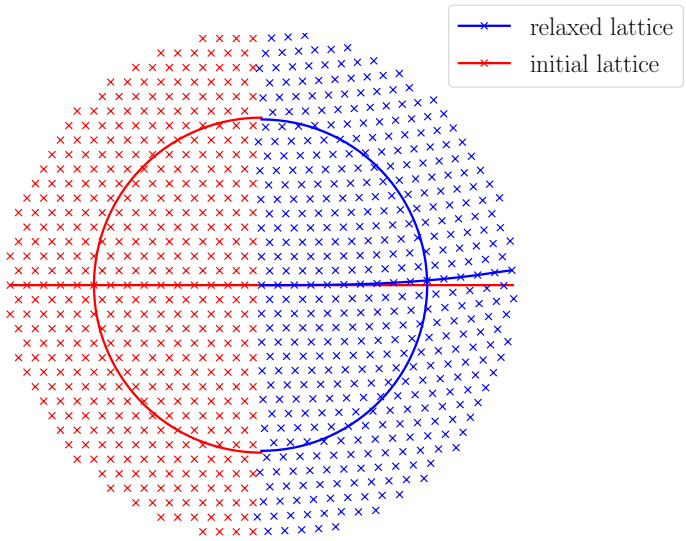

Figure 3.35: **Droplet deformation.** Structure of droplet lattice in the initial configuration (red) and in the stable configuration (blue). The stable configuration rotates as a rigid body.

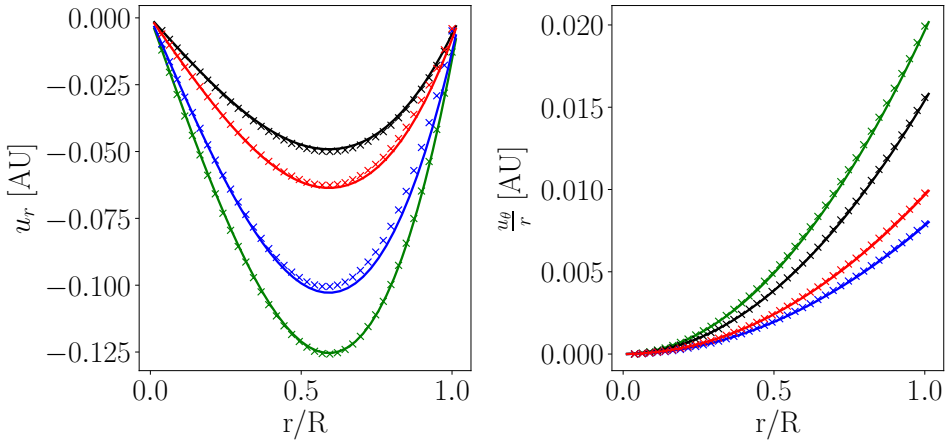

Figure 3.36: **Deformations in the droplet symmetry.** (Left) Radial displacement u_r, and (Right) azimuthal displacement u_θ. In both, full lines denote theory and points denote simulation results. Different colors are different parameters: Green - $k = k_o = 0.5$, Black - $k = 1.0; k_o = 0.5$, Blue - $k = 0.5; k_o = 1.0$. Red- $k = 1.0; k_o = 1.0$. For all simulations, $\eta = 0.01$

extending the predictions of Ref. [10] to include constant transverse forces in an overdamped dynamical system.

3.5.3.2 Elastic strain in the experiment

In Section 3.5.2, we determine the theoretical form of the elastic strain field in a nearly-circular crystal with odd elasticity that is rotating as a rigid body and acted on by substrate friction. We conduct experiments to compare with these predictions by preparing monocrystalline domains of chiral crystal by driving a droplet at a high frequency in alternating directions, as detailed in Section 3.2.1. The resulting crystal is unstable, but maintains its crystalline structure for a number of rotations before yielding to dislocations advancing from the edge, as illustrated in Figure 3.37B.

As the crystal evolves, we measure the displacement of each particle $\boldsymbol{u}$ from the initial position at $t = 0$ and the final position at $t = t_f$ after averaging positions over a temporal window of approximately one particle rotation. We then segment this displacement into the radial u_r and azimuthal u_θ components. The results of this calculation for a simulated droplet with a well-defined reference state are presented in Section 3.5.3.3.

Without need for a reference state, we can also estimate the dilational strain $u^0 = \mathrm{Tr}(\partial_i u_j)$ from the strain tensor $\partial_i u_j$, and compare our results to the simple analytical solution in Section 3.5.2. We perform a simplified computation of the dilational component of the strain tensor by measuring each fully-coordinated particle's voronoi cell area A, which is then coarse-grained as in Section 3.2.2. We then compute the area of an ideal voronoi cell for a triangular lattice with a bond length equal to the average bond length in the crystalline phase A_0, and evaluate $u^0 \sim -\delta\rho/\rho = (\rho_0 - \rho)/\rho = (A - A_0)/A_0$. To improve the resolution of the experimental data, k-means clustering is used to refine each particle's position over time. For both the experiment and simulation data, boundary particles and particles with anomalous voronoi areas are removed when taking aggregate measurements for $-\delta\rho/\rho$ versus r/R.

When plotted against the radial position of the particle and averaged over time, we obtain Figure 3.37A, which demonstrates qualitative agreement with theory. In particular

we observe a state of compression near the center of the droplet becoming dilation at the edge of the droplet, with the crossover occurring in close proximity to the predicted point of crossover. This approach can be repeated for droplets of various radius R driven at variable frequency Ω. Examples of the dilation field for droplets of varying size, all measured at early times, are presented in Figure 3.37C, and the results of (D) reveal no change due to either control variable.

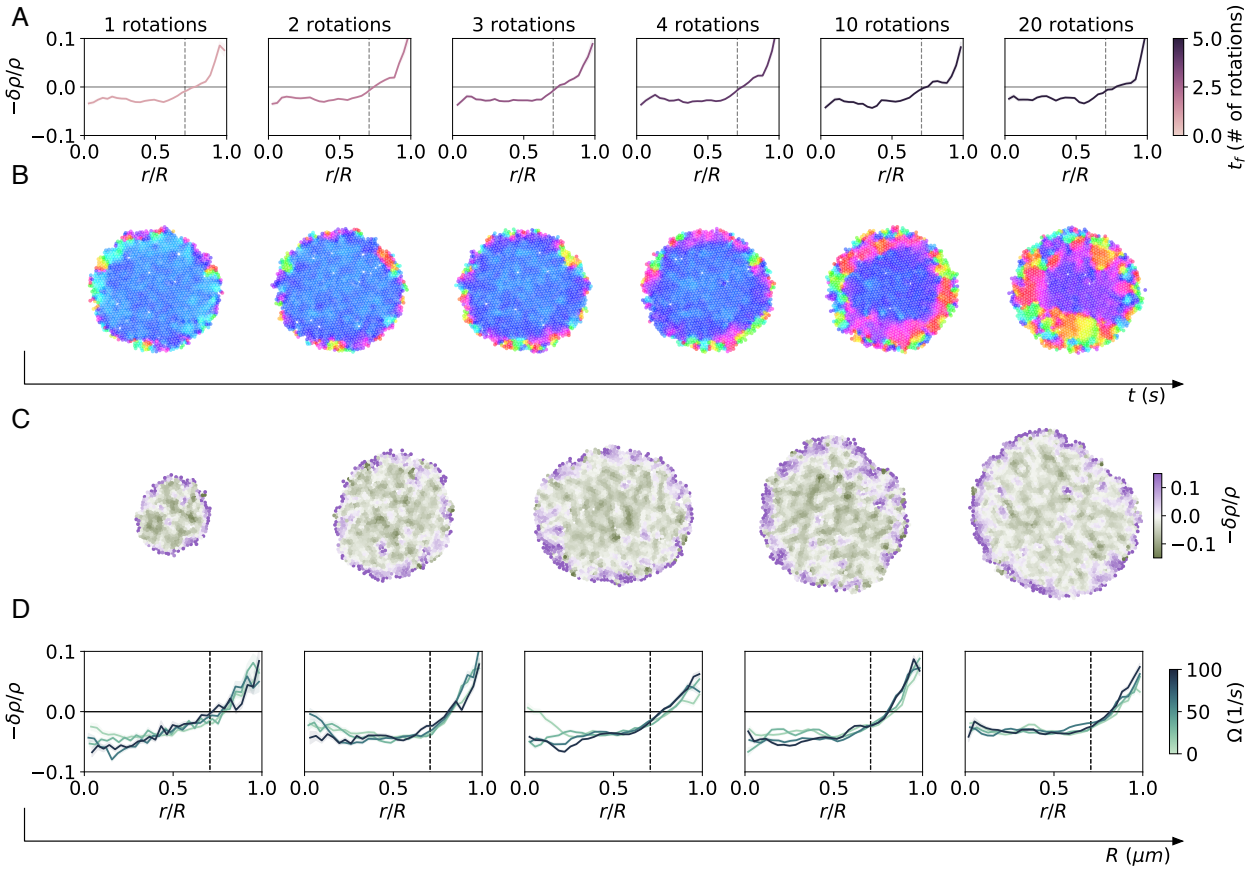

Figure 3.37: **Strain field in an odd elastic crystal.** (A) From the deformation of each particle's voronoi cell, we estimate the strain tensor and plot the dilatational component. (B) Snapshots of the crystalline structure of the droplet over time, showing destabilization from the edge. (C) For droplets of various radius R, and at early measurement times, the strain maintains the same radial structure. (D) For any accessible monocrystalline droplet size and for a reasonable range of rotation frequencies, the strain curves collapse.

3.5.3.3 Elastic strain in the minimal model simulations

In the minimal model simulation at low frequencies, where the boundary of the lattice is stable, there is no production of dislocations near the boundary, if there are no dislocations in the bulk. In this case, the elastic theory developed in detail in Section 3.5.2 can be used to estimate the strains in the droplet symmetry. Using the same procedure as in Section 3.5.3.2, we obtain the radial and azimuthal displacement fields and dilational strain, showing qualitative agreement with both the experiment and theory of Section 3.5.2.2 as presented in Figure 3.38.

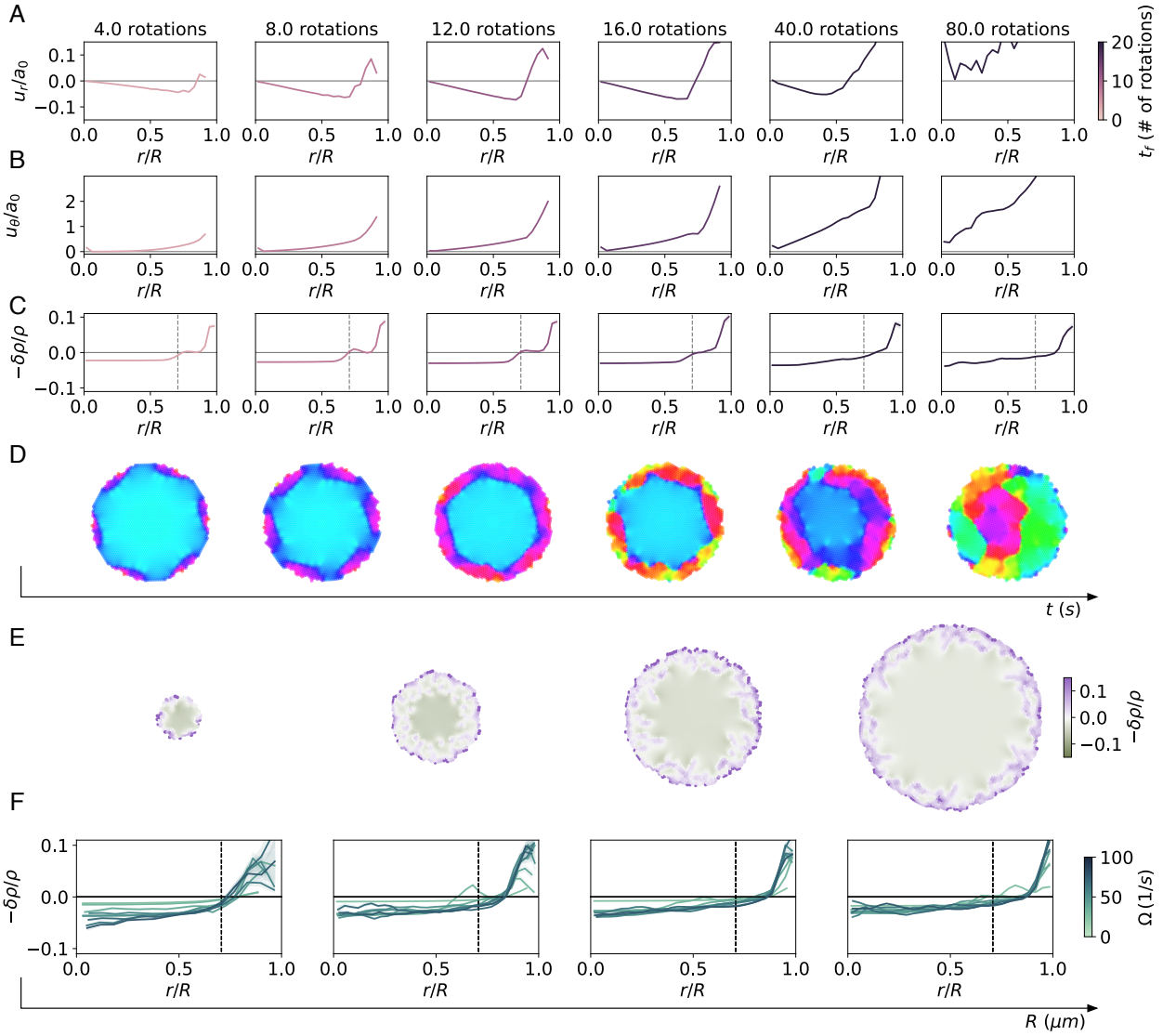

Figure 3.38: **Strain field in an odd elastic crystal.** (A) The radial displacement field u_r as a function of time, measured in rotations. (B) The corresponding azimuthal displacement u_θ. (C) From the deformation of each particle's voronoi cell, we estimate the dilatational component of the strain tensor. (D) Snapshots of the crystalline structure of the droplet over time, showing destabilization from the edge. (E) For droplets of various radius R, the strain maintains the same radial structure. (F) For any experimentally accessible monocrystalline droplet size and for a reasonable range of rotation frequencies, the strain curves collapse.

3.6 Self-kneading instability

A natural question to now ask is whether odd elastic solids powered by odd stresses are linearly stable. We consider the continuum description of an elastic solid with a local displacement $\boldsymbol{u}(\boldsymbol{r},t)$ and local velocity $\boldsymbol{v}(\boldsymbol{r},t)$, that is allowed to experience all stresses consistent with broken parity and time-reversal (Section 3.5.1 and Section 3.6.1.1) [18, 10]. In addition to elastic contributions, the symmetric stress, includes even and odd viscous contributions $\sigma_{ij} = -p\delta_{ij} + K_{ijkl}\partial_k u_\ell + \eta_{ijkl}\partial_k v_\ell$. The inner drive imposed by the spinners is encoded by the antisymmetric stress $\sigma_{ij}^{\text{spin}} = 2\eta_R\epsilon_{ij}\Omega$. Ignoring inertia, the dynamics is given by the balance between viscoelastic stresses and substrate drag defined by a constant friction coefficient Γ:

$$\Gamma\boldsymbol{v} = \nabla\cdot\boldsymbol{\sigma} + \nabla\cdot\boldsymbol{\sigma}^{\text{spin}}, \tag{3.107}$$

and the continuity equation $\partial_t\rho + \nabla\cdot(\rho\boldsymbol{v}) = 0$.

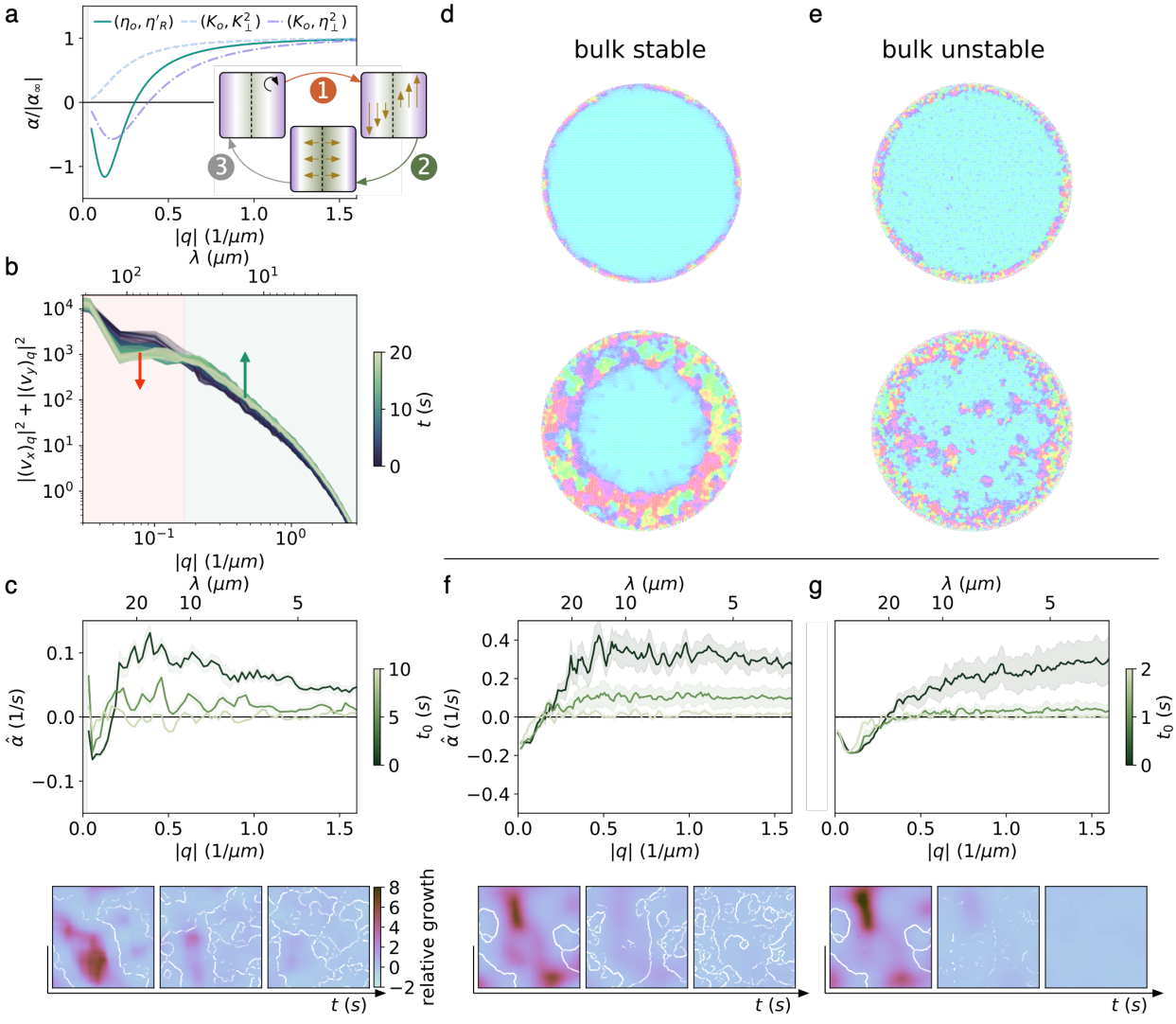
a
(η_o, η'_R)
$(K_o, K_\perp^2)$
$(K_o, \eta_\perp^2)$
$\alpha/|\alpha_\infty|$
1
2
3
$|q|$ (1/μm)
λ (μm)
b
$|\langle v_x\rangle_q|^2 + |\langle v_y\rangle_q|^2$
t (s)
$|q|$ (1/μm)
λ (μm)
c
$\hat{\alpha}$ (1/s)
t_0 (s)
$|q|$ (1/μm)
relative growth
t (s)
d
bulk stable
e
bulk unstable
f
λ (μm)
$\hat{\alpha}$ (1/s)
$|q|$ (1/μm)
t (s)
g
λ (μm)
t_0 (s)
$|q|$ (1/μm)
t (s)

Figure 3.39 *(previous page)*: **Measuring an elasto-hydrodynamic instability. a,** The chiral phase responds to a perturbation in spinner density by (1) coupling internal rotations to flow gradients that are (2) transformed into Hall stresses that (3) destabilize the crystal further (Section 3.6.1.1). A linear stability analysis of this model yields the predicted spectral growth curves arising from the interplay between odd transport coefficients (η_o, K_o) and Magnus-like couplings ($\eta_R', K_\perp^2, \eta_\perp^2$). **b,** As the chiral phase approaches the steady-state of Figure 3.1, we can measure the spectrum of its flow to see decay at large scales and growth at small scales. **c,** The total amount of growth measured at these smaller scales can be mapped over time and compared to the grain boundaries to reveal enhanced growth within initially crystalline patches and vanishing growth at later times (Section 3.6.3). The estimated spectrum of growth $\hat{\alpha}(q)$ reveals stabilization at scales $\lambda \gg \langle \xi_\theta \rangle$ and constant destabilization at scales $\lambda \ll \langle \xi_\theta \rangle$. **d,** In simulations, we tune the inter-particle interaction range to prepare a theoretically stable crystal, for which the crystal is destabilized through dislocation production to reach the whorl state. **e,** Likewise, simulations that are theoretically unstable can go unstable in response to bulk density fluctuations. Same colormap as in Figure 3.1b. **f,** The estimated spectrum and spatial map of growth for a theoretically stable simulation resembles the experiment when a polycrystal is destabilized. **g,** The same signatures are observed in a linearly unstable simulation. **f-g** use the same colormap as **c**.

Linearizing about a homogeneous quiescent base state $\boldsymbol{u} = \boldsymbol{v} = 0$ and $\rho = \rho_0$ and making the ansatz $\boldsymbol{u}, \boldsymbol{v}, \rho \propto \exp(-i\omega t + i\boldsymbol{k} \cdot \boldsymbol{r})$, we readily obtain an expression for the dispersion $\nu \equiv \mathrm{Re}(\omega)$ and damping $\alpha \equiv \mathrm{Im}(\omega)$ of displacement and density waves (Section 3.6.1.2). We find a generic scenario yielding exponential amplification of density fluctuations. A number of different combinations of off-diagonal material parameters in $\boldsymbol{\eta}$ and $\boldsymbol{K}$ result in different instabilities. However, they all reflect the same mechanistic picture, sketched in Figure 3.39a. A density fluctuation is converted to a localized rotation. The resulting net shear across the density fluctuation is in turn converted into an outward force amplifying the initial perturbation and so on to defect unbinding. Competition with the stabilizing influence of the conventional bulk and shear moduli of the elastic solid determine the consistent shape of the dispersion curves shown in Figure 3.39a and Section 3.6.1.2. Crucially, this generic mechanism relies on the coupling between stresses and strains having different spatial symmetries, which is only allowed when time reversal and parity symmetries are broken at the microscopic level [10, 120]. The full model incorporating odd hydrodynamics and elasticity

is detailed, along with the linear stability analysis, in the following sections.

3.6.1 Continuum theory: linear stability analysis

In this section we present a linear stability analysis about a quiescent state for a continuum theory of a generic chiral material. We include all elastic and viscous stresses allowed by symmetry. We also allow viscous and elastic coefficients to depend on density. We find a generic linear instability, sketched in Figure 3.40, that is driven by the interplay of anti-symmetric stresses with symmetric parity-odd stresses.

The presentation is structured as follows: in Section 3.6.1.1 we introduce our generic model, introducing the stress/strain and stress/rate-of-strain relations upon which our analysis is based (Sections 3.6.1.1). In Section 3.6.1.1 we discuss the relevant effects of density variations in the model. In Section 3.6.1.2 we present the full linear stability analysis. We discuss the resulting wavenumber-dependent growth-rates starting with a minimal model containing only viscous effects and even elasticity. We then classify the full range of instabilities that exist in these materials and discuss their common underlying mechanism (sketched in Figure 3.40).

3.6.1.1 General model

Our continuum model of a generic chiral material is cast in terms of the local displacement field $\boldsymbol{u}(\boldsymbol{r},t)$, the local velocity field $\boldsymbol{v}(\boldsymbol{r},t)$ (related by $\boldsymbol{v}=\partial_t\boldsymbol{u}$) and the mass density of spinners $\rho(\boldsymbol{r},t)$. The elasto-hydrodynamics of this material then follow from conservation of mass:

$$\partial_t\rho+\boldsymbol{\nabla}\cdot(\rho\boldsymbol{v})=0, \tag{3.108}$$

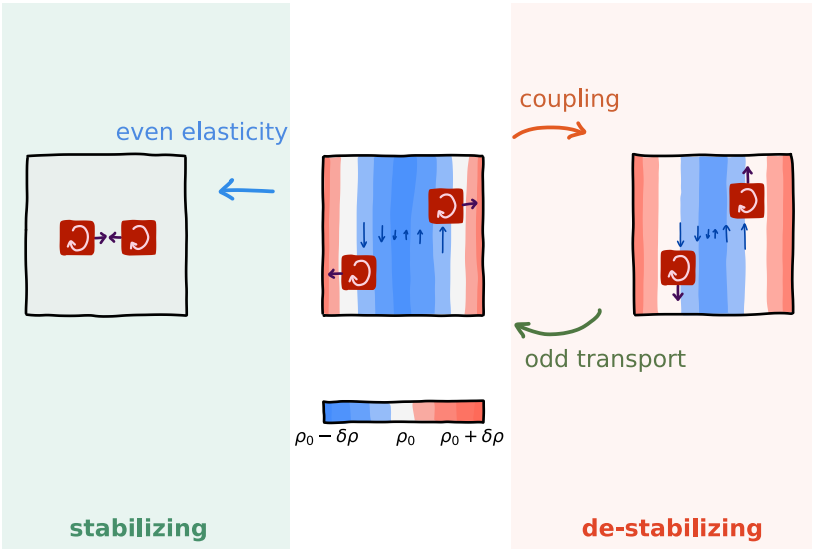

Figure 3.40: **A generic mechanism for chiral crystal destabilization.** A cartoon of our generic chiral material in which all internal stresses are balanced. When this material's density is perturbed conventional even elasticity relaxes the perturbation, conversely the coupling between dilation and rotation, generated for example by a density dependent transverse force (odd stress), leads to a shear flow along the axis of the density perturbation. In the presence of a Hall response, the newly generated gradients in the displacements (flow) along one axis produce displacements (flows) along the transverse axis, pulling the fluid apart further. This coupling between the distinct shear modes amplifies the initial perturbation.

and momentum conservation:

$$\rho\left(\partial_t \boldsymbol{v} + \boldsymbol{v}\cdot\nabla\boldsymbol{v}\right) = \nabla\cdot\left(\boldsymbol{\sigma}^{\mathrm{V}} + \boldsymbol{\sigma}^{\mathrm{E}}\right) - \Gamma\boldsymbol{v}, \tag{3.109}$$

which includes both a hydrodynamic stress tensor $\boldsymbol{\sigma}^{\mathrm{V}}$ and an elastic stress tensor $\boldsymbol{\sigma}^{\mathrm{E}}$, in addition to the familiar substrate drag $\Gamma\boldsymbol{v}$ [18].

Hydrodynamic stress contributions The breaking of parity and time-reversal symmetry in our chiral material allows for a number of viscous stresses in the relation between stress and rate-of-strain, $\sigma_{ij} = \eta_{ijkl}\dot{u}_{kl} = \eta_{ijkl}v_{kl}$:

$$\sigma^{\mathrm{V}}_{ij} = -p\delta_{ij} + \sigma^{\mathrm{b}}_{ij} + \sigma^{\mathrm{v}}_{ij} + \sigma^{\mathrm{os}}_{ij} + \sigma^{\mathrm{spin}}_{ij} + \sigma^{\mathrm{o}}_{ij} + \sigma^{\perp}_{ij}. \tag{3.110}$$

1. The first contribution represents the familiar response to compression or dilation, mediated by the bulk viscosity ζ,

$$\sigma_{ij}^{\mathrm{b}} = \zeta \delta_{ij} \partial_k v_k. \tag{3.111}$$

2. The second contribution represents the familiar response to a gradient in flow, mediated by the shear viscosity η,

$$\sigma_{ij}^{\mathrm{v}} = \eta(\partial_i v_j + \partial_j v_i - \delta_{ij} \partial_k v_k). \tag{3.112}$$

3. The third and fourth contributions arise from an anti-symmetric inter-rotor stress that arises when the two-dimensional vorticity $\omega = \epsilon_{ab} \partial_a u_b$ and externally imposed particle rotation frequency Ω, are mismatched. The result is the antisymmetric stress:

$$\sigma_{ij}^{\mathrm{os}} + \sigma_{ij}^{\mathrm{spin}} = \eta_R \epsilon_{ij} (2\Omega - \omega), \tag{3.113}$$

where η_R is the rotational viscosity. The component $\sigma_{ij}^{\mathrm{spin}} = 2\eta_R \Omega \epsilon_{ij}$ is due to rotational drive, and is independent of strains and strain rates.

4. The fifth contribution is the Hall stress mediated by the odd (or Hall) viscosity η_o:

$$\sigma_{ij}^{\mathrm{o}} = \eta_o \left(\partial_k \epsilon_{ik} v_j + \partial_i \epsilon_{jk} v_k \right). \tag{3.114}$$

5. Finally, we have two additional 'Magnus' stresses with viscosities $\eta_\perp^{1,2}$, which come in two forms:

$$\sigma_{ij}^{\perp} = \delta_{ij} \eta_\perp^1 \epsilon_{kl} \partial_k v_l + \eta_\perp^2 \epsilon_{ij} \partial_k v_k. \tag{3.115}$$

The first term converts rotation relative to a fixed frame into a net pressure, which in principle is permitted in any system where the particles have a transverse mobility coefficient. Similarly, the second term converts isotropic deformations into a net torque.

The notation of [16, 10] provides a succinct and intuitive way to organize contributions to this constitutive relation by expressing the stress and strain-rate tensors as vectors σ_α and $\dot{e}_\beta$, respectively, such that the viscosity tensor can be written as a matrix $\eta_{\alpha\beta}$. For the couplings included in this model, we then have:

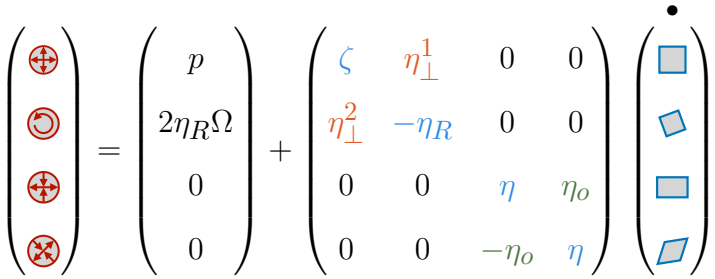

$$= \begin{pmatrix} p \\ 2\eta_R\Omega \\ 0 \\ 0 \end{pmatrix} + \begin{pmatrix} \zeta & \eta_\perp^1 & 0 & 0 \\ \eta_\perp^2 & -\eta_R & 0 & 0 \\ 0 & 0 & \eta & \eta_o \\ 0 & 0 & -\eta_o & \eta \end{pmatrix} \dot{\begin{pmatrix} \square \\ \diamond \\ \square \\ \parallel \end{pmatrix}} . \tag{3.116}$$

We have further colored terms based on their role in the generic instability we find in this SI. Even viscous contributions like the bulk and shear stresses $\boldsymbol{\sigma}^{\mathrm{b}}$ and $\boldsymbol{\sigma}^{\mathrm{v}}$ due to ζ and η are stabilizing. A Hall stress $\boldsymbol{\sigma}^{\mathrm{o}}$ due to the odd viscosity η_o produces transverse displacements feeding density perturbation growth. Finally, the Magnus stresses couple rotation to dilation, permitting gradients in density to give rise to transverse flows.

Equations of motion The stresses intrinsic to our chiral medium including drive, strains $\partial_i u_j$ and strain rates $\partial_i \dot{u}_j$ are thus given by adding they hydrodynamic contributions above to the elastic contributions obtained from coarse-graining a lattice of odd springs (Section 3.5.1.1):

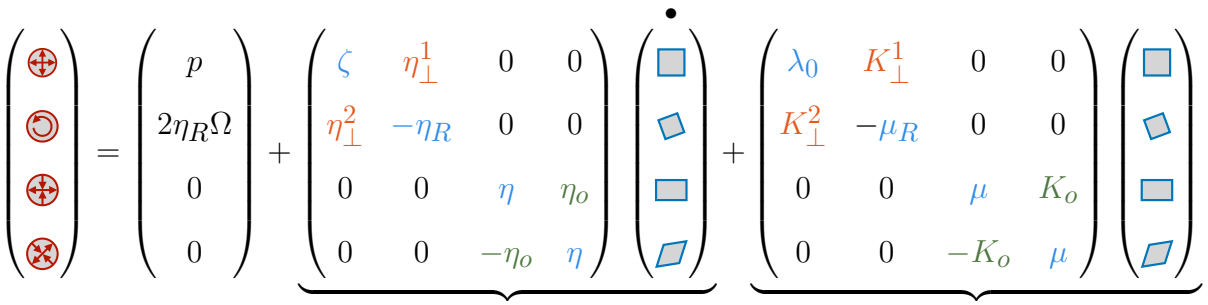

$$= \begin{pmatrix} p \\ 2\eta_R\Omega \\ 0 \\ 0 \end{pmatrix} + \underbrace{\begin{pmatrix} \zeta & \eta_\perp^1 & 0 & 0 \\ \eta_\perp^2 & -\eta_R & 0 & 0 \\ 0 & 0 & \eta & \eta_o \\ 0 & 0 & -\eta_o & \eta \end{pmatrix} \dot{\begin{pmatrix} \square \\ \diamond \\ \square \\ \parallel \end{pmatrix}}}_{\text{viscous}} + \underbrace{\begin{pmatrix} \lambda_0 & K_\perp^1 & 0 & 0 \\ K_\perp^2 & -\mu_R & 0 & 0 \\ 0 & 0 & \mu & K_o \\ 0 & 0 & -K_o & \mu \end{pmatrix} \begin{pmatrix} \square \\ \diamond \\ \square \\ \parallel \end{pmatrix}}_{\text{elastic}} . \tag{3.117}$$

The full conservation of momentum equation is given by Eq. 4.17 where $\boldsymbol{\sigma}^{\mathrm{V}}$ and $\boldsymbol{\sigma}^{\mathrm{E}}$ are given by Eqs. 3.110 and 3.44, respectively. In the analysis that follows, we assume that the dynamics are overdamped and that Ω is spatially uniform, so that the equations of motion simplify to:

$$\partial_t \rho + \boldsymbol{\nabla} \cdot (\rho \boldsymbol{v}) = 0 \tag{3.118}$$

$$\Gamma \boldsymbol{v} = \nabla \cdot \left(\boldsymbol{\sigma}^{\mathrm{V}} + \boldsymbol{\sigma}^{\mathrm{E}} \right). \tag{3.119}$$

Density-dependence The linear viscous and elastic coefficients in the constitutive relations discussed above emerge from the microscopic interactions between our magnetic spinners. Since these interactions are in general separation dependent, it seems natural to allow for a dependence on density of the coefficients.

Within the context of the linear stability analysis described below, in which we linearize about a uniform, quiescent base state, we note that the effect of such a dependence on density appears only in higher order corrections which are mostly excluded by the linearization scheme. The one notable exception is the density dependence of the odd stress in combination with the rotational drive $\eta_R(\rho)\Omega$, whose effect is analogous to the Magnus coupling $K_\perp^2$, and which plays a crucial role in powering the instability.

Similarly, one can imagine the presence of an effective hydrodynamic pressure with a density dependent constitutive relation. We include this below with a linearized compressibility which enters the analysis in an identical manner to the bulk elastic modulus included above.

3.6.1.2 Linear stability analysis

To compute the dispersion and damping of waves in our chiral medium, we linearize about the quiescent base state $\rho(\boldsymbol{r},t)=\rho_0$, $\boldsymbol{u}=\boldsymbol{v}=0$. Our linearization scheme is thus:

$$\rho(\boldsymbol{r},t)\to\rho_0+\varepsilon\rho(\boldsymbol{r},t), \tag{3.120}$$

$$\boldsymbol{u}(\boldsymbol{r},t)\to\varepsilon\boldsymbol{u}(\boldsymbol{r},t), \tag{3.121}$$

$$\boldsymbol{v}(\boldsymbol{r},t)\to\varepsilon\boldsymbol{v}(\boldsymbol{r},t). \tag{3.122}$$

We then make the following ansatz for the density and displacement fields:

$$(\rho,\boldsymbol{u})=(\hat{\rho},\hat{\boldsymbol{u}})\exp\left(i\boldsymbol{k}\cdot\boldsymbol{r}-i\omega t\right), \tag{3.123}$$

from which similar forms follow for other fields. For a given wavenumber k, the solutions are thus stable if the sign of $\mathrm{Im}(\omega)$ is negative and unstable if positive.

To first order in ε, the continuity equation becomes:

$$\partial_t\rho+\rho_0\boldsymbol{\nabla}\cdot\boldsymbol{v}=0. \tag{3.124}$$

Prior to linearizing the momentum equation, we establish that the effective rotational viscosity is increased as the density of spinners increases. Thus, we must have a rotational viscosity that depends on density, $\eta_R\equiv\eta_R(\rho)$. Expanding $\eta_R(\rho)$ in orders of ε yields

$$\eta_R(\rho)\equiv\eta_R(\rho_0+\varepsilon\rho)=\eta_R(\rho_0)+\varepsilon\rho\eta_R'(\rho_0)+\mathcal{O}(\varepsilon^2)\equiv\eta_R+\varepsilon\rho\eta_R'+\mathcal{O}(\varepsilon^2). \tag{3.125}$$

where $\eta_R'=\frac{d\eta_R}{d\rho}(\rho_0)>0$. Finally, we expand the constitutive relation for the pressure in

this medium to linear order in ε:

$$p(\rho) = p_0 + f(\rho) = p_0 + f(\rho_0 + \varepsilon\rho) = p_0' + \varepsilon\kappa\rho + \mathcal{O}(\varepsilon^2), \tag{3.126}$$

where $\kappa = \frac{df}{d\rho}(\rho_0)$.

With these results, we now expand the momentum equation to first order in ε, using Eqs. 3.110 and 3.44. The result is

$$\begin{aligned}\Gamma\boldsymbol{v} = &-\kappa\boldsymbol{\nabla}\rho + (\lambda_0 - \mu_R)\boldsymbol{\nabla}(\boldsymbol{\nabla}\cdot\boldsymbol{u}) + (\mu + \mu_R)\nabla^2\boldsymbol{u} + K_o\nabla^2\boldsymbol{u}^\perp \\ &+ K_\perp^1\boldsymbol{\nabla}(\boldsymbol{\nabla}^\perp\cdot\boldsymbol{u}) + K_\perp^2\boldsymbol{\nabla}^\perp(\boldsymbol{\nabla}\cdot\boldsymbol{u}) \\ &+ (\zeta - \eta_R)\boldsymbol{\nabla}(\boldsymbol{\nabla}\cdot\boldsymbol{v}) + (\eta + \eta_R)\nabla^2\boldsymbol{v} + \eta_o\nabla^2\boldsymbol{v}^\perp \\ &+ \eta_\perp^1\boldsymbol{\nabla}(\boldsymbol{\nabla}^\perp\cdot\boldsymbol{v}) + \eta_\perp^2\boldsymbol{\nabla}^\perp(\boldsymbol{\nabla}\cdot\boldsymbol{v}) \\ &+ 2\Omega\eta_R'\boldsymbol{\nabla}^\perp\rho.\end{aligned} \tag{3.127}$$

where $\boldsymbol{a}^\perp = (a_2, -a_1)$ so that $\nabla^\perp = (\partial_y, -\partial_x)$. We now take the Fourier transform of the above equations, recalling that $\nabla \to i\boldsymbol{k}$, $\boldsymbol{v} \to -i\omega\hat{\boldsymbol{u}}$. For the continuity equation we find

$$\hat{\rho} = -i\rho_0\boldsymbol{k}\cdot\hat{\boldsymbol{u}}. \tag{3.128}$$

For the momentum equation, we obtain

$$\begin{aligned}-i\Gamma\omega\hat{\boldsymbol{u}} = &\rho_0\kappa\boldsymbol{k}(\boldsymbol{k}\cdot\hat{\boldsymbol{u}}) - (\lambda_0 - \mu_R)\boldsymbol{k}(\boldsymbol{k}\cdot\hat{\boldsymbol{u}}) - (\mu + \mu_R)k^2\hat{\boldsymbol{u}} \\ &- K_o k^2\hat{\boldsymbol{u}}^\perp - K_\perp^1\boldsymbol{k}(\boldsymbol{k}^\perp\cdot\hat{\boldsymbol{u}}) - K_\perp^2\boldsymbol{k}^\perp(\boldsymbol{k}\cdot\hat{\boldsymbol{u}}) \\ &+ i\omega(\zeta - \eta_R)\boldsymbol{k}(\boldsymbol{k}\cdot\hat{\boldsymbol{u}}) + i\omega(\eta + \eta_R)k^2\hat{\boldsymbol{u}} + i\omega\eta_o k^2\hat{\boldsymbol{u}}^\perp \\ &+ i\omega\eta_\perp^1\boldsymbol{k}(\boldsymbol{k}^\perp\cdot\hat{\boldsymbol{u}}) + i\omega\eta_\perp^2\boldsymbol{k}^\perp(\boldsymbol{k}\cdot\hat{\boldsymbol{u}}) + 2\rho_0\Omega\eta_R'\boldsymbol{k}^\perp(\boldsymbol{k}\cdot\hat{\boldsymbol{u}}),\end{aligned} \tag{3.129}$$

upon substitution of $\hat{\rho}$ from the continuity equation. For brevity, take $\lambda \equiv \lambda_0 - \rho_0\kappa$.

To predict the dispersion relation from Eq. 3.129, let $\boldsymbol{k} = k\hat{\boldsymbol{k}}$ (i.e. $|\hat{\boldsymbol{k}}| = 1$) and denote the components of the displacement parallel to $\hat{k}$ by: $u_\parallel = \hat{k}_i u_i$ and $u_\perp = \epsilon_{ij}\hat{k}_i u_j$. Projecting Eq. 3.129 onto components parallel and perpendicular to $\hat{\boldsymbol{k}}$ yields:

$$\begin{aligned} -i\Gamma\omega u_\parallel = &-(\lambda - \mu_R)k^2 u_\parallel - (\mu + \mu_R)k^2 u_\parallel + K_o k^2 u_\perp - K_\perp^1 k^2 u_\perp \\ &+ i\omega(\zeta - \eta_R)k^2 u_\parallel + i\omega(\eta + \eta_R)k^2 u_\parallel - i\omega\eta_o k^2 u_\perp + i\omega\eta_\perp^1 k^2 u_\perp \end{aligned} \tag{3.130}$$

$$\begin{aligned} -i\Gamma\omega u_\perp = &-(\mu + \mu_R)k^2 u_\perp - K_o k^2 u_\parallel - K_\perp^2 k^2 u_\parallel \\ &+ i\omega(\eta + \eta_R)k^2 u_\perp + i\omega\eta_o k^2 u_\parallel + i\omega\eta_\perp^2 k^2 u_\parallel \\ &+ 2\rho_0\Omega\eta_R' k^2 u_\parallel, \end{aligned} \tag{3.131}$$

This can be rewritten as the generalized eigenvalue problem

$$i\omega \boldsymbol{A}\boldsymbol{u} = \boldsymbol{B}\boldsymbol{u}, \tag{3.132}$$

where

$$\boldsymbol{A} = \begin{pmatrix} \Gamma + (\zeta + \eta)k^2 & -\eta_o k^2 + \eta_\perp^1 k^2 \\ \eta_o k^2 + \eta_\perp^2 k^2 & \Gamma + (\eta + \eta_R)k^2 \end{pmatrix}, \tag{3.133}$$

$$\boldsymbol{B} = k^2 \begin{pmatrix} \lambda + \mu & K_\perp^1 - K_o \\ K_\perp^2 + K_o - 2\rho_0\Omega\eta_R' & \mu + \mu_R \end{pmatrix}. \tag{3.134}$$

Thus, the dispersion relation is $\omega(k) = -i\,\mathrm{eig}(\boldsymbol{A}^{-1}\boldsymbol{B})$ for $\boldsymbol{A}$ nonsingular.

In the following sections, we analyze the growth rate $\alpha(k) \equiv \mathrm{Im}\ \omega(k)$ and dispersion $\nu(k) \equiv \mathrm{Re}\ \omega(k)$ in various special cases to deduce the minimal possible ingredients necessary to obtain the observed instability.

A taxonomy of instabilities The general eigenvalue problem of Eqs. (3.132)-(3.134) can be readily solved to establish the linear stability of a chiral phase. The full solution for the wavenumber dependent growth rate and dispersion relation does not readily provide intuition because our model allows multiple instability scenarios. To gain intuition we consider a base model that includes bulk (λ) and shear (μ) moduli, shear viscosity (η), and rotational viscosity (η_R). To this we add (in pairs):

- A density-rotation coupling (rows of Figure 3.41: η_R', $\eta_\perp^{1,2}$, $K_\perp^{1,2}$).
- An odd response (columns of Figure 3.41: η_o, K_o).

In each entry, we plot the growth rate $\alpha(k)$, for $\omega(k)$ obtained from solving the aforementioned eigenvalue problem. We vary the odd response parameter to demonstrate its impact on the stability of the spectrum in each model and plot the resulting growth curves.

This analysis reveals the following behaviors:

1. **Stable.** In the absence of an odd transport coefficient or density-rotation coupling, the system is stable.
2. **Unstable at finite wavelengths.** By pairing an odd viscous (elastic) stress with a density-rotation coupling stress that is elastic (viscous), we obtain a spectrum that is stable for small k and unstable for large k. Such models are in agreement with the experimental observations in Figure 3.39.
3. **Unstable at all wavelengths.** Pairing odd elastic stress with non-viscous density-rotation coupling terms yields a spectrum that is either entirely stable for small K_o or entirely unstable for large K_o.

A simple instability To gain intuition on the competition between stabilizing and destabilizing stresses in this zoology of instabilities, we restrict our attention to a model that

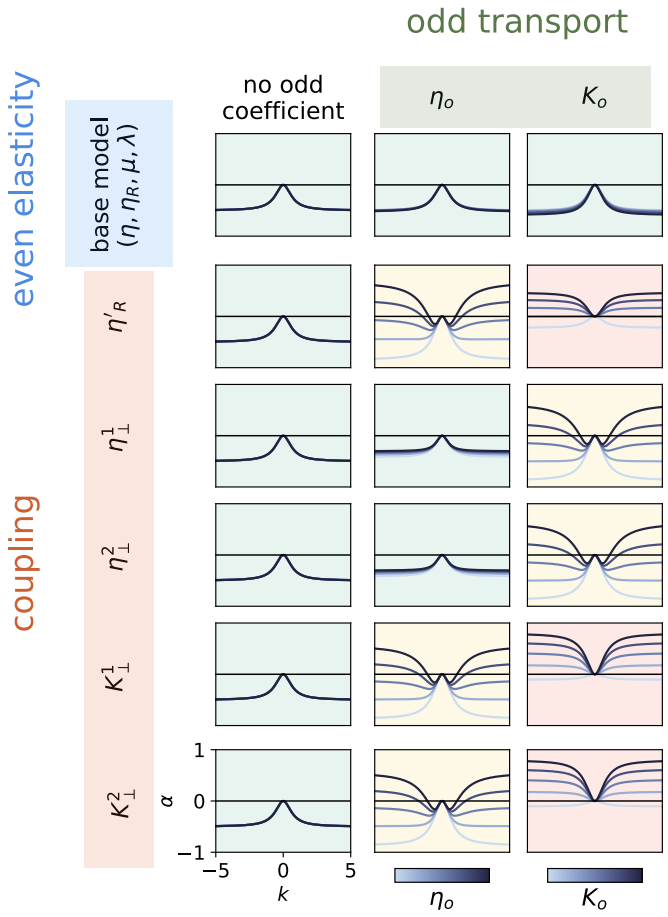

Figure 3.41: **Taxonomy of instabilities.** The instability diagrammed in Figure 3.40 is contingent upon the presence of: (1) odd transport, (2) coupling between rotations and dilation, and (3) stabilization through elasticity or otherwise. We diagram models that incorporate a base level of elasticity and a combination of one odd transport and one coupling coefficient.

includes conventional elastic moduli (λ, μ), a shear viscosity η, a density dependent rotational viscosity η_R with positive derivative η'_R, and an odd viscosity η_o. This is consistent with a prior study of the hydrodynamics of the chiral phase with the addition of conventional elasticity and a density dependence to the odd stress [18], and restricts our attention to finite wavelength instabilities that are relevant to our experiments.

This model produces a dispersion relation and growth rate which have the following

asymptotic limits:

$$\alpha(k) = -\frac{\mu}{\Gamma}k^2 + \frac{(\eta+\eta_R)\lambda - 2\rho_0\Omega\eta_R'\eta_o}{\Gamma^2}\frac{\mu}{\lambda}k^4 + \mathcal{O}(k^5) : |k| \ll 1, \tag{3.135}$$

for the growth rate at large scales, and:

$$\begin{aligned}\nu(k) + i\alpha(k) = \frac{i}{2[{\eta_o}^2 + \eta(\eta+\eta_R)]}\Bigg[&- \eta(\lambda+2\mu) - \eta_R(\lambda+\mu) + 2\rho_0\Omega\eta_R'\eta_o \\ &+ \Big([\eta\lambda + (\lambda+\mu)\eta_R]^2 - 4\rho_0\Omega\eta_R'\eta_o[\eta(\lambda+2\mu) + \eta_R(\lambda+\mu)] \\ &\quad - 4{\eta_o}^2[\mu(\lambda+\mu) - (\rho_0\Omega\eta_R')^2]\Big)^{1/2}\Bigg] \\ &+ \mathcal{O}(k^{-2}) : |k| \gg 1,\end{aligned} \tag{3.136}$$

at small scales, where there can also be dispersive waves. At large length-scales both conventional elasticity and even viscous stress are stabilizing, while the combination $2\rho_0\Omega\eta_R' \times \eta_o$ is destabilizing. At small length-scales, the growth rate is independent of wave-number with a sign determined by a complex interplay of viscous and elastic coefficients.

Figure 3.42, shows plots of the dispersion and growth rate for a range of stabilizing and destabilizing material constants. Density perturbations can be seen to decay at large scales and grow at small scales. Increasing the odd viscosity η_o or the density-response of the rotational viscosity η_R', the model can be tuned between completely stabilizing behavior and destabilizing behavior at finite wavelengths. Likewise, the shear modulus μ (or equivalently, the bulk modulus λ) can be increased to tune the critical wave-number k^* for which $\alpha(k^*) = 0$. In the limit of large elastic forces, $k^* \to \infty$ and destabilization of the homogeneous state is prevented altogether.

Crucially both Hall viscosity and density dependent odd stress are required for unstable behavior at any wave-number. Conversely, eliminating the elastic response makes the model unstable at all wave-numbers. This feature, explored in detail below, is common to all the

instabilities identified in Figure 3.41 and forms the basis for the cartoon in Figure 3.40.

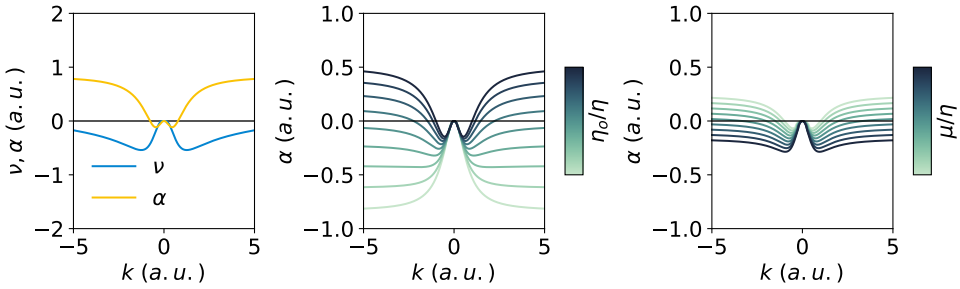

Figure 3.42: **A complete model.** A model that incorporates all the prescribed ingredients for a scale-dependent instability is presented. Dispersive waves are damped at small k and grow at large k (left). Enhancing the odd response makes more of the spectrum unstable (center), while the system can be stabilized at all scales by increasing the even elastic moduli

The limit $\eta_o \to 0$. In the absence of odd viscosity, the mechanism by which the homogeneous state destabilizes is removed and it can be shown directly that waves at every scale are damped. There are two damped modes in this case where one mode has a decay rate with asymptotic large- and small-scale behaviors of

$$\alpha(k) = \begin{cases} -\dfrac{\mu}{\Gamma}k^2 + \dfrac{\mu(\eta+\eta_R)}{\Gamma^2}k^4 + \mathcal{O}(k^6) & : |k| \ll 1, \\ -\dfrac{\mu}{\eta+\eta_R} + \dfrac{\Gamma\mu}{(\eta+\eta_R)^2}\dfrac{1}{k^2} + \mathcal{O}(k^{-4}) & : |k| \gg 1, \end{cases} \tag{3.137}$$

while the other mode has:

$$\alpha(k) = \begin{cases} -\dfrac{\lambda+\mu}{\Gamma}k^2 + \dfrac{(\lambda+\mu)\eta}{\Gamma^2}k^4 + \mathcal{O}(k^5) & : |k| \ll 1, \\ -\dfrac{\lambda+\mu}{\eta} + \dfrac{\Gamma(\lambda+\mu)}{\eta^2}\dfrac{1}{k^2} + \mathcal{O}(k^{-4}) & : |k| \gg 1. \end{cases} \tag{3.138}$$

Increasing the elastic modulus causes modes to be uniformly more strongly stabilized, while increasing the rotational viscosity simply makes this decay uniform over all sufficiently small scales. This is shown for the first mode in Figure 3.43.

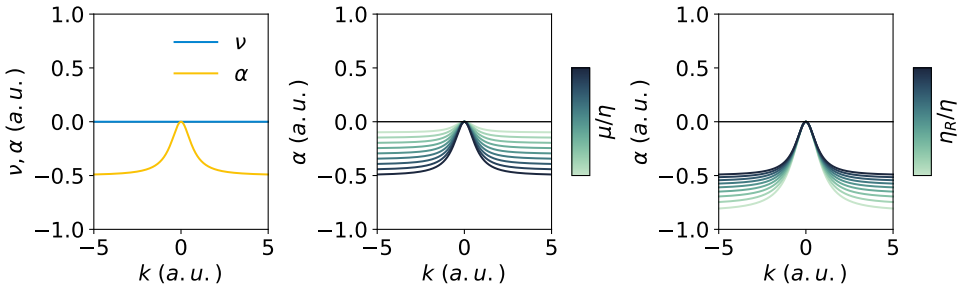

Figure 3.43: **Removing odd viscosity.** By removing the odd response, dispersive waves are eliminated and density perturbations are damped at all scales (left). Modulating both even elastic (center) and viscous (right) parameters universally yields causes the system to be stable.

The limit $\eta_R' \to 0$. Now, we demonstrate that the density-dependence of the rotational viscosity is itself a crucial element that conspires with the odd viscosity to yield instability. Without this crucial dependence on density, the dynamics is dominated by elasticity and it can be shown that all scales are damped. In this case, there are two decaying modes, with one having a decay rate with asymptotic large and small k behaviors

$$\alpha(k) = \begin{cases} -\dfrac{\mu}{\Gamma}k^2 + \dfrac{\mu(\eta+\eta_R)}{\Gamma^2}k^4 + \mathcal{O}(k^5) & : |k| \ll 1, \\ -\dfrac{1}{2[{\eta_o}^2 + \eta(\eta+\eta_R)]}\Big[\eta_R(\lambda+\mu) + \eta(\lambda+2\mu) & \\ \quad -\sqrt{\eta^2\lambda^2 + 2\eta\eta_R(\lambda+\mu)(\lambda+\mu) + (\lambda+\mu)[-4{\eta_o}^2\mu + {\eta_R}^2(\lambda+\mu)]}\Big] & : |k| \gg 1, \end{cases} \tag{3.139}$$

while the other mode has

$$\alpha(k) = \begin{cases} -\dfrac{\lambda+\mu}{\Gamma}k^2 + \dfrac{\eta(\lambda+\mu)}{\Gamma^2}k^4 + \mathcal{O}(k^5) & : |k| \ll 1, \\ -\dfrac{1}{2[{\eta_o}^2 + \eta(\eta+\eta_R)]}\Big[\eta_R(\lambda+\mu) + \eta(\lambda+2\mu) & \\ \quad +\sqrt{\eta^2\lambda^2 + 2\eta\eta_R\lambda(\lambda+\mu) + (\lambda+\mu)[-4{\eta_o}^2\mu + {\eta_R}^2(\lambda+\mu)]}\Big] & : |k| \gg 1, \end{cases} \tag{3.140}$$

The first set of modes are plotted in Figure 3.44. Odd viscosity only appears as a correction to the damping rate at short wavelengths, while the system is stable at all scales due to the

even elastic and viscous terms.

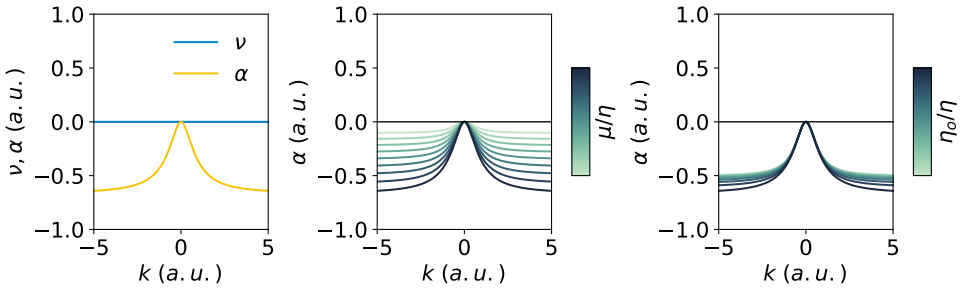

Figure 3.44: **Uniform rotational viscosity.** A model that includes an odd transport coefficient η_o and otherwise even viscous and elastic terms is also stable at all scales and has no waves (left). Increasing the stabilizing shear modulus μ further stabilizes the system (center), while modulating odd viscosity η_o has minimal effect in the absence of density-rotation coupling.

The limit $\lambda, \mu \to 0$. In this case, one mode has $\alpha, \nu \equiv 0$ for all k, while the second mode's dispersion satisfies $\nu \equiv 0$, but has non-zero damping. This is particularly easy to examine. For this mode, the density Fourier amplitude evolves as

$$\hat{\rho}_t = 2\rho_0 \eta_R' \Omega \frac{\eta_o k^4}{\left[\Gamma + (\eta + \eta_R)k^2\right]\left[\Gamma + \eta k^2\right] + {\eta_o}^2 k^4} \hat{\rho} \tag{3.141}$$

The growth rate being the prefactor of ρ we see it is positive for $k > 0$. The large and small k asymptotics in this case are given by

$$\alpha(k) = \begin{cases} \dfrac{2\eta_o \eta_R' \Omega \rho_0}{\Gamma^2} k^4 + \mathcal{O}(k^6) & : |k| \ll 1, \\ \dfrac{2\eta_o \eta_R' \Omega \rho_0}{{\eta_o}^2 + \eta(\eta + \eta_R)} + \mathcal{O}(k^{-2}) & : |k| \gg 1. \end{cases} \tag{3.142}$$

That is, there is wavelength-independent growth for sufficiently small scales that arises from a rapid increase in growth rates from large scales. The interplay of density-rotation coupling and odd response appears as in the full model through $2\rho_0 \Omega \eta_R' \times \eta_o$, but here destabilizes all length-scales in the absence of a balancing stabilizing term. The shear and rotational

viscosities, as in Figure 3.45, only suppress growth marginally at small scales.

The density dynamics above arises from a velocity-density coupling of the form

$$\hat{\boldsymbol{v}} = \frac{2\Omega\eta_R'}{\left[\Gamma + (\eta+\eta_R)k^2\right]\left[\Gamma+\eta k^2\right] + {\eta_o}^2k^4}\left[(\eta_o k^2)i\boldsymbol{k} + (\Gamma+\eta k^2)i\boldsymbol{k}^\perp\right]\hat{\rho}. \tag{3.143}$$

If we consider a simple density perturbation $A\sin(kx)$, where $k > 0$, the corresponding perturbative velocities have the form

$$v_x = Ah(k^2)\eta_o k^3\cos kx, \qquad v_y = -Ah(k^2)(\Gamma+\eta k^2)k\cos kx, \tag{3.144}$$

where $h(k^2) > 0$. This corresponds to a horizontal velocity v_x moving material from low density to high density regions, increasing the amplitude of A, and associated material shear $\omega = \partial_x v_y$, as illustrated in Figure 3.40.

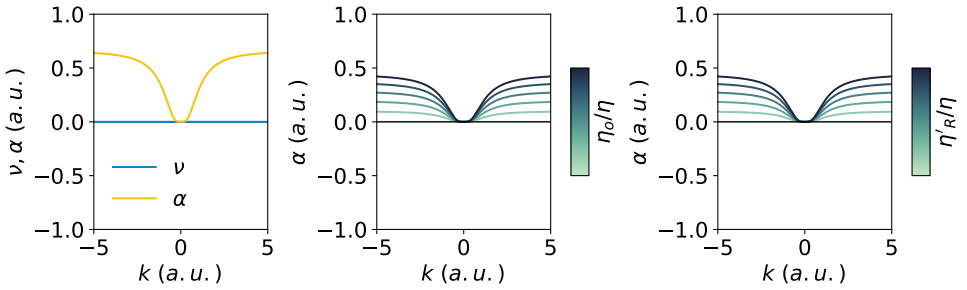

Figure 3.45: **Removing elasticity.** Including only the viscosities η, η_R, and η_o, in addition to η_R' yields unstable solutions without dispersion (left). The destabilizing η_o (center) and η_R' (right) compete with η and η_R to increase the growth rate.

3.6.1.3 Alternative destabilization route

In the description above, we focused on a pathway towards instability that requires both an odd response and coupling between dilation and rotation. A second route to instability is provided by mixing between the pairs $(\eta_\perp^1, K_\perp^2)$ and $(\eta_\perp^2, K_\perp^1)$ which produce similar instabilities to Section 3.6.1.2. Figure 3.46 shows an expansion of Figure 3.41 to include

these couplings. We note that, unlike odd viscosity η_o and a density-dependent rotational viscosity $\eta_R(\rho)$ (see [18]), no measurement of these Magnus terms has been reported to date in a chiral medium.

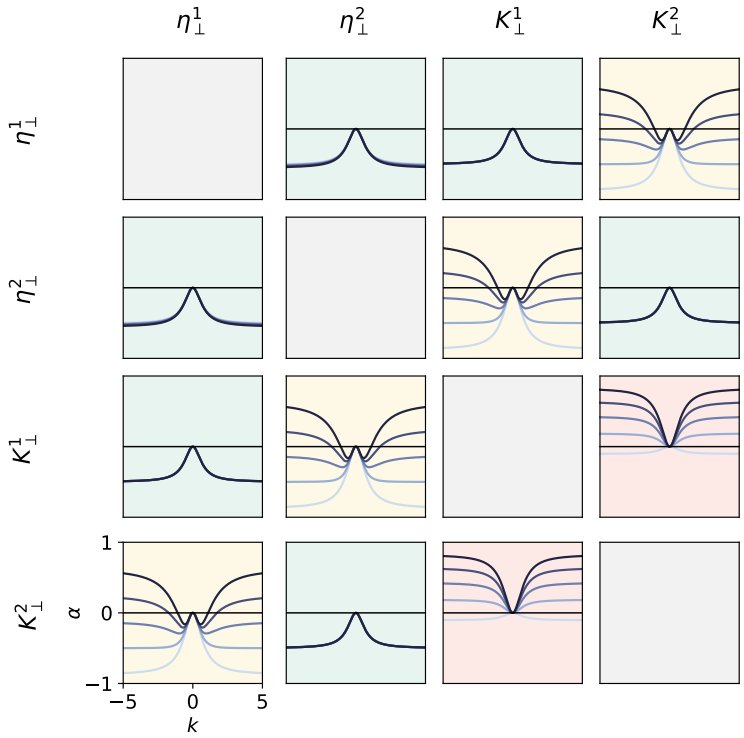

Figure 3.46: **Magnus-Magnus pairings.** Adding two Magnus coefficients (one viscous, one elastic) to the base model can also yield a scale-dependent instability, provided they oppositely couple dilations and rotations in the stress and strain tensors.

3.6.1.4 The elastic instability

We consider one other special case: a purely elastic instability. In this limit, all viscous effects are ignored and the behavior can be summarized by

$$\omega(k) = \frac{-i}{2\Gamma}\left(\lambda + 2\mu + \sqrt{\lambda^2 - 4K_\perp^2 K_o - 4{K_o}^2}\right)k^2. \tag{3.145}$$

There are two primary classes of behavior that arise from this case: (1) stable wave propagation, and (2) instability. The first case is summarized by Figure 3.47, while the second case is

illustrated in Figure 3.48. Unlike the viscoelastic model discussed previously, an odd elastic solid sustains spectral growth that is wavelength-dependent at all scales, and destabilizing everywhere.

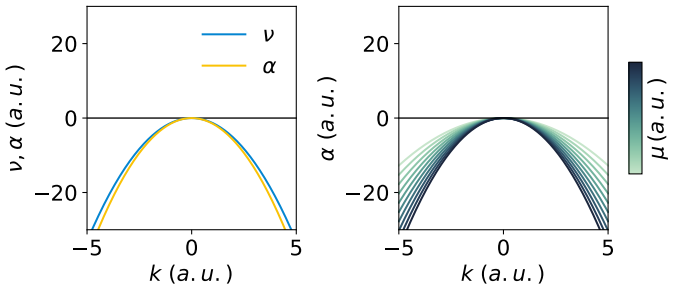

Figure 3.47: **Stable elastic waves.** Including only the elastic moduli λ, μ, $K_\perp^2$, and K_o, yields stable solutions with dispersion in one limit. The even elastic moduli only slows the damping rate in this limit.

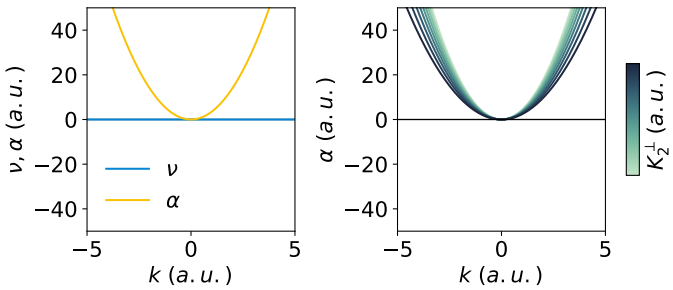

Figure 3.48: **An elastic instability.** Including only the elastic moduli λ, μ, $K_\perp^2$, and K_o, yields unstable solutions without dispersion. The Magnus elastic modulus has little qualitative effect in this limit.

3.6.2 Spectral analysis of the instability

To test this simplified model, we measure the flows $\boldsymbol{v}(\boldsymbol{x})$ that occur in the bulk of a large crystallite driven at finite rotation frequency, and measure the Fourier spectrum of all scalar measures of deformation, including velocity and strain rate. The technical details are described in Section 3.6.3. Figure 3.39b shows that following the onset of rotations the azimuthally averaged spectra evolve before eventually settling into a steady state. By comparing the spectra at different times, we extract the mode growth curves shown in Figure 3.39 for (c)

experiments (Section 3.6.3) and (f, g) simulations (Section 3.6.4). They reveal the presence of an instability at finite wavelength for all modes with relatively constant growth above a characteristic scale. As shown in Figure 3.39c, a spatial map of the integrated growth rate reveals that this instability is consistent with the destabilization of our chiral crystal.

We note, however, that in finite crystalline domains, defects are readily produced at the boundary. Their subsequent propulsion into the bulk could curtail or otherwise affect the full development of the instability. Crucially, we have not observed the spontaneous appearance of defects in the middle of a crystallite in our experiments. These combined observations suggest the existence of an additional mechanism for destabilization in which motile defects nucleate at the boundary and invade the crystal phase, actively fracturing the bulk into whorls.

Our minimal model simulations provide an ideal arena to investigate this possibility. By varying microscopic interaction parameters, we can tune the system from linearly stable to linearly unstable (Section 3.6.4.1 and Section 3.6.4.3), Remarkably, in both the stable and the unstable regime, we observe that initially perfectly crystalline droplets are destabilized by the production of defects at the edges of the droplets, which subsequently invade the bulk in a visible front (Figure 3.39d-e). The only difference is that deep in the unstable regime (e), we also observe defect nucleation in the bulk of the droplet before the front arrives. Notably, in both cases a crystal whorl emerges as the steady state (Section 3.6.4.3). This mechanism of destabilization has a different origin from the linear instability described above; within our continuum approach the presence of a constant background odd stress plays no role in the crystal's stability, rather its primary effect is to drive defect propulsion (Section 3.5.2.3 and Section 3.6.1.2).

Remarkably, measurements of the spectral growth in both regimes, performed for simulations initialized in a polycrystalline phase, display general shapes and spatial maps that are similar to those observed in the experiment (Figure 3.39f-g). The similar shape of the

resulting curves demonstrates the challenge of disentangling the precise origin of the growth in terms of linear response coefficients.

3.6.3 Stability of experimental crystals

As discussed in the Section 3.2 and Section 3.4, our measurements show that a homogeneous crystalline patch of chiral crystal generically breaks up into a polycrystal. We analyze this fragmentation using the tools of Section 3.2.3 to estimate the average grain size and total grain boundary length over time, as plotted in Figure 3.49A-B.

To investigate the break-up process further we track the evolution of Fourier spectra of velocity and strain-rates during this process. We begin with the Lagrangian velocity field $\boldsymbol{v}_i(t)$ and construct the Eulerian velocity field $\boldsymbol{v}(\boldsymbol{r}, t)$ by interpolating the particle velocities onto a grid. Taking a Fourier transform of the components of the velocity field and extracting the power in each spatial mode $|(v_i)_{\boldsymbol{q}}(t)|^2$ reveals an isotropic spectrum. Taking the azimuthal average and convolving with a filter to remove noise yields the one-dimensional spectrum $|(v_i)_q|^2$, which is shown in Figure 3.49C-D.

The resulting spectrum presents a broad distribution that evolves at short times (C) before settling onto a steady state (D). By tracking the evolution of the spectrum in time, we compute a wavenumber-dependent growth rate $\hat{\alpha}(q; t_0, t_1)$, as the difference between the power $P(q)$ of the spectrum at times t_0 and t_1, normalized by the power at time t_0 and divided by $t_1 - t_0$,

$$\hat{\alpha}(q; t_0, t_1) = \frac{1}{t_1 - t_0} \frac{P(q, t_1) - P(q, t_0)}{P(q, t_0)} \tag{3.146}$$

To gain some intuition on the effect of the time intervals we consider, we indicate and vary the values of t_0 and t_1 on Figure 3.50. We find that the growth rates are insensitive to perturbations on the choices of t_0 and t_1. Namely, as presented in Figure 3.50, the growth rate is uniform for all early times and is insensitive to the observation window.

As shown in Figure 3.21 and Figure 3.5, the particle rotation rate Ω, among other pa-

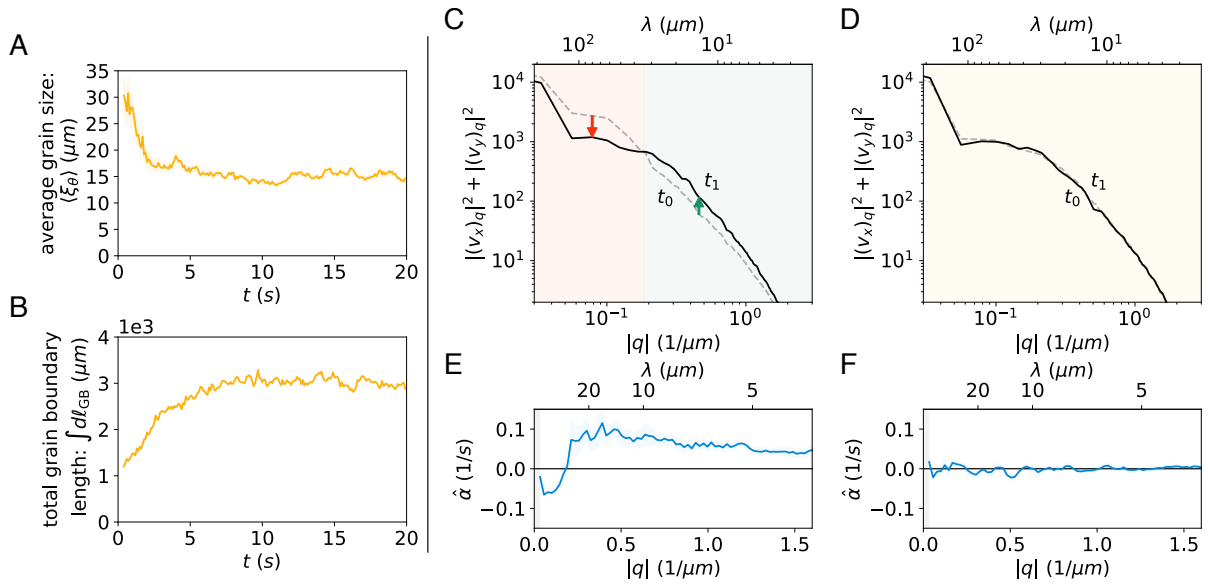

Figure 3.49: **Measuring a growth rate in the velocity spectrum.** A region of chiral crystal is fragments into smaller grains, as viewed through (A) the average grain size $\langle \xi_\theta \rangle$ and (B) the total grain boundary length $\int d\ell_{\mathrm{GB}}$. The averaged velocity power spectrum, $|(v_x)_q|^2 + |(v_y)_q|^2$, is plotted at times t_0 (dashed line) and t_1 (solid line) for (C) an unstable crystal, and (D) a crystal in the steady-state. In the case of the unstable crystal, for sufficiently long intervals $t_1 - t_0$, the spectrum evolves. We compute the growth rate for various initial times t_0, keeping the window $t_1 - t_0$ fixed, and observe that the growth rate of the (E) unstable crystal, levels off at late times to resemble the growth rate of (F) the steady-state crystal. The shaded regions represent scales above the system size.

rameters, sets the characteristic crystallite size in the steady-state. We find that unstable states prepared with roughly the same (B) mean crystal size $\langle \xi_\theta \rangle$ and (C) integrated grain boundary length reach different steady-states in Figure 3.51. Increased levels of crystalline breakup are reflected directly in the spectral evolution of the velocity field, as demonstrated in Figure 3.51A, for which the resulting growth rates $\hat{\alpha}(q)$ are plotted.

In Figure 3.52, we decompose the strain-rate tensor $\dot{e}_\beta$ in terms of the irreducible representations of dilation (), vorticity (), shear 1 (), and shear 2 () (see Section 3.6.1), and show that a similar azimuthally averaged power spectrum $|(\dot{e}_\beta)_q|^2$ is associated to each mode. Beginning from an unstable state, the evolution of each component is similar (A), resulting in nearly identical normalized growth rates $\hat{\alpha}_\beta(q)$ (B). Meanwhile, beginning from

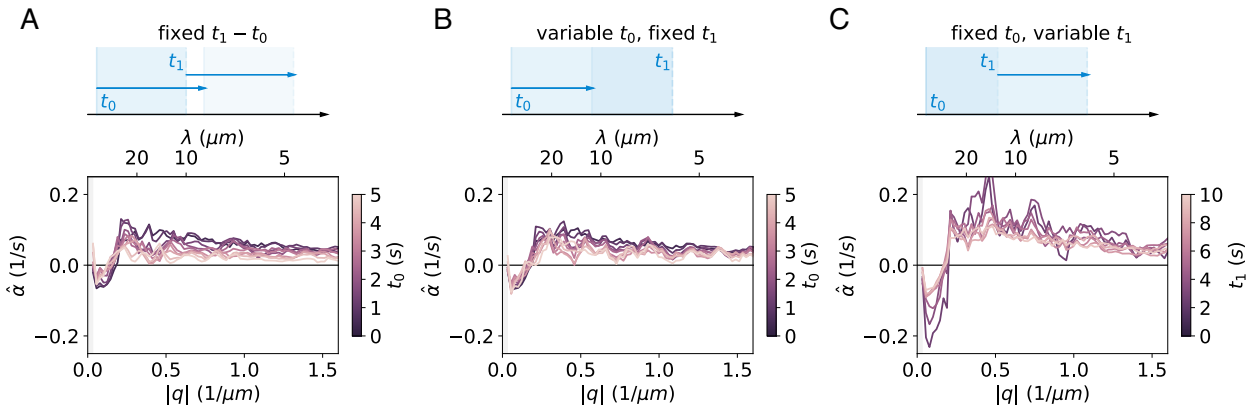

Figure 3.50: **Growth rates measured over various time intervals.** (A) By evaluating the growth rate over time-intervals (t_0, t_1) with a fixed $t_1 - t_0$ but shifted throughout the experimental time, we observe little qualitative impact on the measured growth. (B) Similarly, allowing the time-interval to vary while initializing the computation at successively later times t_0 has little impact. (C) Finally, the same is observed when terminating the computation at successively later times t_1.

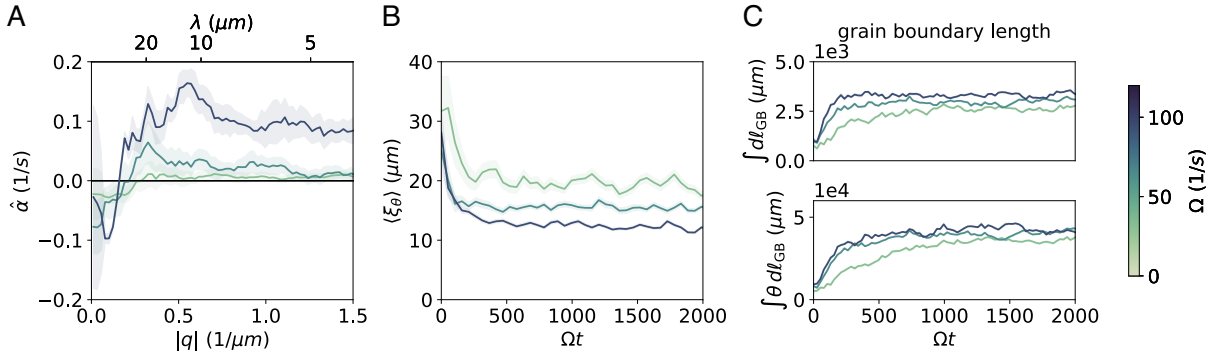

Figure 3.51: **Dependence of growth rate on rotation frequency.** (A) From the evolution of the displacement spectrum, we observe the growth rate in unstable crystals driven at various frequencies. The peak growth rate coincides with a wavelength that roughly decreases with frequency. During this instability, (B) typical domain sizes tend to decrease to near the steady-state values, and (C) the total grain boundary length increases.

a steady-state, the growth vanishes for all components (C).

In order to gain insight on the spatial localization of the growth rate, we measure the integrated growth rate, $I = \int_{q_0}^{q_1} dq \, \hat{\alpha}(q)$ taking q_0 and q_1 to roughly correspond to the window size $2\pi/\ell$ and the particle spacing $2\pi/a$. We measure this quantity for the growth rate

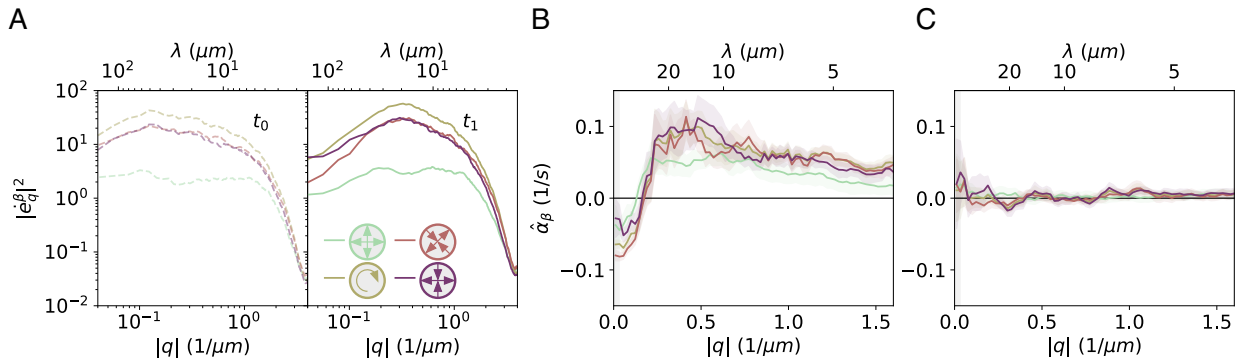

Figure 3.52: **Growth in modes of strain rate decomposition.** By decomposing the strain-rate tensor into the irreducible representation of dilation (), vorticity (), shear 1 (), and shear 2 () (see Section 3.6.1), we can construct a power spectrum for each scalar field and measure a growth rate. This decomposition is performed for systems initialized as a large crystal in (A-B). (A) Power spectrum at early time t_0 (left) and late time t_1 (right). (B) Normalized growth rate for each mode computed over the interval (t_0, t_1). The four deformation modes all participate in the crystal instability and have comparable growth rates at all wavelengths. (C) All the growth rates vanish for a system allowed to reach a steady-state.

computed from a spectral analysis of the flow confined to small ($\ell \approx 50\,\mu m$) regions of the crystal, and interpolate this result to construct a heatmap of the growth as in Figure 3.53A. In Figure 3.39, the relative growth is plotted, which is obtained by normalizing the integrated growth by the mean growth at the initial time t_0: $I_{\text{relative}} = I / \langle |I(t_0)| \rangle$. Superimposed onto this image are white solid lines representing the grain boundaries of the crystallite. This local measure of the instability reveals that the most unstable regions are localized preferentially at the centers of the crystalline domains. In the row below, Figure 3.53B, we see that the most unstable regions also coincide with the centers of large uniformly rotating crystal whorls. Finally, we aggregate integrated growth measurements and plot them against the local magnitude of the bond orientational order parameter $|\psi_6|$ in Figure 3.53C at various times t_0. This plot shows strong correlations between the level of crystal ordering and the strain instability, indicating that the dynamical restructuring of the chiral material primarily affects the bulk of crystallites.

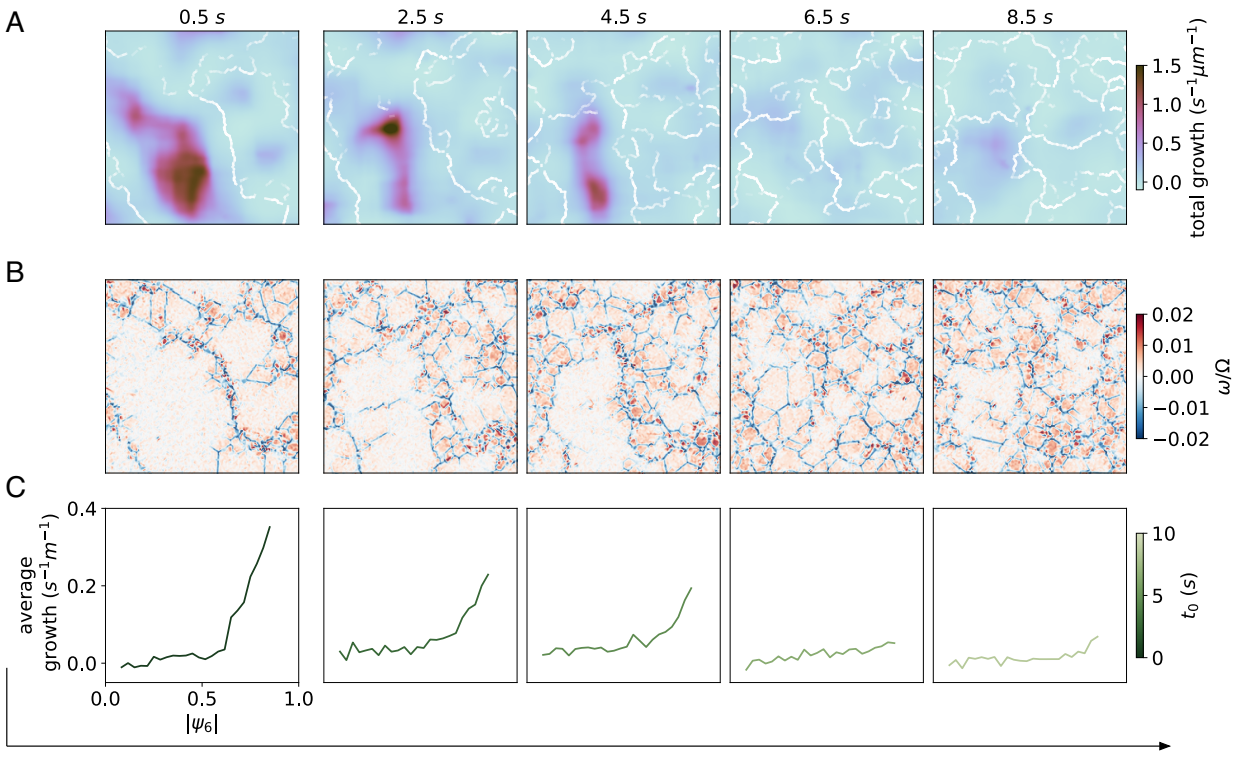

Figure 3.53: **Spatially resolved growth rate.** (A) The integrated growth rate is computed for small patches of the crystal, and interpolated to construct a heatmap. Upon this map, we draw the grain boundaries at each snapshot in time. (B) The material is maximally unstable within crystalline domains, which correspond to large patches of positive vorticity, presented at the same temporal snapshots as the growth above. (C) Aggregating individual measurements of local growth and crystalline order yields a time-sequence of curves relating instability to structure.

3.6.4 Stability of simulated crystals

To understand the origins of the experimentally instability described above, we turn to simulations of odd crystals with directly tunable transverse forces. By first investigating spring simulations (Section 3.6.4.1), we gain an understanding of the relationship between odd crystal stability and effective odd spring constants. We then apply this to both periodic, stable minimal model simulations (Section 3.6.4.2) and a range of variably stable simulations (Section 3.6.4.3) to disentangle the role of odd elasticity and dislocation-mediated melting in the self-kneading instability.

3.6.4.1 Spring-and-ball simulations

By combining the predictions of linear elasticity discussed in Section 3.5.1, with the coarse-graining procedure discussed in Section 3.5.1.3, we can derive a stability criterion for the lattice in terms of microscopic force coefficients:

$$k^2 + \left(k_o - \frac{1}{3}\eta\right)(k_o - 3\eta) < 0 \tag{3.147}$$

An interesting outcome of this prediction is that even in the absence of stabilizing longitudinal spring-like forces, an instability occurs only when $\frac{1}{3}\eta < k_o < 3\eta$.

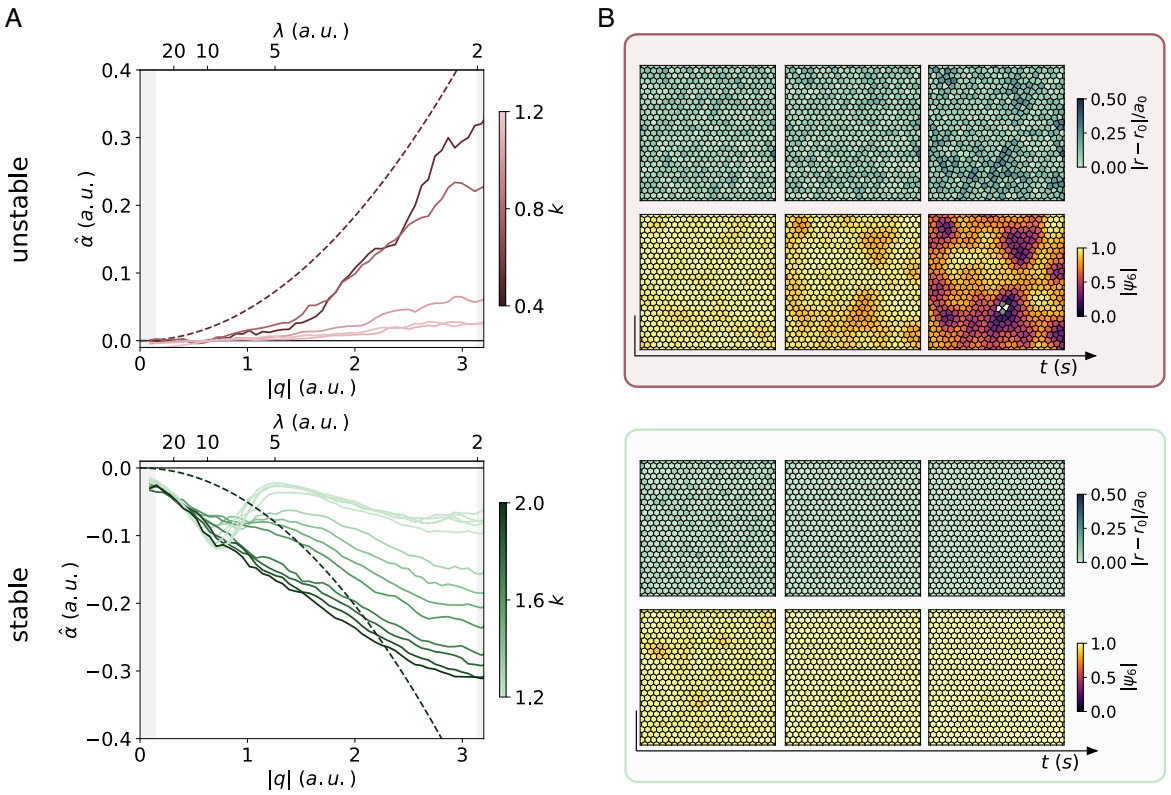

Figure 3.54: **Stability of spring simulations.** (A) Growth curves computed using the method outlined in Section 3.2.1 for simulations with a (top) linearly unstable and (bottom) linearly stable choice of spring constants. Dashed lines represent theoretical growth curves using coarse-grained elastic parameters. (B) Three snapshots from a (top) linearly stable and (bottom) linearly unstable confirmation. For each set of snapshots the displacement of particles from equilibrium is shown as well as the modulus of the order parameter $|\psi_6|$.

In the simulations presented in Figure 3.54, two distinct choices of transverse forces were made, one corresponding to the stable regime and the other to the unstable regime. In both cases some noise was added to the positions of the particles in the initial configuration. As predicted the stable case rapidly relaxes to a un-strained triangular lattice, while the unstable case spontaneously develops strains in the bulk.

The growth curves computed using the method outlined in Section 3.2.1 capture the transition between stability and instability in terms of k, and additionally show qualitative agreement in the linearly unstable case with the theory of Section 3.5.1 with the coarse-grained parameters of Section 3.5.1.3. Here, in place of the velocity field, we conduct a spectral analysis of the displacement field $\boldsymbol{u} = \boldsymbol{x} - \langle \boldsymbol{x} \rangle$, where $\langle \boldsymbol{x} \rangle$ denotes the time-averaged position of a mass.

3.6.4.2 Minimal model simulations in a periodic domain

As discussed in Section 3.5.1.3, the correct estimation of linear elastic coefficients for a nonlinear potential such as the WCA potential used in these simulations is challenging. To establish whether our choices of simulation parameters lie in a linearly stable or unstable regime, we therefore perform numerical simulations in a doubly-periodic square domain. We find that the crystal phase is linearly stable for our default choice of parameters, including all choices of Ω that we tested: a perturbed triangular crystal in a periodic domain readily decays to a perfect triangular lattice. A choice of parameters that leads to a linearly unstable system can be made, but it requires extending the range of interactions beyond nearest-neighbors. We discuss this choice in Section 3.6.4.3.

3.6.4.3 Minimal model simulations in the linearly stable and unstable regimes

The minimal model simulations of large droplets discussed in Section 3.4.2, closely mirroring the behavior of the experiment (Section 3.6.3), demonstrate that droplets generically break

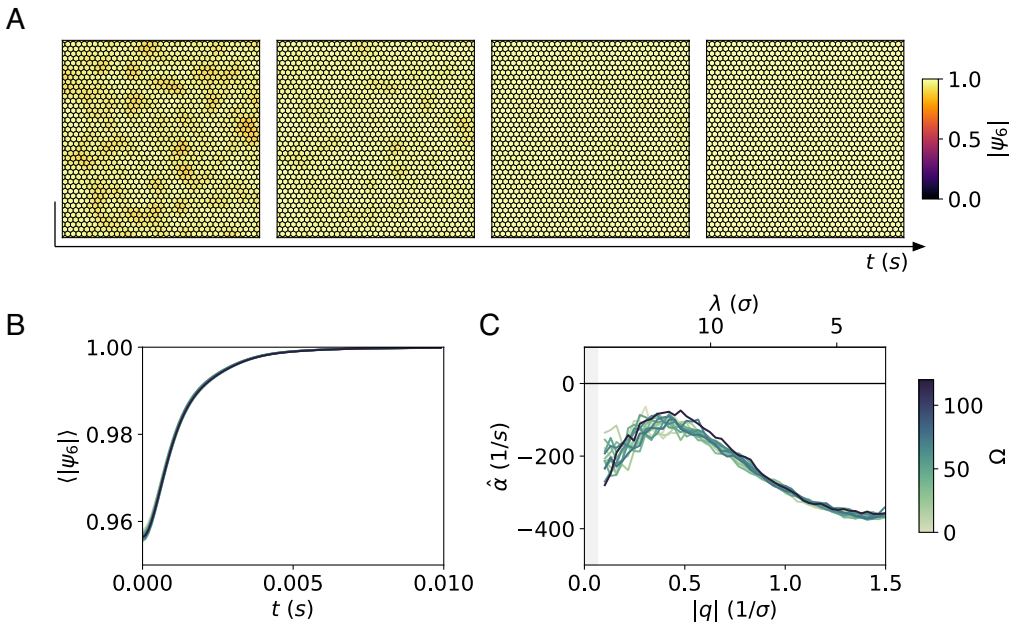

Figure 3.55: **Minimal model simulations are linearly stable.** (A) The order parameter $|\psi_6|$ plotted for a sequence of timesteps in a minimal model simulation shows the decay of disorder. (B) The system average $\langle|\psi_6|\rangle$ plotted versus time shows no relationship to driving frequency Ω. (C) Likewise, the spectral growth computed as in Section 3.2.1 for the velocity field shows stabilizing behavior independent of Ω.

up into crystal whorl states despite the linearly stable choice of interaction parameters. The breakup originates at the boundary of the system and a front of interacting self-propelled dislocations invades the bulk of the initially crystalline state, as seen in Figure 3.57A-B. Thus the crystal whorl state can arise purely as a result of the action of odd stress in an otherwise elastically stable system. In this section we explore how the parameters of our minimal model can be altered to enter a linearly unstable regime. This enables a comparison of the destabilization phenomenology between the linearly unstable and linearly stable regimes.

Choice of parameters in the light of linear stability As discussed in Section 3.5.1.3 the estimation of conventional linear elastic coefficients in the presence of the longitudinal WCA potential is challenging because of the nonlinear repulsive component of the potential. The transverse interactions, however, are more amenable to a treatment by Taylor expansion

about the steady state particle spacing. This enables an informed-guess approach to choosing parameters that might result in a linearly unstable crystal.

The transverse force in the minimal model is presented in Equation (3.8), where the cutoff length is $r_{\text{cutoff}} = 1.5\sigma$. The longitudinal force between has a minimum close to $r = 1\sigma$, and the lattice spacing in the 'steady' state is close to this value. Therefore, one can look at the Taylor expansion of the transverse force near $r = 1\sigma$ to get the spring constant and using the coarse graining approach discussed in Section 3.5.1.3 to estimate the odd moduli for the minimal model:

$$\begin{aligned} \eta = F(\sigma)/\sigma &= \frac{A_t}{\sigma}\left(\frac{1}{\sigma} - \frac{1}{1.5\sigma}\right)^2 = \frac{A_t}{9\sigma^3} \\ k_o = -\left.\frac{dF}{dr}\right|_{r=\sigma} &= 2A_t\left(\frac{1}{\sigma} - \frac{1}{1.5\sigma}\right)\frac{1}{\sigma^2} = \frac{2A_t}{3\sigma^3} \end{aligned} \tag{3.148}$$

And as a result $k_o = 6\eta$. Since the linear elastic instability criteria demands that $\frac{1}{3}\eta < k_o < 3\eta$ for a crystal to be linearly unstable, our default choice of parameters for the minimal model is expected to be stable, as observed (see Section 3.6.4.2).

To seek insight into whether a choice of parameters can be made to make the system linearly unstable, we relax the requirement that particles interact with only their nearest neighbor and re-examine the Taylor expansion of the transverse force defined by Equation (3.8). Expanding about an arbitrary lattice spacing ℓ we obtain:

$$\begin{aligned} \eta = F(\ell)/\ell &= \frac{A_t}{\ell}\left(\frac{1}{\ell} - \frac{1}{r_{\text{cutoff}}}\right)^2 \\ k_o = -\left.\frac{dF}{dr}\right|_{r=\ell} &= 2A_t\left(\frac{1}{\ell} - \frac{1}{r_{\text{cutoff}}}\right)\frac{1}{\ell^2} \\ \implies \frac{\eta}{k_o} &= \frac{1}{2}\left(1 - \frac{\ell}{r_{\text{cutoff}}}\right) \end{aligned} \tag{3.149}$$

This suggests that a linearly unstable regime may be reached if $r_{\text{cutoff}} > 3\ell$. We note that this implies that the interaction is no longer limited to nearest neighbors. The identification of this parameter regime enables the comparison of the breakup phenomenology and growth

rates in a droplet that is in the linearly stable regime from that of a droplet in the linearly unstable regime, as discussed below.

Spectral growth in the linearly stable and unstable regimes We first investigate the generic nature of the instability we observe in our experiments by comparison to the linearly stable model discussed above. We track the velocity $\boldsymbol{v}(\boldsymbol{x}, t)$ and vorticity $\omega(\boldsymbol{x}, t)$ fields using the procedure of Section 3.4.1. For each, we compute the power spectrum as in Figures 3.49 and 3.52 in Figure 3.56A-B. As in Section 3.6.3, we show in (C-D) that the estimated growth rate $\hat{\alpha}(q; t_0, t_1)$ is initially destabilizing and constant at small wavelengths. For later measurement times t_0, the growth is diminished as the system reaches the steady crystal whorl state, before the system becomes stabilizing with $\hat{\alpha} < 0$. During this initial period of destabilization, the metrics used to analyze the experimental system in Section 3.2.3 are applied: (E) total grain boundary length, (F) mean grain size, and (G) total number of defects. In this linearly stable regime, there is no spectral growth without the introduction of grain boundaries and dislocation proliferation from the free surface.

The aforementioned behavior is qualitatively distinct from that of the linearly unstable regime, which we probe by performing simulations with $r_{\text{cutoff}} = 6\sigma$. In Figure 3.57, we contrast the behavior of a linearly stable droplet (A-B), which yields to dislocation proliferation from the free surface, to the behavior of a linearly unstable droplet (C-D), which more rapidly yields to dislocation unbinding in the bulk. This qualitative change is captured through a calculation of the spectral growth for regions of varying proximity to the free surface. In the stable case, spectral growth is negligible until the dislocation front encroaches on the volume considered. Meanwhile, the linear instability leads to spatially uniform spectral growth immediately in the absence of a front.

We then ask: which of these regimes most closely resembles the experimental data presented in Figure 3.39 and Figure 3.50? To answer this question, we conduct simulations in both the linearly stable and unstable regime with an initial state that more closely resemble

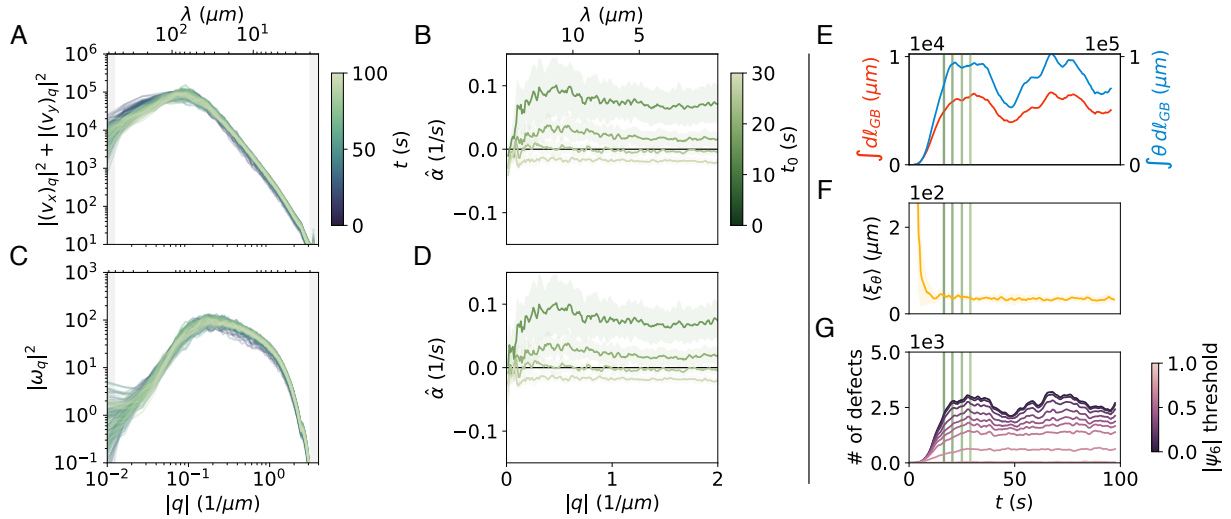

Figure 3.56: **Measuring a continuum instability.** The azimuthally-averaged power spectra over time for (A) the velocity $|(v_x)_q|^2 + |(v_y)_q|^2$, and (C) the vorticity $|\omega_q|^2$. From these spectra, we estimate the growth rate $\hat{\alpha}$ at various initial times t_0 measured in rotations from the start of the simulation. This shows close agreement between the growth rate in (B) the velocity, and (D) the vorticity. (E) The total unweighted and weighted grain boundary length, (F) mean grain size, and (G) total number of defects versus time. The vertical bars highlight the values of t_0 used for the computation of $\hat{\alpha}$.

that of the experiment, as seen in Figure 3.58, by driving a perfect, linearly stable crystal to its crystal whorl state. We then drive the stable ($r_{\text{cutoff}} = 1.5\sigma$) and unstable ($r_{\text{cutoff}} = 6\sigma$) regimes at varying rotational frequencies. For sufficiently low frequencies, the stable model of Figure 3.58A-B yields either negligible or stabilizing spectral growth, but reveals spectral growth resembling the experiment at very high frequencies. Using the procedure of Section 3.6.3, we compute the integrated local growth to show that in the most unstable case, the growth is concentrated between grain boundaries. Likewise, we demonstrate that for lower frequencies, the same behavior can be observed in linearly unstable simulations. The distinguishing feature, therefore, is the qualitative dislocation dynamics observed in these systems. In the stable case, dislocations move together as a front, whereas in the unstable case, dislocations are ejected from grain boundaries at a high rate.

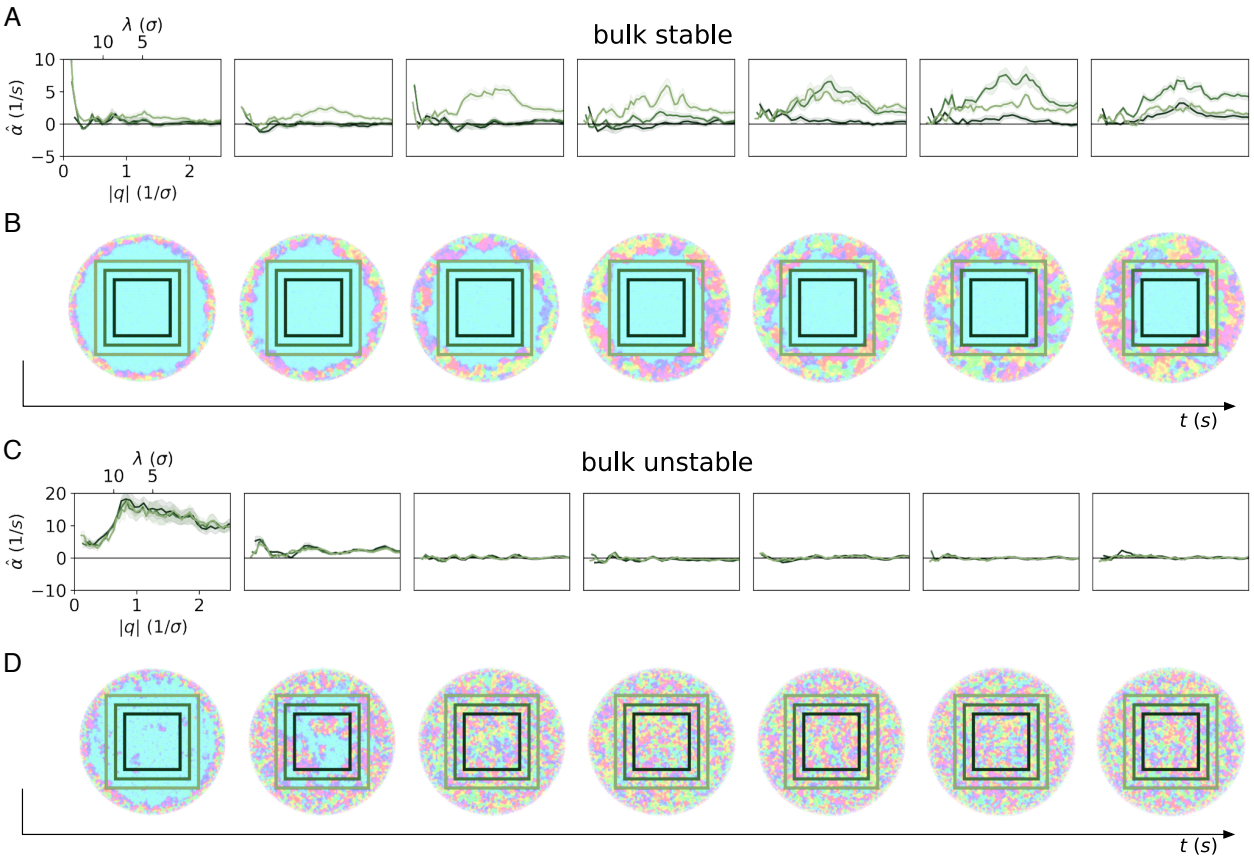

Figure 3.57: **Linearly stable and unstable odd crystals are generally destabilized.** (A) Spectral growth curves for a linearly stable droplet over time, where color denotes a specific volume as denoted in (B). (B) The phase of a droplet at the time of the corresponding growth curve evaluation. (C) Spectral growth curves for a linearly unstable droplet, also for varying times and evaluation volumes. (D) The droplet phase field reveals destabilization in the bulk that precedes the arrival of the front.

3.6.4.4 Full hydrodynamic simulations

To further test the generic nature of the instability we observe in our experiments (Section **??**) and the minimal model simulations (Section **??**), we tracked the velocity $\boldsymbol{v}(\boldsymbol{x}, t)$ and vorticity $\omega(\boldsymbol{x}, t)$ fields using the procedure of Section 3.4.1. For each, we compute the power spectrum as in Figures 3.49 ($|v_q|^2$) and 3.52 in Figure 3.59A-B. As in Section 3.6.2, we show in (C-D) that the estimated growth rate $\hat{\alpha}(q; t_0, t_1)$ is initially destabilizing and constant at small wavelengths. For later measurement times t_0, the growth is diminished as the system reaches the steady-state, before the system becomes stabilizing with $\hat{\alpha} < 0$. During this initial period

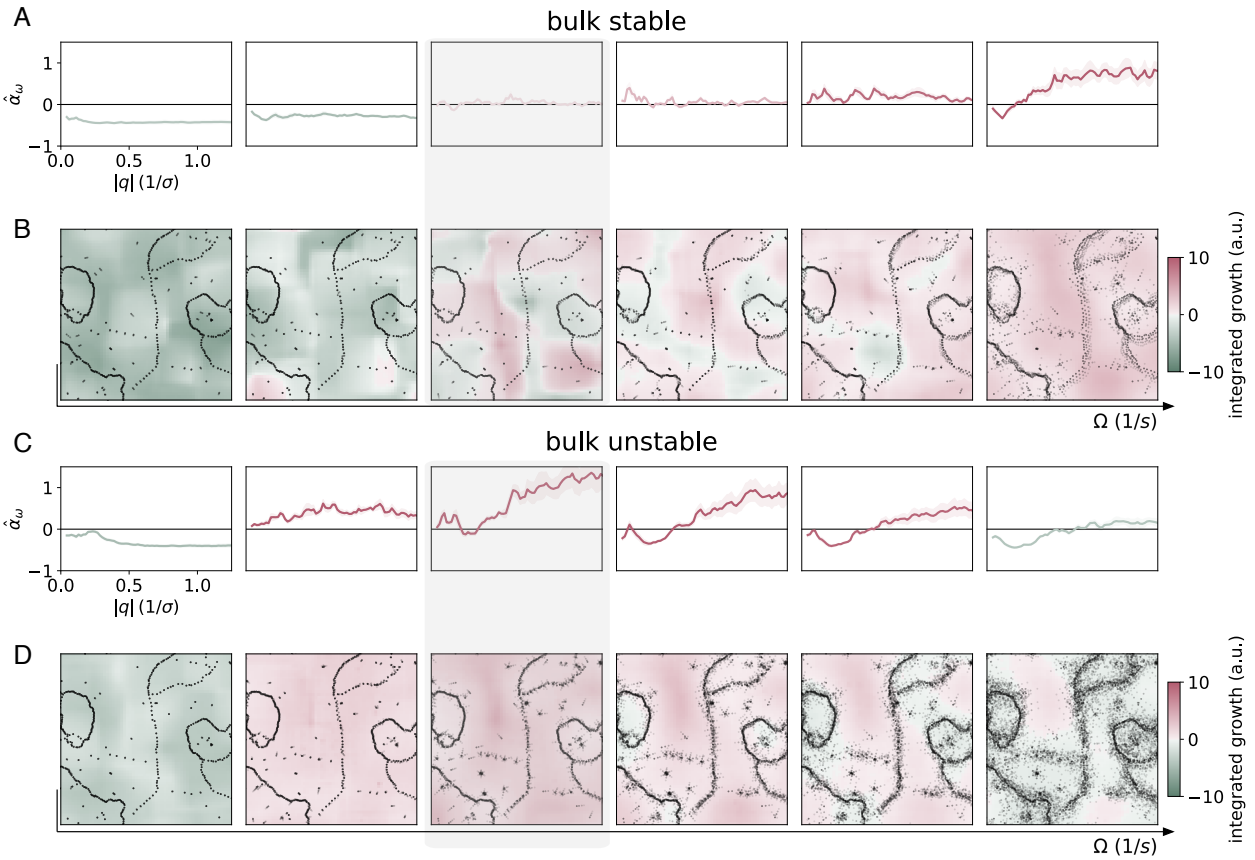

Figure 3.58: **Spatially resolved instability of the polycrystalline phase.** (A) An initially polycrystalline state can be driven at a sufficiently high rotation rate to cause spectral growth that is localized to large $|q|$, resembling strongly the form of the spectral growth shown in Figure 3.39. This is possible for a model that predicts both linear stability and instability. (B) The integrated growth is plotted spatially alongside dislocations, for which opacity indicates time of observation, showing collective motion associated with grain boundaries. (C) By contrast, a simulation of a linearly unstable polycrystal reveals spectral growth of this kind for nearly any driving frequency. (D) Unlike the linearly stable system, the dislocation motion in this case shows proliferation and propulsion away from grain boundaries.

of destabilization, the metrics used to analyze the experimental system in Section 3.2.3 are applied: (E) total grain boundary length, (F) mean grain size, and (G) total number of defects.

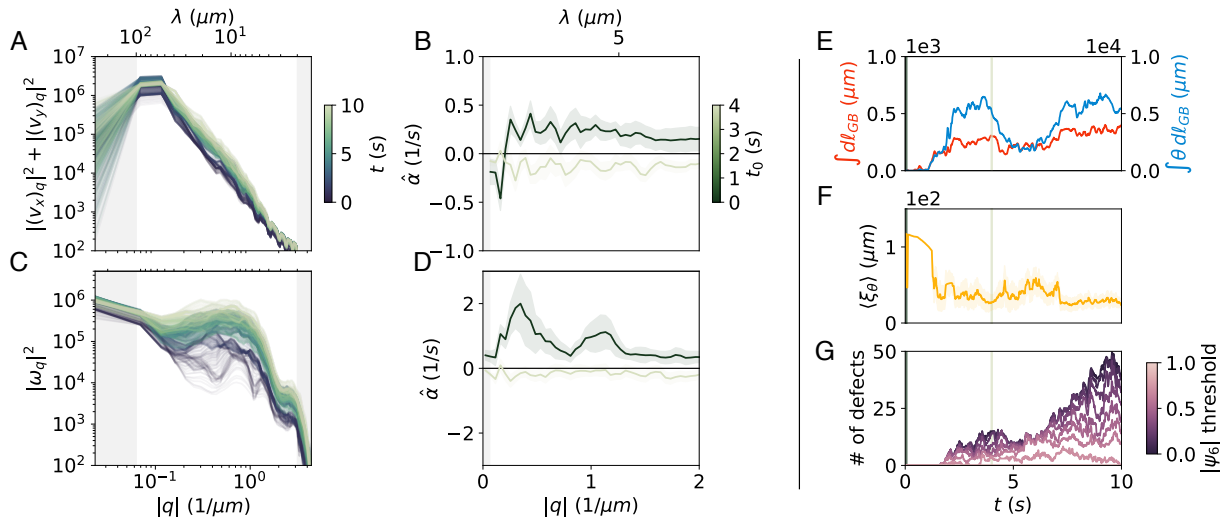

Figure 3.59: **Measuring an instability.** The azimuthally-averaged power spectra over time for (A) the velocity $|(v_x)_q|^2 + |(v_y)_q|^2$, and (C) the vorticity $|\omega_q|^2$. From these spectra, we estimate the growth rate $\hat{\alpha}$ at various initial times t_0 measured in rotations from the start of the simulation. This showed close agreement between the growth rate in (B) the velocity, and (D) the vorticity. (E) The total unweighted and weighted grain boundary length, (F) mean grain size, and (G) total number of defects versus time. The vertical bars highlight the values of t_0 used for the computation of $\hat{\alpha}$.

3.7 Conclusion

Breaking parity by spinning a material's constituents gives rise to transverse forces that fundamentally alter the organization of matter. Spinner crystals generically melt into a dynamical state driven by motile dislocations. The resulting, tunable crystal-whorl state opens new avenues for control of structure and transport from synthetic materials to biological colonies.

CHAPTER 4

TME-MODULATED COLLOIDAL CHIRAL MATTER

This chapter is primarily comprised of currently unpublished work conducted with the help of Ganan, Y. A., Poncet, A., Bartolo, D., & Irvine, W. T. M., who all contributed to valuable discussions and to developing the theory of Section 4.5.

4.1 Introduction

In passive matter, structure and shape are dictated by effective interactions that are a function of the separation and orientation of the material's building blocks. Driving materials out of equilibrium allows these interactions to depend on time, producing new phenomenology that is well known in other systems with broken isotropy, namely quantum systems [121, 122, 123]. In particular, the anisotropic drive of chiral matter is known to introduce new odd nematic-like viscous coefficients [124]. We drive a collection of colloidal magnets to rotate with an angular speed that slows the rotation of the constituents at specific moments in time. The resulting interplay between spatial and temporal order provides effective control of internal structure, global morphology, and free surface stability. We interpret our observations in terms of the competition between time-modulated internal stresses and surface forces.

4.2 Time-modulation of odd systems

We report the engineering of a chiral material with tunable anisotropy using the control scheme of Figure 4.1, and demonstrate a wide range of control over the morphologies of the resulting structures. In the following sections, we describe the rotational time-modulation procedure by which this anisotropy is achieved (Section 4.2.2).

4.2.1 *Experimental preparation*

We prepare a suspension of 'superball'-shaped colloidal particles comprised of hematite with a single magnetic domain. The particles were synthesized and coated according to the procedures referenced in [18], suspended in water, sedimented onto a glass slide, and imaged through crossed polarizers in an inverted microscope. The particles are subjected to rotation from an external magnetic field, but with a slight variation described in the following section.

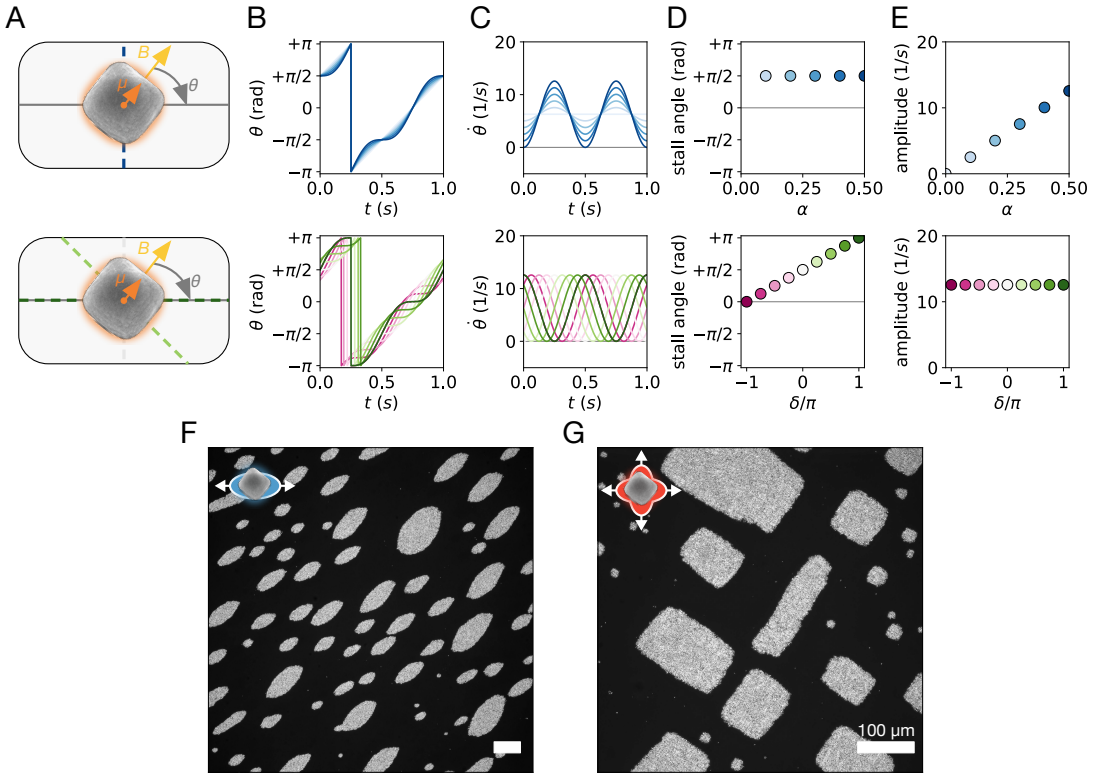

Figure 4.1: **Time-modulated rotation of the external magnetic field.** (A) Cartoon depiction of time-modulated rotation of the magnetic field orientation θ_B, causing the dipole moment μ to stall at specified intervals. (B) The field angle θ_B versus time for varying modulation strength α and phase δ, and (C) its time derivative. (D) The angle of minimum $\dot{\theta}_B$ and (E) the magnitude of the fluctuation in $\dot{\theta}_B$. By varying instead the order of the modulation n, we obtain qualitatively distinct morphologies for collections of particles, namely: (F) ellipsoidal droplets for $n = 2$ and (G) rectanular droplets for $n = 4$.

4.2.2 Time-modulated drive

In prior work, the rotation of the colloids was temporally uniform and spatially isotropic, as dictated by the external magnetic field which rotated with $\theta_B = \Omega t$. We previously reported the formation of a dense liquid-like phase due to self-attraction amongst rotating dipoles. In this work, we relax the aforementioned constraint by allowing the rotation of the magnetic field, and therefore the colloids, to be temporally non-uniform. The time-modulated rotation of the particles is achieved by directly controlling the orientation of the rotating magnetic field as a function of time, thereby inducing relatively fast and slow rotation at specified intervals. Here, we produce the generic formula for the phase of the magnetic field, $\theta_B(t)$,

$$\theta_B = \Omega t - \alpha \cos\left(n\Omega t + \delta\right), \tag{4.1}$$

where $\Omega = 2\pi f$ is the angular frequency of the particle rotation for rotation frequency f, $\alpha \in \left[0, \frac{1}{n}\right]$ is the intensity of the modulation, $n \in \mathbb{N}$ is the degree of modulation, and $\delta \in [-\pi, \pi)$ is the phase of the modulation [124]. In addition, we introduce control over the magnitude of the magnetic field strength $|\boldsymbol{B}|$, which will be presented as a ratio $|B|/B_0$ where $B_0 = 1.3$ mT is the reference magnetic field strength used everywhere unless otherwise noted. Finally, we can introduce a constant out-of-plane contribution to the magnetic field described by an angle θ. This control scheme is illustrated in Supplementary Figure 4.1, where the special cases of the modulation strength and phase are explicitly considered, as illustrated in (A). In (B-C), the orientation θ_B of the magnetic field and its time-derivative $\dot{\theta}_B$ are presented, showing that the modulation strength directly tunes the fluctuations in angular rotation rate, while the modulation phase dictates the phase of these fluctuations. In (D), we demonstrate that this temporal phase leads to a spatial change via the stall angle, and in (E) that the amplitude is meanwhile unaffected.

For the case of two-fold ($n = 2$) modulation, the above description is comprehensive.

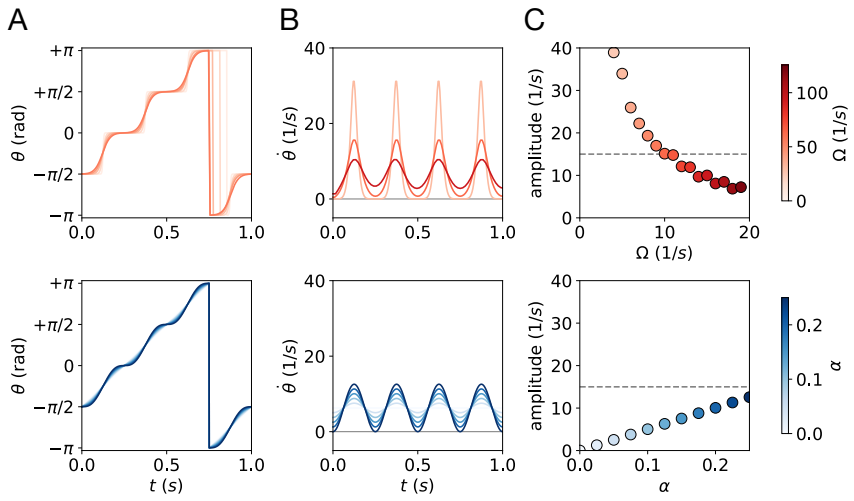

Figure 4.2: **Two approaches to four-fold time-modulated drive.** For a square-wave (top) and sine-wave (bottom) construction of the four-fold ($n = 4$) modulation, we present (A) the magnetic field phase θ_B, (B) rotation rate $\dot{\theta}_B$, and (C) rotation rate amplitude for varying Ω and α, respectively.

However, we also note that an alternative driving scheme is used for the case of four-fold ($n = 4$) modulation, in which we construct a more intensely modulated signal from a temporal square wave that is convolved with a Gaussian kernel in time. The discrepancy between these two forms is highlighted in Figure 4.2, where (A) the magnetic field phase θ_B transitions more abruptly and the (B) rotation rate $\dot{\theta}_B$ sustains greater fluctuations when driven using a modulated square wave. Due to the technical details of this construction, this amplitude decreases with frequency as seen in (C), but the square wave construction introduces a higher amplitude (top) than attainable at the theoretical maximum amplitude for the sinusoidal modulation (bottom).

4.3 Experimental characterization

As the droplets of chiral fluid prepared using the procedure of Section 4.2.1 evolve and reach their steady-states, we characterize the resulting droplet morphology and seek to use other measures of internal structure to construct a predictive model. In the following sections, we

detail the procedures and findings for the study of droplet shape both during equilibration and in the steady-state, bulk structural distortions, and relative rotational phase lag.

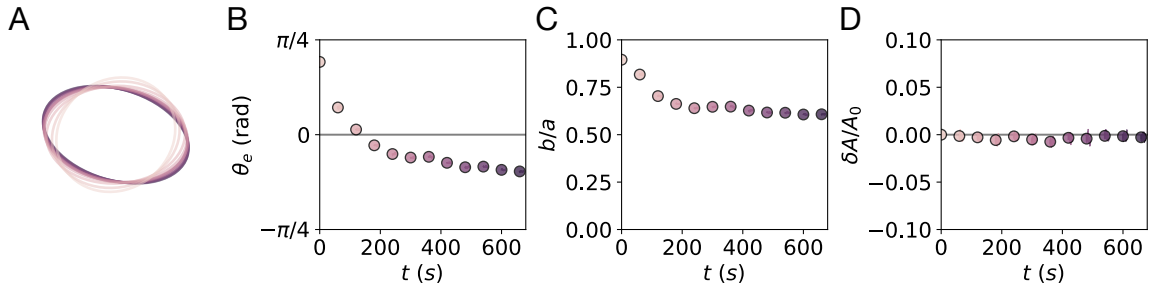

Figure 4.3: **The equilibration of a single initially-circular droplet.** An initially circular droplet evolves instantaneously to an ellipse upon the introduction of time-modulated drive, quickly reaching a steady-state as observed in the temporal evolution of (A) the fits of the droplet outline to an ellipse, (B) the droplet orientation and (C) the droplet aspect ratio. (D) Meanwhile, volume is conserved.

4.3.1 Droplet shape

Immediately upon activating the colloidal system with an isotropic drive, due to time-averaged attraction, the particles immediately form a dense phase that equilibrates to a circular droplet. Under time-modulated drive according to the control scheme of Section 4.2.2, these circular droplets can be deformed slowly to a variety of tunable steady-state morphologies that are cataloged in the following section.

The shape of this chiral fluid droplet under time-modulation can be approximated by identifying the boundary particles from a triangulation of the internal lattice. The local radius $R(\theta)$ can be approximated from the coordinates of the boundary particles where the geometric center of the droplet is taken to be the center of mass. For modulation of order $n = 2$, these boundary points are fit to an ellipse with a form

$$R(\theta) = \frac{ab}{\sqrt[n]{|b\cos(\theta - \theta_e)|^n + |a\sin(\theta - \theta_e)|^n}} \tag{4.2}$$

with fixed order $n = 2$. From this fit, we extract the orientation of the droplet θ_e, and the lengths of the major and minor axes a and b. We can also compute the enclosed area A to demonstrate incompressibility. For modulation of order $n = 4$, we perform this fitting to a super-ellipsoid defined by Eq. 4.2 for free n.

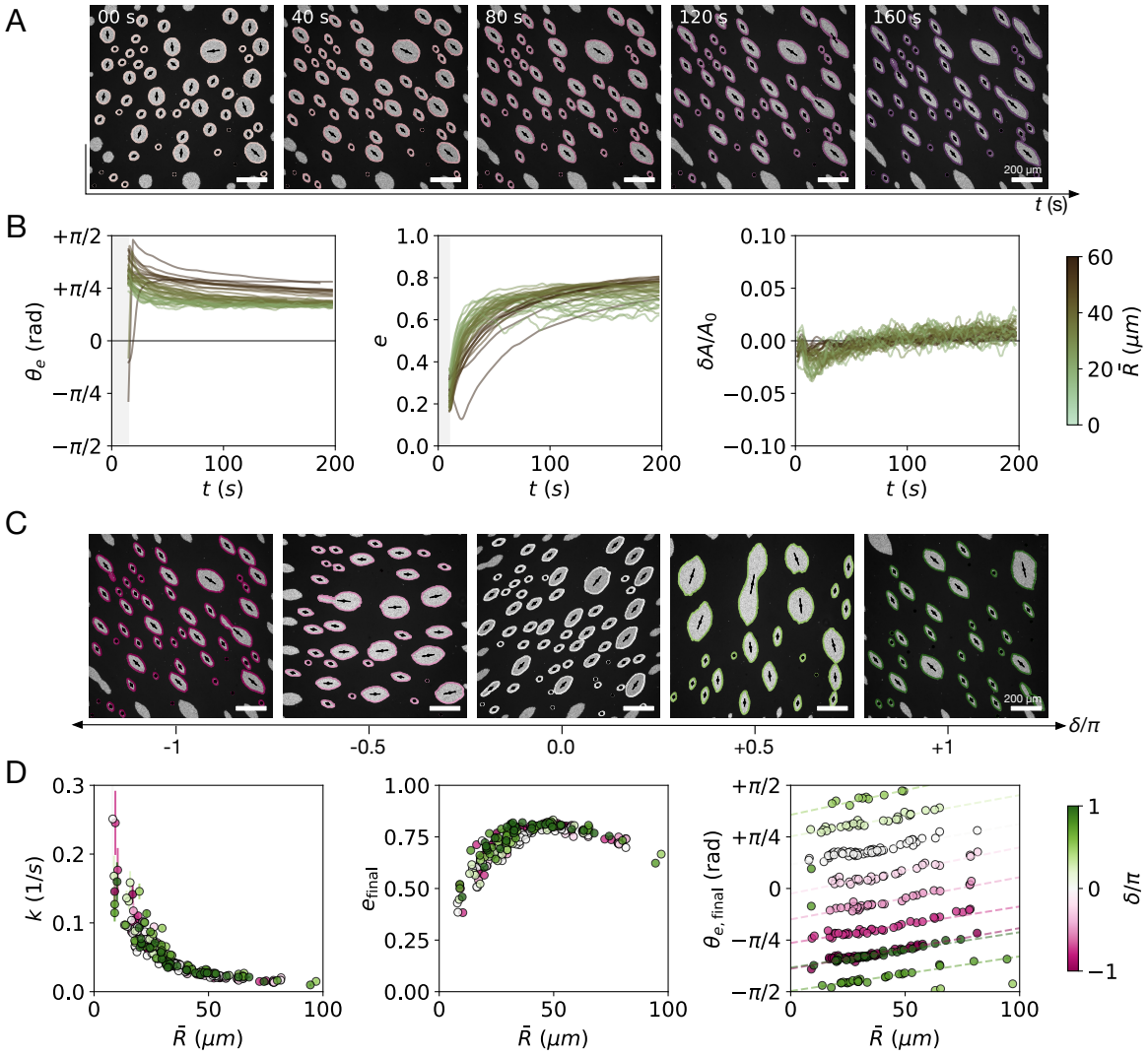

Figure 4.4: **The equilibration of many initially-circular droplets** (A) Snapshots and extracted outlines of a collection of droplets driven by time-modulated rotation from an unmodulated steady-state. (B) The droplet orientation θ_e, eccentricity e, and relative change in volume $\delta A/A_0$ for this collection of droplets. (C) Intermediate snapshots and outlines of droplets driven at varying modulation phase δ. (D) For this collection of droplets, the timescale k of the shape equilibration, final eccentricity e_{final}, and final droplet orientation $\theta_{e,\text{final}}$ versus droplet size $\bar{R}$.

4.3.1.1 Shape equilibration

We can first perform this analysis for a single droplet that is prepared in an initially nearly-circular state. Then, we observe the time-evolution of the orientation θ_e and aspect ratio b/a as the droplet evolves to an ellipse, enabling us to estimate a timescale for the equilibration process. This analysis for a single droplet is presented in Figure 4.3. Here, we see that the (B) orientation and (C) aspect ratio of the ellipse deviate instantaneously from a circle and stop changing within minutes, while the (D) fluctuation in volume $\delta A = A - A_0$ for initial area A_0 is negligible, confirming incompressibility.

This process can be repeated for a collection of many droplets with varying radius $\bar{R} = \sqrt{ab}$, as shown in Figure 4.4A. As shown in (B), we find that the timescale for equilibration of both droplet orientation and aspect ratio, now presented as eccentricity: $e = \sqrt{1 - b^2/a^2}$, depends on the droplet size. We demonstrate, by varying the phase angle of the modulation δ, as illustrated in (C), that these equilibration dynamics are isotropic. To do so, the curves $e(t; \bar{R})$ are fit to the form

$$e(t) = \frac{e_0}{1 + e^{-k(t-t_0)}}, \tag{4.3}$$

and the timescale k for this morphological change is extracted and plotted in (D). This reveals both an inverse relationship between the equilibration timescale k and droplet size, and an increase in the typical steady-state eccentricity e_{final} with droplet size $\bar{R}$. However, within the range considered in subsequent steady-state experiments ($\sim 50 - 100$ μm), both the timescale and steady-state morphology are roughly constant.

4.3.1.2 Steady-state shape

Having identified a timescale for the equilibration of a droplet under time-modulation, we can identify the geometric features of the steady-state of a droplet. In addition to fitting a droplet to an ellipse or super-ellipse, we can directly compute a parameterized form for the edge geometry $R(\theta)$, and subsequently extract the curvature $\kappa(\theta)$ along this surface

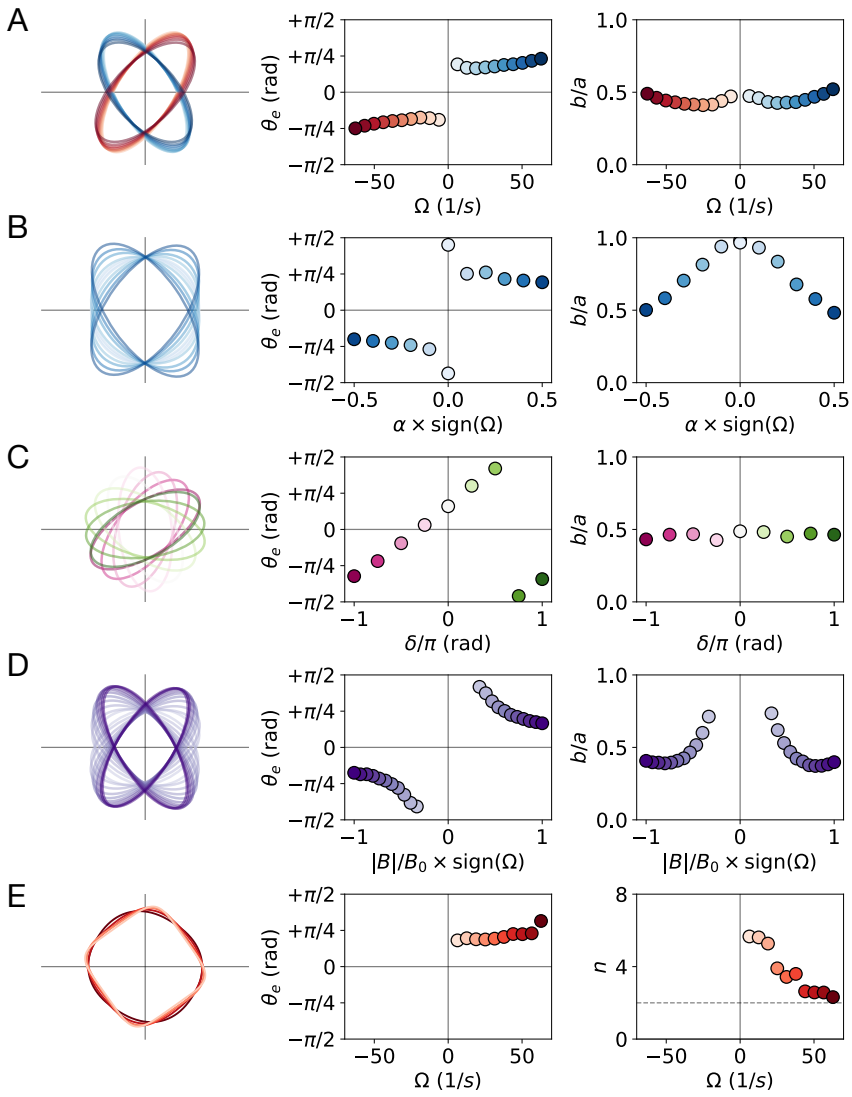

Figure 4.5: **Steady-state droplet morphology.** The steady-state droplet morphologies for a time-modulated system are presented for two-fold and four-fold modulation and for varying control parameters: (A) rotational frequency Ω, (B) modulation intensity α, (C) modulation angle δ, (D) magnetic field strength $|\boldsymbol{B}|$, and (E) modulation order n.

according to

$$\kappa(\theta) = \frac{R^2 + 2R'^2 - RR''}{(R^2 + R'^2)^{3/2}}, \tag{4.4}$$

where $R' = \frac{dR}{d\theta}$. For convenience, in this section we present $\delta\kappa(\theta) = \kappa(\theta) - \kappa_0$ where $\kappa_0 = \langle\kappa(\theta)\rangle_\theta$.

In Figure 4.5, we show the characterization of a wide range of droplets prepared in exper-

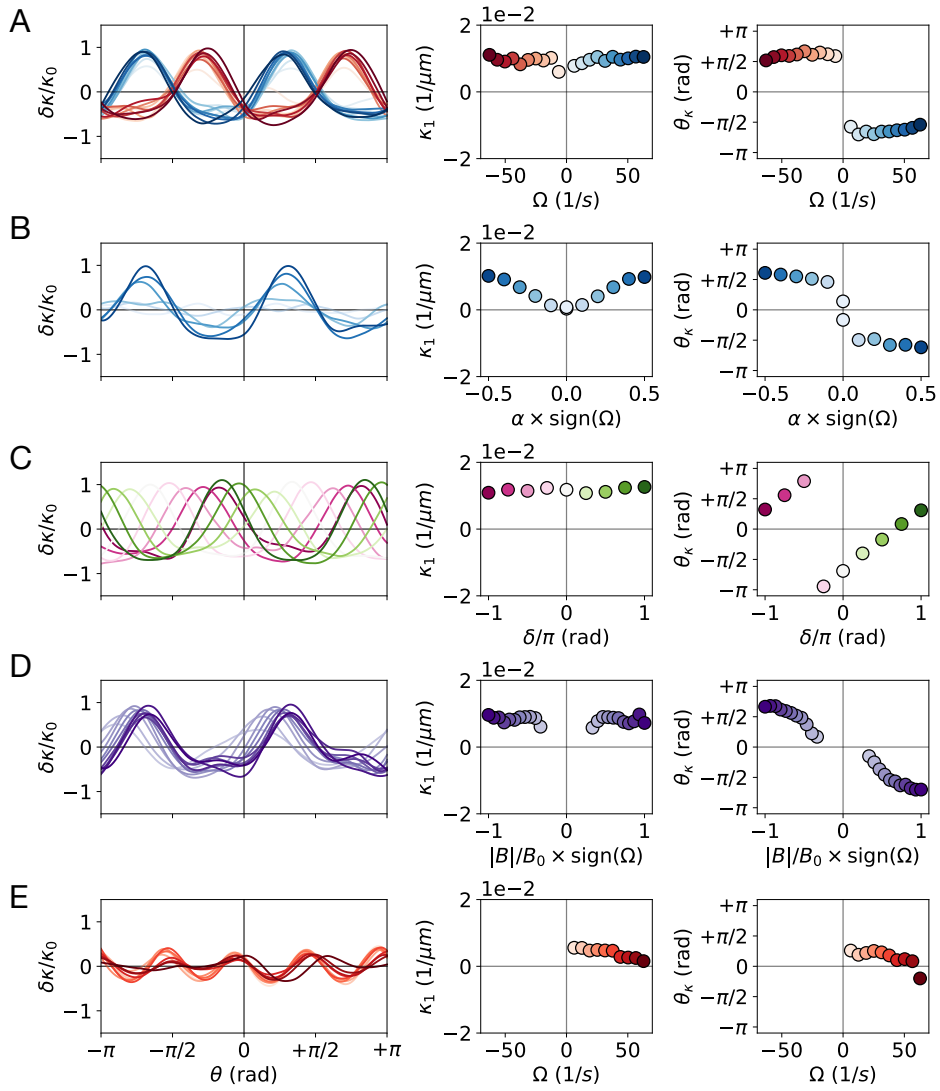

Figure 4.6: **Steady-state droplet surface profiles.** The curvature $\kappa(\theta)$ of the free surface for chiral droplets driven with variable time-modulation are presented for two-fold and four-fold modulation and for varying control parameters: (A) rotational frequency Ω, (B) modulation intensity α, (C) modulation angle δ, (D) magnetic field strength $|\boldsymbol{B}|$, and (E) modulation order n.

iments for which control parameters including rotational frequency Ω, modulation intensity α, modulation angle δ, magnetic field strength $|\boldsymbol{B}|$, and modulation order n are tuned. We find negligible changes in the morphology of droplets in the steady-state with respect to the frequency of rotational drive Ω over the range considered in these experiments. However, the orientation of droplets directly responds to the chirality, represented by sign(Ω), as seen in

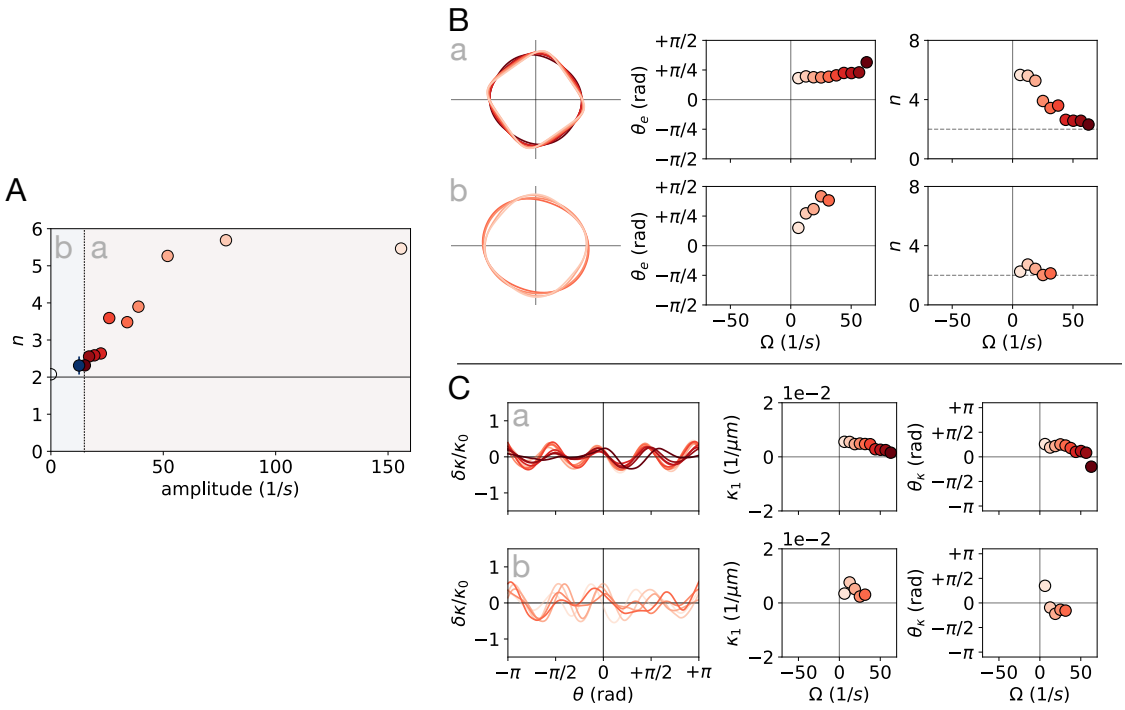

Figure 4.7: **Steady-state droplet morphology depends on four-fold drive.** (A) For (a) sinusoidal four-fold modulation parameterized by α, the amplitude of $\dot{\theta}_B$ is limited, as is the order n the of resulting super-ellipsoids measured, and (b) square modulation bypasses this limit, producing droplets of higher n. (B) Droplet outlines, morphological properties, and (C) surface curvature for (a) square and (b) sinusoidal four-fold modulation parameterized by Ω.

Figure 4.5A. We are capable of controlling the (B) droplet aspect ratio b/a and (C) droplet orientation θ_e in isolation using the modulation intensity α and modulation angle δ, respectively. By contrast, changes to the (D) inter-particle interactions via tuning the magnetic field strength $|\boldsymbol{B}|$ lead to both narrowing and rotating of the steady-state morphology.

In terms of the curvature, as in Eq. 4.4, the deviation from constant is measured and fit to the form $\delta\kappa(\theta) = \kappa_1 \cos(n\theta + \theta_\kappa)$ for the magnitude κ_1 and phase θ_κ, as shown in Figure 4.6. The relationships between control parameter and morphological change observed in the discussion of Figure 4.5 are consistent with these results, which will prove useful in comparisons with the model of Section 4.5.

Additionally, we observe that the symmetry of the droplet morphology can be selected

for two specific cases: (1) the $n = 2$ case documented previously, which produces ellipsoidal droplets, and (2) the $n = 4$ case which produces super-ellipsoidal droplets. As shown in Figure 4.5E, while the semi-diameters a and b of the super-ellipse are roughly equal, the shape parameter n responds to rotational drive (effectively, modulation strength – see Section 4.2.2). We also note that the two forms of four-fold modulated drive considered here produce differing droplet morphologies. Namely, as in Figure 4.7A, we plot the fitted values of n for the surface morphology of droplets driven by (a) sinusoidal modulation via-α, and (b) square modulation via-Ω. This demonstrates that four-fold modulation produces increasingly square droplets in a manner correlated with the parameter that unifies these two drive forms, the amplitude of fluctuations of $\dot{\theta}_B$ shown in Figure 4.2. In (B-C), the analog representations of droplet morphology from Figures 4.5 and 4.6 are shown for both drive forms.

4.3.2 Bulk structural distortions

In this section, we describe the extraction of a time-varying structural deformation at the level of a single unit cell of the odd crystal as it is subjected to time-modulated drive. First, for every particle, we compute the local bond-orientational order of polycrystalline packings at the position $\boldsymbol{r}_j$ of the jth particle as

$$\psi_6(\boldsymbol{r}_j, t) = \frac{1}{N_j} \sum_{i=1}^{N_j} \exp\left(i6\theta_{ij}\right), \tag{4.5}$$

where the jth particle has N_j neighbors and θ_{ij} is the angle formed between the bond $\boldsymbol{r}_{ij} = \boldsymbol{r}_i - \boldsymbol{r}_j$ connecting the ith and jth particles and the x-axis. To enable the detection of clusters, the field ψ_6 is coarse-grained by averaging over a particle's nearest neighbors.

The particles are then binned according to either proximity to the edge of a droplet or $|\psi_6(\boldsymbol{r}_j, t)|$, while bonds are filtered by a threshold to their length $|\boldsymbol{r}_{ij}|$ to first construct

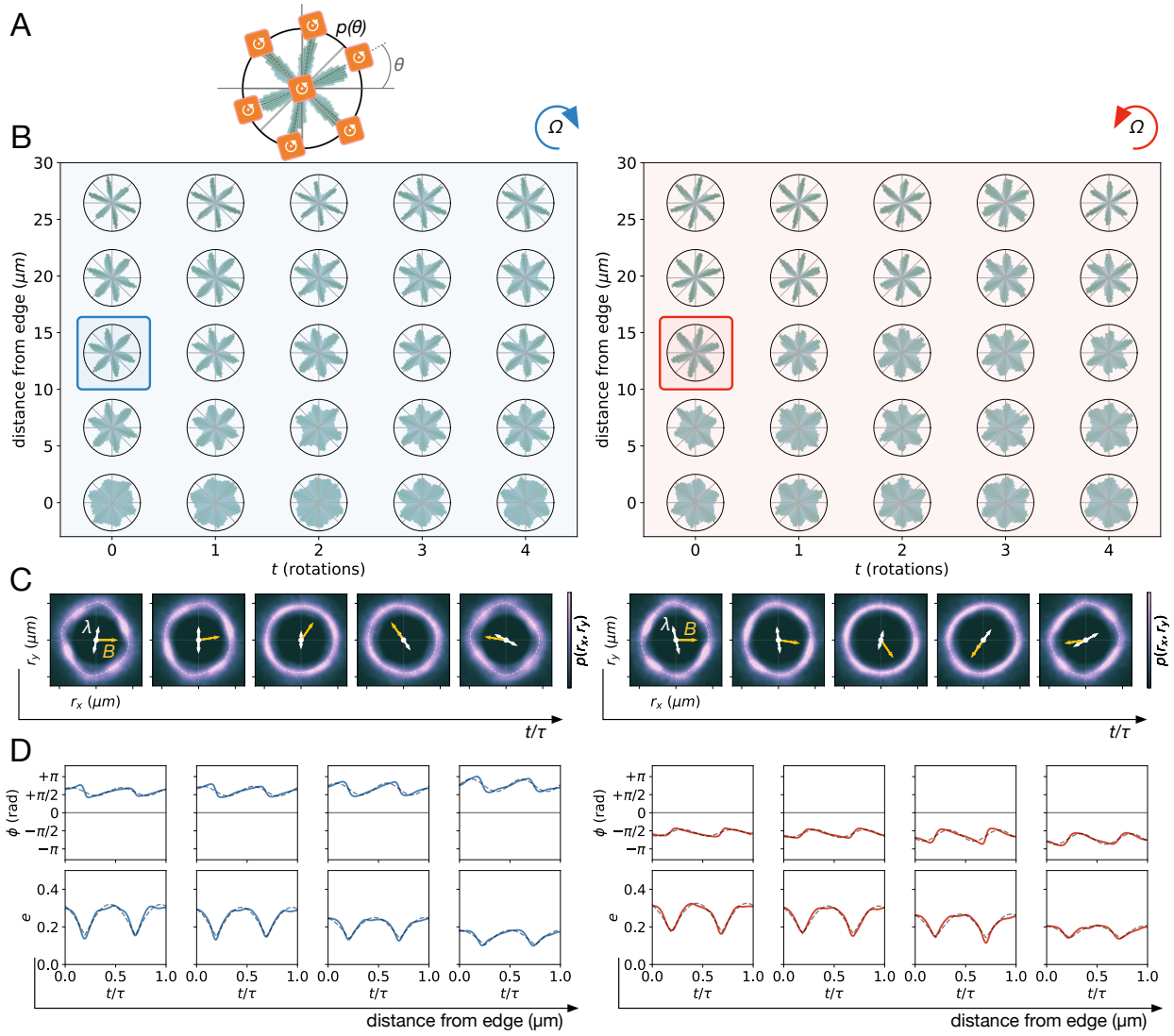

Figure 4.8: **Bond histogram of time-modulated lattice.** (A) The probability distribution $p(\theta)$ for the bond-angles θ of a particle and its nearest neighbors is aggregated over a subset of particles during a period of rotation. (B) This construction is repeated for particles of varying distance to the a droplet edge and over the evolution of a droplet in its steady state for clockwise (left) and counterclockwise (right) rotation. (C) For the highlighted subset, the distribution of bond vectors $p(r_x, r_y)$ is presented over time t/τ over a rotation. The vectors λ and B denote the eigenvalues of the image moment and magnetic field orientation, respectively. (D) The orientation ϕ and eccentricity e representing the lattice distortion of (C) is plotted over time, revealing periodic dynamics.

a histogram of bond angles $p(\theta)$ as shown in Figure 4.8A-B. This analysis reveals only negligible fluctuations in lattice orientation over time, and blurring of order as the droplet

edge is approached. However, we find that the dynamics occurring on the timescale of a single particle rotation reveal surprising structural evolution.

To reveal this phenomenology, we construct two-dimensional histogram, $p(r_x, r_y; t/\tau)$ that describes the density of bonds with projections $r_x = \boldsymbol{r}_{ij} \cdot \hat{x}, r_y = \boldsymbol{r}_{ij} \cdot \hat{y}$ observed at a time t/τ for rotation period τ. An example histogram and its time-evolution are displayed in Figure 4.8. From these histograms, we seek to extract a measure of the distortion of the lattice in time, and consider two approaches throughout the rest of this text. In the first, we treat the histogram as an image and extract the central image moments, from which we can define an orientation and deformation strength. In the second, we consider the case in which there are discrete peaks in the histogram, and instead identify average 'particle' trajectories from the histogram.

4.3.2.1 Image moment extraction

For histograms $p(r_x, r_y; t/\tau)$ constructed from interior pointsets of droplets observed at a specified time t/τ, we treat the histogram as a density heatmap and compute the central image moments

$$M_{ij}(t/\tau) = \sum_{r_x} \sum_{r_y} r_x^i r_y^j p(r_x, r_y; t/\tau), \tag{4.6}$$

throughout a rotation period. Note that the centroid is assumed to be $\bar{r}_x = \bar{r}_y = 0$. We then extract the image orientation using the second-order moments via $\mu_{ij} = M_{ij}/M_{00}$. This allows the computation of the image orientation via

$$\phi(t/\tau) = \tfrac{1}{2} \arctan\left(\frac{2\mu_{11}}{\mu_{20} - \mu_{02}}\right), \tag{4.7}$$

and the eccentricity of the image is given by,

$$e(t/\tau) = \sqrt{1 - \lambda_2/\lambda_1}, \tag{4.8}$$

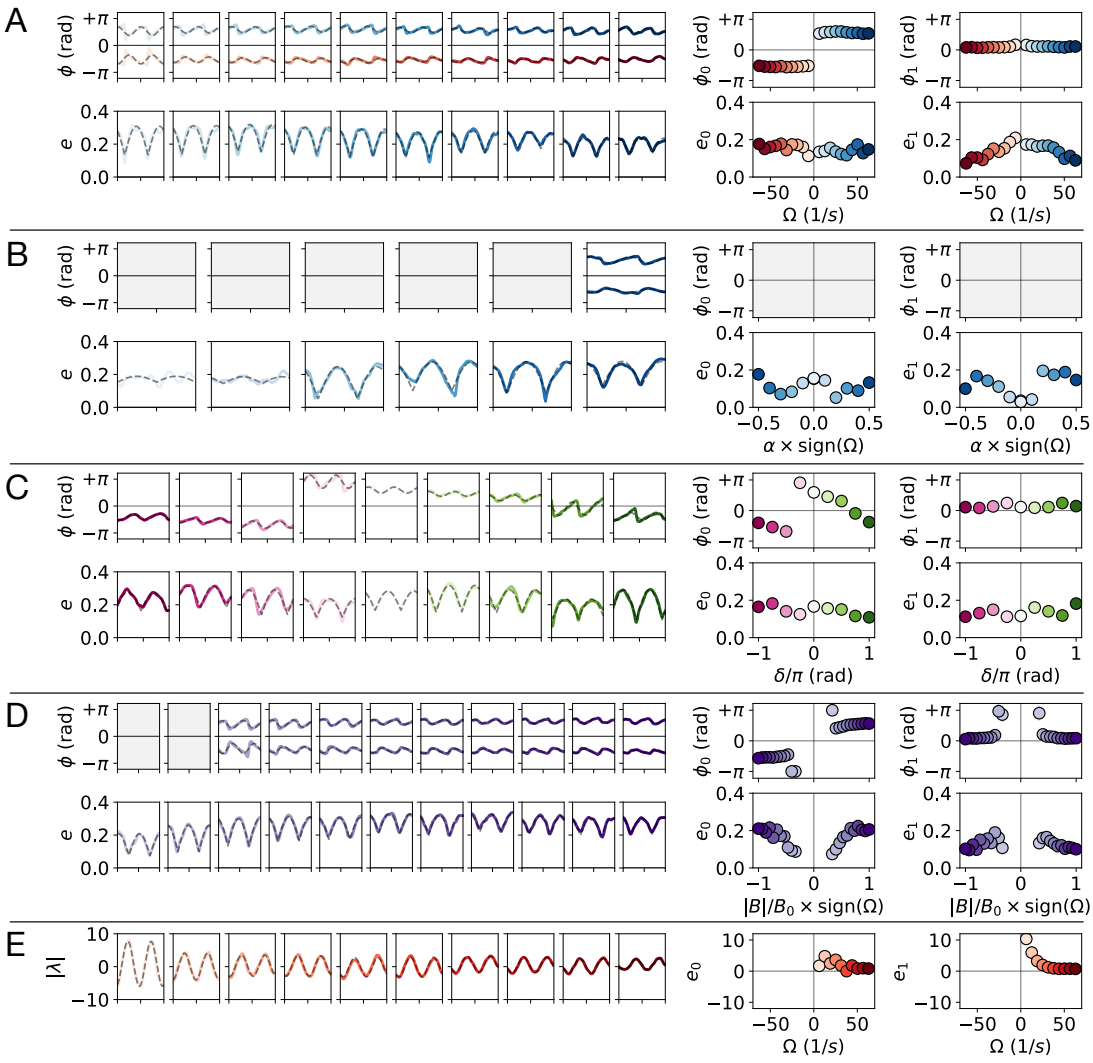

Figure 4.9: **Distortions to orientation and eccentricity.** For time-modulated rotation experiments in which the (A) rotational drive Ω, (B) modulation strength α, (C) modulation phase δ, (D) magnetic field strength $|B|$, and (E) modulation order n are varied, we report (left) the time-evolution of the phase ϕ and eccentricity e of the bulk structural distortions as illustrated in Figure 4.8. By fitting these curves, we estimate (right) parameters representing the mean (ϕ_0, e_0) and amplitude (ϕ_1, e_1) of the distortions over a period of particle rotation.

which effectively represent the orientation and aspect ratio of an ellipse representing the distortion of the unit cell. Note that the eigenvalues are

$$\lambda_{1,2} = \frac{\mu_{20} + \mu_{02}}{2} \pm \frac{\sqrt{4\mu_{11}^2 + (\mu_{20} - \mu_{02})^2}}{2}. \tag{4.9}$$

In sum, we extract an orientation $\phi(t)$ and an eccentricity $e(t)$ for the distortion of the lattice by considering a histogram of the bonds from any given particle to its nearest neighbors. For a selection of the experiments considered in this work, we present these results and fits to the form $\phi = \phi_0 + \phi_1 \cos\left[2(2\pi t/\tau - \xi_\phi)\right]$ and $e = e_0 + e_1 |\sin\left(2\pi t/\tau - \xi_e\right)|$ in Supplementary Figure 4.9. The extracted means (ϕ_0, e_0) and amplitudes (ϕ_1, e_1) are displayed, and reveal a number of relationships between internal structure and time-modulated drive. Namely, drive chirality via $\text{sign}(\Omega)$ sets the average orientation of lattice distortions ϕ_0, while otherwise not dictating dynamics. The modulation strength α and modulation phase δ both directly tune the amplitude of distortion eccentricity e_1 and average angle ϕ_0, respectively. Meanwhile, the magnetic field strength $|B|$ tunes both simultaneously.

4.3.2.2 Particle trajectory extraction

For crystals that are driven with a modulation of $n = 4$, the above procedure is unnecessary, as discrete particle positions can be identified in (r_x, r_y) space. We identify the N brightest local maxima at each moment in time and use the pointset $\{\boldsymbol{x}_j : j = 1 \ldots N\}$ for future computations. A sequence of snapshots of the histogram, labelled with the identified maxima, is presented in Figure 4.10. The choice of N is made to correspond with the order of the lattice, and is $N = 6$ for the triangular lattices observed here unless otherwise noted. As seen in (A), there are noticeable distortions to the average lattice at lower drive frequencies than at (B) higher drive frequencies, suggesting a relationship between the order of droplet morphology and distortions to internal structure.

4.3.2.3 Structural distortion equilibration

As observed in Section 4.3.1.1, the equilibration of the shape of a droplet under time-modulation is a slow process that takes minutes. A natural question is then: what is the time-scale for the equilibration of the internal structural deformation? To address this ques-

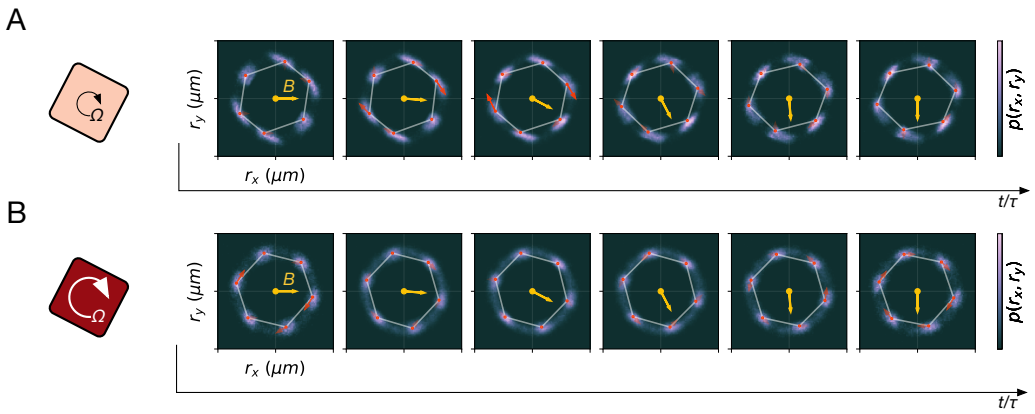

Figure 4.10: **Distortions to the particle trajectories.** Under four-fold modulation, we plot bond distributions $p(r_x, r_y)$ and track the six maxima to identify distortions in the average unit cell over time. Larger distortions are observed for (A) lower rotation frequencies than (B) higher rotation frequencies.

tion, we perform the above analysis on the lattice associated with the experiment of Figure 4.3, revealing the results of Figure 4.11. We show in (A) that the droplet's morphological evolution is relatively slow compared to the fast evolution of (B) the internal structure as quantified by $\phi(t)$ and $e(t)$, plotted in each frame over a cycle of rotation, where each frame is separated by a minute. As shown in (C), the parameters that fit these curves are effectively constant in time after the initial frame, suggesting that the internal structural equilibration is nearly immediate.

4.3.3 Relative phase lag

The orientations of the dipoles in the odd crystal, θ_j typically lag behind the externally imposed magnetic field orientation θ_B. We assume the phase lag is spatially and temporally uniform in the bulk, and estimate it by exploiting the birefringence of the colloids. We assign an intensity I_j to each particle by first computing the total intensity of the microscope image in the vicinity of the jth particle, and then subsequently averaging I_j across each particle's nearest neighbors. The average intensity $\bar{I}(t) = \langle I_j(t) \rangle_j$ completes four oscillatory periods during each rotation of a particle, such that the relative phase between two experiments β

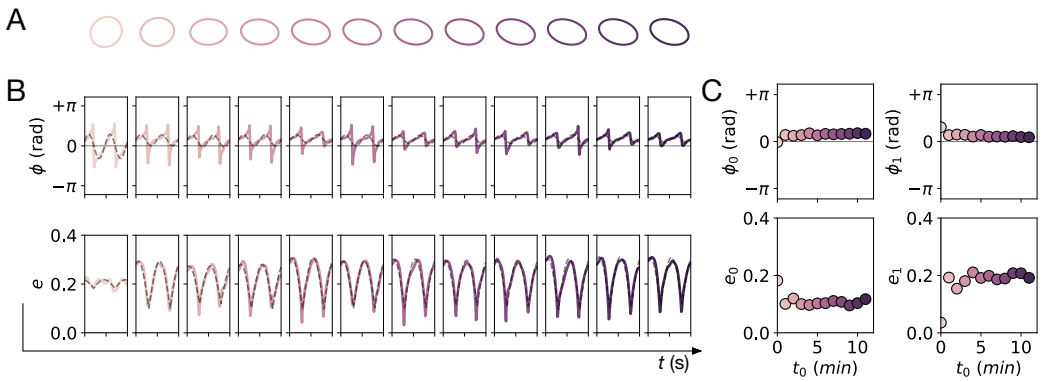

Figure 4.11: **Distortions to orientation and eccentricity during droplet equilibration.** As a typical droplet reaches the time-modulated steady-state from the un-modulated state, we track its (A) morphology evolution alongside its (B) bulk structural distortion, as quantified by the phase ϕ and eccentricity e. (C) By fitting these curves, we estimate (right) parameters representing the mean (ϕ_0, e_0) and amplitude (ϕ_1, e_1) of the distortions over a period of particle rotation, revealing little change over time.

can be read off from the phase lag, as shown in Figure 4.12A. Here, we show that there is a phase lag that is increased as the particle rotation frequency Ω is increased (B), and a phase lag that increases as the magnetic field strength $|\boldsymbol{B}|$ is decreased (C).

4.3.4 Surface instability

In the above sections, we have characterized the properties of an isolated droplet that equilibrates to a circle without time-modulated rotation. Here, we observe the effect of time-modulation on a large flat interface, in which the modulated rotation has a phase at an angle φ to the surface normal $\hat{n}$ of the colloidal medium, as in Figure 4.13A. The effect of chirality in this system is to generate an edge current $\boldsymbol{u}$ that flows to the right in this diagram. In addition, we vary the surface tension directly by tuning the out-of-plane component of the magnetic field via the angle θ (Section 4.2.2). In Section 4.4.3, we discuss the relationship between the field orientation and surface tension.

Upon activating the time-modulated rotation of the colloids, the surface abruptly becomes uneven and surface perturbations rapidly grow, quickly forming asymmetric spikes as in

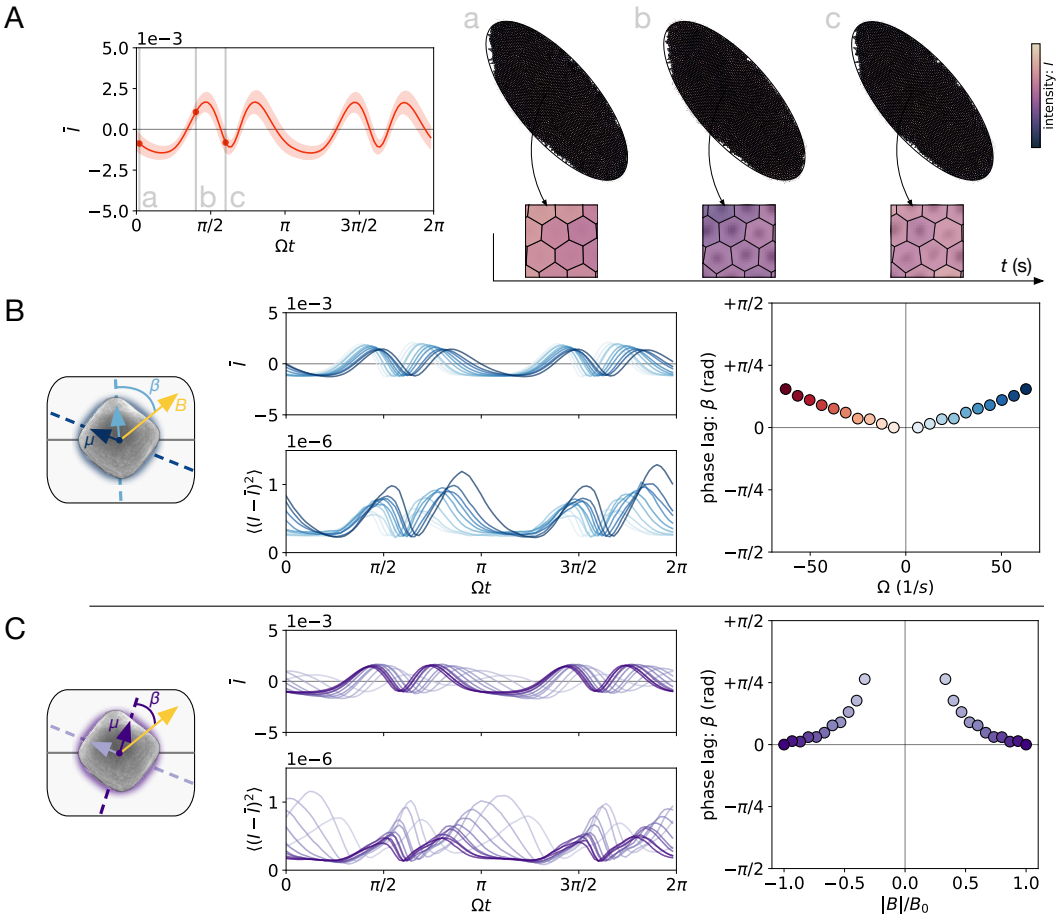

Figure 4.12: **Relative phase lag between a set of experiments.** (A) The average image intensity, or brightness, of the collection of particles within a droplet is plotted versus time for a droplet that experiences time-modulated rotation. As highlighted in (a-c), the phase of the particles oscillates both non-uniformly in time and in space. (B) We assume that all particles driven with a particular form have a phase lag β between their dipole orientation and magnetic field orientation, and we assume that this response is symmetric under $\Omega \to -\Omega$. Increasing the driving frequency causes the intensity to respond on a delay (top) and increases the variance in the intensity throughout a droplet (bottom), producing a phase lag linear in Ω (right). (C) Decreasing the magnetic field strength has the same effect on the intensity, and (right) produces a less trivial relationship between field strength and phase lag.

Figure 4.13C. We track the evolution of this surface and measure both the height $h(x,t)$ of the interface and the geometry of the surface $\theta_n(s,t)$ and $\kappa(s,t)$, the normal angle and curvature. Here, we have parameterized the interface by the arc length s for a total curve of length L. As in (B), we are able to observe the growth and translation of individual spikes

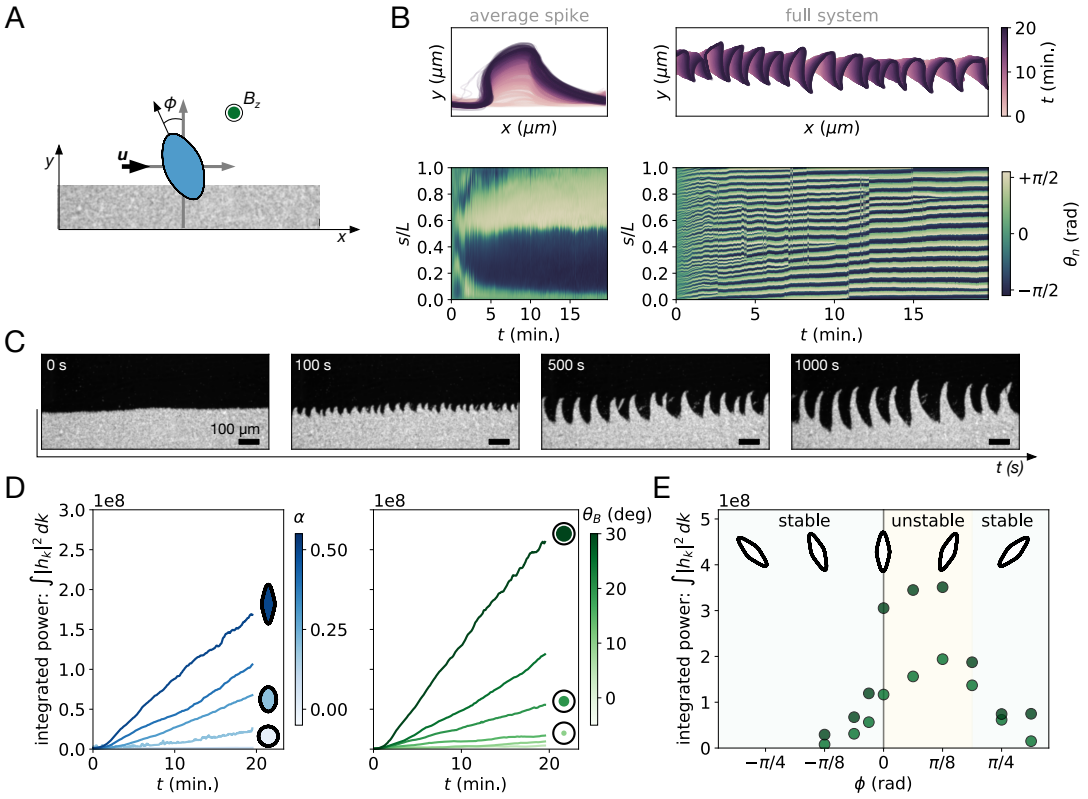

Figure 4.13: **A time-modulated 'spiky' instability.** (A) The time-modulation in these experiments is performed along an axis with angle ϕ to the surface normal $\hat{n}$, and has an out-of-plane contribution B_z. (B) The edge of the average spike is plotted both in real coordinates over time (left, top) and as a kymograph defined by its normal angle θ_n (left, bottom). This same procedure is repeated for the full experiment without collapsing the individual spikes (right). (C) For a representative experiment, we show snapshots of the surface evolution as a function of time. (D) We estimate the integrated power of the height spectrum as the spikes evolve for variable modulation strength (left) and B_z (right). (E) A phase diagram reveals that the surface is only unstable to these spikes for a small range of angles and only when B_z is large.

(right, top) and their progressive coarsening (right, bottom). By aligning all of the spikes in a single temporal snapshot according to their surface normal angle θ_n, we observe that there is a characteristic shape that is constant in time (left).

As in the other experiments reported here, we also vary the modulation strength and the strength of the out-of-plane field. We then measure the total power of the surface perturbation as $\int |h_k|^2 \, dk$ where h_k is the Fourier transform of $h(x)$, the height profile. Using this as a metric for the magnitude of the instability, we see in Figure 4.13D that

the instability is amplified by increased modulation strength (left) and increased out-of-plane field strength (right). Fascinatingly, this same analysis for the maximum modulation strength, but varying modulation phase, reveals that the instability is strongly peaked at angles $\phi \geq 0$. Further, the signature of the instability is only observed within a limited range of angles, suggesting that there is an interplay between the bulk stress due to time-modulation (see Section 4.4.2) and the hydrodynamic and magnetic surface stresses. This competition must then give rise to the asymmetry of both the characteristic spike and the relationship with phase.

4.4 Magnetic stresses

Using the experimental inputs described in Section 4.3, we predict the bulk and surface stresses generated due to magnetic interactions.

Parameter	Symbol	Numerical estimate
particle length	ℓ	1.6×10^{-6} (m)
particle spacing	a	2.1×10^{-6} (m)
magnetization	M	2.2×10^{3} (A/m)
dipole moment	m	9.0×10^{-15} (A m^2)
vacuum permeability	μ_0	$4\pi \times 10^{-7}$ (N/A^2)

4.4.1 Time-modulated interactions

We simplify the interactions between particles to be purely magnetic dipole-dipole interactions, such that for a pair of particles $\boldsymbol{r}_{i,j}$ with dipole moments $\boldsymbol{m}_{i,j}$, the force acting on the ith particle due to the magnetic field generated by the jth is

$$\boldsymbol{F}_{ij} = \frac{3\mu_0}{4\pi r_{ij}^5}\left[\boldsymbol{m}_j(\boldsymbol{m}_i \cdot \boldsymbol{r}_{ij}) + \boldsymbol{m}_i(\boldsymbol{m}_j \cdot \boldsymbol{r}_{ij}) + \boldsymbol{r}_{ij}(\boldsymbol{m}_i \cdot \boldsymbol{m}_j) - \frac{5\boldsymbol{r}_{ij}(\boldsymbol{m}_i \cdot \boldsymbol{r}_{ij})(\boldsymbol{m}_j \cdot \boldsymbol{r}_{ij})}{r_{ij}^2}\right], \tag{4.10}$$

where $\boldsymbol{r}_{ij} = \boldsymbol{r}_j - \boldsymbol{r}_i$. For the dipole moments, we assume

$$\boldsymbol{m} = m\cos(\theta_B + \beta)\hat{x} + m\sin(\theta_B + \beta)\hat{y}, \tag{4.11}$$

for phase lag β and magnetic field orientation θ_B, where the phase lag is measured as in Section 4.3.3 and the magnetic field orientation is prescribed as in Section 4.2.2. The dipole moment magnitude m for a hematite cube is determined from the bulk magnetization of hematite M and the approximate particle side-length ℓ by $m = M\ell^3$. We also consider the potential energy for a system of two non-overlapping point dipoles,

$$U = \frac{\mu_0}{4\pi r_{ij}^3}\left[3(\boldsymbol{m}_i \cdot \hat{r}_{ij})(\boldsymbol{m}_j \cdot \hat{r}_{ij}) - \boldsymbol{m}_i \cdot \boldsymbol{m}_j\right]. \tag{4.12}$$

In the following sections, we apply these rules for the forces between dipoles to construct a bulk magnetic stress and surface magnetic stress.

4.4.2 Bulk magnetic stresses

To compute the interior magnetic stress due to time-modulated interaction, we apply the Irving-Kirkwood formula

$$\boldsymbol{\sigma}^b = -\frac{1}{2A}\sum_{i\neq j} \boldsymbol{F}_{ij} \otimes \boldsymbol{r}_{ij} \tag{4.13}$$

for a unit cell configuration comprised of a single particle and its nearest neighbors, which are assigned to positions determined by either of two approaches:

1. For two-fold ($n = 2$) modulation: $\boldsymbol{x}_j = (R(\theta_j)\cos\theta_j, R(\theta_j)\sin\theta_j)$ where R is determined from an ellipse that represents the time-evolving distortions of a lattice measured in Section 4.3.2. Explicitly,

$$R(\theta) = \frac{ab}{\sqrt{a^2\sin^2(\theta+\phi) + b^2\cos^2(\theta+\phi)}}, \tag{4.14}$$

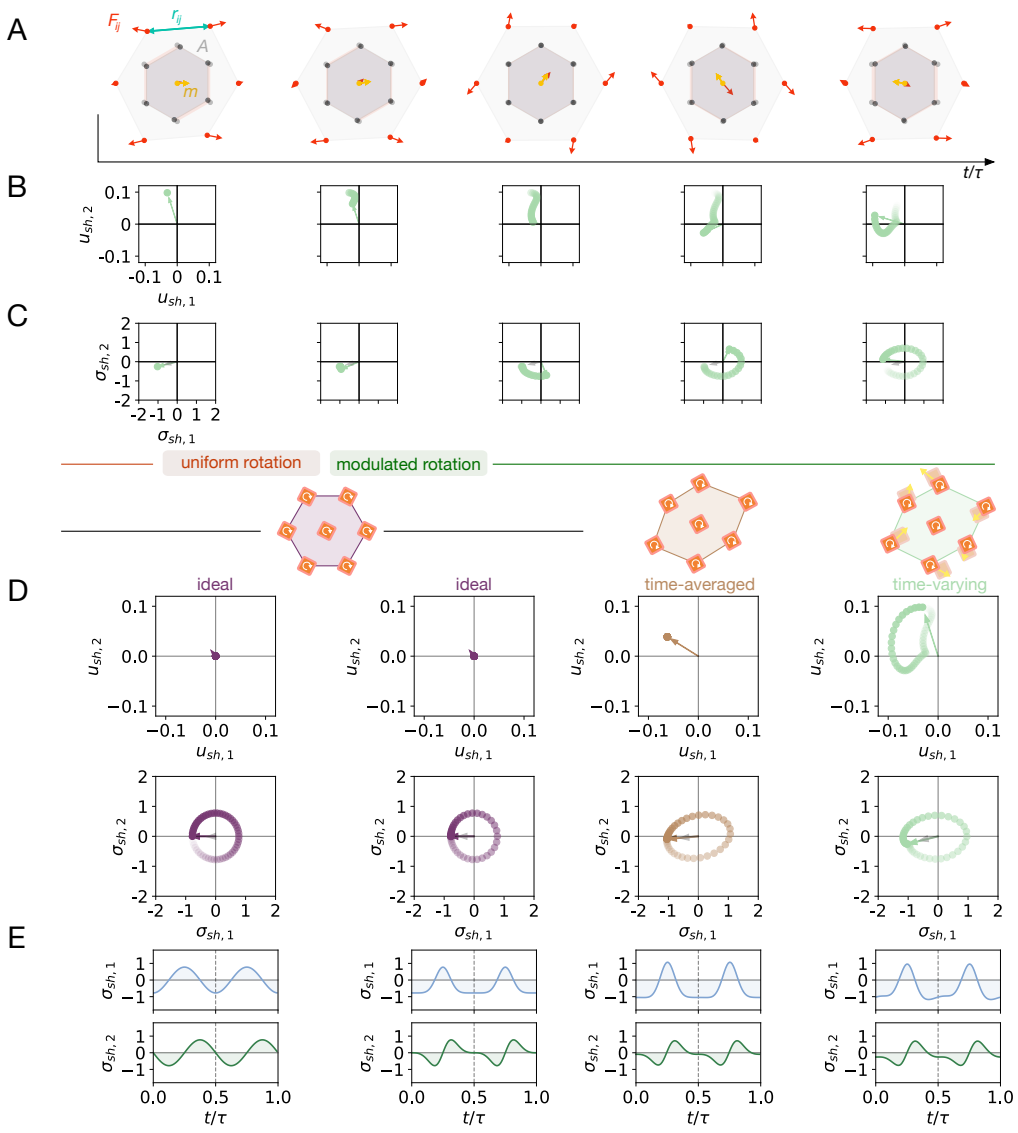

Figure 4.14: **Shear stresses over a cycle due to time-modulation interactions and structural distortion.** (A) The average unit cell is deformed over time while maintaining a system volume A. This deformation couples with the dipole moment $\vec{m}$ rotation over a cycle to produce a force F_{ij} on each particle due to interactions between each pair over a distance r_{ij}. (B) The unit cell strain is decomposed into shear components $u_{\mathrm{sh},1,2}$ and plotted as a function of time, alongside the (C) magnetic stress resulting from the aforementioned forces. The gray arrow represents the cycle-averaged net stress. Under uniform rotation and time-modulated rotation, for various assumptions regarding the unit cell deformation, we plot (D) the strain and magnetic stress in shear space and (E) the magnetic stress against time.

where $a = a_0$ and $b = a_0(1 - e^2)$ where a_0 is the average particle spacing and e is the eccentricity of the ellipse representing the local structural deformation.

2. For four-fold ($n = 4$) modulation: $\boldsymbol{x}_j$ directly extracted from averaged particle trajectories as discussed in Section 4.3.2.2.

We can then decompose $\boldsymbol{\sigma}$ into components, including two shears: $\sigma_{sh,1} =$  $= (\sigma_{xx} - \sigma_{yy})/2$ and $\sigma_{sh,2} =$  $= (\sigma_{xy} + \sigma_{yx})/2$. Not considered in the following sections are the explicit magnetic pressure  $= (\sigma_{xx} + \sigma_{yy})/2$ or the torque density  $= (\sigma_{xy} - \sigma_{yx})/2$.

4.4.2.1 Two-fold modulation

In Figure 4.14, we diagram this calculation for the case of $n = 2$ modulation by showing (A) the deformation of a typical unit cell over a cycle of particle rotation, where the inter-particle forces F_{ij} and separations r_{ij} are highlighted. At each snapshot, and for the immediately preceding moments in time, we plot (B) the strain on the unit cell decomposed into shear components, $u_{sh,1} =$  $= (u_{xx} - u_{yy})/2$ and $u_{sh,2} =$  $= (u_{xy} + u_{yx})/2$, where u_{ij} is constructed by computing the shape deformation between the measured unit cell and a reference ideal cell. Finally, we plot the magnetic stress for each configuration, also plotted in shear space, in (C), revealing a non-zero average shear stress indicated by the gray arrow.

To more carefully understand the origin of this cycle-averaged non-zero shear stress in both components, $\int_0^\tau dt \, \langle$  ,  $\rangle \neq 0$, we incorporate observed features of the experiment, namely the modulated rotation and unit cell distortion, in isolation. First, we perform this analysis for an ideal unit cell in the absence of time-modulated rotation for which $e = 1$, $\phi = 0$, and $\theta_B = \Omega t$. In this case, we recover a uniformly rotating total shear $|\boldsymbol{s}| = \sqrt{$  $^2 +$  ^{2} in the plane as in (D) that leads to a vanishing average shear stress as in (E). Surprisingly, we then find that the minimal ingredient needed to obtain a non-vanishing average shear stress is modulated rotation. By maintaining the assumption of an ideal unit cell but applying a modulated rotation as in Section 4.2.2, we still obtain a constant total shear $|\boldsymbol{s}|$ that rotates in the plane, but now stays longer at particular angles θ_s as illustrated in (D) and (E), which gives rise to a shear stress purely in one component, $\int_0^\tau dt \, \langle$  $\rangle \neq 0$.

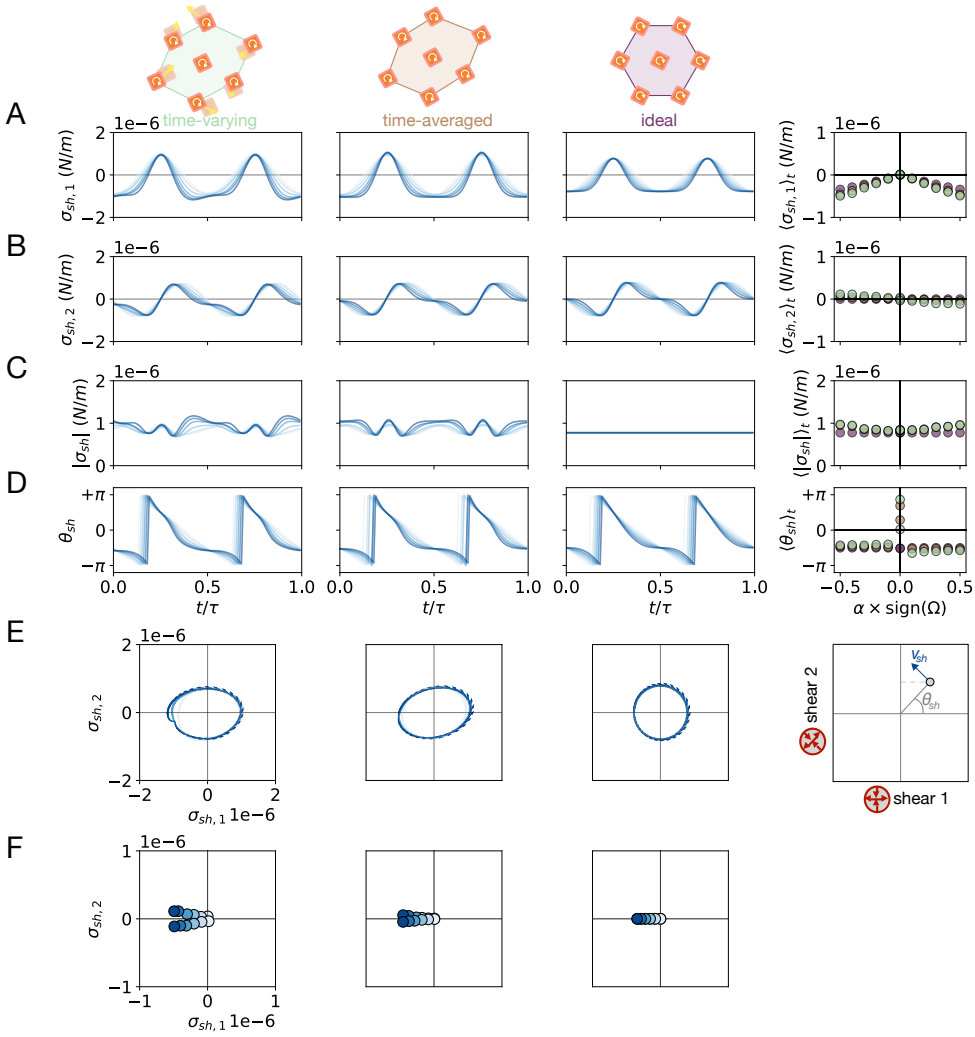

Figure 4.15: **Shear stresses over a cycle due to time-modulation interactions and structural distortion.** For a time-varying deformation, a time-averaged deformation, and no deformation to the unit cell, we plot the shear stress modes (A) $\sigma_{sh,1}$ and (B) $\sigma_{sh,2}$, (C) the magnitude of the shear stress, and (D) the angle in shear space as computed for varying modulation strength α. In the rightmost column, the time-averages are plotted against α. (E) The temporal evolution can be presented as a trajectory in shear space, and (F) the time-averages can be plotted as points to reveal a nontrivial shear due to the coupling of unit cell deformation and time-modulated dipole rotation.

We then consider the case where the functions $e(t)$ and $\phi(t)$ defining the evolution of the lattice deformation are made constant, $e \equiv \langle e(t)\rangle_t$ and $\phi \equiv \langle\phi(t)\rangle_t$, which introduces a constant strain and a deformation of the trajectory in shear space as in (D). By viewing the components of the shear stress against time as in (E), we reveal that the breaking of temporal

symmetry introduces an additional source of stress not present without the combination of time-modulation and a static structural deformation, producing now a rotated net shear stress $\int_0^\tau dt\ \langle \otimes \rangle \neq 0$. Incorporating the full time-evolution of the unit cell deformation in conjunction with modulated rotations further amplifies this symmetry breaking.

In Figure 4.15, we present these results for experiments in which α, the modulation intensity, is slowly increased from $\alpha = 0$, and contrast the three cases discussed above: (1) a time-varying lattice deformation described by $e(t)$ and $\phi(t)$, (2) a time-averaged lattice deformation described by $\langle e(t) \rangle_t$ and $\langle \phi(t) \rangle_t$, and (3) no lattice deformation. While one shear component is increased with α independent of lattice deformation as seen in (A), (B) shows that the second shear component is only non-vanishing with the introduction of either a static or dynamical lattice deformation. In (C) we show that this broken symmetry additionally introduces temporal fluctuations in the magnitude of the shear that grow with α, while the shear angle θ_{sh} rotates more non-uniformly with increasing α, but irrespective of deformation. In shear space, as in (E), the evolution of the shear can be plotted as a trajectory that reveals that modulation strength dictates the flow magnitude, but deformation sets the path. As a consequence, (F) reveals that the introduction of deformation enables the rotation of the net shear, which has a magnitude set by the modulation strength α. This rotation respects the chirality of the drive, as can be seen from the two separated lines for the deformed cell in (F), which represents cells driven with opposite chirality.

We can perform a similar analysis to observe the impact of the other parameters of the time-modulated drive on the predicted bulk stresses, as shown in Figure 4.16. For each parameter, we present the components of the shear stress, the total magnitude of the shear stress, and the angle in shear space as a function of time under the assumption of a time-varying unit cell. By then computing the cycle-averaged quantities for experiments conducted under both clockwise and counterclockwise rotation, we reveal in (A) that the effect of rotational drive is primarily to rotate the net shear while leaving the magnitude

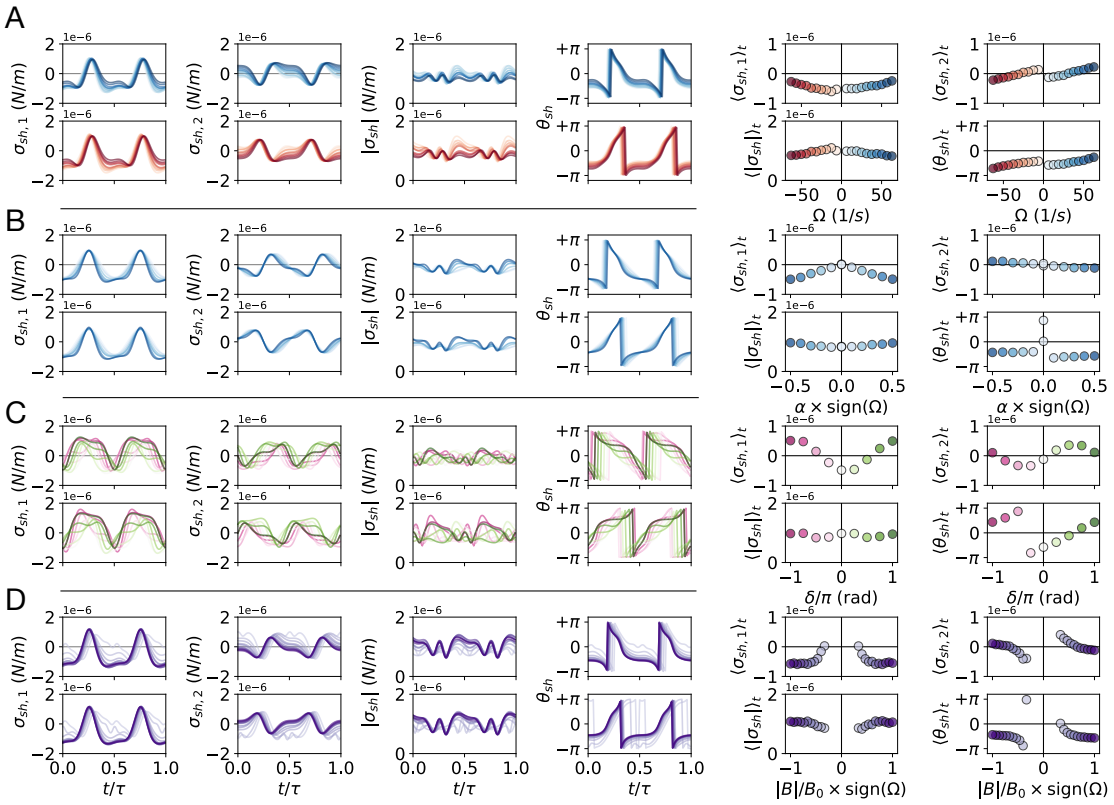

Figure 4.16: **Bulk stresses due to time-modulated rotation with varying control parameters.** The components of the magnetic shear stress, magnitude of the shear stress, and angle in shear space are plotted against time t/τ for rotation period τ. The top row represents clockwise rotation, while the bottom row represents counterclockwise rotation. In the right column, the time-averaged quantities are plotted against the parameter that is varied, namely: (A) rotation frequency Ω, (B) modulation strength α, (C) modulation phase δ, and (D) magnetic field strength $|B|$.

constant. By contrast, in (B) it is shown that the modulation strength controls only the magnitude of the two shear components, while the chirality informs the sign of $\sigma_{sh,2}$. Notably, without modulation ($\alpha = 0$), there is a constant but uniformly rotating shear stress. Tuning the modulation phase, as in (C), rotates the axis of the net shear stress without impacting its magnitude. In (D), we finally show that the magnetic field strength can be decreased to both decrease the magnitude of the shear stress and convert between one mode ($\sigma_{sh,1}$) to another ($\sigma_{sh,2}$).

It is informative to observe that these features are contingent upon the inclusion of the

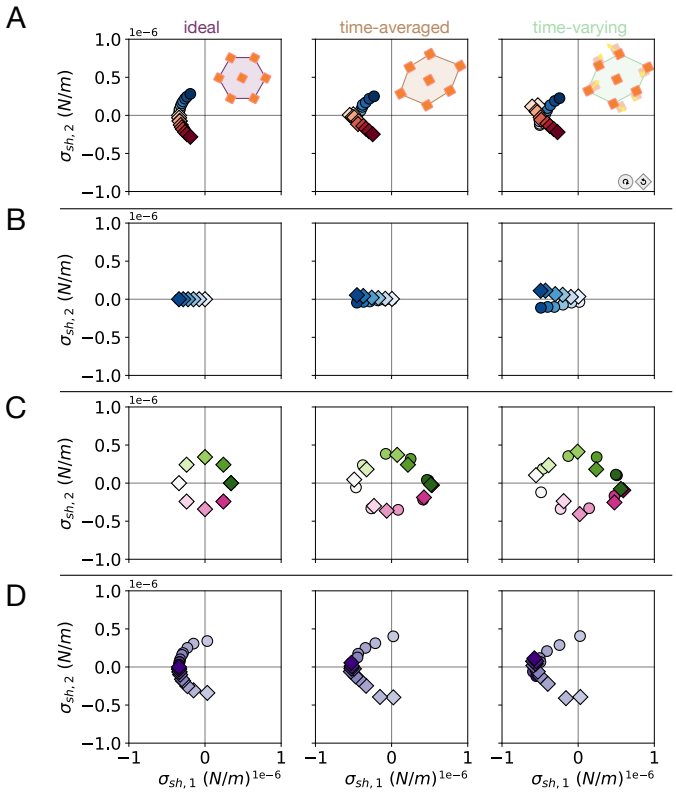

Figure 4.17: **Bulk stresses due to time-modulated rotation as computed for different choices of unit cell distortion.** The magnetic stress on the typical unit cell is computed for three choices: (left) an ideal unit cell, (middle) a time-averaged, but deformed unit cell, and (right) a unit cell that sustains a time-varying deformation over a cycle. The cycle-averaged shear stresses are plotted in shear space to show mode-mixing and shear rotation due to changes in (A) rotation frequency Ω, (B) modulation strength α, (C) modulation phase δ, and (D) magnetic field strength $|B|$. Circles represent CCW rotation, and squares represent CW rotation.

full deformation of the unit cell. To do so, we reproduce the analysis of Figure 4.15F for the aforementioned parameters in Figure 4.17. We observe that both the angle and magnitude of the net shear is corrected by the inclusion of a dynamically evolving unit cell in the stress calculation.

4.4.2.2 Four-fold modulation

Surprisingly, for $n = 4$ modulation, we find that there is zero cycle-averaged shear stress, $\int_0^\tau dt\ \langle \text{⊕}, \text{⊗} \rangle = 0$, and that the effect of removing the time-evolution of the structural

distortion, and removing the distortion altogether, is to alter the specifics of the orbit made in shear space during a cycle of rotation, as seen in Figure 4.18A. As seen in (B), the introduction of a time-varying strain does lead to a broken symmetry in the stress as a function of time, suggesting that a time-resolved analysis of the stress balance on a droplet will be necessary to predict the morphological change accompanied by four-fold modulated rotation.

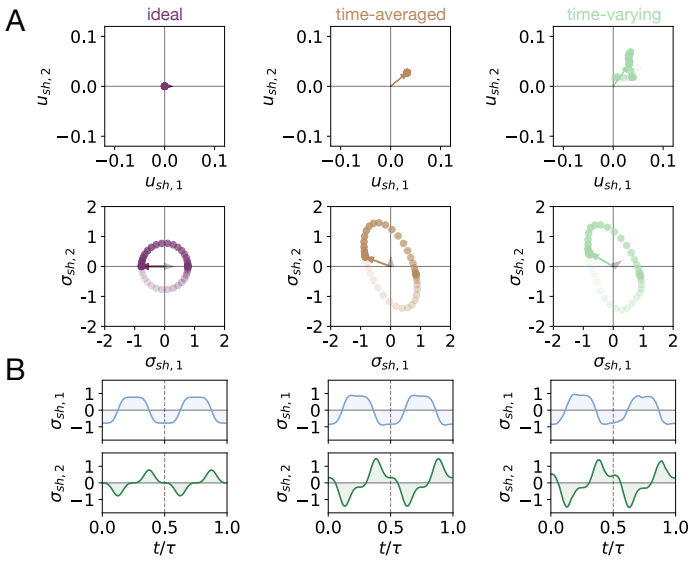

Figure 4.18: **Shear stresses and strains during a rotation under four-fold time modulation.** (A) For (left) an ideal, (middle) time-averaged, and (right) time-varying deformation to a unit cell, we compute the strain and magnetic stress and plot the shear components over a cycle. (B) For the same configurations, we plot the magnetic shear stress against time.

Repeating the analysis performed for the case of two-fold modulation, we compute the decomposition of the magnetic stress into shear components and present the time-averaged quantities against the rotational drive frequency Ω for (A) sinusoidal and (B) square four-fold modulation in Figure 4.19. This reveals that the net stress is largely independent of the specifics of the drive, but the temporal evolution within a cycle is very responsive to the drive form, but not frequency.

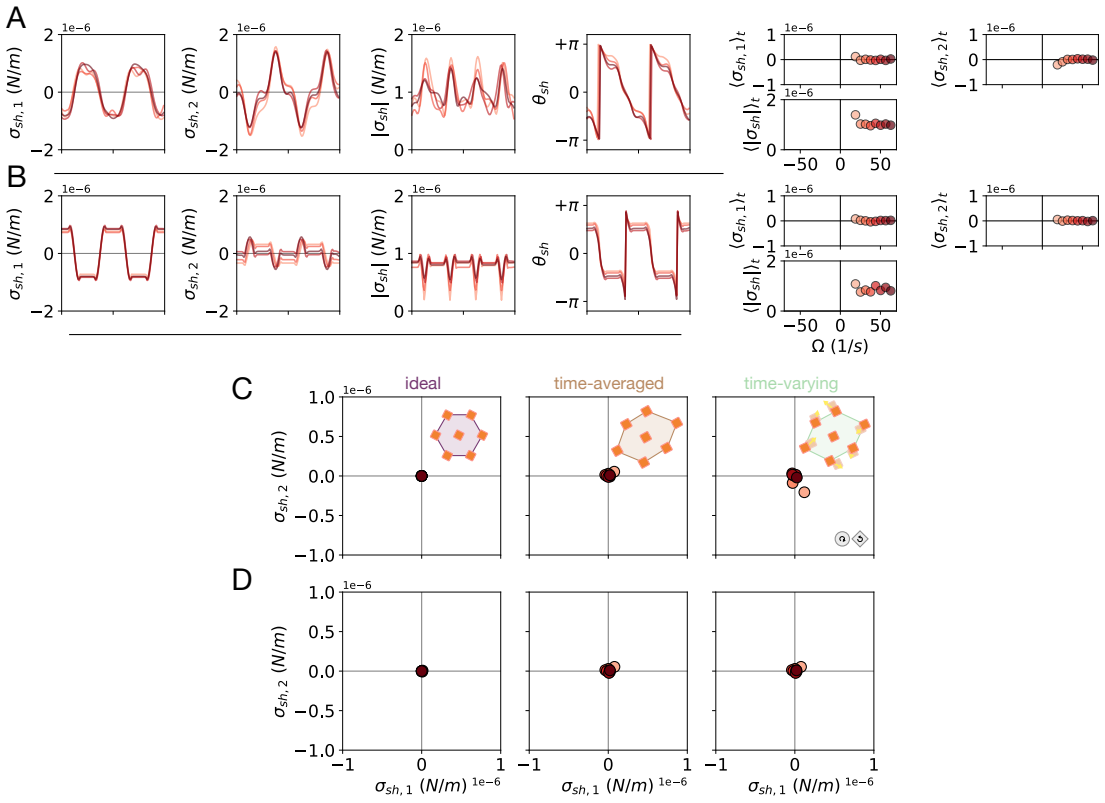

Figure 4.19: **Bulk stresses estimated for varying four-fold time modulated drives and choices of unit cell distortion.** The components of the magnetic shear stress, magnitude of the shear stress, and angle in shear space are plotted against time t/τ for rotation period τ and for (A) sinusoidal four-fold modulation and (B) square four-fold modulation. In the right column, the time-averaged quantities are plotted against the rotational frequency Ω. For (C) sinusoidal and (D) square four-fold modulation, the time-averaged magnetic stress on the typical unit cell is plotted for three choices: (left) an ideal unit cell, (middle) a time-averaged, but deformed unit cell, and (right) a unit cell that sustains a time-varying deformation over a cycle.

4.4.3 Surface magnetic stresses

To estimate the surface magnetic stresses, we consider three approaches: (1) a two-particle pairwise potential energy argument, (2) a three-particle approach accounting for surface curvature, and (3) a many-particle numerical computation. We then contrast the anisotropic surface tension resulting from time-modulated rotation with the isotropic surface tension of uniform rotation, and discuss the consequences in the following sections.

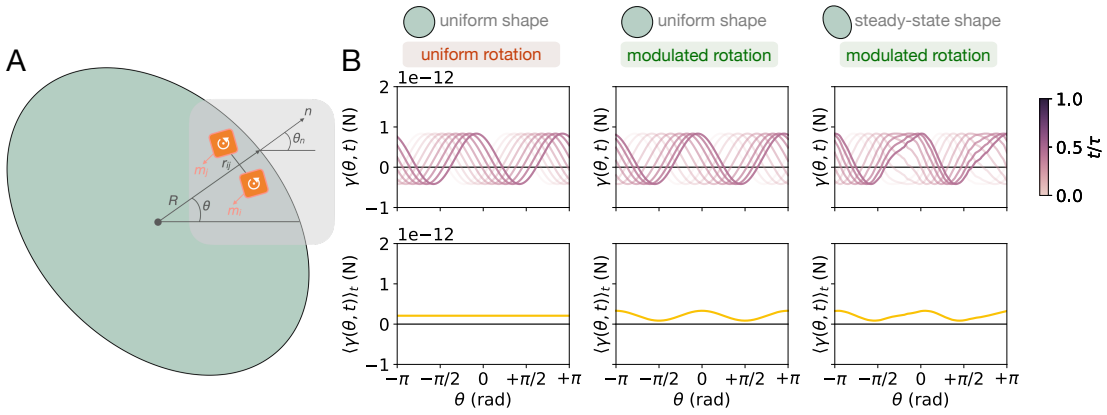

Figure 4.20: **Anisotropic surface tension estimated from $N = 2$ particles.** (A) A diagram of the estimate of surface tension from the magnetic potential energy between two particles on the surface of a droplet. (B) For varying droplet shapes and rotational drives, we compute the time-evolution of the surface tension $\gamma(\theta, t)$ (top) and the time-average (bottom).

4.4.3.1 $N = 2$: estimating stress via-energy

First, we estimate the anisotropic surface stress by treating it as an effective surface tension and estimating $\gamma \sim U/a_0$, where U is the potential energy between a pair of particles along the edge of a curved surface, as illustrated in Figure 4.20A. Taking a surface that is parameterized by a normal angle $\theta_n(\theta)$ and radius of curvature $R(\theta)$, the vector separating two dipoles along the edge of a surface with orientation $\hat{n} = (\cos\theta_n, \sin\theta_n)$ is $\boldsymbol{r}_{ij} = r_{ij}(-\sin\theta_n, \cos\theta_n)$. Incorporating the form of the modulated magnetic field phase, we compute the instantaneous potential energy and then the surface tension. For this approach, we produce a stress $\sigma^s_{nn} = \gamma(\theta)\kappa(\theta)$, where $\gamma(\theta) = U[\theta_n(\theta)]/a$, or

$$\gamma(\theta_n, \theta_B) = \frac{\mu_0 m^2}{8\pi a^4}\left(3\cos\left[2(\theta_n - \theta_B)\right] - 1\right), \tag{4.15}$$

where θ_n is the orientation of the surface and θ_B is the orientation of the magnetic dipole moments.

In Figure 4.20B, we show the estimated surface tension $\gamma(\theta_n, \theta_B) \to \gamma(\theta, t)$, where $\theta_n(\theta)$

is chosen to correspond to either a shape with uniform curvature or the steady-state shape measured for an experimental droplet, while $\theta_B(t)$ is chosen to correspond to either uniform rotation or weakly modulated rotation. Without time-modulation, the time-averaged surface tension is isotropic as previously reported, arising from the uniform translation during a rotational cycle of the curve $\gamma(\theta, t)$. Under modulated rotation, this translation is non-uniform, resulting in an anisotropic surface tension on the surface of a circular droplet. This anisotropy is sharpened by the fluctuations in curvature along the surface of an ellipsoidal droplet.

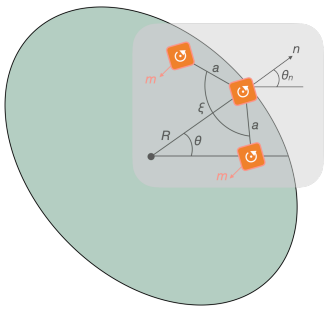

Figure 4.21: **Anisotropic surface tension estimated from $N = 3$ particles.** A diagram of the estimate of surface tension from the net magnetic force acting on a particle due to its nearest neighbors on the surface of a droplet.

4.4.3.2 $N = 3$: estimating stress via-forces

This approach can be generalized to consider three particles, this time considering a surface that is parameterized by a normal angle $\theta_n(\theta)$, radius of curvature $R(\theta)$, and curvature $\kappa(\theta)$. As illustrated in Figure 4.4.3.1, the interior angle $\xi(\theta)$ can be used as a proxy for the local curvature, $\kappa = \frac{2\cos(\xi/2)}{a}$, where a is the particle spacing. We compute the force $\boldsymbol{F}[\xi(\theta), \theta_n(\theta)] = F_n(\xi, \theta_n)\hat{n} + F_t(\xi, \theta_n)\hat{t}$ on the central particle, where $\hat{n} = (-\sin\theta_n, \cos\theta_n)$. The normal force per unit length yields a stress that is equivalent to a normal surface stress, so for this approach we produce a stress $\sigma^s_{nn} = F_n[\xi(\theta), \theta_n(\theta)]/a$. Unlike the previous approach, this calculation explicitly takes the curvature of the surface into consideration via

the angle $\xi(\theta)$.

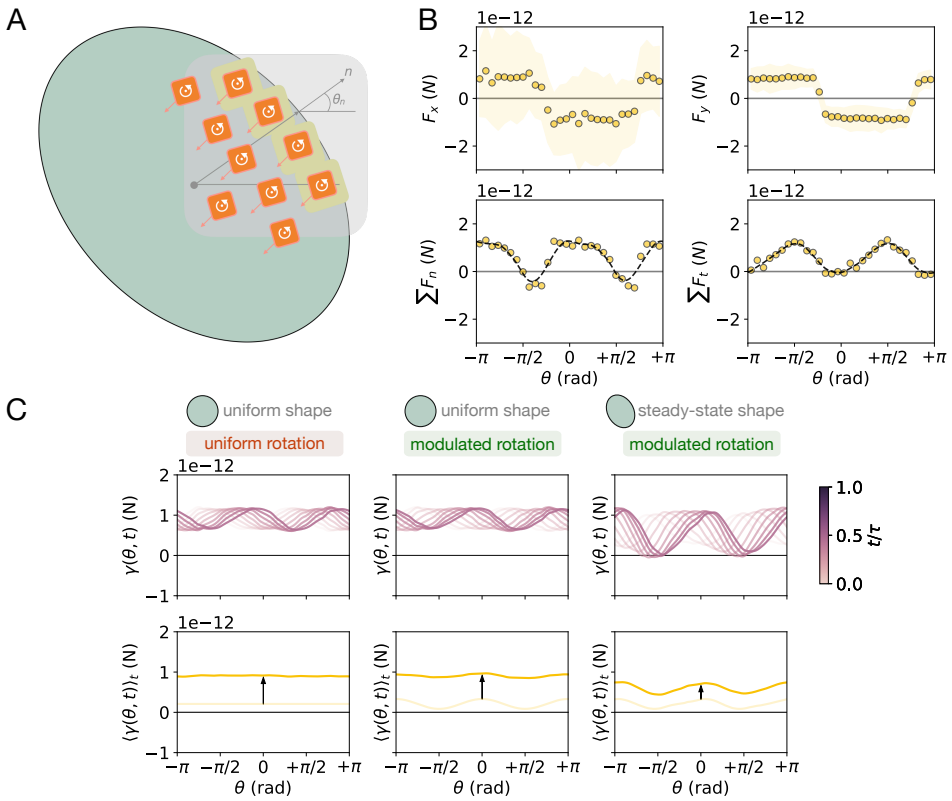

Figure 4.22: **Anisotropic surface tension estimated from N particles.** (A) A diagram of the estimate of surface tension from the magnetic potential energy between two particles on the surface of a droplet. (B) For varying droplet shapes and rotational drives, we compute the time-evolution of the surface tension $\gamma(\theta, t)$ (top) and the time-average (bottom).

4.4.3.3 $N = N$: summing all dipole-dipole forces

Finally, we can perform an estimate of the surface tension by summing the magnetic forces on the boundary particles of a droplet due to the interactions with their nearest neighbors on the interior of the droplet. Again, parameterize the droplet by the normal angle $\theta_n(\theta)$ and radius of curvature $R(\theta)$, as illustrated in Figure 4.22A. In (B), the we plot the net force $\boldsymbol{F}$ on the edge particles at angle θ with respect to the center of the droplet. To extract the surface tension, we project this force onto the surface normal. The resulting estimate for the surface tension is qualitatively consistent with the $N = 2$ particle estimates, as seen in (C),

but with an offset that causes the surface tension to be positive at all angles.

For both the $N = 2$ and $N = N$ particle approximations to the surface tension, and for both uniform and non-uniform surface geometries, we compute the estimated surface tension for varying control parameters in Figure 4.23. We observe a consistent offset in the surface tension as estimated numerically for many particles when compared to the pairwise approximation, and further observe that the degree of anisotropy grows with modulation strength while the axis of the anisotropy rotates with modulation phase and field strength. Meanwhile, increasing the strength of the out-of-plane magnetic field has the expected effect of decreasing the attraction between rotating dipoles, and accordingly decreases the surface tension while not impacting the anisotropy. We also observe that for four-fold modulation of any rotational frequency, the surface tension is isotropic when averaged over a rotation. This, coupled with the observation that the time-averaged bulk stress is negligible, suggests that a shape prediction predicated on stress balance must be resolved on a timescale below that of a rotation to predict the experimental observations.

4.5 Predicting shape

In the previous sections, we showed that time-modulated interactions introduce anisotropic bulk magnetic stresses $\boldsymbol{\sigma}^b$ as computed in Section 4.4.2) in addition to surface stresses $\sigma^s_{nn} = \gamma\kappa$ computed as in Section 4.4.3. These stresses were computed using the known morphological properties in conjunction with microscopic structural details observed in the experiments. With this in hand, we seek to write down a model that describes both the instantaneous evolution of the droplet shape and the stable steady-state shapes that are produced through time-modulated rotation. We begin with the most generic hydrodynamic model for a local velocity field $\boldsymbol{u}(\boldsymbol{r}, t)$. The hydrodynamics of this material then follow from conservation of mass,

$$\boldsymbol{\nabla} \cdot \boldsymbol{u} = 0, \tag{4.16}$$

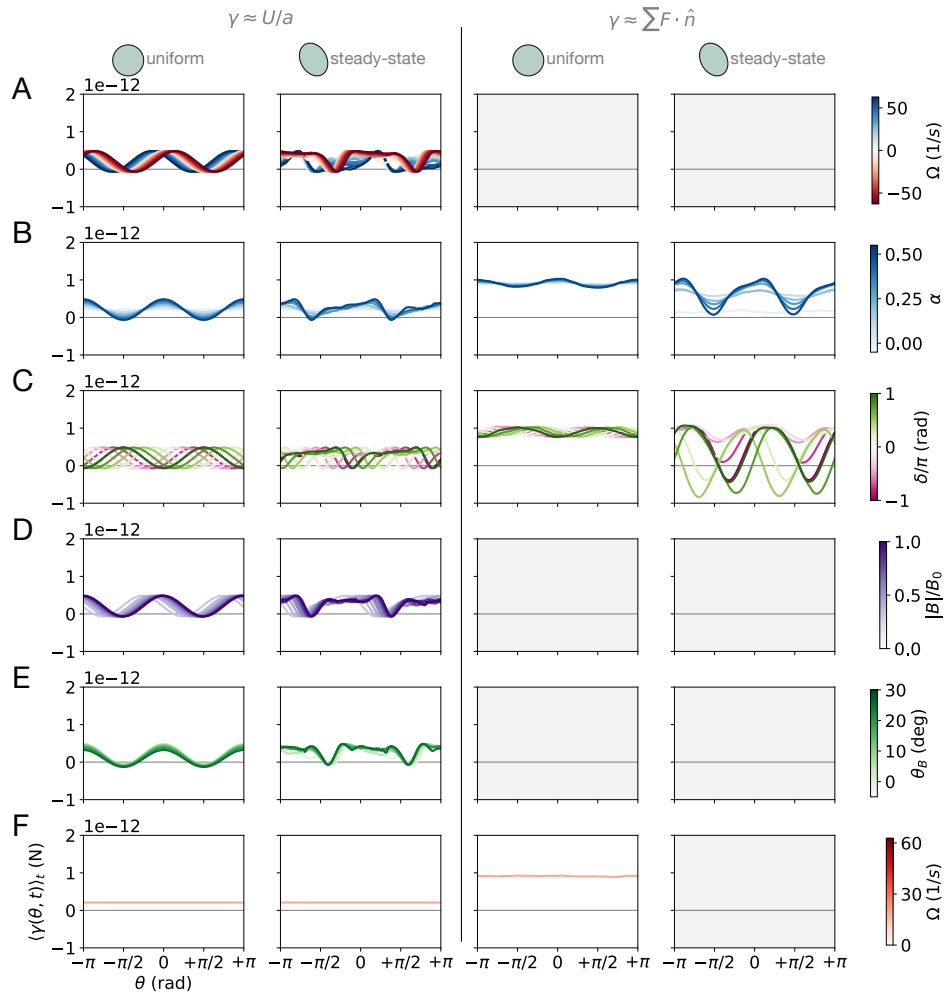

Figure 4.23: **Anisotropic surface tension estimates depend on parameters of the magnetic drive.** The surface tension as estimated from the magnetic potential energy of a pair of particles (left) and the sum of magnetic forces on a layer of boundary particles (right) on both a uniform and steady-state droplet surface for variable (A) rotation frequency Ω, (B) modulation strength α, (C) modulation phase δ, and (D) magnetic field strength $|B|$, (E) out-of-plane magnetic field angle θ_B, and (F) four-fold modulation $n = 4$.

and conservation of momentum for an incompressible material,

$$\nabla \cdot \left(\boldsymbol{\sigma}^v + \boldsymbol{\sigma}^b \right) - \boldsymbol{\nabla} p = \Gamma \boldsymbol{u}, \tag{4.17}$$

which includes a hydrodynamic stress tensor $\boldsymbol{\sigma}^v$,

$$\boldsymbol{\sigma}^v = \begin{pmatrix} \\ \\ \\ \end{pmatrix} = \begin{pmatrix} -\eta_R & 0 & 0 \\ 0 & \eta & \eta_o \\ 0 & -\eta_o & \eta \end{pmatrix} \begin{pmatrix} \\ \\ \\ \end{pmatrix} \dot{} \,. \tag{4.18}$$

in addition to the familiar substrate drag $\Gamma \boldsymbol{u}$ and the bulk stress computed previously, but reproduced here:

$$\boldsymbol{\sigma}^b = \begin{pmatrix} \\ \\ \end{pmatrix} = -\frac{1}{2A} \sum_{i \neq j} \boldsymbol{F}_{ij} \otimes \boldsymbol{r}_{ij}. \tag{4.19}$$

The newly computed surface stresses enter the equations of motion through the boundary condition on the surface $\partial\Omega$,

$$(\boldsymbol{\sigma}^v + \boldsymbol{\sigma}^b + p) \cdot \hat{n}\Big|_{\partial\Omega} = \gamma\kappa\hat{n}. \tag{4.20}$$

In the following sections, we first outline an approach to the problem of solving these equations perturbatively in the modulation strength α to obtain small corrections to the droplet radius $R(\theta)$ and pressure $p(\theta)$. Then, we consider a steady-state simplification that yields an expression amenable to direct evaluation from the experimental data shown previously.

4.5.1 Perturbative approach: instantaneous evolution

4.5.1.1 Basic equations of motion

Under the assumptions that this material is an overdamped, incompressible fluid, and that the stress is uniform other than the pressure term which is forcing the incompressibility, we

parameter	meaning	function of	units
t	time	parameter	s
r	polar radius	parameter	mm
θ	polar angle	parameter	
Ω	angular frequency	Constant	$1/s$
n	modulation number	Constant (integer)	
α	modulation strength	Constant (small)	
β	wobbling of the droplet	Constant (small)	
θ_B	Angle of the external field	Ω, n, α, t	
δ_B	Relative lag between bulk and surface	Constant	$1/s$
σ_{ij}	Magnetic bulk stress	$\theta_B\ (t)$	$\mu g/s^2$
R	radius of the droplet	θ, t	mm
R_0	unperturbed radius of the droplet	Constant	mm
R_1	first order perturbation in α	θ, t	mm
R_2	first order perturbation in β	θ, t	mm
θ_n	angle of the normal the surface	$\theta, R\ (t)$	
$\hat{n}$	unit vector normal to the surface	$\theta, R\ (t)$	
κ	curvature	$\theta, R\ (t)$	1/mm
γ	surface tension	$\theta_n, \theta_B, \delta_B\ (\theta, t)$	$\mu g\ mm/s^2$
p	pressure (Lagrange multiplier)	r, θ, t	$\mu g/s^2$
Γ	substrate friction	Constant	$\mu g/mm^2 s$
$\mathbf{u}$	velocity field	r, θ, t	mm/s
a	Distance between particles	Constant	mm
μ	Dipole moment	Constant	some units
μ_0	Vacuum permeability	Constant	some units

Table 4.1: **Time-modulated droplet perturbation parameters.** All the parameters in the perturbative calculation of a droplet subjected to time-modulated rotation.

can write the following two bulk equations of motion:

$$\begin{aligned} \mathbf{u} &= \frac{1}{\Gamma}\nabla p \\ \nabla \cdot \mathbf{u} &= \nabla^2 p = 0 \end{aligned} \tag{4.21}$$

The boundary condition has two equations. First, the jump on the stress of the boundary has to cancel with the surface tension, which gives:

$$\hat{n}_i(\theta,t)\sigma_{ij}(t)\hat{n}_j(\theta,t) + p(R(\theta,t),\theta,t) = \gamma(R(\theta,t),t)\kappa(R(\theta,t)) \tag{4.22}$$

The other boundary condition is a kinematic condition, which states that the boundary advects in the velocity of the bulk behind it, meaning:

$$\frac{dR(\theta,t)}{dt} = \mathbf{u}(r = R(\theta,t),\theta,t)\cdot\hat{r} \tag{4.23}$$

The solution process goes as follows: (1) write Eq. 4.22 to first order in α and then (2) use Eq. 4.21 to get the velocity field, promising (3) closure using Eq. 4.23. The linearization scheme is discussed below.

4.5.1.2 Linearization of the stress boundary condition

Bulk stress In order to linearize the stress boundary condition in the parameter α we need to calculate the stress in the bulk and the surface force as function of t, θ and α. Let us start by writing $\theta_B = \Omega t + \alpha/n\cos(n\Omega t)$. The magnetic stress for an ideal unit cell can be written as $\sigma_{ij} = A(\sin(2\theta_B){\sigma_x^{\text{Pauli}}}_{ij} + \cos(2\theta_B){\sigma_z^{\text{Pauli}}}_{ij}) + P\delta_{ij}$, where $A = \frac{\sqrt{3}\mu_0\mu^2}{16\pi a^5}$ and has units of stress. Now we can expand to first order in α and get:

$$\begin{aligned} \sin(2\theta_B) &= \sin(2\Omega t + 2\alpha/n\cos(n\Omega t)) \approx \sin(2\Omega t) + 2\alpha/n\cos(2\Omega t)\cos(n\Omega t) \\ \cos(2\theta_B) &= \cos(2\Omega t + 2\alpha/n\cos(n\Omega t)) \approx \cos(2\Omega t) - 2\alpha/n\sin(2\Omega t)\cos(n\Omega t), \end{aligned} \tag{4.24}$$

giving the first order of the bulk stress.

Geometrical approximations Consider the most general perturbation to a circular droplet with $R(\theta) = R_0 + \delta R(\theta)$ where $\delta R/R_0 \ll 1$. One can use Eq. 4.4 to estimate the perturbed curvature to first order in δR:

$$\kappa(\theta) = \frac{1}{R_0} - \frac{\delta R''}{R_0^2} - \frac{\delta R}{R_0^2}. \tag{4.25}$$

Or, to first order in α, $\kappa = \frac{1}{R} - \frac{\delta R''}{R_0^2}$. The surface for this perturbed droplet has a unit normal defined by the gradient along an infinitesimal line segment $d\ell = R(\theta + d\theta)\hat{\boldsymbol{e}}_{\theta+d\theta} - R(\theta)\hat{\boldsymbol{e}}_\theta$,

$$\begin{pmatrix} -\sin\theta_n \\ \cos\theta_n \end{pmatrix} = \frac{d\ell}{|d\ell|} = \frac{1}{\sqrt{R^2 + R'^2}} \begin{pmatrix} R'\cos\theta - R\sin\theta \\ R'\sin\theta + R\cos\theta \end{pmatrix} = \frac{1}{\sqrt{1 + (R'/R)^2}} \begin{pmatrix} -\sin\theta + \frac{R'}{R}\cos\theta \\ \cos\theta + \frac{R'}{R}\sin\theta \end{pmatrix}. \tag{4.26}$$

For small deformations, $R' = \delta R' \ll R_0$, and

$$\begin{pmatrix} -\sin\theta_n \\ \cos\theta_n \end{pmatrix} = \begin{pmatrix} -\sin\left(\theta - \frac{\delta R'}{R_0}\right) \\ \cos\left(\theta - \frac{\delta R'}{R_0}\right) \end{pmatrix}, \tag{4.27}$$

so we can read off $\theta_n = \theta - \delta R'/R_0$.

We can now parameterize the surface using the more specific form $R(\theta) = R_0 + \alpha R_1(\theta, t) + \beta R_2(\theta, t)$. In this parameterization $\kappa \approx \frac{1}{R_0} - \frac{\alpha R_1 + \beta R_2}{R_0^2} - \frac{\alpha R_1'' + \beta R_2''}{R_0^2}$ where the derivative is taken with respect to the parameter θ. The angle of the normal to the surface satisfies: $\theta_n = \theta + \frac{\alpha R_1' + \beta R_2'}{R_0}$, and the normal vector satisfies:

$$\hat{n} = \left(\cos(\theta - \frac{\alpha R_1'}{R_0} - \frac{\beta R_2'}{R_0}), \sin(\theta - \frac{\alpha R_1'}{R_0} - \frac{\beta R_2'}{R_0})\right) =$$
$$= \left(\cos(\theta) + \sin(\theta)\left(\frac{\alpha R_1'}{R_0} + \frac{\beta R_2'}{R_0}\right), \sin(\theta) - \cos(\theta)\left(\frac{\alpha R_1'}{R_0} + \frac{\beta R_2'}{R_0}\right)\right)$$

Surface tension The magnetic surface surface tension, allowing the angles on the surface to be lagging with respect to the bulk, satisfies:

$$\gamma(\theta_n, \theta_B) = \gamma_c(1 + 3\cos(2(\theta_B - \theta_n - \delta_B)) \approx$$
$$\approx \gamma_c \left[1 + 3\cos(2(\Omega t - \theta - \delta_B)) + 6\sin(2(\Omega t - \theta - \delta_B)) \left(\frac{\alpha R_1' + \beta R_2'}{R_0} - \alpha/n \cos(n\Omega t)\right)\right]. \tag{4.28}$$

4.5.2 Experimental approach: steady-state simplification

Recall that the statement of surface stress balance, assuming we can ignore viscous stresses, is

$$\boldsymbol{\sigma}^b \cdot \hat{n} + p\hat{n}\Big|_{\partial\Omega} = \gamma\kappa\hat{n}. \tag{4.29}$$

By expanding each term to show explicit dependence on the angle along the surface θ and time t, and projecting into $\hat{n}$ on both sides, we obtain

$$\hat{n}_i(\theta, t)\sigma_{ij}(t)\hat{n}_j(\theta, t) + p(\theta, t) = \gamma(\theta, t)\kappa(\theta, t). \tag{4.30}$$

Since we operate in the limit of large substrate friction and in the steady-state, and $dR/dt \propto 1/\Gamma$, we assume $R(\theta, t) \equiv R(\theta)$, and the same for $\hat{n}$ and $\kappa(\theta)$. Then, solving for $\kappa(\theta)$,

$$\kappa(\theta) = \left\langle \frac{\sigma_{nn}(\theta, t) + p(\theta, t)}{\gamma(\theta, t)} \right\rangle_t. \tag{4.31}$$

Finally, since we operate in the steady-state, there should be no spatially-varying pressure, as there is no flow $\boldsymbol{u} \propto \nabla p = 0$. Thus, $\langle p(\theta, t)/\gamma(\theta, t)\rangle_t \approx p_0/\gamma_0 = \kappa_0$, which is the Laplace pressure relation for the uniform curvature of the base state κ_0 and un-modulated surface tension γ_0. Finally,

$$\delta\kappa(\theta) = \left\langle \frac{\sigma_{nn}(\theta, t)}{\gamma(\theta, t)} \right\rangle_t, \tag{4.32}$$

where $\delta\kappa(\theta) = \kappa(\theta) - \kappa_0$ represents the perturbation to the curvature in the steady-state.

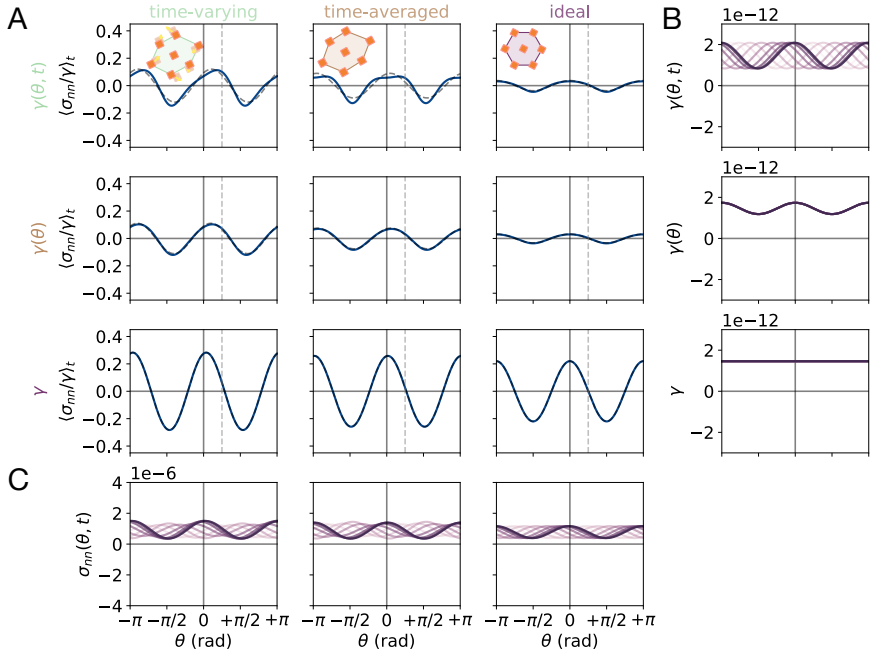

Figure 4.24: **Predicting steady-state shape from the balance of surface and bulk stresses.** (A) We compute the time-averaged stress ratio to estimate $\delta\kappa(\theta)$ for different assumptions regarding the unit cell deformation (columns) and surface tension anisotropy (rows). The time-evolution of the (B) surface tension and bulk normal stress (C) is indicated over a period of rotation.

For the computed magnetic bulk stress from Section 4.4.2 and estimated surface tension, with the inclusion of an offset consistent with the numerical calculation performed in Section 4.4.3, we can evaluate Eq. 4.5.2. In Figure 4.24, we compute this time-averaged ratio for bulk stresses computed using the assumption of a time-varying, time-averaged, and ideal unit cell. In addition, we highlight the role of time-varying surface tension by considering the case of a spatially and temporally uniform surface tension. In each entry of (A) is the estimated ratio $\delta\kappa(\theta)$ for each combination of bulk and surface stress, which themselves are shown in row (C) and column (B) respectively. We find that any combination predicts a curvature perturbation consistent with an ellipsoid. However, only when both (1) the unit cell sustains a deformation and (2) the surface tension is anisotropic does this approach predict the ellipsoidal orientation observed in the experiment.

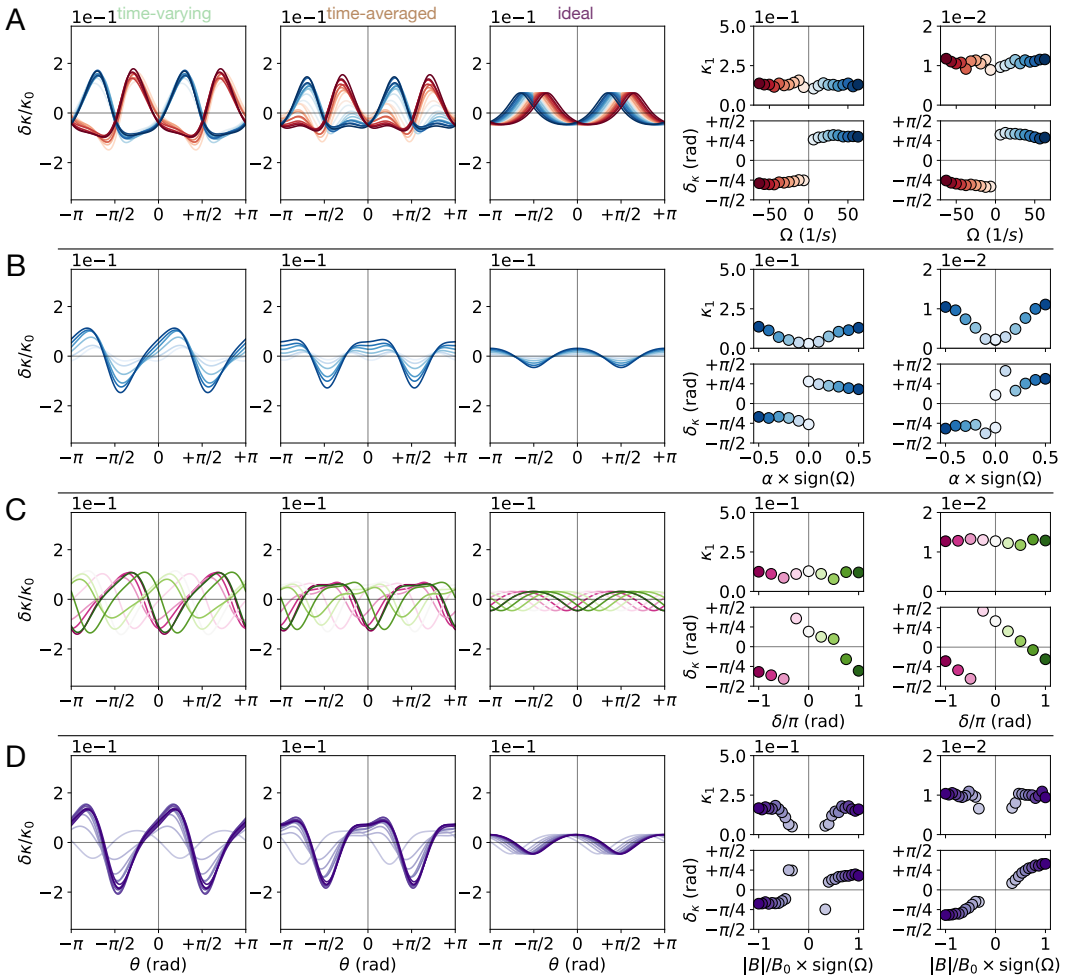

Figure 4.25: **Steady-state shape predictions for various drive parameters.** The ratio is computed for each labelled unit cell assumption and over the range of parameters indicated in each row, and plotted over an average rotation cycle (left). The time-varying case is fit to obtain the amplitude and phase and compared to the comparable measurement in the experiment (right) for variable (A) rotation frequency Ω, (B) modulation strength α, (C) modulation phase δ, and (D) magnetic field strength $|B|$.

We observe that this excellent agreement with the experimentally measured curvature fluctuations is consistently observed across all parameters discussed previously, as displayed in Figure 4.25. Here, we compare the predictions for $\delta\kappa(\theta)$ made using varying choices for the unit cell deformation for each control parameter in the left columns. On the right, we present the results of fitting these curves to the form $\delta\kappa(\theta) = \kappa_0 + \kappa_1 \cos(n\theta + \delta_\kappa)$, where κ_1 represents the amplitude of the deformation to the surface, and δ_κ represents the phase.

Recall that we performed this procedure previously in Section 4.5, and the results are reproduced in the right-most column for comparison. Namely, for variable rotation frequency, this approach accurately predicts the effect of chirality on droplet orientation, while also predicting unchanged droplet morphology with respect to $|\Omega|$ as in (A). In (B-C), the expected isolated control over droplet aspect ratio and orientation through modulation strength and phase, respectively, is also captured by this minimal model. Finally, the simultaneous control over both aspects of droplet morphology, and the non-linear experimentally observed trends with respect to field strength are recovered in (D).

The conditions for predicting the correct droplet geometry in the four-fold case, a superellipsoid characterized by a curvature as presented in Section 4.5, are more particular than in the two-fold case. Repeating the same calculation of Figure 4.24 produces Figure 4.26, where (A) reveals that the time-dependence of the surface tension is crucial, when paired with the bulk stress computed on a deformed unit cell, to predict the experimental result. In (D), we show that a deformation of the unit cell is crucial to predict the variation of the curvature with rotational frequency. Finally, by extracting the amplitude and phase of the curvature modulation and comparing it to the experimental result in (E), we observe qualitative agreement with the trend relating raised rotational frequency to more circular droplets.

4.6 Conclusion

We have demonstrated the ability to tune the morphology of chiral matter from a seemingly innocent time-modulation to the rotational drive. The model we have used to predict this control incorporates our current understanding of both chiral fluid hydrodynamics and odd crystalline mechanics to achieve promising qualitative agreement with both experiments and simulations alike.

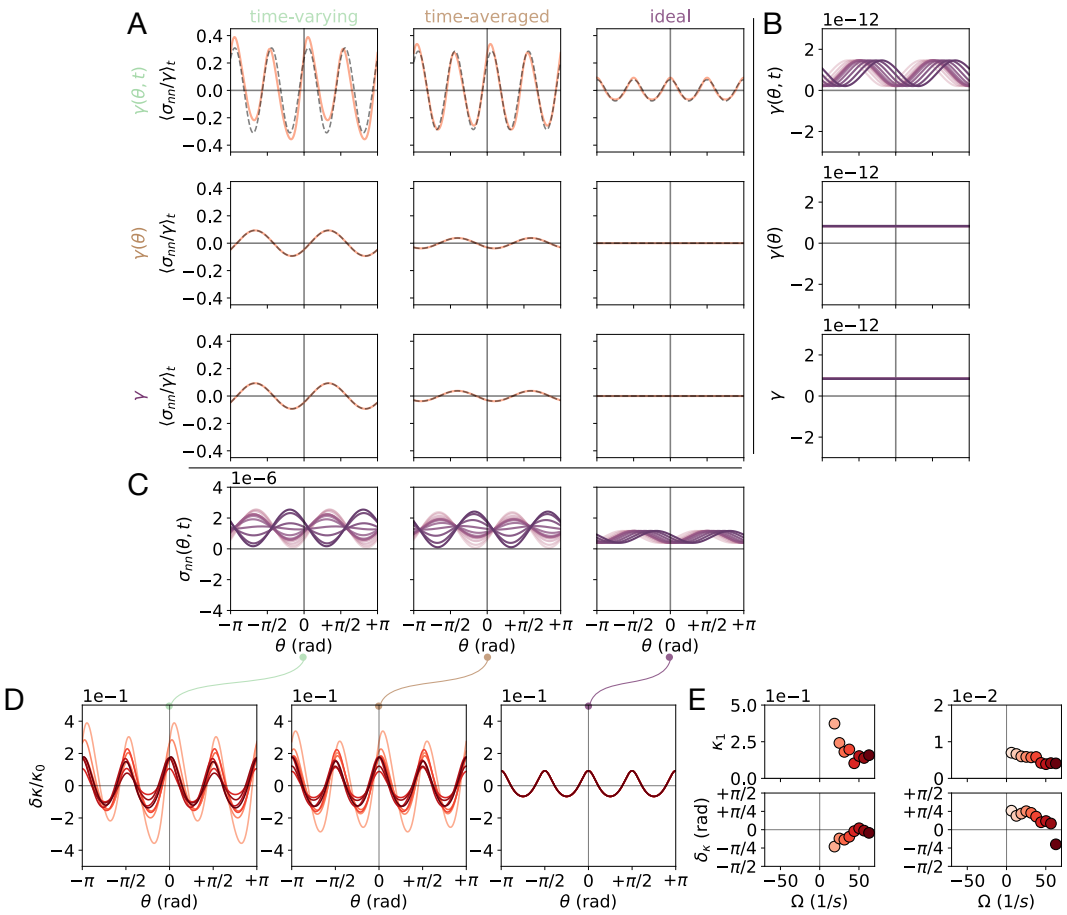

Figure 4.26: **Steady-state shape predictions for four-fold modulated drive.** (A) We compute the time-averaged stress ratio to estimate $\delta\kappa(\theta)$ in the four-fold modulated case for different assumptions regarding the unit cell deformation (columns) and surface tension anisotropy (rows). The time-evolution of the (B) surface tension and bulk normal stress (C) is indicated over a period of rotation. (D) The ratio is computed for each of these unit cell assumptions and for each drive frequency measured in the experiment. (E) The time-varying case is fit to obtain the amplitude and phase (left) and compared to the comparable measurement in the experiment (right).

REFERENCES

[1] Newton, I. *The Principia: mathematical principles of natural philosophy* (Univ of California Press, 1999).

[2] Gurtin, M. E. The linear theory of elasticity. In *Linear theories of elasticity and thermoelasticity*, 1–295 (Springer, 1973).

[3] Landau, L. D. & Lifshitz, E. M. *Fluid Mechanics: Landau and Lifshitz: Course of Theoretical Physics, Volume 6*, vol. 6 (Elsevier, 2013).

[4] Landau, L. D., Lifšic, E. M., Lifshitz, E. M., Kosevich, A. M. & Pitaevskii, L. P. *Theory of elasticity: volume 7*, vol. 7 (Elsevier, 1986).

[5] Wiegmann, P. & Abanov, A. G. Anomalous Hydrodynamics of Two-Dimensional Vortex Fluids. *Physical Review Letters* **113**, 034501 (2014).

[6] Avron, J. E., Seiler, R. & Zograf, P. G. Viscosity of Quantum Hall Fluids. *Physical Review Letters* **75**, 697–700 (1995).

[7] Avron, J. E. Odd Viscosity. *Journal of Statistical Physics* **92**, 543–557 (1998).

[8] Read, N. Non-Abelian adiabatic statistics and Hall viscosity in quantum Hall states and $p_x + ip_y$ paired superfluids. *Physical Review B* **79**, 045308 (2009).

[9] de Groot, S. P. & Mazur, P. *Non-Equilibrium Thermodynamics* (Dover Publications, New York, 1962).

[10] Scheibner, C. *et al.* Odd elasticity. *Nature Physics* **16**, 475–480 (2020).

[11] Poncet, A. & Bartolo, D. When soft crystals defy newton's third law: Nonreciprocal mechanics and dislocation motility. *Physical Review Letters* **128**, 048002 (2022).

[12] Brandenbourger, M., Scheibner, C., Veenstra, J., Vitelli, V. & Coulais, C. Limit cycles turn active matter into robots. *arXiv preprint arXiv:2108.08837* (2021).

[13] Chen, Y., Li, X., Scheibner, C., Vitelli, V. & Huang, G. Realization of active metamaterials with odd micropolar elasticity. *Nature Communications* **12**, 1–12 (2021).

[14] Tan, T. H. *et al.* Odd dynamics of living chiral crystals. *Nature* **607**, 287–293 (2022).

[15] Banerjee, D., Souslov, A., Abanov, A. G. & Vitelli, V. Odd viscosity in chiral active fluids. *Nature Communications* **8**, 1573 (2017).

[16] Han, M. *et al.* Fluctuating hydrodynamics of chiral active fluids. *Nature Physics* **17**, 1260–1269 (2021).

[17] Braverman, L., Scheibner, C., VanSaders, B. & Vitelli, V. Topological defects in solids with odd elasticity. *Physical Review Letters* **127**, 268001 (2021).

[18] Soni, V. *et al.* The odd free surface flows of a colloidal chiral fluid. *Nature Physics* **15**, 1188–1194 (2019).

[19] Bandurin, D. A. *et al.* Negative local resistance caused by viscous electron backflow in graphene. *Science* **351**, 1055–1058 (2016).

[20] Pringle, J. E. & King, A. *Astrophysical Flows* (Cambridge University Press, 2007).

[21] Secchi, E. *et al.* Massive radius-dependent flow slippage in carbon nanotubes. *Nature* **537**, 210–213 (2016).

[22] van Zuiden, B. C., Paulose, J., Irvine, W. T. M., Bartolo, D. & Vitelli, V. Spatiotemporal order and emergent edge currents in active spinner materials. *Proceedings of the National Academy of Sciences* **113**, 12919–12924 (2016).

[23] Lenz, P., Joanny, J.-F., Jülicher, F. & Prost, J. Membranes with Rotating Motors. *Physical Review Letters* **91**, 108104 (2003).

[24] Fürthauer, S., Strempel, M., Grill, S. W. & Jülicher, F. Active Chiral Processes in Thin Films. *Physical Review Letters* **110**, 048103 (2013).

[25] Kokot, G. *et al.* Active turbulence in a gas of self-assembled spinners. *Proceedings of the National Academy of Sciences* **114**, 12870–12875 (2017).

[26] Yeo, K. & Maxey, M. R. Rheology and ordering transitions of non-Brownian suspensions in a confined shear flow: Effects of external torques. *Physical Review E* **81**, 062501 (2010).

[27] Nguyen, N. H., Klotsa, D., Engel, M. & Glotzer, S. C. Emergent Collective Phenomena in a Mixture of Hard Shapes through Active Rotation. *Physical Review Letters* **112** (2014).

[28] Ariman, T., Turk, M. A. & Sylvester, N. D. Microcontinuum fluid mechanics–A review. *International Journal of Engineering Science* **11**, 905–930 (1973).

[29] Scaffidi, T., Nandi, N., Schmidt, B., Mackenzie, A. P. & Moore, J. E. Hydrodynamic Electron Flow and Hall Viscosity. *Physical Review Letters* **118**, 226601 (2017).

[30] Abanov, A., Can, T. & Ganeshan, S. Odd surface waves in two-dimensional incompressible fluids. *SciPost Physics* **5**, 010 (2018).

[31] Knaap, H. & Beenakker, J. Heat conductivity and viscosity of a gas of non-spherical molecules in a magnetic field. *Physica* **33**, 643–670 (1967).

[32] Hulsman, H. & Knaap, H. Experimental arrangements for measuring the five independent shear-viscosity coefficients in a polyatomic gas in a magnetic field. *Physica* **50**, 565–572 (1970).

[33] Petroff, A. P., Wu, X.-L. & Libchaber, A. Fast-Moving Bacteria Self-Organize into Active Two-Dimensional Crystals of Rotating Cells. *Physical Review Letters* **114**, 158102 (2015).

[34] Belovs, M. & Cēbers, A. Hydrodynamics with spin in bacterial suspensions. *Physical Review E* **93**, 062404 (2016).

[35] Grzybowski, B. A., Stone, H. A. & Whitesides, G. M. Dynamic self-assembly of magnetized, millimetre-sized objects rotating at a liquid-air interface. *Nature* **405**, 1033–1036 (2000).

[36] Grzybowski, B. A., Jiang, X., Stone, H. A. & Whitesides, G. M. Dynamic, self-assembled aggregates of magnetized, millimeter-sized objects rotating at the liquid-air interface: Macroscopic, two-dimensional classical artificial atoms and molecules. *Physical Review E* **64**, 011603 (2001).

[37] Grzybowski, B. A., Stone, H. A. & Whitesides, G. M. Dynamics of self assembly of magnetized disks rotating at the liquid-air interface. *Proceedings of the National Academy of Sciences* **99**, 4147–4151 (2002).

[38] Grzybowski, B. A. & Whitesides, G. M. Dynamic Aggregation of Chiral Spinners. *Science* **296**, 718–721 (2002).

[39] Yan, J., Bae, S. C. & Granick, S. Rotating crystals of magnetic Janus colloids. *Soft Matter* **11**, 147–153 (2014).

[40] Yan Jing, Bae Sung Chul & Granick Steve. Colloidal Superstructures Programmed into Magnetic Janus Particles. *Advanced Materials* **27**, 874–879 (2015).

[41] Rosensweig, R. E. *Ferrohydrodynamics* (Courier Corporation, 2013).

[42] Torres-Díaz, I. & Rinaldi, C. Recent progress in ferrofluids research: novel applications of magnetically controllable and tunable fluids. *Soft Matter* **10**, 8584–8602 (2014).

[43] Tsai, J.-C., Ye, F., Rodriguez, J., Gollub, J. P. & Lubensky, T. C. A Chiral Granular Gas. *Physical Review Letters* **94**, 214301 (2005).

[44] Scholz, C., Engel, M. & Pöschel, T. Rotating robots move collectively and self-organize. *Nature Communications* **9**, 931 (2018).

[45] Bacri, J.-C., Perzynski, R., Shliomis, M. I. & Burde, G. I. "negative-viscosity" effect in a magnetic fluid. *Physical Review Letters* **75**, 2128–2131 (1995).

[46] Climent, E., Yeo, K., Maxey, M. R. & Karniadakis, G. E. Dynamic Self-Assembly of Spinning Particles. *Journal of Fluids Engineering* **129**, 379–387 (2006).

[47] Goto, Y. & Tanaka, H. Purely hydrodynamic ordering of rotating disks at a finite Reynolds number. *Nature Communications* **6**, 5994 (2015).

[48] Yeo, K., Lushi, E. & Vlahovska, P. M. Collective Dynamics in a Binary Mixture of Hydrodynamically Coupled Microrotors. *Physical Review Letters* **114** (2015).

[49] Snezhko, A. Complex collective dynamics of active torque-driven colloids at interfaces. *Current Opinion in Colloid & Interface Science* **21**, 65–75 (2016).

[50] Sugimoto, T., Sakata, K. & Muramatsu, A. Formation Mechanism of Monodisperse Pseudocubic $\alpha - Fe_2O_3$ Particles from Condensed Ferric Hydroxide Gel. *Journal of Colloid and Interface Science* **159**, 372–382 (1993).

[51] Rossi, L. *Colloidal superballs* (Utrecht University, 2012). OCLC: 6893354969.

[52] Cladé, P. PyDAQmx: a Python interface to the National Instruments DAQmx driver. URL `http://pythonhosted.org/PyDAQmx/`.

[53] Allan, Daniel and, Caswell, Thomas and, Keim, Nathan and & van der Wel, Casper. trackpy v0.3.2 (2016). URL `https://doi.org/10.5281/zenodo.60550`.

[54] Bacri, J.-C., Cebers, A. O. & Perzynski, R. Behavior of a magnetic fluid microdrop in a rotating magnetic field. *Physical Review Letters* **72**, 2705–2708 (1994).

[55] Bonthuis, D. J., Horinek, D., Bocquet, L. & Netz, R. R. Electrohydraulic Power Conversion in Planar Nanochannels. *Physical Review Letters* **103**, 144503 (2009).

[56] Dahler, J. S. & Scriven, L. E. Theory of Structured Continua. I. General Consideration of Angular Momentum and Polarization. *Proceedings of the Royal Society of London A: Mathematical, Physical and Engineering Sciences* **275**, 504–527 (1963).

[57] Huang, H.-F., Zahn, M. & Lemaire, E. Continuum modeling of micro-particle electrorotation in Couette and Poiseuille flows:The zero spin viscosity limit. *Journal of Electrostatics* **68**, 345–359 (2010).

[58] Cowin, S. C. Polar Fluids. *The Physics of Fluids* **11**, 1919–1927 (1968).

[59] Brenner, H. & Nadim, A. The Lorentz reciprocal theorem for micropolar fluids. *Journal of Engineering Mathematics* **30**, 169–176 (1996).

[60] Radin, S. Lorentz Plasma in a Strong Magnetic Field. *The Physics of Fluids* **15**, 91–95 (1972).

[61] Robinson, B. B. & Bernstein, I. B. A variational description of transport phenomena in a plasma. *Annals of Physics* **18**, 110–169 (1962).

[62] Pitaevskii, L. P. & Lifshitz, E. M. *Physical Kinetics* (Butterworth-Heinemann, Oxford, UK, 1981).

[63] Rossi, L. *et al.* Self-organization in dipolar cube fluids constrained by competing anisotropies. *Soft Matter* **14**, 1080–1087 (2018).

[64] Krauß, R., Reimann, B., Richter, R., Rehberg, I. & Liu, M. Fluid pumped by magnetic stress. *Applied Physics Letters* **86**, 024102 (2005).

[65] Krauß, R., Liu, M., Reimann, B., Richter, R. & Rehberg, I. Pumping fluid by magnetic surface stress. *New Journal of Physics* **8**, 18 (2006).

[66] Chaves, A. & Rinaldi, C. Interfacial stress balances in structured continua and free surface flows in ferrofluids. *Physics of Fluids* **26**, 042101 (2014).

[67] Andreotti, B., Forterre, Y. & Pouliquen, O. *Granular Media* (Cambridge University Press).

[68] Souslov, A., Dasbiswas, K., Fruchart, M., Vaikuntanathan, S. & Vitelli, V. Topological Waves in Fluids with Odd Viscosity. *Physical Review Letters* **122**, 128001 (2019).

[69] Eggers, J. Nonlinear dynamics and breakup of free-surface flows. *Reviews of Modern Physics* **69**, 865–930 (1997).

[70] Kropinski, M. C. A. An Efficient Numerical Method for Studying Interfacial Motion in Two-Dimensional Creeping Flows. *Journal of Computational Physics* **171**, 479–508 (2001).

[71] Bililign, E. S. *et al.* Motile dislocations knead odd crystals into whorls. *Nature Physics* **18**, 212–218 (2022).

[72] Chaikin, P. M., Lubensky, T. C. & Witten, T. A. *Principles of condensed matter physics*, vol. 10 (Cambridge university press Cambridge, 1995).

[73] Strandburg, K. J. Two-dimensional melting. *Reviews of Modern Physics* **60**, 161–207 (1988).

[74] Bishop, D. J. & Reppy, J. D. Study of the superfluid transition in two-dimensional ^{4}He films. *Physical Review Letters* **40**, 1727–1730 (1978).

[75] Zahn, K., Lenke, R. & Maret, G. Two-stage melting of paramagnetic colloidal crystals in two dimensions. *Physical Review Letters* **82**, 2721–2724 (1999).

[76] Alsayed, A. M., Islam, M. F., Zhang, J., Collings, P. J. & Yodh, A. G. Premelting at defects within bulk colloidal crystals. *Science* **309**, 1207–1210 (2005).

[77] Meng, G., Paulose, J., Nelson, D. R. & Manoharan, V. N. Elastic instability of a crystal growing on a curved surface. *Science* **343**, 634–637 (2014).

[78] Thorneywork, A. L., Abbott, J. L., Aarts, D. G. A. L. & Dullens, R. P. A. Two-dimensional melting of colloidal hard spheres. *Physical Review Letters* **118**, 158001 (2017).

[79] Cafiero, R., Luding, S. & Herrmann, H. J. Rotationally driven gas of inelastic rough spheres. *EPL (Europhysics Letters)* **60**, 854 (2002).

[80] Kokot, G., Piet, D., Whitesides, G. M., Aranson, I. S. & Snezhko, A. Emergence of reconfigurable wires and spinners via dynamic self-assembly. *Scientific Reports* **5** (2015).

[81] Shen, Z. & Lintuvuori, J. S. Two-phase crystallization in a carpet of inertial spinners. *Physical Review Letters* **125**, 228002 (2020).

[82] Liu, P. *et al.* Oscillating collective motion of active rotors in confinement. *Proceedings of the National Academy of Sciences* **117**, 11901–11907 (2020).

[83] Armitage, P. J. Turbulence and angular momentum transport in a global accretion disk simulation. *The Astrophysical Journal Letters* **501**, L189 (1998).

[84] Petroff, A. P., Wu, X.-L. & Libchaber, A. Fast-moving bacteria self-organize into active two-dimensional crystals of rotating cells. *Physical Review Letters* **114**, 158102 (2015).

[85] Oppenheimer, N., Stein, D. B. & Shelley, M. J. Rotating membrane inclusions crystallize through hydrodynamic and steric interactions. *Physical Review Letters* **123**, 148101 (2019).

[86] Aubret, A., Youssef, M., Sacanna, S. & Palacci, J. Targeted assembly and synchronization of self-spinning microgears. *Nature Physics* **14**, 1114–1118 (2018).

[87] Lim, M. X., Souslov, A., Vitelli, V. & Jaeger, H. M. Cluster formation by acoustic forces and active fluctuations in levitated granular matter. *Nature Physics* **15**, 460–464 (2019).

[88] Bouchet, F. & Venaille, A. Statistical mechanics of two-dimensional and geophysical flows. *Physics reports* **515**, 227–295 (2012).

[89] Baroud, C. N., Plapp, B. B., She, Z.-S. & Swinney, H. L. Anomalous self-similarity in a turbulent rapidly rotating fluid. *Physical Review Letters* **88**, 114501 (2002).

[90] Korving, J., Hulsman, H., Knaap, H. & Beenakker, J. Transverse momentum transport in viscous flow of diatomic gases in a magnetic field. *Physics Letters* **21**, 5–7 (1966).

[91] Hoyos, C., Moroz, S. & Son, D. T. Effective theory of chiral two-dimensional superfluids. *Physical Review B* **89**, 174507 (2014).

[92] Souslov, A., Dasbiswas, K., Fruchart, M., Vaikuntanathan, S. & Vitelli, V. Topological waves in fluids with odd viscosity. *Physical Review Letters* **122**, 128001 (2019).

[93] Eyink, G. L. & Sreenivasan, K. R. Onsager and the theory of hydrodynamic turbulence. *Reviews of Modern Physics* **78**, 87 (2006).

[94] Lavergne, F. m. c. A., Aarts, D. G. A. L. & Dullens, R. P. A. Anomalous grain growth in a polycrystalline monolayer of colloidal hard spheres. *Physical Review X* **7**, 041064 (2017).

[95] Meijer, J.-M. & Rossi, L. Preparation, properties, and applications of magnetic hematite microparticles. *Soft Matter* (2021).

[96] Lavergne, F. m. c. A., Aarts, D. G. A. L. & Dullens, R. P. A. Anomalous grain growth in a polycrystalline monolayer of colloidal hard spheres. *Physical Review X* **7**, 041064 (2017).

[97] Dillmann, P., Maret, G. & Keim, P. Polycrystalline solidification in a quenched 2d colloidal system. *Journal of Physics: Condensed Matter* **20**, 404216 (2008).

[98] Anderson, J. A., Glaser, J. & Glotzer, S. C. Hoomd-blue: A python package for high-performance molecular dynamics and hard particle monte carlo simulations. *Computational Materials Science* **173**, 109363 (2020).

[99] Blake, J. R. A note on the image system for a stokeslet in a no-slip boundary. *Mathematical Proceedings of the Cambridge Philosophical Society* **70**, 303 (1971).

[100] Gimbutas, Z., Greengard, L. & Veerapaneni, S. Simple and efficient representations for the fundamental solutions of stokes flow in a half-space. *Journal of Fluid Mechanics* **776**, R1 (2015).

[101] Jackson, J. D. *Classical Electrodynamics* (John Wiley and Sons, 1962).

[102] Balboa Usabiaga, F. *et al.* Hydrodynamics of suspensions of passive and active rigid particles: a rigid multiblob approach. *Communications in Applied Mathematics and Computational Science* **11**, 217–296 (2016).

[103] Rotne, J. & Prager, S. Variational treatment of hydrodynamic interaction in polymers. *Journal of Chemical Physics* **50**, 4831 (1969).

[104] Wajnryb, E., Mizerski, K. A., Zuk, P. J. & Szymczak, P. Generalization of the rotne–prager–yamakawa mobility and shear disturbance tensors. *Journal of Fluid Mechanics* **731**, R3 (2013).

[105] Swan, J. W. & Brady, J. F. Simulation of hydrodynamically interacting particles near a no-slip boundary. *Physics of Fluids* **19**, 113306 (2007).

[106] Yan, W. & Shelley, M. Universal image system for non-periodic and periodic stokes flows above a no-slip wall. *Journal of Computational Physics* **375**, 263–270 (2018).

[107] Yan, W. & Blackwell, R. Kernel aggregated fast multipole method: Efficient summation of laplace and stokes kernel functions. *Advances in Computational Mathematics* **47**, 69 (2021).

[108] Kim, S. & Karrila, S. J. *Microhydrodynamics: principles and selected applications* (Butterworth-Heinemann, 1991).

[109] Yan, W. & Brady, J. F. The swim force as a body force. *Soft Matter* **11**, 6235–6244 (2015).

[110] Jeffrey, D. J. & Onishi, Y. Calculation of the resistance and mobility functions for two unequal rigid spheres in low-reynolds-number flow. *Journal of Fluid Mechanics* **139**, 261–290 (1984).

[111] Durlofsky, L., Brady, J. F. & Bossis, G. Dynamic simulation of hydrodynamically interacting particles. *Journal of Fluid Mechanics* **180**, 21 (1987).

[112] Peierls, R. Reports on progress of physics. *The Physical Society,(London) Vol. VI* **78** (1939).

[113] Nabarro, F. Dislocations in a simple cubic lattice. *Proceedings of the Physical Society* **59**, 256 (1947).

[114] Schall, P., Cohen, I., Weitz, D. A. & Spaepen, F. Visualization of dislocation dynamics in colloidal crystals. *Science* **305**, 1944–1948 (2004).

[115] Weinberger, C. R. & Cai, W. Surface-controlled dislocation multiplication in metal micropillars. *Proceedings of the National Academy of Sciences* **105**, 14304–14307 (2008).

[116] Irvine, W. T. M., Hollingsworth, A. D., Grier, D. G. & Chaikin, P. M. Dislocation reactions, grain boundaries, and irreversibility in two-dimensional lattices using topological tweezers. *Proceedings of the National Academy of Sciences* **110**, 15544–15548 (2013).

[117] Amir, A. & Nelson, D. R. Dislocation-mediated growth of bacterial cell walls. *Proceedings of the National Academy of Sciences* **109**, 9833–9838 (2012).

[118] Deutschländer, S., Dillmann, P., Maret, G. & Keim, P. Kibble–zurek mechanism in colloidal monolayers. *Proceedings of the National Academy of Sciences* **112**, 6925–6930 (2015).

[119] Sanchez, T., Chen, D. T., DeCamp, S. J., Heymann, M. & Dogic, Z. Spontaneous motion in hierarchically assembled active matter. *Nature* **491**, 431–434 (2012).

[120] Epstein, J. M. & Mandadapu, K. K. Time-reversal symmetry breaking in two-dimensional nonequilibrium viscous fluids. *Physical Review E* **101**, 052614 (2020).

[121] Kitagawa, T., Berg, E., Rudner, M. & Demler, E. Topological characterization of periodically driven quantum systems. *Physical Review B* **82**, 235114 (2010).

[122] Choi, S. *et al.* Observation of discrete time-crystalline order in a disordered dipolar many-body system. *Nature* **543**, 221–225 (2017).

[123] Zhang, J. *et al.* Observation of a discrete time crystal. *Nature* **543**, 217–220 (2017).

[124] Souslov, A., Gromov, A. & Vitelli, V. Anisotropic odd viscosity via a time-modulated drive. *Physical Review E* **101**, 052606 (2020).